Characterization of Steels
by
Anomalous Small-Angle X-ray Scattering

Peter René Jemian

June 1990

Abstract

Characterization of Steels by Anomalous Small-Angle X-ray Scattering
Peter René Jemian

The size distribution and volume fraction of $Cr_{23}C_6$ have been isolated from the distributions of all other precipitates in aged samples of a ferritic alloy, Modified Fe9Cr1Mo steel, by the technique of anomalous small-angle X-ray scattering (ASAXS), in what is believed to be the first application of this technique to precipitation in an engineering alloy. The steel has been proposed for use at elevated temperatures for long times in power generation equipment and the stability of the microstructure must be verified. Six samples were aged for 5000 hours at either room temperature, 482, 538, 593, 649, or 704° C to simulate a typical in-service condition. Synchrotron radiation was used as a variable-wavelength source of X-rays. Three X-ray wavelengths near the Cr K absorption edge were used to vary the scattering contrast of $Cr_{23}C_6$ while leaving that of the other precipitates fixed. A double-crystal diffractometer and a silicon photodiode X-ray detector were specially designed for use at the synchrotron to measure the scattered radiation. The three small-angle scattering curves from each sample were analyzed by a maximum entropy technique to obtain three scattering contrast-weighted size distributions of all the precipitates that give rise to the observed scattering. A scattering contrast gradient analysis combined the three experiments to isolate the $Cr_{23}C_6$ volume fraction distributions. The mean diameter of $Cr_{23}C_6$ particles was found to increase with temperature for 5000 hour aging between 538 and 704° C, consistent with prior transmission electron microscopy results.

The ultra-high strength steel alloy AF1410, currently used for arresting hooks on carrier-based aircraft, derives its desirable properties by a delicate heat treatment that carefully balances the formation of one carbide with the depletion of another. The lack of ASAXS near the Cr and Fe K absorption edges indicates that the distributions of precipitates observed (presumably M_3C and austenite) are iron-enriched and chromium-deficient.

Approved by Professor Julia R. Weertman

Preface

ceiiinosssttuv - Robert HOOKE, 1676

Chapter 1 provides information about the ASAXS investigations of other workers and also some background on the two steel alloys investigated by the ASAXS technique. In Chapter 2, the theory underlying small-angle scattering and the specific ASAXS application, equations that describe the design and operation of the DCD optics, the process of resonant Raman scattering, and a general description of the silicon photodiode detector are given. The experimental equipment and procedure are described in Chapter 3. Chapter 4 describes the experimental commissioning of the new DCD and photodiode detector using the scattering of polystyrene spheres and bulk microporous silica. Also given there are the SAXS and ASAXS results for the two steels alloys being investigated. These data are summarized in Chapter 5 and suggestions for future investigations with the DCD are presented. In the first appendix, the results of SAXS experiments on other materials of interest in materials science are given. These materials are bulk microporous silica and porous Vycor^{TM} glass. Other appendices contain the electrical schematics for the Si photodiode detector, the computer programs for collimation correction, `Lake.FOR`, and interpretation of small-angle scattering, `MaxSAS.FOR`, and the experimental SAXS data for the steels.

SI units are reported throughout with the exception of degrees Celsius, rather than Kelvins, and mass density in g·cm^{-3}. The wavelength, λ, of X-ray photons is described in terms of their photon energy, E, where the relation $E\lambda = 1.239857804$ nm keV is used. Usage of nomenclature will be kept consistent within each section of the text or explicitly noted. For style, this work follows guidelines set forth by Michaelson,[98] but also takes advice from the remarks of Mermin.[97] Arguments on computer programming style[15, 17, 100] were also considered.

Acknowledgements

ut tensio sic vis - Robert Hooke, 1678

I am grateful to my advisor, Professor Julia R. Weertman, for her encouragement, guidance, and financial support throughout this study. I would like to express my great appreciation to Dr. Gabrielle G. Long of the National Institute of Standards and Technology for numerous illuminating discussions and many$^{\infty}$ long hours at the synchrotron. Additionally, I would like to thank Dr. Joe Georgopoulos for materials, advice, and assistance in the early stages of this project and Dr. Greg Olson for samples and helpful advice. Special thanks go to Mr. Rich Matteson for advising a change of career from jazz music. I think he would be proud. This research was supported by the United States Department of Energy under grant DE-FG02-86ER45229. Dean J. B. Cohen is to be acknowledged for his initial suggestion that anomalous dispersion might be used to separate the small-angle scattering from one type of scatterer in a multi-component alloy. From the Oak Ridge National Laboratory, Dr. Vinod Sikka is acknowledged for providing the Modified Fe9Cr1Mo steel, Dr. George Wignall and Dr. S. Spooner for conducting small-angle X-ray scattering measurements at the National Center for Small-Angle Scattering Research, and Dr. A. Habenschuss for the `fPrime.FOR` code which was obtained via Dean J. B. Cohen. The UKAEA-Harwell laboratory is acknowledged for the `Maxe.FOR` maximum entropy SAS analysis code. Dr. Richard D. Spal of NIST is to be acknowledged for his support of the experimental phase by providing assistance at the synchrotron beam line.

To the members of the All-Night Scattering Crew at the synchrotron who engaged themselves in a practical study of the long-term effects at ambient to cryogenic temperatures of low-cycle fatigue of materials scientists: Dr. Andrew Allen, Dr. David Black, Dr. Didier Gavillet, Dr. Gabrielle Long, Dr. Julia Weertman, Mr. John Barker, and Mr. Kishio Hidaka are to be commended for their abilities to fight the Four AM fatigue. Special thanks go to Mr. Harold *Hal of the Golden Hands* Burdette of NIST for assistance in design, mechanics, and construction of the DCD SAXS camera.

Appreciation is extended to my colleagues at Northwestern University, both past and present for their valuable discussion, friendly harangues, and general camaraderie. Particular thanks go to Mr. Mike Verrilli whose graphical machinations with SAS data provided the realization of how to process the SAS data more efficiently. Also, special thanks are extended to the personnel in the Chemistry Department Electronics Shop (especially the late Mr. Jim Baker), Materials Science "world's friendliest" Machine Shop, Metallography Lab, TEM facility, and X-ray diffraction facility. Last but not least, I acknowledge the guidance of my parents who at key bifurcation points in my development provided a gentle nudge or even a strong tug in what time has proven to be the right direction.

Contents

1 Introduction **1**

1.1 Anomalous Dispersion Small-Angle X-ray Scattering (ASAXS) . . . 1

1.1.1 Metallurgical Applications . . . 2

1.1.2 Other Applications . . . 2

1.2 Steel Alloy Descriptions . . . 2

1.2.1 Modified Fe9Cr1Mo Steel . . . 2

1.2.2 AF1410 Steel . . . 4

2 Theory **7**

2.1 Small-Angle Scattering (SAS) . . . 7

2.1.1 Basic SAS Theory . . . 7

2.1.2 Scattering from Spherical Particles . . . 9

2.1.3 Instrumental Collimation Correction . . . 9

2.1.4 Size Distribution Analysis by Maximum Entropy Technique . . . 11

2.2 Anomalous Dispersion Small-Angle X-ray Scattering (ASAXS) . . . 14

2.2.1 Anomalous Dispersion and the Dispersion Corrections . . . 14

2.2.2 Scattering Length Density, Contrast, and Strength . . . 15

2.2.3 Experiment Requirements for ASAXS . . . 18

2.2.4 Limits of Detectability . . . 18

2.2.5 Isolation of a Single Scatterer by ASAXS . . . 18

2.3 Resonant Raman Scattering . . . 21

2.4 Double-Crystal Diffractometer Camera (DCD) . . . 22

2.4.1 Bonse-Hart Design . . . 22

2.4.2 Optimization of the Optics for the Synchrotron Source . . . 24

2.4.3 Rocking Curve Calculation . . . 25

2.4.4 Asymmetric Reflection . . . 26

2.5 Silicon Photodiode Detector . . . 27

2.5.1 Principles of Operation . . . 27

2.5.2 Amplifier Electronics . . . 28

3 Experimental **31**

3.1 Steel Samples . . . 31

3.1.1 Heat Treatment . . . 31

3.2 SAXS Sample Preparation . . . 31

3.3 Equipment . . . 32
3.3.1 X-ray Source . . . 32
3.3.2 Monochromator . . . 33
3.3.3 Experimental Hutch . . . 34
3.3.4 Beam Transport and Incident Beam Monitor . . . 34
3.3.5 Double-Crystal Diffractometer Analyzer Monolith . . . 34
3.4 Silicon Photodiode X-ray Detector . . . 35
3.5 Computer Data Acquisition . . . 36
3.6 Data Reduction . . . 36
3.7 Raw Data . . . 37
3.8 Absolute Intensity Conversion . . . 37
3.9 Slit-Length Desmearing . . . 38
3.10 Size Distribution Analysis . . . 38

4 Results and Discussion **41**
4.1 Validation of Equipment . . . 41
4.1.1 Polystyrene Spheres: 255 and 460 nm diameters . . . 41
4.1.2 Silicon Photodiode Detector vs. Scintillation Counter . . . 43
4.1.3 Absolute Intensity Correlation . . . 44
4.1.4 Slit-Width Correction . . . 45
4.2 Modified Fe9Cr1Mo Steel . . . 48
4.2.1 Sample Thickness Measurements . . . 48
4.2.2 Measurement of Anomalous Dispersion Corrections . . . 49
4.2.3 Scattering Strength-Weighted Size Distribution Analyses . . . 52
4.2.4 Calculation of the Scattering Contrasts . . . 57
4.2.5 $Cr_{23}C_6$ Volume Fraction Distribution Isolated by ASAXS . . . 60
4.2.6 Summary of Modified Fe9Cr1Mo Steel Analyses . . . 67
4.3 AF1410 Steel . . . 68
4.3.1 ASAXS Analyses . . . 68
4.3.2 Austenitized at 1000° C . . . 70
4.3.3 Austenitized at 830° C . . . 73
4.3.4 Discussion . . . 73
4.3.5 Summary of the AF1410 SAXS analysis . . . 76

5 Summary **77**
5.1 Suggestions for Future Work . . . 79

Appendix: Other Samples **81**
A Bulk Microporous Silica . . . 81
B Porous Vycor™ Glass . . . 83

Appendix: Silicon Photodiode Detector **85**
C Implementation of the Silicon Photodiode Detector . . . 85
D Circuit Diagrams for the Modular Detector . . . 87

Appendix: FORTRAN Computer Programs **89**
E `Lake.FOR`: Iterative Collimation-Correction 89
F `MaxSAS.FOR`: Size Distribution Analysis 105

Index **137**

List of Tables

1.1 Composition (weight percent) of Modified Fe9Cr1Mo steel. . . . 3
1.2 Observed metal site percentages of carbides in Modified Fe9Cr1Mo steel, crept at 650° C. . . . 3
1.3 Nominal composition of AF1410 steel. . . . 5
1.4 Carbides observed[45] in as-quenched AF1410 steel. . . . 5

2.1 Observed minimum limits of ASAXS detectability. . . . 19
2.3 Measured Intensity at the Sample Position in the Diffraction Orders. . . . 24
2.2 X-ray Source, Ge_{111} Asymmetric ($\alpha = 7°$) Crystal, and DCD Camera Parameters . . . 25

4.1 Parameters of the model Gaussian distribution for polystyrene spheres samples. . . . 43
4.2 Thickness, μm, of the Modified Fe9Cr1Mo steel SAXS samples. . . . 49
4.3 Backgrounds of SAXS experiments on the Modified Fe9Cr1Mo steel. . . . 55
4.4 Modified Fe9Cr1Mo steel crystal structure information for calculating $|\Delta\rho|^2$. . . . 59
4.5 X-ray scattering contrast, $|\Delta\rho|^2$, (with respect to the matrix composition) of carbo-nitrides in Modified Fe9Cr1Mo. . . . 59
4.6 Volume fraction size distribution summary of the $Cr_{23}C_6$ scatterers in Modified Fe9Cr1Mo steel as determined by ASAXS. . . . 62
4.7 Number density size distribution summary of the $Cr_{23}C_6$ scatterers in Modified Fe9Cr1Mo steel as determined by ASAXS. . . . 62
4.8 Total particle surface area summary of the $Cr_{23}C_6$ scatterers in Modified Fe9Cr1Mo steel as determined by ASAXS. . . . 62
4.9 Definition of each term in the statistical summary of the size distributions. . . . 63
4.10 Compositions of cementite at para-equilibrium and 510° C ortho-equilibrium. . . . 69
4.11 Summary of maximum entropy distributions for AF1410 austenitized at 1000° C. . . . 72
4.12 V_f of precipitates in AF1410 steel austenitized at 1000° C. . . . 73
4.13 Summary of maximum entropy distributions for AF1410 austenitized at 830° C. . . . 75
4.14 V_f of precipitates in AF1410 steel austenitized at 830° C. . . . 75
4.15 AF1410 steel crystal structure information for calculating $|\Delta\rho|^2$. . . . 76

A1 Parameters from 10 keV SAXS analysis of bulk microporous silica samples. . . . 82
B2 Parameters from SAXS analysis of porous Vycor™ glass. . . . 84

List of Figures

1.1 Morphological evolution of principal carbides in steels with 9–12% Cr and 1–2% Mo. 3
1.2 Carbide reaction sequence[103] applicable to low silicon Fe12Cr1.5MoVNb steel. 4
1.3 Reaction sequence[102] applicable to the tempering of Fe2.25Cr1Mo steel. 4
1.4 Precipitate reactions reported[83] on tempering of AF1410 steel. 5
1.5 Bright field transmission electron micrographs of AF1410 steel. 6

2.1 The slit-length weighting function, P_l. 9
2.2 Anomalous dispersion terms $f'(E)$ and $f'(E)$. 16
2.3 The (1,-1) geometry of the 1×1 two crystal *spectrometer* for small-angle scattering.[68] 23
2.4 Intensity profile, $D(y)$, of a single reflection from a perfect single crystal. 26
2.5 X-ray beam spatial magnification using an hypothetical crystal with an asymmetric cut. 26
2.6 Schematic of a current-to-voltage (CV) converting amplifier. 29

3.1 SAXS camera at NSLS beam line X23A3. 33
3.2 SAXS camera analyzer stage. 36
3.3 Plot of the standardized residuals. 39

4.1 Collimation-corrected SAXS of 255 nm PS spheres. 42
4.2 Collimation-corrected SAXS of 460 nm PS spheres. 42
4.3 SAXS data recorded using a scintillation counter. 44
4.4 SAXS data recorded using a silicon photodiode detector. 45
4.5 Comparison of DCD SAXS with pinhole SAXS intensity for Modified Fe9Cr1Mo steel. 46
4.6 Comparison of absolute SAXS and SANS intensity for bulk microporous silica. 46
4.7 Magnification 460 nm spheres SAXS: effect of optics on central width. 47
4.8 Magnification 460 nm spheres SAXS: effect of optics on SAXS. 48
4.9 $I/I_o(E)$, of N&T Modified Fe9Cr1Mo steel near Cr K edge. 50
4.10 Mass absorption coefficient of a normalized and tempered Modified Fe9Cr1Mo steel. 50
4.11 Mass absorption coefficient of Cr in Modified Fe9Cr1Mo steel. 50
4.12 $f''_{Cr}(E)$ (from transmission measurements on Modified Fe9Cr1Mo steel). 51
4.13 $f'_{Cr}(E)$ near the Cr K edge. 51
4.14 Magnification of Fig. 4.13 in the bottom region of the $f'(E)$ well. 52
4.15 Argand diagram of measured $f''(E)$ vs. $f'(E)$ data for Cr. 52
4.16 SAXS from a sample of Modified Fe9Cr1Mo steel aged 5000 hours at 482° C. 53
4.17 Maximum entropy scattering strength distributions for the 482° C sample. 54

4.18 Total scattering strength, X, of all scatterers in Modified Fe9Cr1Mo steel. 56
4.19 $\bar{D}(T)$ of all scatterers in Modified Fe9Cr1Mo steel. 56
4.20 TEM of Modified Fe9Cr1Mo steel: N&T, 482°, and 538° C. 57
4.21 TEM of Modified Fe9Cr1Mo steel: 593°, 649°, and 704° C. 58
4.22 $|\Delta\rho|^2(E)$ for carbides in Modified Fe9Cr1Mo steel. 59
4.23 Size distributions of $Cr_{23}C_6$ in Modified Fe9Cr1Mo steel. 61
4.24 V_f of $Cr_{23}C_6$ in Modified Fe9Cr1Mo steel. 64
4.25 $\bar{D}_v$ of $Cr_{23}C_6$ in Modified Fe9Cr1Mo steel. 64
4.26 N_v of $Cr_{23}C_6$ in Modified Fe9Cr1Mo steel. 64
4.27 Λ of $Cr_{23}C_6$ in Modified Fe9Cr1Mo steel. 64
4.28 S_v of $Cr_{23}C_6$ in Modified Fe9Cr1Mo steel. 67
4.29 Raw data SAXS from the AF1410 steel samples showing the typical low signal-to-noise ratio. 69
4.30 $x_T(D)$ of sphere-equivalent scatterers in AF1410 steel austenitized at 1000°C. 71
4.31 Total scattering strength from distributions of scatterers in AF1410 steel austenitized at 1000° C. . . . 72
4.33 Total scattering strength of scatterers in AF1410 steel austenitized at 830° C. 73
4.32 $x(D)$ of scatterers in AF1410 steel samples austenitized at 830° C. 74
4.34 X-ray scattering contrast calculated for cementite in AF1410 steel. 76

A1 SAXS of 10:90 bulk microporous silica, 10 & 11 keV. 82
A2 SAXS of bulk microporous silica samples at 10 keV. 82
B3 SAXS from porous Vycor™ glass 83

C1 Photodiode detector block diagram. 85
C2 Circuit schematic of photodiode detector. 86
D3 DC power supply modifications. 87
D4 Circuit for detector amplifier board. 87
D5 Circuits for detector control and inverter boards. 88
D6 Circuits for detector remote control and V/f converter. 88

Chapter 1

Introduction

Several topics are addressed by this dissertation, inspired by the goal of observing the population of a single type of precipitate in the presence of several different types, especially in ferritic steels of engineering significance. Anomalous small-angle X-ray scattering (ASAXS) is the method used for the investigations and much of the information presented describes this relatively new technique.

The specific application of SAXS to observe precipitates of size 0.05 to 1 μm in steel alloys required the development of new experimental equipment. Although a pinhole SAXS camera with an associated area detector provides a simple experimental arrangement, the angular resolution for realistic physical camera lengths is not sufficient to resolve scatterers within this size range. Other portions of this work describe the theory, design, operation, and commissioning of a double-crystal diffractometer (DCD) SAXS camera, capable of resolving scatterers as large as a few micrometers. Results from the DCD demonstrate the enormous benefit in angular resolution obtained by the increase in experimental complexity. An important advantage of the DCD over pinhole cameras is its compact design.

The advantage of high source flux offered by the synchrotron is usually a serious problem for X-ray detectors such as scintillation counters and gas proportional counters. These detectors operate in a photon counting mode, and with high counting rates become decidedly non-linear, possibly incurring physical damage. High count rates are inherent in SAXS, when the largest dimensions are observed in close angular proximity to the direct beam. The pulse-mode detector limitations are overcome by using the silicon photodiode X-ray detector described here. Photodiodes operate in current mode so that they integrate the number of photons absorbed over time rather than count individual photons. Physical damage by exposure to high intensity synchrotron beams has not been observed in the photodiodes used by beam lines X23 and X24 at the NSLS.

With a new experimental technique, as well as new instrumentation, much of the experimental work described in the results dwells on the operation of the instrumentation, verifying that the SAXS recorded are free of instrumental artifacts. Analysis of the scattering patterns from a variety of samples supports the quality of the reported SAXS from the steel; that it is devoid of instrumental artifacts. These ancillary results are further used to highlight advantages and limitations of the instrument and the procedures of data reduction and interpretation.

1.1 Anomalous Dispersion Small-Angle X-ray Scattering (ASAXS)

Anomalous dispersion small-angle X-ray scattering (ASAXS) refers to a multiple-wavelength series of small-angle X-ray scattering measurements that exploit the physical phenomenon of anomalous dispersion to affect a variation in the contrast of scatterers. This phenomenon, reviewed on pp. 135-192 of the book by James,[64] occurs when the X-ray photon energy ($E = hc/\lambda$) is close to the binding energy of an electron of an element in the sample. Here, h is Planck's constant, c is the speed of light, and λ is the photon wavelength. As the binding energy

is approached, the atomic scattering factor drops anomalously. The drop is produced by resonance effects on the X-ray photon by the bound electron. As the energy of the X-ray photons is increased above the binding energy, there is a significant increase in the absorption of X-rays, as required for the liberation of the bound electron.

Each of the SAXS experiments in the multiple-wavelength series is conducted under monochromatic conditions where the experiments differ only by the energy of the incident X-ray photons. An X-ray source of relatively constant intensity across the entire energy range is required. Bremsstrahlung radiation from a laboratory X-ray source exhibits this behavior but that intensity is too low for small-angle scattering work. Characteristic radiation also offers high intensity in the laboratory but is available at select photon energies. Only with the advent of synchrotron radiation has the practical application of ASAXS been a practical possibility because of the high intensity across a broad X-ray spectrum. Evidence of this comes from the number of recent publications[29,31,32,46–48,58–62,88–91,115,120–126,133–138] as well as anomalous wide-angle X-ray scattering.[41]

SAXS experiments are used to characterize the nanometer- to micrometer-scale structure of a sample. The scattering is produced by differences in the scattering length density. For X-rays, the scattering length density is the dimension of an electron multiplied by the effective electron density averaged over about a nanometer. When the electrons respond in resonance to the X-ray photons, via the anomalous dispersion effect, the effective electron density drops. For scatterers with a strong concentration difference in the anomalous element, the scatterers are then labeled. This is the mechanism by which multiple-photon energy ASAXS, can be used to extract information from experiments that were indeterminate with a single photon energy SAXS experiment.

1.1.1 Metallurgical Applications

All the metallurgical studies from the above list (work of Goudeau, Hoyt, Lyon, and Simon) have used ASAXS to reveal information about phase diagrams during the early stages of unmixing in binary and ternary solid solutions. This was accomplished by extracting the partial structure functions from the scattering curve to obtain information about each of the elements in the sample. With de Fontaine, Simon and Lyon[120] compared ASAXS to another well-known contrast variation technique, isotopic substitution in small-angle neutron scattering (ISANS). The contrast variation in ISANS is affected by substituting a different atomic isotope in the alloy but that occasionally leads to different metallurgical states between samples. Using ASAXS, a series of measurements with different contrasts can be conducted on a single sample. Also, the number of different contrasts possible with ISANS is limited by the available isotopes. A recent publication[122] described the first ASAXS experiments conducted on a material with engineering application: an Fe-Cr-Co ductile permanent magnet alloy. These types of experiments serve to demonstrate the maximal information extraction possible from ASAXS in collaboration with other techniques such as atom-probe field-ion microscopy (AP/FIM) or transmission electron microscopy (TEM).

1.1.2 Other Applications

Early synchrotron ASAXS experiments were conducted by Stuhrmann and co-workers who examined problems in the field of biophysics. By using many photon energies near the iron K absorption edge, the location of the four iron atoms in dissolved human hæmoglobin was discovered. Further, a tetrahedral arrangement of those iron atoms was determined and found to be in good agreement with crystallographic data.

1.2 Steel Alloy Descriptions

1.2.1 Modified Fe9Cr1Mo Steel

A ferritic steel, Fe9Cr1Mo modified by the addition of small amounts of the strong carbide formers V and Nb (hereafter referred to as Modified Fe9Cr1Mo steel) has been proposed for use in power-generation applications at elevated temperatures.[8,74,102,116,140,146] Ferritic steels containing nine weight percent or more of chromium have found considerable acceptance for high temperature use in corrosive environments.[108,148] This particular steel, the composition of which is given in Table 1.1, was developed as part of the Advanced Alloy Program at the Oak Ridge National Laboratory (ORNL).[7,13,94,119,144] Modi-

Table 1.1: Composition (weight percent) of Modified Fe9Cr1Mo steel, Carpenter Technology heat #30394. Principle alloying elements are emphasized in bold face.

C	N	Al	Si	P	Ti
0.084	0.053	0.014	0.4	0.01	0.005
V	**Cr**	Mn	**Fe**	Co	Ni
0.198	8.57	0.46	bal.	0.055	0.09
Cu	**Nb**	**Mo**	W		
0.04	0.073	1.02	0.05		

fied Fe9Cr1Mo steel has a number of attractive features, *e.g.*, high rupture strength at both room and elevated temperatures, good weldability, low thermal expansion, and resistance to radiation-induced void swelling. An extensive effort to characterize this material has been carried out at ORNL and elsewhere.[67,71–73,93]

It is essential that a candidate material for power-generation applications exhibit good microstructural stability over very long periods of exposure to high temperature service conditions. Otherwise an unfavorable change in mechanical properties is likely to occur. The present research has been concerned with the investigation of changes in the precipitate size distributions in Modified Fe9Cr1Mo steel produced by prolonged exposure to high temperatures, concentrating specifically on the size distribution of $Cr_{23}C_6$ to determine the stability of that phase under long-term aging conditions at service temperatures.

In the Modified Fe9Cr1Mo steel, three types of precipitates have been consistently reported:[67,94,144] vanadium-rich MC, niobium-rich MC and chromium-rich $M_{23}C_6$. The total amount of precipitate found by extraction and observed in the TEM was a few weight percent. Compositions of the metal content in each of the three carbides have been reported by Maziasz and are tabulated in Table 1.2.

Fujita[34–39] has reported on steels with chromium composition from nine to twelve percent and molybdenum from one to two percent. The morphological evolution of the principle carbide in these steels, $M_{23}C_6$, was reported to proceed as shown in Fig. 1.1 where the $M_{23}C_6$ were found on martensitic lath boundaries. In a specimen that was crept at 550° C, two precipitates were found in the thin foils by the TEM, MX and $M_{23}C_6$, where X can be carbon or nitrogen For times in excess of 3000 hours,

Table 1.2: Observed metal site percentages of carbides found in a sample of Modified Fe9Cr1Mo steel, heat #30394 that was crept at 650° C. Concentrations are in atomic %, as reported by,[129] determined in the TEM from extracted precipitates.

carbide	Cr	Fe	V	Nb	Mo
Cr-rich $M_{23}C_6$	65	25	2	—	7
V-rich MC	15	5	70	10	—
Nb-rich MC	5	1	15	79	—

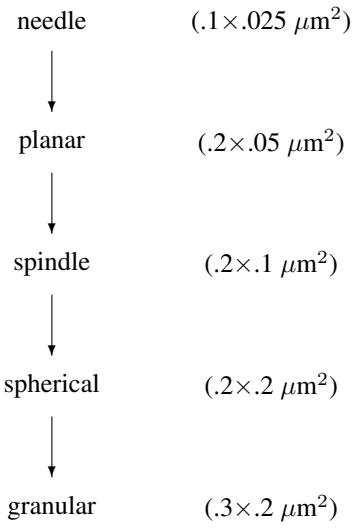

Figure 1.1: Morphological evolution[34–39] of principal carbides in steels with chromium composition ranging from nine to twelve percent and molybdenum from one to two percent.

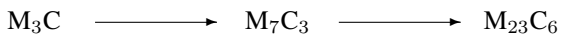

Figure 1.2: Carbide reaction sequence[103] applicable to low silicon Fe12Cr1.5MoVNb steel.

the sizes were 0.02 μm and 0.15$\times$0.05 μm^2 respectively. The MX precipitates were found to lie within the laths.

Fujita also shows that, for a Fe11CrVNb steel with 0.2% C and 0.1% (V,Nb), that after 10^3 hours tempering at 650° C, 20% of the chromium is in carbides regardless of varying V or Nb initial concentrations. Also, when 0.1% (by weight) Nb is added, it is almost entirely in carbides by 500 hours at 650° C. Additionally, 70 - 80% of V is in carbides by 10^3 hours at 650° C and appears to approach 90% asymptotically for infinitely-long tempering. It is reasonable to expect that, in the Modified Fe9Cr1Mo steel, all the Nb and most (>70%) of the vanadium is in carbides. Because there are five times more V atoms than Nb atoms in the alloy, one should expect to find a ratio of VC:NbC of four:one or five:one.

Fig. 1.2 show the reaction kinetics of the carbides reported[103] for a low silicon Fe12Cr1.5MoVNb steel. 1000 hours were required to complete the reaction of Fig. 1.2 at 550° C, while the time decreased to 200 hours at 600° C, and approximately 1 hour at 650° C. The kinetics of the second stage of the reaction were measured by the drop in the diamond pyramid microhardness from 550 DPH for M_7C_3 to 300 DPH for $M_{23}C_6$. For the long aging times used in the present work, little M_3C or M_7C_3 should be found. The reaction sequence[102] of Fig. 1.3 is applicable to the tempering of Fe2.25Cr1Mo steel.

At the initiation of this research project, almost all existing small-angle scattering cameras were capable of resolving only those scatterers with dimensions less than 100 nm. Using such a camera for neutron scattering, Kim[71] discovered that for Modified Fe9Cr1Mo, the number of carbides drops significantly between the aging temperatures of 538° and 704° C. However, as is typical of many engineering alloys, Modified Fe9Cr1Mo steel contains more than one carbide type and Kim was unable to determine if this change was attributable to a decrease in the population of (V,Nb)C or of $Cr_{23}C_6$. Isolation of the small-angle scattering from a single carbide type, either (V,Nb)C or $Cr_{23}C_6$, is not possible with a single scattering

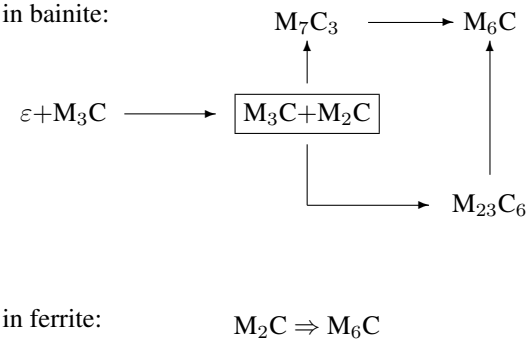

Figure 1.3: Reaction sequence[102] applicable to the tempering of Fe2.25Cr1Mo steel.

experiment because the contrast, with respect to the matrix, is different for each type of carbide. Additionally, his SANS cameras were not capable of clearly resolving features larger than some tens of nanometers although transmission electron microscopy reveals that scatterers larger than 100 nm are present in this alloy. The conclusion of Kim's SANS work was that the largest number of small carbides, ca. 30 – 40 nm diameter, were produced by 5000 hours aging at 538° C, which was in agreement with the observed peak in microhardness.[53,73]

1.2.2 AF1410 Steel

A multi-institutional research program comprising units from academia, government, and industry known as the Steel Research Group (SRG) has been underway since 1985, directed at the scientific basis for a new steel technology motivated by specific property objectives of importance to industry. In one of the key classes of steel selected for research, the ultrahigh-strength martensitic alloy steels for advanced structural applications, the alloy AF1410, the composition of which is given in Table 1.3, is currently being used in the critical application of aircraft arresting hooks on carrier-based jet fighters as well as structural members in other aircraft. The objective for improvements to this alloy are to increase the fracture toughness, K_{I_c}, and also the hardness, while preserving good hydrogen stress corrosion resistance so that $K_{I_{SCC}}$ approaches K_{I_c}.

Table 1.3: Nominal composition (weight percent) of AF1410 steel, produced by Carpenter Technology. Trace elements are not listed.

C	Cr	Fe	Co	Ni	Mo
0.163	2.1	bal.	14.24	10.21	1.03

$$M_3C \longrightarrow M_2C \longrightarrow M_{23}C_6 + M_6C$$

Figure 1.4: Precipitate reactions reported[83] on tempering of AF1410 steel.

The retardation of dislocation recovery imparted by the cobalt allows an unusually high dislocation density to remain during secondary hardening. Secondary hardening is the result of the precipitation on dislocations of a low volume fraction of finely-dispersed metastable M_2C (principally Mo_2C) carbides during high temperature tempering.[19,49,51,82] The M_2C distribution exhibits sufficient coarsening resistance to maintain the alloy strength and so the M_3C (cementite) platelets, which limit the fracture toughness, can be re-solutioned by slight overaging. However, tempering times must be limited due to a later-stage precipitation of M_6C and possibly $M_{23}C_6$ in areas separate from the M_2C[83] An optimal heat treatment of the steel will produce a population of coherent M_2C at the expense of all the M_3C. A summary description of the reported precipitate reactions during tempering suggests the carbide reaction sequence shown in Fig. 1.4.

Montgomery reports[99] that austenitizing at 1000° C for 1 hour will cause all carbides to completely dissolve while some carbides will remain undissolved after austenitizing at 830° C for 1 hour. However, a substantial body of research already exists for AF1410 austenitized at the lower temperature which is the standard, commercial austenitizing temperature. Information learned from the cleaner microstructure offered by the higher austenitizing temperature may be used in clarifying the analysis of the microstructure obtained from the standard austenitizing temperature. By increasing the austenitizing temperature to 885° C, Gore[45] found a significant reduction in the number of carbide types, as shown in Table 1.4. The trace amounts of the titanium nitrides found by Gore ($< 0.1\%$ by volume) are due to TiN added to the alloy as a grain-refining dispersion and are undissolved at the 830° C temperature.

Table 1.4: Carbides observed[45] in as-quenched AF1410 steel.

830° C austenitizing	
carbide	size range, nm
$(Fe,Ni,Co)_3C$	50 - 100 rods
$(Ti,Mo)_x(C,N)$	10 - 180
$(Cr,Fe,Mo)_{23}C_6$	50 - 125
$(Fe,Cr,Mo)_{23}C_6$	75 - 105
$(Mo,Cr)_xC$	30 - 65
$(Mo,Fe)_xC$	40 - 50
Mo_xC	5 - 10
885° C austenitizing	
carbide	size range, nm
$(Fe,Ni,Co)_3C$	40 - 230 rods
$(Ti,Mo)_x(C,N)$	20 - 35

Using small-angle neutron scattering, the evolution of the M_2C population was traced[1] as a function of aging time at 510° C for samples austenitized at 830° C and samples austenitized at 1000° C. Less total scattering was observed in the 1000° samples corroborating the result of Gore, but for both temperatures, the population of M_2C was followed from 510° C aging times as early 1/4 hour up to 100 hours and the average particle dimension was found to be in good agreement with that observed in the atom probe field ion microscope and the transmission electron microscope.

The present study will concentrate on observing the changes in the M_3C population using samples prepared at the same time as those of Allen. Transmission electron microscopy[99] has shown that the shape of the M_3C is most closely lenticular with outside dimensions of 2 to $5\times100\times1000$ nm^3, as shown in Fig. 1.5a. Fig. 1.5b, after Gavillet,[40] shows a larger, spherical precipitate that could be a TiN that was undissolved during the 830° C treatment. Dark field images have revealed that several M_3C precipitates are in the background of this micrograph.

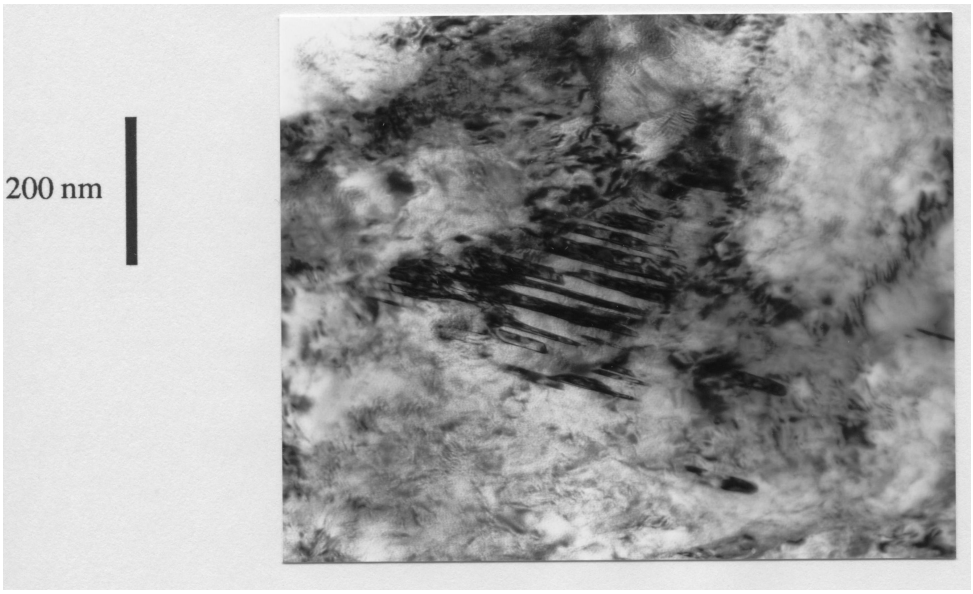

(a)

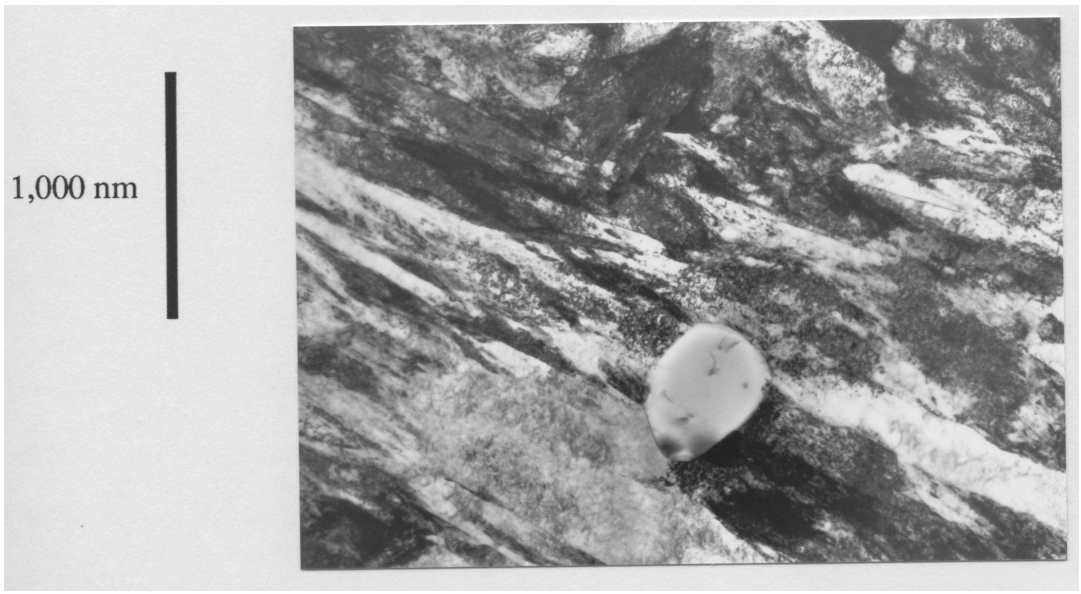

(b)

Figure 1.5: Bright field transmission electron micrographs of AF1410 steel. The condition is austenitized at 830° C for 1 hour / oil quench and then aged at 510° C for 1 hour / water quench. (a) Plate 3235. The diagonal features are the M_3C carbides. Micrograph[99] using a Phillips EM400T at an accelerating voltage of 120 kV. (b) Plate 3702. The large precipitate could be a TiN that was undissolved during the 830° C treatment. Micrograph from Gavillet[40] using an Hitachi H700 at 200 kV.

Chapter 2

Theory

Five principle topics are addressed in the theoretical section of this dissertation; small-angle scattering in general, anomalous dispersion small-angle X-ray scattering (ASAXS), resonant Raman scattering, the double-crystal diffractometer (DCD) SAXS camera, and the operational theory of the silicon photodiode detector.

2.1 Small-Angle Scattering (SAS)

A brief summary is presented of the general theory of small-angle scattering, covered in detail by many authors.[16,43,50,79] Equations will then be presented which use this theory to describe the scattering from arbitrary distributions of scatterers of spherical shape. The correction of the measured data for instrumental collimation smearing will be discussed and then the method for determining the distribution of scatterers will be described.

2.1.1 Basic SAS Theory

In small-angle X-ray scattering (SAXS), the intensity, I, of radiation scattered by nanometer- to micrometer-size electron density inhomogeneities is measured as a function of angle, q, within a few degrees of the unscattered beam of intensity, $I_0 = \Phi_0 A$, transmitted through a sample as photon energy, E, (or wavelength, λ) is held constant. Φ_0 is the incident flux in ph·s^{-1}·area^{-1} illuminating an area, A, on the sample. Precipitates, voids, oxides, and composition-modulated structures are typical of the electron density inhomogeneities observed in metallurgical samples. The magnitude of the reciprocal-space scattering vector,

$$\left|\vec{h}\right| = h = (4\pi/\lambda)\sin\theta \tag{2.1}$$

where 2θ is the scattering angle. The intensity profile in ph·s^{-1},[56,113]

$$I(h) = \Phi_0 A t T \epsilon \Omega \frac{d\Sigma}{d\Omega}(h), \tag{2.2}$$

is measured by a detector with efficiency, ϵ, and subtending a solid angle, Ω, with a sample of uniform thickness, t, and transmission, T. The measured transmission is related to the specimen thickness by $T = e^{\mu t}$, where μ is the linear absorption coefficient. $d\Sigma/d\Omega(h)$ is the differential scattering cross-section per unit volume per unit solid angle. The scattering is coherent and either a single scattering event occurs within the sample or none occurs. The optimal sample thickness is usually taken to be

$$t_{opt} = \mu^{-1}. \tag{2.3}$$

For $t < t_{opt}$, the intensity is limited by the number of scatterers in the beam. For $t > t_{opt}$, the potential for multiple scattering increases.[117]

$d\Sigma/d\Omega(h)$ is an intensive property; it is not dependent on the physical dimensions or amount of the sample. It is described as the Fourier transform of the local (electron) scattering length density, $\rho(\vec{r})$, where $\vec{r}$ is a position vector within the sample,

$$\frac{d\Sigma}{d\Omega}(\vec{h}) = V_s^{-1}\left|\int_{V_s}\rho(\vec{r})\,e^{-i\vec{h}\cdot\vec{r}}\,d^3\vec{r}\right|^2, \tag{2.4}$$

and the integral is over the sample volume, V_s. If $\rho(\vec{r})$ is constant over all $\vec{r}$, then $d\Sigma/d\Omega$ will be zero, thus only in the changes of the scattering length density, $\Delta\rho(\vec{r})$, between a scatterer and its surroundings are involved. For scattering from finely-divided solids, the scattering can be interpreted in terms of a particle size distribution. Lord Rayleigh[104,109] has described the scattering from a single homogeneous particle of radius r and volume $V_p(r)$ as

$$\frac{d\Sigma}{d\Omega}(h,r) = V_s^{-1}|\Delta\rho(r)|^2\,|V_p(r)\,F_p(h,r)|^2 \qquad (2.5)$$

where $F_p(h,r)$ is a dimensionless form factor for the particle that describes the scattered amplitude of radiation from a particle of a specific shape. The form factor is

$$F_p(h,r) = F_p(\vec{h},\vec{r}) = V_p^{-1}\int_{V_p} e^{-i\vec{h}\cdot\vec{r}}\,d^3\vec{r}. \qquad (2.6)$$

In the work of Shull and Roess,[112,118] the particle-to-particle scattering was assumed to be negligible for their derivation of the particle form factor for randomly-oriented ellipsoids of revolution. The intensity from a number distribution of scatterers per unit volume, $N(r)$, where $N(r)\,dr$ is the number of scatterers per unit volume of dimensions between r and $r+dr$, was described by

$$\frac{d\Sigma}{d\Omega}(h) = |\Delta\rho|^2\int_0^\infty |V_p(r)\,F_p(h,r)|^2\,N(r)\,dr. \qquad (2.7)$$

In terms of the volume fraction distribution, $f(r) = V_p(r)N(r)$,

$$\frac{d\Sigma}{d\Omega}(h) = |\Delta\rho|^2\int_0^\infty |F_p(h,r)|^2\,V_p(r)\,f(r)\,dr. \qquad (2.8)$$

The latter definition of $d\Sigma/d\Omega$ will be used later in the section on size distribution analysis.

Simplifications of $d\Sigma/d\Omega$ exist for two limiting cases of scattering vector. The Guinier region[50] for identical, randomly-oriented, non-interacting particles, applies for $hr \leq\sim 1.5$.[79] $d\Sigma/d\Omega$ reduces to

$$\lim_{h\to 0}\frac{d\Sigma}{d\Omega}(h) = N_v\,|\Delta\rho|^2 V_p^2\exp\left[-\frac{1}{3}(hR_G)^2\right]. \qquad (2.9)$$

N_v is the number of particles per unit volume and R_G is the radius of gyration of the overall particle size distribution $N(r)$, determined from the slope of a plot of $\log(d\Sigma/d\Omega)$ versus h^2 as h goes to zero.

The other limiting case is the Porod region, in the tail of the SAS curve, for $hr > 10$. The Porod region provides information about the average surface area per unit volume of sample, S_v, where the average is weighted towards the smaller particles if there is a distribution of sizes.

$$\lim_{h\to\infty}\frac{d\Sigma}{d\Omega}(h) = 2\pi\,S_V\,|\Delta\rho|^2\,q^{-4}. \qquad (2.10)$$

S_v is the total scattering surface area per unit volume of sample irradiated by the beam and is determined from the slope of a plot of $\log(d\Sigma/d\Omega)$ versus $\log(h)$ or from the intercept of a plot of $h^4 d\Sigma/d\Omega$ *vs.* h^4. The slope of the latter plot is often interpreted as the experimental background. In cameras with perfect collimation (*i.e.*, pinhole geometry), the scattering is proportional to h^{-4} whereas for slit-collimation cameras, the scattering is proportional to h^{-3}. The Porod relation holds for $hR_p \geq 3$ where R_p is the average radius predicted from S_v.

Each intensity measurement is a statistical representation of the entire size distribution, weighted by the particle form factor for that particular scattering vector. Consequently, there is no unique correspondence between a given dimension, $D = 2r$, and the scattering vector h. The experimental parameters limit the range of dimensions directly resolved by a SAXS experiment. Both Guinier and Porod approximations may be used to determine the range of dimensions directly accessible to the SAS experiment from the range of available scattering vectors, $\Delta h < h_{min} \leq h \leq h_{max}$. The largest dimension fully defined by the SAXS experiment, determined by the Guinier limit, is $D_{max} = 2(1.5/h_{min})$ while the smallest dimension is defined by the Porod limit as $D_{min} \geq 2(\pi/h_{max})$. These limits are applicable to spherical particles.

Scattering from particle dimensions outside this range may be detected in the periphery of the experimental range of scattering vectors but the extraction of the information content of this peripheral information is less statistically reliable than those dimensions between D_{min} and D_{max}. The extent of this "peripheral vision" is about a factor of two beyond D_{min} and D_{max}. For dimensions outside $D_{min}/2 \leq D \leq 2D_{max}$, the range of scattering vectors is insufficient to fully describe the scattering and the data are considered incomplete.

2.1.2 Scattering from Spherical Particles

The form factor for spherical particles of radius r at scattering vector (magnitude) h is

$$F(h,r) = \frac{3}{(hr)^3}\left[\sin(hr) - (hr)\cos(hr)\right] \qquad (2.11)$$

and the volume of that sphere

$$V_p(r) = \frac{4}{3}\pi r^3 \qquad (2.12)$$

which combine to describe the small-angle scattering from an arbitrary number distribution, $N(r)$ of spherical scatterers

$$\begin{aligned}\frac{d\Sigma}{d\Omega}(h) &= 16\pi^2 \left|\Delta\rho\right|^2 h^{-6} \qquad (2.13)\\ &\times \int_0^\infty \left[\sin(hr) - (hr)\cos(hr)\right]^2 N(r)\, dr\end{aligned}$$

or, in terms of the volume distribution, f(r),

$$\begin{aligned}\frac{d\Sigma}{d\Omega}(h) &= 12\pi^2 \left|\Delta\rho\right|^2 h^{-6} \qquad (2.14)\\ &\times \int_0^\infty \frac{\left[\sin(hr) - (hr)\cos(hr)\right]^2}{r^3} f(r)\, dr.\end{aligned}$$

2.1.3 Instrumental Collimation Correction

There are three instrumental weighting functions that can distort, or smear, the small-angle scattering data: wavelength smearing (P_λ), slit-width smearing (P_w), and slit-length smearing (P_l), where P_λ, P_w, and P_l are probability distributions of unit area. The circularly-symmetric perfectly-collimated $d\Sigma/d\Omega$ are smeared by P_λ, P_w, and P_l by

$$\begin{aligned}\frac{d\tilde{\Sigma}}{d\Omega}(h) = \qquad (2.15)\\ \int_0^\infty P_\lambda(\lambda) \int_{-\infty}^\infty P_w(w) \int_{-\infty}^\infty P_l(l)\\ \times \frac{d\Sigma}{d\Omega}\left[\frac{\sqrt{(h-w)^2 + l^2}}{\lambda}\right] dl\, dw\, d\lambda\end{aligned}$$

Double-crystal collimation greatly simplifies this equation. The double crystal monochromator has a wavelength resolution, defined as $\Delta\lambda/\lambda$, of $\simeq 0.0003$, rendering wavelength smearing negligible. Slit-width smearing is also negligible because of the narrow rocking curve of the DCD analyzer. What remains is the slit-length weighting function, P_l. In the slit-length direction, perpendicular to the scanning direction, the detector subtends an angle $\Delta\theta_l$ with a point within the illuminated area of the sample. This angle is just the ratio of the diameter of the photodiode detector divided by the distance between the sample and the detector. The characteristic slit-length in reciprocal space,

$$l_0 = \frac{1}{2}\left[\frac{4\pi}{\lambda}\sin\left(\frac{\Delta\theta_l}{2}\right)\right] \qquad (2.16)$$

is then derived in a manner similar to that of the scattering vector h, where the additional factor of two is derived according to Fig. 2.1. Assuming that the detector sensitivity is constant across its surface,[76] P_l can be taken to be a rectangular profile.

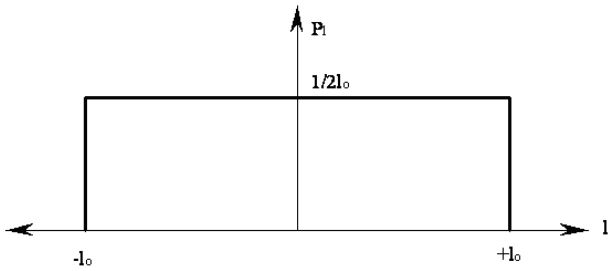

Figure 2.1: The slit-length weighting function, P_l, for the double-crystal analyzer and a silicon photodiode detector for monochromatic X-rays of normal incidence. The sensitivity of the photodiode is assumed to be constant across its surface.[76]

Although the DCD analyzer is between the sample and detector, it in no way limits or alters the beam in the slit-length direction, which is perpendicular to the diffraction direction. The instrumentally-smeared SAS then reduces to

$$\begin{aligned}\frac{d\tilde{\Sigma}}{d\Omega}(h) &= \int_{-\infty}^\infty P_l(l)\frac{d\Sigma}{d\Omega}\left(\sqrt{h^2+l^2}\right) dl\\ &= l_0^{-1}\int_0^{l_0} \frac{d\Sigma}{d\Omega}\left(\sqrt{h^2+l^2}\right) dl \qquad (2.17)\end{aligned}$$

While an exact solution for the slit-length smearing equation exists for a slit of arbitrary profile,[26–28,86] a numer-

ical implementation of the algorithm given in the literature failed to regenerate a perfectly-collimated test case. Furthermore, the method requires the pre-calculation of a non-trivial function, derived indirectly, from the slit-length profile, P_l. A less direct but more flexible approach was taken to desmear the small-angle scattering data as explained below. The data were corrected for slit-length instrumental smearing using the technique of Lake[81] as implemented in the FORTRAN program `Lake.FOR`. The program will run on a variety of computers including the Digital Equipment Corporation VAX, IBM PC, and the Apple Macintosh. The source code is presented in an appendix to this dissertation.

The technique of Lake seeks a solution of the instrumental smearing equation for the ideal, perfectly-collimated data ($I = d\Sigma/d\Omega$ above) from the measured data $\tilde{I}$ by an iterative technique. This technique has been applied to problems in absorption spectroscopy[6,52,65] although it appears that the method shown by Lake has superior convergence properties and inherently avoids the creation of unphysical negative intensities. Glatter[42] sought to improve the technique of Lake by smoothing the feedback term to the iterative correction and accelerating the convergence near sharp minima. However, the smoothing requires a selection which can prejudice the result and can lead to the introduction of a systematic error in the ideal pattern, especially near sharp features such as sharp minima. Since some SAS data have no sharp minima and other SAS data do, introduction of such an algorithm leads to a loss of generality.

The method implemented for iterative desmearing involves only forward smearing of a trial solution with feedback to improve the trial solution. The argument, which is intuitively satisfying although without rigorous mathematical foundation, is that the difference between trial solution I_i and the perfectly-collimated data I_0 should vanish as the difference between the smear of the trial solution $\tilde{I}_i$ and the measured data $\tilde{I}_0$ vanishes. Formally:

$$\lim_{i\to\infty} I_i - I_0 = \lim_{i\to\infty} \tilde{I}_i - \tilde{I}_0 = 0 \tag{2.18}$$

which leads to the feedback equation

$$I_0 \approx \lim_{i\to\infty} \tilde{I}_{i+1} = I_i - \left(\tilde{I}_i - \tilde{I}_0\right) \tag{2.19}$$

An infinite number of iterations would result in perfectly collimated data but in practice, one declares a solution when the feedback term on the far right of Eq. 2.19 has become negligible. The *feedback equation* is common to the work of Lake, Blass, Halsey, and Jansson although the latter three appear to have arrived at it independently from Lake. None of them have presented a rigorous mathematical proof that such a series will eventually converge. Experience, however, shows that convergence is certain for a wide variety of problems including desmearing and deconvolution. To decrease the number of iterations, all four investigators sought to improve the rate of convergence by multiplying the feedback term by an empirical function A. The methods offered by Blass, Halsey, and Jansson achieved a modest improvement (ten to twenty percent). It was Lake who reported, four years prior, that

$$A = I_i \div \tilde{I}_i \tag{2.20}$$

offered significant improvement (ten-fold) in the rate of convergence.

The feedback loop is thus modified to

$$I_0 \approx \lim_{i\to\infty} \tilde{I}_{i+1} = I_i \times \left(\tilde{I}_0 \div \tilde{I}_i\right) \tag{2.21}$$

which converges, for the majority of cases, in about ten iterations. Because it does not employ a subtraction, the modified feedback equation has the remarkable property of not producing negative numbers, since the measured data is always positive. The technique works best on model data which has no random statistical errors. In this case, numerical precision still tends to influence the iterates after about twenty-five iterations or so, even when using eighteen significant figures (IEEE standard ten byte floating-point precision). On real data, the scatter of the iterative solution becomes magnified three to five times over that of the measured data.

The initial guess with the least bias is one which is perfectly flat. Since the analytical application of the modified feedback equation to a flat initial guess was shown by Lake to invariably yield a trial solution equal to the measured data, an initial guess of

$$I_1 = \tilde{I}_0 \tag{2.22}$$

is used to set the process in motion.

The instrumental smearing equations require integration of the trial solution data out to infinite scattering vector or at least out to the slit-length which is often beyond

the range of available measured data. Extrapolation has often been used to overcome this termination effect of the available data. One assumes that the data obeys a particular functional relationship over the entire scattering range beyond the available data, and this is usually a good assumption. Experimentally, an exact choice of the extrapolation function is not as important as the implementation of an extrapolation function. In short, it is better to attempt an extrapolation, even if the exact functional relationship is unknown, than to accept the termination effect. The form of the extrapolation function has the largest effect on the final few data points. It has been found advantageous to defer subtraction of the experimental background until after desmearing, thereby potentially allowing any features buried within the background to be recovered. In addition to the SAXS, the experimental background also figures into the instrumentally-smeared scattering data. By not subtracting this background from the measured data to be desmeared, the termination effect can be further diminished. Mathematically, its does not matter whether the background is subtracted prior to desmearing. Measurements of this typically flat background are often collected to quite large scattering vectors, beyond what is considered the hmax of the SAXS information, enabling a good estimation of the slope and intercept of a linear extrapolation function. The termination effect will then have its greatest effect on points which will be sacrificed to background subtraction after desmearing, so that the effect of an assumed extrapolation function can be almost completely eliminated from the SAXS. The Lake desmearing technique employed here does not require a particular functional form for the measured data, the desmeared data, or the instrumental smearing functions. It has been employed with success on a wide variety of small-angle scattering data without problem as will be shown. Success of the desmearing algorithm need not be dependent on absolute units of small-angle scattering intensity although, in practice, all of the results presented here have been placed on an absolute scale before desmearing.

2.1.4 Size Distribution Analysis by Maximum Entropy Technique

From the small-angle scattering experiments carried out in this work, we seek to derive the dimensions and volume fraction of the scatterer by measuring the scattering intensity profile. The equation relating the intensity, I, and the size distribution, $f(D)$, as given above is an example of a practical linear inverse problem.[106] Finding a unique solution is complicated by the fact that many different arrangements of particle size and volume fraction may give rise to the same measured intensity profile. The maximum entropy technique provides a method by which a unique solution may be derived, biasing the result by a choice of morphological model. The arrangement so selected has the least structure consistent with the data.

For M independent observations of the small-angle scattering which span a finite range of scattering vectors,

$$\begin{aligned} I(h_j) &\equiv I_j = \int_0^\infty G_j(D)\, f(D)\, dD \quad (2.23) \\ j &= 1, \ldots M \end{aligned}$$

where $G_j(D)$ is the scattering for a single particle of linear dimension D and a scattering vector h_j, and $f(D)$ is the differential volume distribution as before. All of the scattering effects, including particle interference and instrumental collimation can be included within $G_j(D)$ as long as the relation remains linear with respect to D.

Maximum entropy is the constraint on a curve-fit of the data I_j where the distribution $f(D)$ serves as the constrained set of linear coefficients to the model scattering function $G_j(D)$. While the solution of the intensity equation to obtain a size distribution is but one example of a practical linear inverse problem, solution of the non-linear slit-length desmearing problem must be effected by other methods such as those of Lake or Deutsch. However, it is possible to incorporate the slit-length smearing operations into the model scattering function[106] $G_j(D)$ and, because such an operation does not alter the linear relation between $f(D)$ and I_j, thereby determine size distributions directly from the smeared intensity data.

By assuming that $f(D)$ is constant over the range D to $D+\Delta D$, the integral may be replaced by a summation and $f(D)\Delta D$ replaced by f_i.[1] The problem is to determine

[1] The choice of where to position the ΔD term is important to maxi-

the coefficients of the distribution, f_i, over some range of dimensions D_i, where $i = 1, \ldots N$. First, f_i must be positive for all D_i. Also, the intensity,

$$y_j = \sum_{i=1}^{N} G_{i,j}\, f_i, \quad j = 1, \ldots M, \tag{2.24}$$

calculated from f_i is required to match the experimental observations, I_j, within the experimental errors σ_j. The constraint imposed by the maximum entropy technique is that the configurational entropy S of the distribution f_i, be at a maximum. Borrowing from statistical thermodynamics, the configurational entropy[127] of the distribution f_i,

$$S = -\sum_{i=1}^{N} p_i\, \log(p_i), \tag{2.25}$$

represents the disorder of the distribution where

$$p_i = f_i \div \sum_{k=1}^{N} f_k. \tag{2.26}$$

so that the $\sum p_i = 1$. In an information-theoretic sense, the entropy measures the partitioning of the volume fraction of scatterers required to localize the observed small-angle scattering at each h_j. Much simplification of the calculation of entropy gradients with respect to the distribution f_i is made by Skilling's modification of the entropy definition to

$$S^{mod} = -\sum_{i=1}^{N} \frac{f_i}{b_i}\, \log\left(\frac{f_i}{b_i}\right), \tag{2.27}$$

which aids the search technique for the f_i by the introduction of a featureless constant baseline, b_i. The total number of equivalent permutations of this distribution

$$W = \frac{\left(\sum_{i=1}^{N} f_i/b_i\right)!}{\prod_{i=1}^{N}(f_i/b_i)!} \tag{2.28}$$

is analogous to the thermodynamic probability of the particular distribution. The number of bits of information in bin i of the distribution in excess of the baseline, f_i/b_i, is a large integral number and Stirling's approximation then becomes valid. Both W and S^{mod} reach a maximum when all the f_i are the same. In the present case, deviations from this flat distribution are produced only by experimental evidence. Use of b_i further avoids the normalization of p_i. Potton, et al˙ reported that the choice of b_i influences the rate of convergence of the Skilling and Bryan search technique and they took all the b_i equal to a constant b. The initial trial distribution is taken as $f_i = b$ for all i, a flat distribution. Replacement of p_i by f_i/b_i presumably has no effect on the maximization of the configurational entropy of f_i. A least-squares constraint will require the y_j to closely match the experimental intensities I_j but such solutions interpret statistical errors as due to microstructure. The present technique uses the chi-squared statistic,

$$\chi^2 = \sum_{j=1}^{M} \left(\frac{I_j - y_j}{\sigma_j}\right)^2, \tag{2.29}$$

to gauge the misfit between experiment and prediction, where σ_j is the standard deviation of each measurement. On average, each point contributes unity so that the mean χ^2 is M, the number of observations. The maximum entropy search technique implemented by Skilling and Bryan seeks to solve for the coefficients f_i by maximizing

$$Q = S - \lambda\chi^2 \tag{2.30}$$

subject to the constraint that χ^2 is equal to the number of data points. In this context, λ is the Lagrange multiplier required to constrain the χ^2. Thus, not only are the experimental intensities used in the determination of the distribution, but so are the experimental errors. *The operation of the maximum entropy algorithm is always checked*[127] by the gradients with respect to the f_i of entropy, ∇S, and misfit, $\nabla C \equiv \nabla(\chi^2)$. Final acceptance of a distribution is contingent on the alignment between the two gradients,

$$\eta = \frac{1}{2}\left|\frac{\nabla S}{|\nabla S|} - \frac{\nabla C}{|\nabla C|}\right|^2, \tag{2.31}$$

tending towards zero. The single distribution of maximum entropy consistent with the data is located at $\eta = 0$.

mum entropy solution. Here, we describe maximizing the entropy of the *volume fraction size distribution* by means of its histogram. If the proposed move of ΔD into the G matrix were to be implemented, then we would be maximizing the height of each bin in the distribution without regard to the volume fraction described by that bin. This is important when the ΔD_i are not all equal. For bins of constant ΔD, this makes no difference.

Special emphasis must be placed on a strict definition of the σ_j as the standard deviation of each experimental intensity, I_j. If the σ_j are uniformly over- or underestimated, it is a simple procedure to multiply the σ_j by the appropriate constant. However, the consequences of an improper estimation of σ_j in a portion of the SAS curve are very serious. Because of the underestimated σ_j in part of the curve, the information content from that region will be overestimated. Because of the constraint that $\chi^2 = M$, the information content from other regions of the curve will be diminished. The resulting distribution will have additional features similar to a least-squares solution where statistical errors from this region have been interpreted as microstructure, while information will be missing from other parts of the distribution. A similar argument may be made for over estimation of the σ_j in some part of the curve. In the present case, the σ_j were determined from shot-noise counting statistics.

The maximum number of independent coefficients predicted by the Nyquist sampling theorem is the larger of $N_{max} = h_{max}/h_{min}$ or $h_{max}/\Delta h$. Using more than N_{max} bins in the size distribution will provide overlapping information in the distribution without adverse effects on the analysis due to the $\chi^2 = M$ constraint.

A rigorous test of the maximum entropy method implemented by Potton[105] has been presented elsewhere,[23] where the matrix $G_{i,j}$ was defined using the $|\Delta\rho|^2$ of the scatterer and the form-factor for spheres presented earlier. Application of the Backus-Gilbert[2] method for estimating the margin of error in a maximum entropy analysis was also discussed by Potton[107] but that method has not been implemented in computer code and it will not be discussed here.

While the replacement of p_i by f_i/b_i simplifies the math for the determination of ∇S and ∇C, this replacement may cause an imbalance between the magnitude of S and χ^2 that favors χ^2 minimization, thereby sensitizing the Skilling and Bryan search technique to oscillations in the model scattering function $G_j(D)$. Small features develop in distributions during the late stages of the iterative analysis and may be observed in the published work of Culverwell where the $G_j(D)$ were defined using the trigonometric spheres function from Eq. 2.11. In that work, the scattering had been calculated from two model Gaussian distributions. Random statistical error was added to the intensities and then the result was analyzed by the maximum entropy method. The distribution derived by the maximum entropy analysis shows greater commitment towards a least-squares solution than one would expect from a maximum entropy constraint. Use of less oscillatory scattering models presented here diminishes the oscillations in the resultant f_i while retaining the principle features of the two Gaussian distributions.

The maximum entropy method has been highly touted as producing the most uniform distribution consistent with the data yet small oscillations in the distributions obtained using the Skilling and Bryan search technique appear to suggest a greater information content in the SAS data than are supported by the statistics. However, the fundamentals of the Skilling and Bryan method are based upon the replacement of p_i by f_i/b_i. The maximum entropy method will, in theory, deliver a very good representation of the true distribution giving rise to the observed scattering but the Skilling and Bryan implementation of the search technique is somewhat flawed in this regard. As the flaw is of minor significance, the method of Potton which relies on the Skilling and Bryan method will be used to analyze most of the scattering data presented here. The computer code used, `MaxSAS.FOR`, which is a modification of the Potton code, `Maxe.FOR`, is presented in an appendix to this dissertation.

The program `Maxe.FOR` estimates a value for the constant background from the given data and also from the fitted intensities derived from the size distribution. It further suggests that this is the correct background, B, to be subtracted from the input intensities. If a background has already been subtracted from the input data, then the calculated B is the additional amount to be removed. The maximum entropy algorithm will tolerate a few negative intensities, as long as their magnitudes are comparable to or less than their reported errors. The background estimated by `Maxe.FOR`,

$$B = \frac{\sum_{j=1}^{M} \sigma_j^{-2}(I_j - y_j)}{\sum_{j=1}^{M} \sigma_j^{-2}} \tag{2.32}$$

is the weighted average difference between input, I, and fitted, y, intensities, where the weighting is specified by the input errors, σ. A high background reduces the information content of the data by lowering the ratio of signal to noise (S/N) as well as lowering the largest available scattering vector, h_{max}. Therefore, a good estimation of

the background is essential to the success of the maximum entropy analysis.

In summary, the maximum entropy size analysis technique is a curve fit of the experimental intensities using χ^2 statistics to generate a series of trial size distributions constrained by configurational entropy. Discrepancies in the intensities calculated from each trial distribution are used as feedback where the trial distribution is modified to increase the functional $Q = S - \lambda\chi^2$. Iteration is required to fix the value of the Lagrange multiplier, λ. The first trial distribution is completely flat, thereby introducing no bias towards a particular distribution shape. Only misfits between calculated and experimental intensities are used as feedback to the trial distributions so that the experimental intensity profile is never directly converted into a distribution. In this regard, the size analysis technique works in a manner analogous to the desmearing technique of Lake; in both cases, a trial solution is repeatedly compared with experimental data and then modified until the convergence criteria are satisfied.

Furthermore, while the general shape of the maximum entropy distributions may be assumed to accurately represent the scatterers, caution must be exercised to avoid over-interpreting small features in the distributions due to the sensitivity of the Skilling and Bryan maximum entropy search technique to oscillations in the model scattering function. This is of utmost importance when examining number distributions that are derived from the $f_i(D)$, especially at low values of D where the particle volume is quite small. Finally, negative intensities, due to background subtraction, are tolerated by the analysis technique as long as their magnitudes are comparable to or less than their reported errors.

2.2 Anomalous Dispersion Small-Angle X-ray Scattering (ASAXS)

The technique used to isolate the scattering of chromium carbide in the Modified Fe9Cr1Mo steel from that of the MX precipitates is the contrast variation technique called anomalous dispersion small-angle X-ray scattering (ASAXS) where the contrast variation is obtained by the physics effect of anomalous dispersion. Because this effect is a function of the X-ray energy (or wavelength) all measurements can be carried out on a single sample. This section describes the effect and the calculation of terms that are necessary to the analysis. Practical limits of detectability for ASAXS will be described as will the experimental equipment necessary to make the measurements. Finally, the method for isolating a particular scatterer will be described.

2.2.1 Anomalous Dispersion and the Dispersion Corrections

The atomic scattering factor f is the *ratio of the radiation amplitude scattered by the actual electron distribution in an atom to that scattered by one electron localized at a point.*[77] When the energy of an X-ray photon incident on an atom, of atomic number Z, is near the binding energy for a core electron of that atom, the atomic scattering factor decreases anomalously. This effect, called anomalous dispersion, occurs because of resonance of the bound electron due to the energy of the incident photon. The scattering factor is modified

$$f(Z,k,E) = f_0(Z,k) + f'(Z,E) + i\,f''(Z,E). \quad (2.33)$$

The first term, $f_0(Z,k)$, where $k = \lambda^{-1}\sin\theta$, is a first approximation to the scattering factor. Tables of f_0, for each element as a function of k may be found in the International Tables for X-ray Crystallography, Vol. III, pp. 201-227 and in X-ray diffraction reference texts.[22] Taking Z as the number of electrons,

$$\lim_{k\to 0} f_0 = Z, \quad (2.34)$$

and is independent of photon energy (wavelength) and scattering angle. For experiments involving a quantitative measure of the intensity of the scattering from a sample, it is necessary to consider all the terms in Eq. 2.33. The second and third terms are the complex anomalous dispersion corrections to the scattering factor and depend on both atomic number of the elements in the sample and the photon energy.

Absorption of X-rays increases sharply as the incident photon energy is increased above the binding energy of an electron in the sample. This increase in absorption is described in the imaginary part, $f''(Z,E)$. With further

increases in the photon energy, the absorption decreases smoothly. The discontinuity in the absorption of X-rays in a sample as the X-ray photon energy passes the binding energy of an electron in that sample is referred to as the absorption edge for that electron of that atom. To illustrate, the binding energy of a $1s$ (K-shell) electron of chromium is 5989 eV, so the Cr K absorption edge is at 5989 eV. For a sample of only one element at an incident photon energy E, the optical theorem,[62,64]

$$f''(Z,E) = \frac{E}{2r_{e^-}ch}\,\frac{A}{\rho_m N_A}\,\mu_l(E) \quad (2.35)$$

$$= \frac{E}{2r_{e^-}ch}\,\frac{A}{N_A}\,\mu_m(E) \quad (2.36)$$

relates f'' of the element with its linear absorption coefficient, μ_l, and mass absorption coefficient, μ_m, where r_{e^-} is the classical radius of an electron, c is the velocity of light, h is Planck's constant, N_A is Avogadro's number, and ρ_m and A are the mass density and atomic weight of the element. The real part of the anomalous dispersion correction, f', at an incident photon energy, E, is obtained from f'' by the Kramers-Kronig integral,[80]

$$f'(E) = \frac{2}{\pi}\int_0^\infty f''(\varepsilon)\,\frac{\varepsilon}{E^2-\varepsilon^2}\,d\varepsilon, \quad (2.37)$$

where ε is the variable (X-ray energy) of integration.

The anomalous dispersion effect may be seen in the real term, $f'(Z,E)$ when E is near the binding energy of a bound electron. The real term tends to zero for photon energies well above the K-shell absorption edge, E_k. As E decreases to near E_k, f' falls sharply due to the resonance. As E continues to decrease below E_k, f' will be seen to recover almost back to zero only to decrease again near the binding energies of the other electrons in the sample. A relativistic quantum-mechanical method for calculating f' and f'' has been given by Cromer and Liberman[21] and is implemented in the FORTRAN code `fPrime.FOR`, by A. Habenschuss of the Oak Ridge National Laboratory and obtained from J.B. Cohen. Fig. 2.2 has been calculated by means of that code for photon energies near the chromium K edge of 5989 eV.

Fluorescence, which is constant as a function of θ, occurs when the incident photon energy is above the electron binding energy, leading to an increased background in a small-angle X-ray scattering experiment. Because of this, ASAXS experiments are restricted to the region $E/E_K < 1$ (for the K edge) to avoid fluorescence.

The $1s$ electron binding energies of the transition elements Ti through Ga are accessible to X-ray monochromators with Ge optics at X-ray synchrotrons and are well-separated with respect to the energy range over which the anomalous dispersion effect occurs. Thus, the effect may be exploited to change the scattering factor of a single element in a multi-element system, such as a large number of engineering alloys, while leaving the scattering factors of the other elements relatively constant. To illustrate, in a metal alloy where the anomalous element is not enriched in the matrix, the small-angle scattering from a precipitate that is enriched with the anomalous element may be isolated both qualitatively and quantitatively, even in the presence of other scatterers which are not enriched in this anomalous element.

2.2.2 Scattering Length Density, Contrast, and Strength

The scattering length density is the total scattering length b of a substance per unit volume V is calculated from the composition and structure of the unit volume. In general, the density of the scattering entity,

$$\rho = \sum_i \varrho_i b_i \quad (2.38)$$

which uses the density of scatterers per unit volume, ϱ_i, and scattering length, b_i, of scatterers of type i, respectively. For crystalline materials, ϱ_i is calculated from the structure of the unit cell and the site occupancy fractions. For noncrystalline materials, it is calculated from the mass density and the atomic weight. In the case of neutrons, tables of b_i, which are different for each isotope.[79]

The X-ray scattering length density is written as, ρ_{e^-}, where the subscript e^- signifies the *effective* density of electrons. For X-ray energies near an electron binding energy, as in Eq. 2.33, this effective density will decrease. Consequently, b_i is the effective scattering length of the electrons. On average, the scattering length of a single electron is its classical (Thomson) radius,

$$r_{e^-} = \frac{e^2}{4\pi\varepsilon_0 mc^2}, \quad (2.39)$$

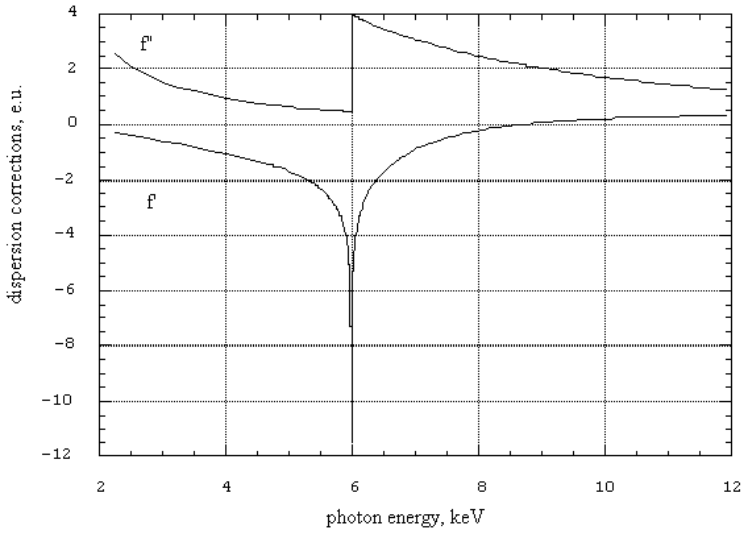

Figure 2.2: Anomalous dispersion terms $f'(E)$ and $f'(E)$ calculated[21] by means of the FORTRAN code `fPrime.FOR` for photon energies near the chromium K edge (5989 eV).

which is approximately 2.818 fm. The total effective scattering length of electrons in a type i atom is given as

$$b_i = (r_{e^-}) f_i. \tag{2.40}$$

By summation over all of the atoms in the sample, where Z is the atomic number,

$$\rho_{e^-} = (r_{e^-}) \sum_Z \varrho_Z f_Z. \tag{2.41}$$

Due to the complex nature of the atomic scattering factor, f_Z, the scattering length density for X-rays, ρ_{e^-}, is also a complex number. The same argument may also be made in the case of neutrons where b_i is complex for some isotopes. However, the scattering contrast, which is defined as $|\Delta\rho|^2$, is real-valued. In the section above describing the basic SAS theory, the scattering cross-section, $d\Sigma/d\Omega$, was shown to be proportional to $|\Delta\rho|^2$. The scattering contrast enables the separation of scatterers from the matrix.

For precipitates in a metal alloy,

$$|\Delta\rho|^2 = \left|\rho_{e^-,\text{ppt}} - \rho_{e^-,\text{mat}}\right|^2 \tag{2.42}$$

where $\rho_{e^-,\text{ppt}}$ is the scattering length density of the precipitate and $\rho_{e^-,\text{mat}}$ is that of the matrix. Combining with the equation for the ρ_{e^-} of each substance,

$$|\Delta\rho|^2 = \left|(r_{e^-}) \sum_Z \Delta\varrho_Z \, f_Z\right|^2 \tag{2.43}$$

where

$$\Delta\varrho_Z = \varrho_{Z,\text{ppt}} - \varrho_{Z,\text{mat}}. \tag{2.44}$$

Now, it is readily apparent that the SAS is produced by the *local changes* in composition, $\Delta\varrho_Z$. Including the dispersion corrections,

$$|\Delta\rho|^2(E) = \left|(r_{e^-}) \sum_Z \Delta\varrho_Z \left[Z + f'_Z(E) + i f''_Z(E)\right]\right|^2 \tag{2.45}$$

which includes the dependence on photon energy. One can predict how $|\Delta\rho|^2$ will change with E by means of calculations involving the relevant dispersion corrections and their weighting by the atomic density differences $\Delta\varrho_Z$.

Three general situations arise for photon energies (wavelengths) near an absorption edge:

- $|\Delta\rho|^2(E)$ will increase monotonically
- $|\Delta\rho|^2(E)$ will decrease monotonically
- $|\Delta\rho|^2(E)$ will pass through a minimum

Exactly which of these three general situations will occur must be calculated on a case-by-case basis. The first two situations correspond to the scattering length densities diverging or converging, respectively, and are dominated by changes in the f' of the anomalous element. The last situation is the most unusual where the scattering length densities are almost equal; the minimum corresponds to the case of contrast matching where the summation of $\Delta\varrho_Z(Z + f')$ terms cancels and the contrast is defined only from the summation of $\Delta\varrho_Z f''$ terms. The value at the minimum is the lowest possible value for $|\Delta\rho|^2(E_k)$ between those two media at that absorption edge, E_k.

As mentioned before, f_0 is a first approximation, useful for some cases but in general, the dispersion corrections must be included. One may be tempted to include the dispersion corrections in the calculation of $|\Delta\rho|^2$ for only the elements with the largest $\Delta\varrho_Z$ or only for the anomalous element. While this may provide a sense of the change in contrast with energy, it will, in most cases, lead to inexact values for the scattering contrast and amount of change in that contrast as the absorption edge is approached. Therefore, it is necessary to extend the summation over all known elements in the composition and to include the dispersion corrections for each of those elements.

To characterize the amount of scattering, a figure-of-merit called the scattering strength,

$$X \equiv V_f \ |\Delta\rho|^2 \tag{2.46}$$

combines the volume fraction, V_f, and scattering contrast, $|\Delta\rho|^2$, of the scatterer. If X is low, one should expect difficulty in recording the scattering. However, X is the single most-deciding factor on the viability of an ASAXS experiment. In the ideal system for ASAXS, X of the anomalous scatterer should be higher than that of any other scatterer in the system.

A relationship exists between the scattering strength and the total scattered intensity. If $f(D)$ is the differential volume fraction distribution of scatterers of a single contrast, $|\Delta\rho|^2$, such as obtained via the maximum entropy method above, then the volume fraction of those scatterers is

$$V_f = \int_0^\infty f(D)\, dD \tag{2.47}$$

But V_f is also related to the well-known scattering invariant, Q, in equation (2.32) of Porod,[104] by integration of the isotropic, total scattered intensity over all h,

$$Q = \int_0^\infty I(h)\, h^2\, dh = 2\pi^2 |\Delta\rho|^2 V_f. \tag{2.48}$$

Both Q and X are invariant of the size distribution of the scatterers. In fact,

$$Q = 2\pi^2 X. \tag{2.49}$$

Successful evaluation of Q from SAS data depends upon the availability of a sufficient range of h so that the integrand tends to zero for both $h \sim 0$ and $h \sim \infty$. The evaluation is complicated by two problems:

1. uncertain extrapolation of the data beyond the measured range of scattering vectors,
2. magnification of random statistical errors at high h

An improved evaluation may be made directly from the maximum entropy size distribution which was derived by an entropy-constrained curve-fitting technique that minimizes random statistical noise. Limiting forms of extrapolation were avoided by modeling all of the scattering simultaneously using a model scattering function. Because the maximum entropy distribution represents all of the *statistically significant* dimensions present in the scattering and is the distribution of maximum configurational entropy that is consistent with the intensity data, it is possible to obtain a more reliable measure of the invariant by combining Eq. 2.47, 2.48, and 2.49,

$$Q = 2\pi^2 \int_0^\infty x(D)\, dD, \tag{2.50}$$

where $x(D) = |\Delta\rho|^2 f(D)$. As the scattering strength X is the product of the contrast and volume fraction, the preceding integration is valid for both simple systems with a single scattering contrast and complex systems where there is more than one type of particle. For the situation where there are i different types of scatterers,

$$Q = 2\pi^2 \sum_i |\Delta\rho|_i^2 \int_0^\infty V_p(D)\, N_i(D)\, dD, \tag{2.51}$$

from the differential number distributions, $N_i(D)$, and scattering strengths of each different type of particle. Additional information must be supplied in the latter case to separate the various component distributions.

2.2.3 Experiment Requirements for ASAXS

Because the drop in f' due to the anomalous dispersion is highly localized to the vicinity of the electron binding energies, a basic requirement of ASAXS is a variable-photon energy source of X-ray photons, such that the intensity does not change appreciably as a function of photon energy over the desired range of photon energies. The new generation of synchrotrons provide such a source as well as other desirable characteristics making them well-suited to the needs of SAXS, in general. Low emittance, good angular collimation, and high flux are among these, but also at the newer synchrotrons such as the National Synchrotron Light Source (NSLS) at Brookhaven National Laboratory, lifetimes of the stored electron beam producing the X-rays are upwards of 8 hours, thereby providing practical time frames for the completion of a single SAXS experiment. The broad high-intensity spectrum offered by the synchrotron is superior to the Bremsstrahlung spectrum from a sealed X-ray tube or rotating anode X-ray source. The latter is of such low intensity that impractically-long counting times are required to develop adequate counting statistics for the scattering measurements.

The range of energies available for ASAXS at a synchrotron is usually 5 to 25 keV, dependent on the design of the beam line monochromator and the energy-dependent intensity profile of the synchrotron radiation. The high intensities of the synchrotron allow relatively rapid counting intervals to acquire adequate counting statistics. Because the synchrotron experiment is of much shorter duration then the lab experiment to get the same statistics, materials science investigations of practical significance can be carried out.

Energy resolution, defined as $\Delta E/E$, is also important for discrimination of the photon energy-dependence of the scattering contrast, $|\Delta\rho|^2(E)$, near and far from the absorption edge. A quantitative measure of the minimum required energy resolution is dependent on the scattering system. To illustrate, a contrast change of a few ten percent demands better energy resolving power than does a contrast change of three times. The energy resolution of a double-crystal monochromator, typically $\simeq 0.0003$, is sufficient to handle a change in scattering contrast as low as ca. 25% but this limit requires a high volume fraction, $V_f >\sim 5\%$, for practical measurements of the ASAXS intensity differences.

2.2.4 Limits of Detectability

In a metal alloy, the ASAXS technique is used to isolate the scattering of a single type of scatterer in the presence of other types of scatterers. While many metallurgical alloys exist with several types of scatterer present, especially engineering alloys, not all are good candidates for ASAXS. On the basis of the experiments reported here, minimum limits of detectability have been established for application of the ASAXS technique at an X-ray synchrotron described here. Those limits appear in Table 5. Note from item 6, that a large number of important metallurgical systems potentially may be addressed by the ASAXS technique.

2.2.5 Isolation of a Single Scatterer by ASAXS

In this section, the procedure of isolating a single scattering type (from a distribution of many types) will be presented. The SAS intensity, $d\Sigma/d\Omega$ written here as I, is the product of three terms: contrast, amount in terms of a distribution function, and scattering profile per unit amount. The generalized matrix form,

$$\mathcal{I}(E,h) = \mathcal{C}(E,s)\,\mathcal{F}(s,r)\,\mathcal{G}(s,r,h), \qquad (2.52)$$

where $\mathcal{I}(E,h)$ are the intensities of the ASAXS experiments at different energies, E, and different scattering vectors, h, $\mathcal{C}(E,s)$ are the $|\Delta\rho|^2$ of each different type of scatterer, s, for each E, $\mathcal{F}(s,r)$ are the distributions of each s at each dimension r, and $\mathcal{G}(s,r,h)$ are the scattering profiles of each s at r and h.

Generally, SAXS experiments are conducted under monochromatic conditions. In this case, $\mathcal{C}$ reduces to a scalar, $\mathcal{F}$ reduces to a column vector, and $\mathcal{G}$ is reduced to two-dimensions. This is the situation addressed by

Table 2.1: Observed minimum limits of ASAXS detectability for precipitation in a steel alloy, estimated from the present experimental data.

1. The size of the scatterer should be within the range of 1 nm to 1,000 nm, as limited by the resolution of the small-angle scattering camera. For a double-crystal diffractometer, the lower limit increases to ca. 40 nm.
2. The precipitate to be studied by ASAXS should be highly enriched (or depleted) in the anomalous element within only that precipitate, with respect to the bulk alloy.
3. The minimum detectable total scattering strength, $X = V_f|\Delta\rho|^2$, is $3 - 5 \times 10^{27} m^{-4}$. The scatterer is termed weak if $X < 10^{28} m^{-4}$.
4. The change in total scattering strength due to ASAXS should be greater than 30%.
5. The energy resolution of the monochromator, $\Delta E/E$, should be less than 0.0005.
6. For Ge optics: the accessible K-shell absorption edges are the $3d$ transition elements: Ti, V, Cr, Mn, Fe, Co, Ni, Cu, Zn, and Ga. The accessible L edges are Cs, Ba, and the lanthanides.

the maximum entropy size distribution analysis code discussed above, which seeks a solution to

$$\mathcal{I} = \mathcal{F}(C\,\mathcal{G}). \tag{2.53}$$

Written as such, it is but one special case of the generalized equation. Three approaches may be used to extract useful information from the generalized equation, each of which involve groupings of two of the RHS terms in the generalized equation (in parentheses) and solving for the third:

$$\text{I.} \qquad \mathcal{I} = \mathcal{C}(\mathcal{F}\,\mathcal{G}) \tag{2.54}$$

$$\text{II.} \qquad \mathcal{I} = \mathcal{F}(\mathcal{C}\,\mathcal{G}) \tag{2.55}$$

$$\text{III.} \qquad \mathcal{I} = (\mathcal{C}\,\mathcal{F})\mathcal{G} \tag{2.56}$$

Grouping I (Eq. 2.54) corresponds, roughly, to the method used by Lyon, *et al.*,[88] to determine the three partial structure functions, for example, S_{AA}, S_{AB}, and S_{BB}, for the AA, AB, and BB scattering events in binary systems. The work was also extended to ternary systems. In the nomenclature used there, S corresponds to our $(\mathcal{F}\,\mathcal{G})$, and the assumption of vanishing scattering interference terms is relaxed. Using this method, unmixing in several binary and ternary alloys was studied by determining the tie-lines in the corresponding phase diagrams.[89,91] An advantage of their approach is that systems with scattering interference may be examined and it is not necessary for those systems to have precipitation, just unmixing. However, the partial structure functions, S, so determined must be further reduced if dimensional information, analogous to $\mathcal{F}$, is sought.

Grouping II (Eq. 2.55) is the form best suited for a maximum entropy determination of $\mathcal{F}$ for all types of scatterer s, using ASAXS scattering intensities, $\mathcal{I}$, from all energies simultaneously. By this method, the entropy of each distribution is maximized, subject to the input data, energy-dependent scattering contrasts, and assumed scattering form-factors. Such a method is the most direct determination of the distributions, with the potential for introducing the least bias on the part of the interpreter. But the problem is unwieldy on a computational level, requiring the use of a four-dimensional representation of $\mathcal{G}$ which must be calculated for each combination of E, s, r, and h. It is unlikely that so many floating-point values should be maintained in a pre-calculated array for use by the entropy maximization search technique. Such an array would encompass some one hundred thousand floating-point elements, requiring more than one megabyte of random access memory. A more memory-conservative approach would be to calculate each element in $\mathcal{G}$ as it is needed. Because the iterative search technique of Skilling and Bryan[127] accesses each element in $\mathcal{G}$ about seven times per iteration, and the number of iterations required to converge upon a solution is a few 10 to 100, repetitive calculations of $\mathcal{G}$ at run-time seems an unnecessary expense of CPU-time, hence the method is abandoned.

Finally, grouping III (Eq. 2.56) solves for the scattering strength distributions, $\mathcal{X} \equiv (\mathcal{C}\,\mathcal{F})$, at each separate energy, deferring the determination of the individual distributions of scatterers, f, until a later step. While the f so obtained are inferior in theory to the distributions obtained from a solution using grouping II in the sense that they are not necessarily the volume fraction distribution of overall maximum entropy, the method is straightforward and can yield a satisfactory numerical result.

Furthermore, the method provides a simple technique for assessing a margin of error in the determined f. The

technique for a maximum entropy determination of the size distribution is used as before, but a different problem is to be solved. Assuming that all the scatterers have the same morphology and consequent model scattering function, the transformed problem seeks a scattering strength distribution by

$$\mathcal{I} = (\mathcal{C}\,\mathcal{F})\mathcal{G} = \mathcal{X}\,\mathcal{G} \tag{2.57}$$

and is solved for each energy independently. $\mathcal{X}$ is the summation of the scattering strengths of all scatterers at that photon energy. To extract the distributions of the individual scatterers,

$$\mathcal{X} = \mathcal{C}\,\mathcal{F} \tag{2.58}$$

must be solved separately for each dimensional bin in the distribution by combining results from different energies. It is obvious that the stronger the variation in $\mathcal{C}$, the more detailed the information about $\mathcal{F}$ may be. Direct matrix inversion, $\mathcal{X}\mathcal{C}^{-1} = \mathcal{F}$, is not practical as $\mathcal{C}$ is usually ill-conditioned except for the anomalous scatterer. Linear least squares can lead to the generation of negative values of $\mathcal{F}$, an unphysical result. The maximum entropy approach would be the most satisfying method, however the error margins of $\mathcal{F}$ are not well known and it would be most difficult to determine such values as precisely as the maximum entropy approach requires. Therefore, a modification of the linear least-squares approach has been taken.

To illustrate, consider the case of three types of scatterers, each of the same morphology so that the $G(h_i, D_j)$ are identical for all three scatterers. The problem can be exactly solved for the volume fraction distributions of the three scatterers by SAXS experiments at three different photon energies. For convenience, the photon energy-dependent scattering contrast of each scatterer is defined

$$C_s(E_k) \equiv |\rho_s(E_k) - \rho_m(E_k)|^2. \tag{2.59}$$

Eq. 2.57 is then re-written

$$\begin{bmatrix} I(h_i,E_1) \\ I(h_i,E_2) \\ I(h_i,E_3) \end{bmatrix} = \sum_j G(h_i,D_j) \left\{ \begin{bmatrix} C_1(E_1) & C_2(E_1) & C_3(E_1) \\ C_1(E_2) & C_2(E_2) & C_3(E_2) \\ C_1(E_3) & C_2(E_3) & C_3(E_3) \end{bmatrix} \begin{bmatrix} f_1(D_j) \\ f_3(D_j) \\ f_3(D_j) \end{bmatrix} \right\}^T \tag{2.60}$$

which is then written in terms of the scattering strength distribution

$$\begin{bmatrix} I(h_i,E_1) \\ I(h_i,E_2) \\ I(h_i,E_3) \end{bmatrix} = \sum_j G(h_i,D_j) \begin{bmatrix} x_T(D_j,E_1) \\ x_T(D_j,E_2) \\ x_T(D_j,E_3) \end{bmatrix}. \tag{2.61}$$

Each of the scattering strength distributions, for each photon energy, is determined separately from each experiment by the maximum entropy method using

$$I(h_i,E_k) = \sum_j G(h_i,D_j)\, x_T(D_j,E_k). \tag{2.62}$$

The scattering strength distributions are written

$$\begin{bmatrix} x_T(D_j,E_1) \\ x_T(D_j,E_2) \\ x_T(D_j,E_3) \end{bmatrix} = \left\{ \begin{bmatrix} C_1(E_1) & C_2(E_1) & C_3(E_1) \\ C_1(E_2) & C_2(E_2) & C_3(E_2) \\ C_1(E_3) & C_2(E_3) & C_3(E_3) \end{bmatrix} \begin{bmatrix} f_1(D_j) \\ f_3(D_j) \\ f_3(D_j) \end{bmatrix} \right\}^T. \tag{2.63}$$

The scattering contrast matrix of Eq. 2.63 is ill-conditioned with respect to scatterers 2 and 3 if the change in scattering contrast with photon energy is significant only for scatterer 1. In this case, Eq. 2.63 reduces to the ASAXS gradient method,

$$\begin{bmatrix} x_T(D_j,E_1) \\ x_T(D_j,E_2) \\ x_T(D_j,E_3) \end{bmatrix} = f_1(D_j) \begin{bmatrix} C_1(E_1) \\ C_1(E_2) \\ C_1(E_3) \end{bmatrix} + x_{2+3}(D_j), \tag{2.64}$$

---

and $f_1(D_j)$ is the slope of a plot of $x_T(D_j,E_k)$ *vs.* $C_1(E_k)$. The complete volume fraction distribution is defined by repeated applications of Eq. 2.64 for each diametral bin, D_j. The standard deviation of the slope of a linear least-squares fit, $\sigma[f_1(D_j)]$, provides an estimate of the margin of error in the analysis. While it is possible for the situation $f_1(D_j) < 0$ to occur, it is observed in such cases that $0 < |f_1(D_j)| < \sigma[f_1(D_j)]$, indicating a lack of statistical certainty about dimension D_j. Therefore, negative $f_1(D_j)$ values are set to a small, positive value generally considered below the threshold of detectability. At least three different scattering contrasts are required to develop sufficient statistics about the distribution of the anomalous scatterer. For more than one anomalous scatterer, energies near another absorption edge must be used and the number of energies must be increased.

2.3 Resonant Raman Scattering

A source of background becomes important to ASAXS experiments when the incident photon energy, E_1, is close to the binding energy of a core electron (e.g., E_{1s} for a $1s$ electron) of some element in the sample. The background is due to an inelastic resonance scattering process known as resonant Raman scattering (RRS). This scattering has been observed to be constant as a function of angle[130,131] while the intensity spectrum was shown to be dependent on E_1. For $2p_j$-electron RRS, the energy range of the

intensity spectrum was

$$E_{RRS} = E_1 - (E_{2p_j} + E_{\varepsilon p}), \tag{2.65}$$

where $0 < E_{\varepsilon p} \ll E_{2p_j}$ and E_{2p_j} is the binding energy of a $2p_j$ electron. Thus for $2p_j$-electron RRS, the photon energy of RRS is always lower than the incident photon energy by at least the binding energy of a $2p_j$ electron. The peak intensity in the spectrum, apparent from Spark's figures, is for $E_{\varepsilon p}$ just greater than zero.

A special case of the statistical theory of RRS is described by Tulkki and Åberg,[142] where it was shown how RRS develops into fluorescence as the incident photon energy is raised above the absorption edge energy. Further papers[141,143] showed the intensity of RRS to increase as the incident photon energy increased towards the absorption edge energy, confirmed by the experiments of Sparks as well as others.[30,92]

The DCD optics can be exploited to reject any possible RRS intensity from these ASAXS experiments. Since $E_{RRS} < E_1$, the Bragg angle for RRS is greater than the Bragg angle for the incident photons by a few degrees when using Ge_{111} monochromator optics for 6-11 keV incident photons. When the DCD analyzer optics are tuned to the Bragg angle of the incident photon energy, the RRS is suppressed $10^{-11} \sim 10^{-10}$ by the rocking curve of the optics. By measuring the ASAXS at angles smaller than the Bragg angle for the incident photons, RRS is effectively eliminated from the experiment by the optics. The same argument may be applied to any fluorescence the photon energy of which is less than that of the incident photons.

2.4 Double-Crystal Diffractometer Camera (DCD)

A description of the theory of the double-crystal diffractometer (DCD) and important references in its development are presented. Also presented are the optimizations of the instrument for the synchrotron X-ray source. In the last section, equations are given to calculate the rocking curve and associated terms. The reader is referred to Zachariasen[149] for a more complete description of the theory. Exact details of the construction of the DCD will be presented in Chapter 3 (refchap:3).

2.4.1 Bonse-Hart Design

Optimal utilization of the X-ray source depends on the scientific problem that is being addressed.[78] The objective of the current study was to measure the small-angle scattering from features as large as one μm, requiring a scattering vector variation, $\Delta h \leq 0.003$ nm^{-1}. Only SAXS cameras of the double-crystal, or Bonse-Hart design[9] have such capability. (Note: In this discussion, double-crystal instruments refer to the use of one or more crystal reflections before the sample position and one or more crystal reflections after the sample position.) A second objective was to use the ASAXS technique of contrast variation which meant using synchrotron radiation. As there are no permanent installations of Bonse-Hart cameras at any synchrotrons in this country available for X-ray research, it was necessary to design and build one. By considering the properties of the synchrotron radiation source, the optics were designed to maximize the X-ray power available for scattering while still maintaining a low Δh.

The double flat crystal instrument in the non-dispersive (1,-1) setting with the sample between the two crystals was first used for SAXS by Fankuchen and Jellinek.[33] The (1,-1) notation refers to the first-order Bragg reflection in both collimator and analyzer crystals. As shown in Fig. 2.3,[68] the first crystal acts as a collimator for the source and the second crystal analyzes the scattered radiation from the sample by rotating about an axis positioned on the surface of the second crystal. Because collimation is achieved by Bragg reflection rather than geometry, the illuminated sample area can be allowed to become quite large, 4×3 mm^2 in the case of Kaesberg, *et al.*[69,70] Thus, Δh is limited only by the angular width of the rocking curve.

The intensity profile, with no sample in place, is the convolution of the rocking curve of the first crystal with that from the second crystal. As mentioned above, the tails of the intensity profile from a single flat crystal will fall as θ^{-2}, and so shall the tails of this so-called 1×1 crystal pair. The $m \times n$ notation refers to the number of reflections in the collimator and analyzer crystals, respectively. Making both the collimating and analyzing crystals asymmetric,[20] a 1×1 camera allows one to make SAXS measurements closer to the direct beam than any m$\times$n camera with symmetric crystals.

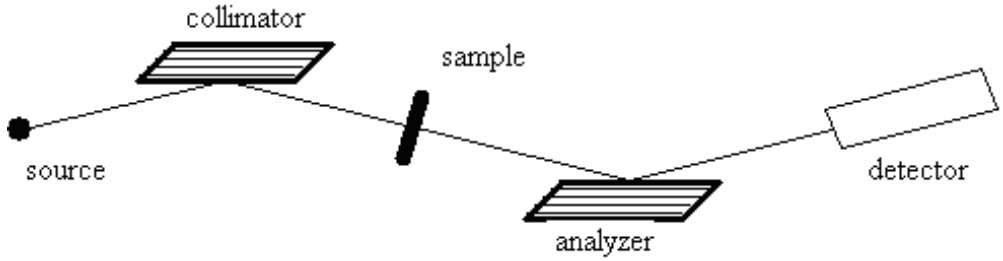

Figure 2.3: The (1,-1) geometry of the 1×1 two crystal *spectrometer* for small-angle scattering.[68] As wavelength is constant and angle is scanned, *diffractometer* is the correct term.

Previously, it was shown that the perfectly-collimated small-angle scattering intensity at the highest θ in the experiment falls as θ^{-4} while the slit-smeared intensity available with the double-crystal diffractometer goes as θ^{-3}. Without adequate precaution then, it is possible for the instrumental empty beam signal to be larger than the small-angle scattering signal at high θ with a 1×1 double-crystal diffractometer. A method of circumventing this possibility, described in the classic paper of Bonse and Hart,[10] replaces each of the single-reflection flat crystals in Fig. 2.3 with an n-reflection channel-cut crystal. The tails of the intensity profile from each channel-cut crystal will fall proportional to $(\theta^{-2})^n$ so that $n \geq 2$ is adequate insurance. An asymmetrically-cut fore-crystal was also used by Bonse and Hart to increase the angular acceptance, the cross-sectional area, and the throughput of the instrument.

In general, an m×n double-crystal diffractometer will have an instrumental profile that will fall off as $(\theta^{-2})^{\nu}$ where n is the lesser of m or n. Therefore it is necessary for small-angle scattering experiments to have at least two reflections both in the collimator and the analyzer so that the instrument profile falls off at least as rapidly as the scattering.

The 2×2 arrangement enjoys the highest throughput[24,25] of the possible m×n double-crystal diffractometer SAXS cameras and the greatest flexibility for wavelength selection at a synchrotron X-ray source while still maintaining a low instrumental intensity profile. As with any double-crystal instrument, special attention must be given to suppress the harmonics[12] as well as to the avoid any *spurious reflections* due to Laue diffraction (Kostroun, 1980). Bonse and Materlik[11] suggested using single crystal reflections for which the refraction index correction for the Bragg angle is different for the fundamental and its harmonics in order to separate the diffraction orders.

For two symmetric crystals in the (1,-1) diffractometer setting, the resultant positions of the harmonics are centered on the fundamental. The harmonics are detuned by using a setting near $y' = +1$ or $y' = -1$ for the fundamental but this also reduces the fundamental intensity as well. For two asymmetric crystals in the same (1,-1) diffractometer setting, the resultant positions of the harmonics become re-centered on the fundamental and the improvement of the first asymmetric reflection is lost by the second crystal. So to reduce the harmonics but maintain the fundamental intensity, it is necessary to use crystals of different asymmetry angle in the monochromator. Unfortunately, this is not good enough for SAXS experiments because the scattering from the fundamental and the harmonics are offset but the scattering due to the harmonics is not eliminated.

The instrument used in this work, described elsewhere in this dissertation as well as Long, *et al.*,[85] includes an asymmetric first crystal in magnification mode and a symmetric second crystal in a separated-function, fixed-exit monochromator. In the historical sense, these crystals would serve as the collimation system. Presently, they determine the photon energy bandpass from the white synchrotron X-ray source, which is already highly collimated. A pair of symmetric crystals, held in a monolithic fixture, act as the analyzer. All of the crystals are germanium with flat surfaces and use (111) Bragg reflection. The asymmetric first crystal is cut with the surface

inclined 7.02° towards the nearest (110).

Silicon would offer a Δh smaller than that from germanium, but the more narrow rocking curve decreases the X-ray power available for scattering. Based upon the body of existing electron microscopy data for the steels under examination, the smaller Δh provided by the Si optics (over the Ge optics) is not justified by the loss of source intensity.

2.4.2 Optimization of the Optics for the Synchrotron Source

Germanium was chosen because of its structure factor, its high reflectivity, its relative perfection, and the width of its intrinsic rocking curve. The full width at half maximum for Ge_{111} is ≈20 seconds of arc at 6 keV. The opening angle for 6 keV photons at the National Synchrotron Light Source is ≈44 seconds of arc. An asymmetrically-cut crystal can be oriented so as to increase the photon energy bandpass, increase the angular acceptance, and decrease the angular emittance (improve the collimation) from the synchrotron source. In particular, a 7° offset increases the angular acceptance of the Ge_{111} crystal to ≈30 seconds of arc at 6 keV. This means that approximately 75% of the available photons at this energy are accepted by the experiment.

The cross sectional area of the beam is modestly enlarged (2.2×) and none of it is lost if the crystals are adequately large (∼50 mm diameter). Table 2.2 shows the parameters of importance for matching the optics of the first crystal to the opening angle of the source over the photon energy range of interest. The resulting ΔE (eV) is also indicated. It is especially important to keep the energy resolution, $\Delta E/E$, in mind because the ASAXS experiments are performed at various photon energies near an absorption edge to achieve a variation in scattering contrast. Exact calibration of the energy scale of the monochromator is essential as the absorption edges of the $3d$ transition elements are 20 eV wide and fluorescence must not be allowed.

In the present instrument, the harmonic contribution to the signal is 10^{-4} (see Table 2.3) and is achieved because of the qualities of the source and the effect of the intervening Ge K-edge on the X-ray structure factor. The X-ray flux from the bending magnet source is a factor $\sim 10^2$ less at 18 keV than at 6 keV and the drop is even more precipitous for the harmonics at 24, 30, 42, ... keV. The helium beam path between the ultra-high vacuum front end of the beam line and the first monochromator crystal is the only area of the experiment which discriminates against the photon energy of interest. The transmission through 20 m of He is 81% for 6 keV X-rays and 94% for 18 keV X-rays. The structure factor for 18 keV is 10% of that for 6 keV and this is multiplied for each reflection. The silicon PIN photodiode discriminates strongly against higher energy photons because its efficiency is 100% at 6 keV and only 36% at 18 keV but the 18 keV photons generate a photocurrent three times that of the 6 keV photons, canceling out the improvement due to detector efficiency.

Table 2.3: Measured Intensity at the Sample Position in the Diffraction Orders.

E (keV)	(hkl)	I_{hkl}/I_{111}
6	(111)	1.0
18	(333)	1.9×10^{-4}
24	(444)	5.2×10^{-5}
30	(555)	1.1×10^{-5}
42	(777)	9.3×10^{-7}
48	(888)	9.3×10^{-7}

Collecting all of these factors together by comparing Ge_{111} to Ge_{333}, the source discriminates against the harmonic by a factor of $10^2 \sim 10^3$, the He beam path causes an enhancement of the harmonic by a factor of $\sim$ 1.2, and the crystal monochromator discriminates against the harmonic by a factor of $\sim 10^2$. In all, a reduction of $10^4 \sim 10^5$ is predicted. To test this estimate, the actual intensity through a 3×3 mm^2 area at the sample position was measured using calibrated filters, a scintillation detector, and a pulse height analyzer. The results are shown in Table 2.3. Each harmonic was maximized in turn by means of slight adjustments of the crystals so that the measurements would accurately represent the true peak in the number of photons at each energy. It can be seen that even the first available harmonic contains $\sim 10^{-4}$ fewer photons than the primary energy. Thus the harmonic contribution to the experiment is at the 0.02% level.

Table 2.2: X-ray Source, Ge_{111} Asymmetric ($\alpha = 7°$) Crystal, and DCD Camera Parameters

E (keV)	5	6	7	8	9	10	11
$2\sigma_v$ (arc sec)[2]	47.3	43.8	41.0	38.8	36.9	35.3	33.9
$\Delta\theta_{cr}$ (arc sec)[3]	34.6	29.8	25.8	22.9	21.2	19.3	19.2
$\Delta E/E(\times 10^{-5})$[4]	41	43	44	45	47	48	50
ΔE (eV)[5]	2.0	2.6	3.1	3.6	4.2	4.8	5.5
h_{min} (nm^{-1})[6]	0.0061	0.0059	0.0055	0.0051	0.0049	0.0044	0.0043
I_0 (ph s^{-1})[7]	2	6	9	18	14	10	6
θ_B (°)[8]	22.307	18.440	15.731	13.723	12.173	10.940	9.935
m[9]	1.85	2.17	2.55	3.02	3.64	4.48	5.69
w_0 (nm^{-1})[10]	n/a	0.00147	0.00138	0.00128	0.00122	0.00117	0.00108
l_0 (nm^{-1})[11]	0.249	0.285	0.327	0.374	0.403	0.448	0.493

2.4.3 Rocking Curve Calculation

The intensity profile, P_H/P_0, of a single Bragg reflection, $H = (hkl)$, from a perfect single crystal, including absorption within the crystal, is given by

$$\frac{P_h}{P_0} \equiv D(y) = \left| y \pm \sqrt{y^2 - 1} \right|^2 \text{ [3.192]} \tag{2.66}$$

where

$$y = y' + iy'' \tag{2.67}$$

is a reduced variable of angle (or wavelength), generally complex. The bracketed numbers in the next equations refer to numbered equations in Zachariasen.[149] When $y' < 0$, the positive sign is taken, whereas for $y' \geq 0$, the negative sign is taken, so that $0 < D(y) \leq 1$ is valid for all y. For$|y| >\sim 4$, $D(y)$ tends to $|y|^{-2}$. With n such reflections, the composite intensity profile,

$$\hat{D}(y) = \prod_{i=1}^{n} D(y + \xi_i), \tag{2.68}$$

where ξ_i is the offset in the reduced angular scale for each reflection, i, from the first reflection. For $|y| >\sim 4$, $D(y)$ tends to $|y|^{-2n}$. In Fig. 2.4 are plots of the single reflection $D(y)$, both with and without absorption. The definition of y, given in several locations in Zachariasen,[149]

$$y = \frac{(1-m)F_0 + 2m(\theta_B - \theta)\Gamma^{-1}\sin(2\theta_B)}{2T\sqrt{|m|\,F_H\,F_{\bar{H}}}} \quad \text{[3.116,3.141,3.148,3.181]} \tag{2.69}$$

The structure factors of the participating atomic planes (considering that the crystal is not necessarily centrosymmetric) are

$$\begin{aligned} F_0 &= \text{structure factor at}(000) \\ F_H &= \text{structure factor at}(hkl) \\ F_{\bar{H}} &= \text{structure factor at}(\bar{h}\bar{k}\bar{l}) \end{aligned} \tag{2.70}$$

The magnitude of the deviation from unity of the index of refraction,

$$\Gamma = \frac{r_{e^-}\lambda^2}{\pi V_c} \text{ [3.101]}, \tag{2.71}$$

where r_{e^-} is the radius of an electron (2.818 fm), λ is the wavelength, and V_c is the unit cell volume. The polarization correction,

$$T = \frac{\sigma + (1-\sigma)\cos^2(2\theta_m)\cos^2(2\theta)}{\sigma + (1-\sigma)\cos^2(2\theta_m)}, \tag{2.72}$$

where θ_m is the anlge of the monochromator and σ is the fraction of σ polarization in the incident beam. Typical X-ray synchrotron monochromators use Bragg reflection and strong σ-polarization. The magnification factor,

$$m = \frac{\sin(\alpha + \theta_B)}{\sin(\alpha - \theta_B)}, \tag{2.73}$$

is due to the angle, α, between the crystal surface and diffracting planes (hkl). In wavelength terms, $\theta_B = |\alpha|$ defines the (theoretical) maximum wavelength possible for a specific crystal by Bragg's law. By inverting

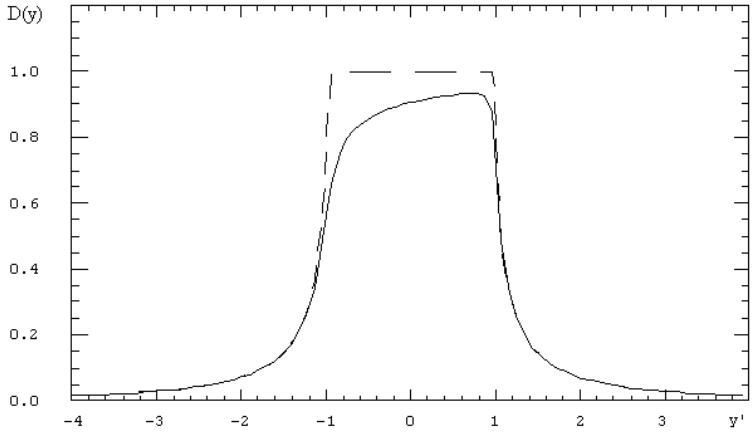

Figure 2.4: Intensity profile, $D(y)$, of a single reflection from a perfect single crystal; (dashed) without absorption ($y'' = 0$), and (solid) including absorption within the crystal.

Eq. 2.69, taking only the real parts of the complex terms, the scattering angle,

$$\theta = \theta_B - \frac{2y'T\sqrt{|mF_H F_{\bar{H}}|} - (1-m)|F_0|}{2m\sin(2\theta_B)/\Gamma} \qquad (2.74)$$

where θ_B is the Bragg angle. It is clear that the center of the rocking curve, at $y' = 0$, will only coincide exactly with θ_B in the symmetric Laue case where $|\alpha| = \pi/2$ and $m = +1$. The full width of $D(y)$ extends from $y' = -1$ to $y' = +1$ so the rocking curve width

$$\Delta\theta = \frac{2T\Gamma}{\sin(2\theta_B)}\sqrt{\left|\frac{F_H F_{\bar{H}}}{m}\right|} \qquad (2.75)$$

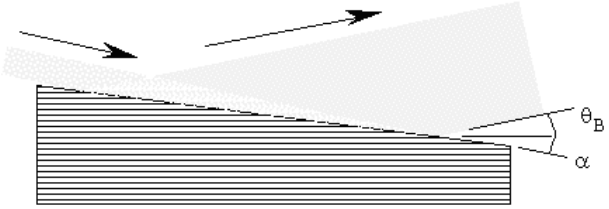

Figure 2.5: Demonstration of X-ray beam spatial magnification using an hypothetical crystal with an asymmetric cut. The Bragg reflection is specular with respect to the atomic planes (indicated by horizontal lines). When the crystal surface is not parallel to the atomic planes, the X-ray beam is either magnified (in this case) or demagnified, depending on the direction of inclination.

2.4.4 Asymmetric Reflection

A spatial magnification of the incident radiation is effected by $0 < \alpha \leq \theta_B$ (demagnification is $-\theta_B \leq \alpha < 0$). This is most easily shown by Fig. 2.5, using an hypothetical crystal, where a beam incident from the left on the asymmetrically-cut crystal intersects the atomic planes at $\theta_B \approx 11^\circ$. Its cross-section is magnified 4.5$\times$ on diffraction due to the $\alpha = 7^\circ$ asymmetry angle.

2.5 Silicon Photodiode Detector

A silicon photodiode and custom-design electrometer amplifier were implemented to remove deficiencies of existing types of X-ray detectors.[66] The SAXS intensity measured in an experiment is three to seven orders of magnitude less than the beam transmitted directly through the sample and generally decreases with increasing angle. The maximum angle at which scattered intensity can be measured, thereby defining the smallest features directly resolved in the experiment, is the angular position at which the SAXS intensity is comparable to the parasitic scattering background. For this reason, good signal-to-noise detectors such as scintillation counters (SC) or gas-proportional counters (GPC) are employed in pulse counting mode. The sample transmission coefficient, $T_s = exp(-\mu_m \rho_m t)$, is also an important parameter in a SAXS experiment for an accurate background subtraction and absolute scaling of the intensities. The transmission measurement is usually made by comparing the intensity at zero degrees scattering angle with the sample in and out of the beam.

With a SC or GPC, it is always necessary to attenuate the X-ray beam so that the detector is not damaged by the high flux and so that the output is linear with intensity. The spectral characteristics of the beam incident upon the detector are altered by attenuators, which can be an important problem if the incident X-ray beam includes harmonic contamination. Sometimes a current mode detector, such as an ionization chamber (IC), is used to directly measure the transmission but it also has a spectral response different from that of the SC or GPC, leading to the same problem as above. Unfortunately, the IC can not be used for measuring SAXS intensity because of its high noise level.

An ideal SAXS detector would be capable of measuring the sample transmission without attenuation and also performing the experiment without interruption. Interruptions occur during SAXS experiments using an SC when the need to install or remove an attenuator arises. The IC delivers an output current proportional to the X-ray intensity and is capable of measuring the direct X-ray beam without suffering radiation damage as mentioned above. However, its usefulness is limited because of its high intrinsic noise. A silicon photodiode operated in photovoltaic (unbiased) mode can be treated as if it were an IC[63] but delivers a higher signal and consequently higher signal-to-noise than the IC by virtue of its higher quantum efficiency. The PD detector can be used in conjunction with very high intensity X-ray sources, such as synchrotron radiation which has been rendered nearly monochromatic (mSR), and offers the most efficient operation with the advantage of a wide dynamic range with linear response.

2.5.1 Principles of Operation

The principles of operation of PIN diode detectors operated in photovoltaic mode for synchrotron X-rays have been explained previously.[14,63,75] In summary, an incident X-ray photon is absorbed within the photodiode thickness, t, and excites valence or core electrons to high lying conduction band states. The absorption length, $1/\mu_m(E)\rho_m$ for 6 keV photons is one-tenth the photodiode thickness, hence the efficiency for absorption,

$$\eta(E) = 1 - \exp[-\mu_m(E)\rho_m t], \tag{2.76}$$

is almost one hundred percent. In Eq. 2.76, $\mu_m(E)$ is the mass absorption coefficient and ρ_m is the mass density of the photodiode. These electrons excite other electrons into the conduction band. The original photoelectron is thereby thermalized into a number of electron-hole pairs, proportional (ω_b = 3.6 eV average per electron-hole pair for silicon) to the energy of the photon. The number of electron-hole pairs generated, the quantum yield, is given by

$$q(E) = \frac{E}{\omega_b}\eta(E). \tag{2.77}$$

The lifetime of these pairs is sufficiently long for them to diffuse across the entire thickness of the photodiode and produce a photocurrent,

$$i(E) = q(E)\, e\, N(E)\, \Delta E. \tag{2.78}$$

Here, e is the charge of an electron and $N(E)\Delta E$ is the number of ph·s^{-1} with energy between E and $E + \Delta E$. The total photocurrent generated by the photodiode is the integral over all the energies of photons absorbed plus the photodiode noise and offset (dark) current and is written:

$$I = e\int_0^\infty q(E)\, N(E)\, dE + i_{\text{offset}} + i_{\text{noise}} \tag{2.79}$$

For a monochromatic X-ray beam, the integral of Eq. 2.79 reduces to Eq. 2.78. Typically the noise current from a PIN photodiode is 10 to 100 fA/$\sqrt{\text{Hz}}$. For photocurrents above the noise current and below the p-i-n junction saturation current (ca. 0.1 to 1 mA), the photocurrent is proportional to the photon intensity. The linear intensity range for a monochromatic beam of 6 keV photons is then 10^2 to 10^{12} ph·s^{-1}!

The PD is most efficient for low energy (up to 10 keV) photons and the efficiency decreases dramatically above 10 keV. When used with a monochromator, this effect suppresses (but does not eliminate) the monochromator harmonics. With the wide dynamic range, it is not necessary to attenuate the beam in any manner and SAXS data acquisition may proceed at the rate of a few seconds per angular position.

Silicon photodiodes, used individually, are not position sensitive devices.[75,76] It is possible, however, to utilize a photodiode array for such purposes but that application is not discussed here.

2.5.2 Amplifier Electronics

The fact that the wide dynamic range of the photodiode detector (PD) is linear requires a comparable degree of linearity in the associated circuitry. Commercial electrometers are available which, using multiple scales, can measure the resulting wide range of photocurrents. With such a device, one needs to *zero* each scale separately. In a SAXS experiment, regardless of how carefully the ranges are adjusted, the data would be interrupted by imperfect overlap regions as the scales change. The cabling required to carry the photocurrent to the electrometer can be a significant source of capacitance and noise, effectively raising the lowest measurable intensity. By incorporating a custom-built electrometer into the PD housing, this potential source of noise is reduced significantly. The cost of the components to build such a PD detector / electrometer system can be significantly less than other types of X-ray detectors.

The problem of applying the photodiode to measure SAXS efficiently is reduced to one of building an electrometer to span the full dynamic range of output from the photodiode. The electrometer can be constructed in one of three ways:

1. a log ratio amplifier
2. a charge integrating amplifier
3. current-to-voltage (CV) converter

The log ratio amplifier is often used for signals with a wide dynamic range, such as light transmission measurements, where measurement of an input 'signal' current is made against a 'reference' current. The output is the logarithm of the ratio of signal to reference. Commercial log ratio amplifiers[101] usually have a five decade dynamic range which is not sufficient to span the range of photocurrents in SAXS measurements.

The charge integrating amplifier[87] has the advantage of having fewer components than a log ratio amplifier. The input current is integrated over time until a reset relay is closed or the operational amplifier saturates. The output voltage is proportional to the amount of charge accumulated. For constant photocurrents, this means that the output voltage is proportional to the integration time which, depending on the value of the capacitor, can vary from mS to kS. Dynamic range is limited by the practical limits of integration time for low photocurrents. The main disadvantage of the charge integrating amplifier is the necessity to *zero* the integrator for each new measurement. This requires active control to operate a reset relay. With a single capacitor, the dynamic range of this circuit is about 3.5 decades, limited by the range of the operational amplifier, but it is possible to incorporate multiple capacitors to change integration rates.

The most common form of electrometer circuit is the CV converting electrometer shown Fig. 2.6, the noise and frequency response of which has been analyzed by Hamstra.[54] The number of circuit components is comparable to that of the charge integrating amplifier. The feedback resistance is selected to measure a specific range of photocurrents. The value of the smoothing capacitor, C, should be chosen so as to roll off the response of the amplifier below the frequency where noise poles occur due to the inherent capacitance of the photodiode.[75] Input capacitance is further minimized by shortening the distance between photodiode and amplifier. As in the case of the charge integrator, the dynamic range of this circuit is about 3.5 decades which may be extended by switching feedback resistances which is also shown.

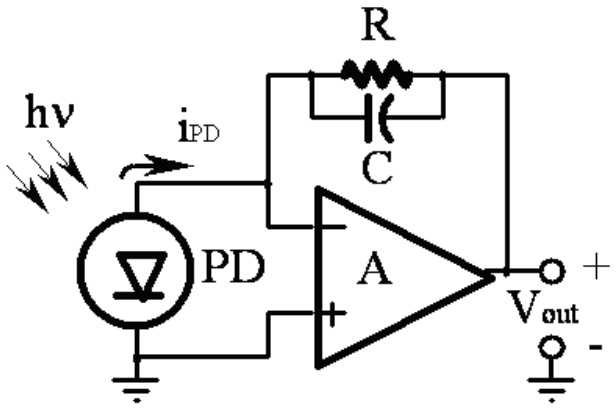

(a)

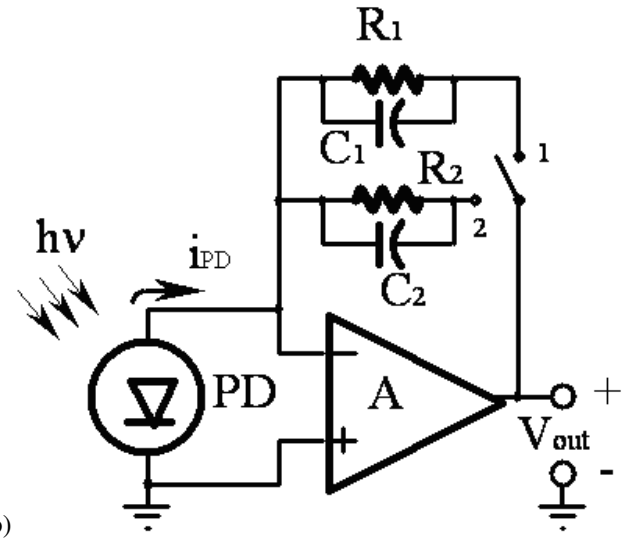

(b)

Figure 2.6: Schematic of a current-to-voltage (CV) converting amplifier with (a) a single range of amplification and (b) two different time-constants and amplifier gains, selected by a switch. 3.5 decades of dynamic range are typical for each scale.

Chapter 3

Experimental

The experimental procedure and equipment will be described as will the metallurgical state of the as-received samples. A room-temperature chemical polishing solution for the preparation of steel samples for small-angle X-ray scattering will be given. This solution may also be used to pre-thin TEM samples prior to jet-polishing. Drawings of the double crystal diffractometer SAXS camera are given which detail the essential parts. Finally, equations are given to reduce the raw data to experimental SAXS data, including the process of collimation correction.

3.1 Steel Samples

3.1.1 Heat Treatment

25 mm thick by 150 $\times$ 150 mm^2 plates of Modified Fe9Cr1Mo steel, Carpenter Technology heat #30394, were obtained from Dr. Vinod Sikka of the Advanced Alloy Program at the Oak Ridge National Laboratory in the normalized and tempered (N&T) condition, which is the standard condition used in actual service. Prior to the N&T treatment, the plates had been hot-rolled from an argon-oxygen-decarburized / electroslag remelted ingot (Bodine & McDonald, 1983). Normalization, to remove the effects of any prior mechanical or thermal treatments, consists of heating a large plate, ca˙ 25$\times$300$\times$3000 mm^3, for one hour at 1038° C and then cooling to room temperature in air. The microstructure produced is lath martensite. The tempering temperature of 760° C was maintained for one hour and then followed by air cooling. The resultant microstructure is ferrite (tempered martensite). Upon receipt at Northwestern University, each plate was aged 5000 hours at either 25°, 482°, 538°, 593°, 649°, or 704° C to simulate a typical in-service condition. Slices of the AF1410 steel measuring 40$\times$20$\times$0.15 mm^3 were received from the Steel Research Group, headquartered at Northwestern University. The slices had been subjected to a solution heat treatment for one hour at either the standard temperature of 830° C or 1000° C which was believed to deliver a cleaner microstructure. Subsequent to solution heat treatment, each slice was aged at 510° C for times ranging from 1/4 hour to 100 hours. The resultant microstructure is ferrite (tempered martensite). These samples were then thinned for SAXS using the technique described below.

3.2 SAXS Sample Preparation

The optimum thickness for steel SAXS samples is of the order of 15-20 μmwhen the experiments are conducted at monochromatic photon energies from 5000 eV up to the absorption edge energy of iron (7112 eV). Just above the iron absorption edge, this optimum thickness drops to about 4 μm. In the present case, all experiments were conducted below the iron absorption edge. From each plate of Modified Fe9Cr1Mo steel, a 25$\times$25$\times$25 mm^3 cube was cut using a band saw. From this, a wafer ca˙ 0.4 mm thick was sliced from the interior, to avoid edge effects of the sample due to the heat treatment, using a Buehler Isomet^{TM} diamond wafering saw. The as-received thicknesses of the AF1410 steel samples were sufficient to skip this step. Each wafer was then immersed in a polishing / thinning solution of 80% (volume) concentrated hydrogen

peroxide, 5% hydroflouric acid, and 15% distilled water operating at room temperature. This solution is an exceptional general purpose thinning solution for most ferritic steels. It leaves smooth surfaces and does not appear to attack the sample edges appreciably. The solution is quite dangerous because of the presence of the hydroflouric acid and special handling precautions were taken.

Nalgene™ beakers were used for the solution, Teflon™ forceps were used to hold Teflon™ coated magnets which were use to remove the steel sample from the solution, and face shield, HF-proof lab apron, and HF-proof gloves were worn. Most importantly, the base that was used to neutralize the solution after thinning was ammonium hydroxide instead of the more commonly-used sodium hydroxide to avoid a toxic reaction product. It was necessary to conduct the thinning in a fume hood because the reaction between the hydroflouric acid and the iron evolves much gas. Periodically, the wafer (now resembling a foil) was removed from the solution, neutralized in a solution of 20% (volume) ammonium hydroxide in water, rinsed thoroughly in methanol, and then dried.

Foil thickness was measured using a hand-held micrometer with an accuracy of ca˙ 5 μm. The micrometer was calibrated against a series of metal foils of known thickness and was used to determine if the sample thickness was within a factor of two of the optimum thickness. As each foil became sufficiently thin, it became quite flexible and also tended to *swim* in the thinning solution. The solution was diluted at this stage to slow the chemical reaction so that the sample would not be completely eroded. Thinning was discontinued when the sample thickness was below 30 μm or when sample dimensions had reduced below 3×3 mm^2. The foil was then preserved by taping it, along one edge, to a microscope slide and storing in a cool dry location while awaiting beam time at the synchrotron.

3.3 Equipment

The small-angle scattering measurements were conducted on beam line X23A3, of the National Synchrotron Light Source at Brookhaven National Laboratory. As a guest user of that facility, the equipment was designed as a temporary installation but it was also designed to take advantage of particular features of the X23A3 beam line. In this section, that installation is detailed.

3.3.1 X-ray Source

The X23A3 beam line, primarily used for X-ray topography, is operated by the Materials Science and Engineering Laboratory of the National Institute for Standards and Technology. A drawing of X23A3 follows that shows the installation of the double-crystal diffractometer SAXS camera. Experiments may either make use of a monochromatic X-ray beam in the energy range 4 to 25 keV or use the unmodified white synchrotron beam. Harmonics of the fundamental X-ray photon energy are suppressed by specialized design of the Ge optics. No grazing incidence mirrors are used. The entire beam line operates in one atmosphere helium from the water-cooled mask at the exit of the storage ring front end up to the experimental hutch. Beam line hardware is controlled and monitored by a single-user Digital Equipment Corporation MINC™ 11/23 minicomputer running the RT11 real-time operating system.

In Fig. 3.1, a white synchrotron X-ray beam is emitted from the storage ring (1) and enters the monochromator some 17 meters distant, after passing through a water-cooled Be window (2). The entire monochromator operates in just above one atmosphere of helium. Monochromator entrance slits (3) have been moved out of the white beam, the intensity of which is always monitored by ionization chamber (4). The white beam is monochromated by the first monochromator crystal (5), a Ge_{111} crystal cut 7.02°asymmetric, oriented in *mag* mode as shown. The second monochromator crystal (6), a Ge_{111} symmetrically-cut crystal, is oriented so the beam which exits the monochromator is parallel to the white synchrotron beam that enters the monochromator. The exit-side ionization chamber (7), which measures the intensity of the monochromatic beam, is used in tuning the monochromator to the desired photon energy. The cross-section of the monochromatic X-ray beam is defined by the exit slits (8) before it leaves the monochromator. Monochromator helium pressure is maintained by the beryllium window (9). Beyond this, the beam line operates in air. Should an experiment require the white synchrotron radiation, the first crystal (5) in the monochromator is moved out of the beam and the beamstop (10) for the white beam is removed. To maximize the incident

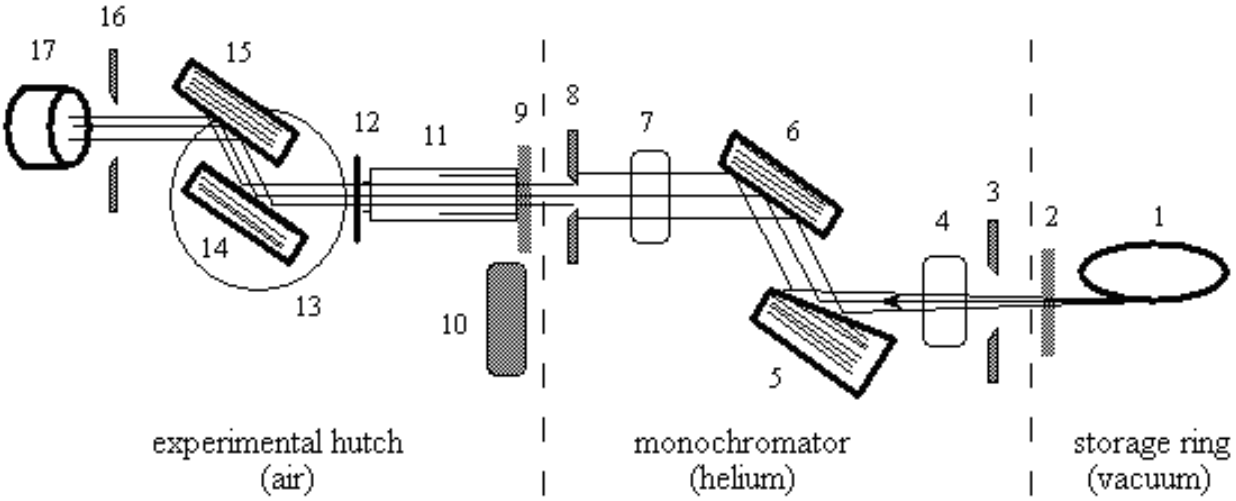

Figure 3.1: Installation of the double-crystal diffractometer SAXS camera on the X23A3 beam line at the National Synchrotron Light Source at Brookhaven National Laboratory. See the text for a description of each element.

monochromatic X-ray flux on the sample (12), a beam transport tube (11) pressurized to just above one atmosphere with helium is installed. Contained within this transport tube is an ionization chamber, used to monitor the intensity of monochromatic X-rays incident on the sample. Two pins project on the exit side of the tube and serve to position the sample support ring in a reproducible manner. The two symmetric Ge_{111} analyzer crystals (14 and 15) are rotated together as a monolith (13) to measure the small-angle scattering profile from the sample. The surface of the first analyzer crystal is positioned at the center of the monolith rotational axis to avoid precession of the beam as the monolith is rotated. The silicon photodiode X-ray detector (17) is shielded from the parasitic scatter of radiation by the scatter slit (16).

3.3.2 Monochromator

The monochromator is a double-crystal, fixed-exit design that allows the changing of the crystal optics. The surfaces of both crystals in the monochromator are flat and may be cut parallel or asymmetric to the diffracting planes. Each crystal is mounted on a stage which provides two axes of rotation (surface normal and Bragg). Additionally, the second crystal may be fine-tuned about the Bragg angle using a piezoelectric transducer. The first crystal stage is mounted on a vertical translation arm to adjust to the position of the incident synchrotron radiation. The second crystal stage is mounted on a horizontal translation arm to provide a fixed-exit position for the monochromatic beam. All mechanical motions and ionization chambers are under control of the beam line MINC^{TM} computer.

In the small-angle scattering experiments, monochromatic X-rays of energy ca. 6 keV were obtained from a double flat-crystal, fixed-exit monochromator. The energy spread of the monochromated beam was about 3 eV. We supplied monochromator crystals prepared by Eagle-Picher Industries, Inc. from a single boule of single crystal germanium, grown along the (111) crystallographic axis. The first crystal was cut asymmetrically from the (111) planes with the surface inclined 7.02°toward the nearest (110). The second crystal was cut symmetrically, parallel $\pm$0.02°to the (111) axis, as shown in Fig. 3.1. Two symmetrically-cut single crystals of germanium were taken from the same boule as the monochromator crystals to be used as the double-crystal analyzer, located in the experimental hutch. All four crystals were cut with flat surfaces. The perfection of each of these perfect single crystals was verified by X-ray topography. A second,

comparable set of four dislocation-free silicon crystals were also prepared, should the three-fold improvement in angular resolution be required.

It was necessary at the beginning of each block of experimental time, to allow one day for the installation and alignment of the germanium crystals by the resident beam line scientist. An additional half-day of beam time was required to prepare the equipment for SAXS operation. Spatial definition of the beam was performed using the monochromator tank exit slits. The entrance slits were wide open. The slits are positioned using a stepping motor with a linear precision of 10 μm. During each experiment, the exit slits were usually fixed at 3×3 mm^2.

After the beam line preparations, transmission radiography was used to verify the uniformity of sample thickness within the area illuminated by the X-ray beam. This technique allowed the sample position to be adjusted on the sample support ring so that any pinholes or variations in thickness of the sample due to chemical preparation technique could be avoided. The transmission radiography experiments were conducted by replacing the DCD analyzer with a video camera and fluorescent screen. X-ray absorption contrast could thus be directly observed on a television monitor.

3.3.3 Experimental Hutch

The experimental hutch, located downstream of the monochromator is equipped with mechanical arms which provide two independently-operating systems of three-dimensional translation motions and two-dimensional rotation motions. The white beam window was sealed with a lead block and locked with a Kirk^{TM} key. The monochromatic beam from the monochromator enters the experimental hutch through a beryllium window which provides a mechanical seal for the monochromator helium. The double-crystal diffractometer analyzer is mounted on one of the mechanical arms, the photodiode detector on the other.

3.3.4 Beam Transport and Incident Beam Monitor

A helium-filled beam transport tube was constructed with a built-in ionization chamber to avoid attenuation and air scattering of the monochromatic beam in the space between the beryllium window and the sample position. The 250 mm long ionization chamber with 300 VDC applied potential between two copper plates, is located inside the transport tube that is filled to just above one atmosphere of helium gas and served as the incident beam monitor (M) for the SAXS experiments. Attenuation of a 6 keV beam in this detector is less than 0.5%. A single layer of Kapton^{TM} tape was used to seal each end of the tube. Two pins project from the metal wall on the exit side of this tube and serve to position the sample holding ring in a reproducible manner, to within an estimated precision of 100 μm. The sample position is thereby fixed in space, in line with the fixed exit of the monochromator.

3.3.5 Double-Crystal Diffractometer Analyzer Monolith

The separated-function double-crystal diffractometer analyzer measures the small-angle scattering from the sample that is within the rocking curve width at the selected angle and photon energy. The two crystals are supported on a monolithic structure, simulating a two-reflection channel-cut crystal. While being more difficult to align than a channel-cut crystal, the two crystal arrangement provides flexibility of operation unavailable by any other method.

Part of this flexibility is derived from the large spatial definition of the incident X-ray beam on the sample. A large beam is desired to illuminate a sample volume as large as possible and to provide the greatest number of incident photons for scattering. It is not possible to design a channel-cut crystal that will a conduct a beam of dimensions 3×3 mm^2 at any monochromatic photon energy between the K absorption edges of the $3d$ transition elements through Cu, Zn, and Ga. The separated-function design allows both the spacing between the diffracting surfaces to be adjusted as well as the offset between the centers of the two crystals, so that a beam of any energy within the above range will be fully intercepted by both crystal surfaces. Furthermore, the two crystals may be rotated to suppress any spurious reflections, a feature not possible with the channel-cut design.

The two crystals are held in the (1,-1) orientation, as shown in Fig. 3.1 and in greater detail in Fig. 3.2, by mounting each on a stage that provided three rotational

axes (tilt, surface-normal, and Bragg) and two translational motions (surface-normal and beam line axis). The stage consists of a Huber™ 1006(a) goniometer head, which provide the translational motions and the tilt and surface-normal rotations, attached to an Oriel™ rotator with Motor Mike™ attachment, which provides the Bragg rotation. The DC motor-controlled Bragg rotational precision of the Oriel rotator was reported by the manufacturer to be ca˙ 0.12 arc-seconds (0.6 μ-radians).

The spacing between the two Ge_{111} flat crystal surfaces was fixed at 10 mm by mounting the crystals on the DCD analyzer monolith. The DCD analyzer was attached to a Daedel™ rotary table on the beam line hutch mechanical arm. The effective stepper motor-controlled rotational precision of the rotary table is 0.6 arc-seconds (2.9 μ-radians) which is obtained using a gear reducer. Three translational motions are provided by the hutch mechanical arm.

After fine-tuning each of the two crystals in the analyzer in turn to the photon energy of the monochromator, all DC motors were disconnected to prevent accidental disturbance of the alignment. At this time, the two crystal surfaces are nominally parallel. During a scan, the entire DCD analyzer was rotated as a monolithic structure by step-scanning the Daedel rotary table about an axis located at the center of the monolith. The center of the diffracting surface of the first analyzer crystal is positioned exactly on this axis of rotation. The angle of rotation between the incident beam and the crystal surfaces is defined as θ. The center of the rocking curve, as measured from the data, is defined as θ_o.

Experimental SAXS scans were conducted in a progression of sample – empty – sample so that each sample scan has an adjacent empty scan, ensuring that any instabilities in the source, such as the position of the stored electron beam orbit, will have minimal influence on the SAXS measurements. After the progression of three scans was complete, the monochromator energy was tuned to the next photon energy and the progression was repeated for the same two samples. It is possible to reposition the sample in a precise manner so the same sample volume is always measured.

Each scan was broken up into segments of fixed step-size. Data from three to five overlapping segments comprise one complete scan which required approximately 30-40 minutes to complete. One segment was always made to include the central peak so that an accurate value for the center of the rocking curve, θ_o, would be available from the data. For those scan segments which do not pass directly through θ_o, it was still possible to estimate a value for θ_o by overlapping the intensity region with the central peak segment. One complete SAXS curve was the result of scans with the sample both in and out, therefore between six and ten segments were required to define the small-angle scattering curve for a single sample.

3.4 Silicon Photodiode X-ray Detector

The scattered X-ray beam was measured by means of a photodiode detector circuit designed with the assistance of the electronics staff of the Chemistry Department, Northwestern University, especially the late Jim Baker. In a SAS experiment, it is necessary to cover many orders of magnitude of intensity to profile, including both the SAS and the main beam. Existing detectors (gas proportional counters, scintillation counters, lithium-drifted silicon detectors) were found to be inferior in this regard as none of these could measure an unattenuated synchrotron beam, hence a new approach was taken. Although ionization chambers have been used historically to measure the full synchrotron beam, they were also rejected for this task due to poor detection efficiency and noise. Complete electrical schematics of this detector with its custom-designed electronics appears in an appendix to this dissertation. The detector made use of an unbiased EG&G photodiode (#UV-215-BQ) designed for ultraviolet radiation. Typical currents measured in the SAS experiments were of the order of 100 fA to 1 μA. The noise of the photodiode detector is about 60 fA, established by the Johnson noise of the electrometer operational amplifier. This noise limits the sensitivity of this photodiode detector to a few hundred 6 keV photons per second.

In a double-crystal diffractometer with a fixed spacing between the two crystals, the offset distance between the entrance and exit beam will vary slightly ($\simeq$1 mm·degree^{-1}) as a function of rotation angle. The photodiode detector was translated vertically as a function of analyzer rotation angle such that the X-ray beam always intercepted the same position on the detector. To

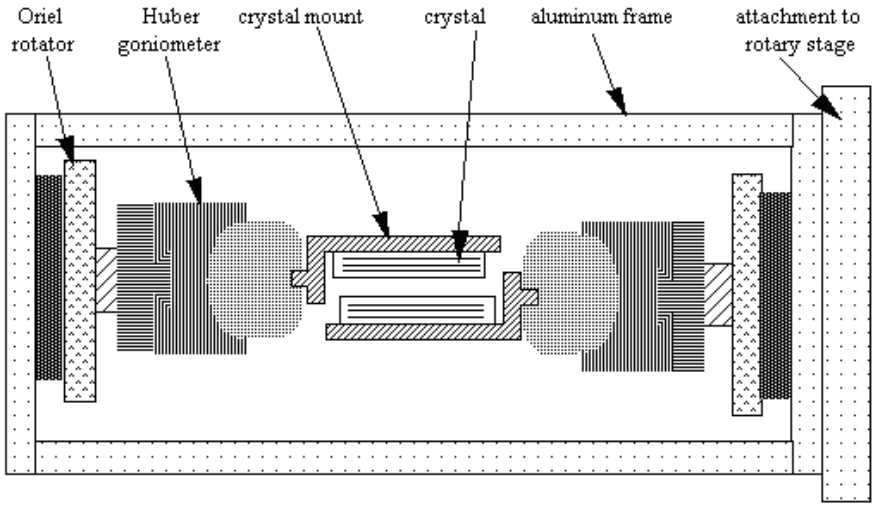

Figure 3.2: View towards the detector of the double-crystal diffractometer analyzer monolith. The attachment to the rotary stage on the beam line mechanical arm is on the right. Each crystal is mounted on an L-shaped support, attached to a Huber™ 1006(a) goniometer stage which is, in turn, mounted on top of an Oriel™ precision rotator. All motions on the monolith are controlled by DC motors that are not connected to the beam line computer.

accomplish this, the detector was mounted on a rotary table connected to the second set of three translational motions on the hutch mechanical arms.

3.5 Computer Data Acquisition

The MINC™ computer controls the operations of most of the hardware on beam line X23A3. The MINC™ instructs the monochromator to tune to a particular photon energy. The monochromator is then left undisturbed for a set of scattering measurements. The MINC™ computer was also used to step-scan the DCD analyzer monolith to perform the SAXS measurements. During a single step, the MINC™ records the counts acquired in a fixed time, t, from the monitor ionization chamber, M, and the photodiode detector, D. The amplification, A, of the photodiode detector is controlled manually using a hand-held remote control. The dark noise, d, in the photodiode detector is measured when there are no X-rays incident on the monochromator.

3.6 Data Reduction

Columns of DCD analyzer angle, detector counts, and monitor counts comprise the data that are recorded by the beam line MINC™ computer. Each scan is recorded and stored as one data file. Also included at the top of each file is the counting time (coded as a 12-bit integer) which is constant for each angle in the file. The files of about 6000 text characters each were copied from the MINC™ printer port to the Macintosh modem port over a serial interface (RS-232C) by issuing a print command on the MINC™. The MockTerminal version 4.3 terminal emulation software was used on the Macintosh to record and store the incoming text. An additional column of detector range number was added to each data file. After adding the detector ranges manually, the files are then in a format to be read by a custom-designed, graphically-oriented, relational database software package for the Macintosh titled `SAXS Reduction`, which converts the columns described into typical SAS data. This software runs on an Apple Macintosh SE using the Finder system software version 6.0.2. It is not presently compatible with the Mul-

tiFinder system software. The source code is in Think's Lightspeed C, version 3.02p.

3.7 Raw Data

DCD angle, θ, is converted into scattering vector (actually scattering vector magnitude) by

$$h = \frac{4\pi}{\lambda} \sin\left(\frac{\theta - \theta_o}{2}\right) \tag{3.1}$$

where θ_o is the observed center of the rocking curve. The ratio, $R(h)$, of detector counts, D, in time, t, to monitor counts, M, corrected for detector range dark current, d_r, and adjusted for detector range amplification, A_r, measured at each different h, is

$$R(h) = \frac{A_r\,[D(h) - \tau d_r]}{M(h)}. \tag{3.2}$$

The intensity ratio, $R(h)$, is a superposition of the small-angle scattering from the sample, small-angle scattering from the Kapton™ and beryllium windows between the monochromator and the DCD analyzer, convolution of the X-ray source profile with the rocking curves of the monochromator and DCD analyzer crystals, and parasitic, background scattering of the X-ray beam in the 285 mm air path between the sample position and the detector. The source convolution will be shown later to be negligible. At θ_o, the double crystal analyzer conducts the full intensity of the unscattered beam which is the I_o apparent at the detector, so the sample transmission,

$$T_s = \frac{R_s(0)}{R_e(0)}, \tag{3.3}$$

where $R_s(h)$ and $R_e(h)$ are the curves measured for the sample and empty beam, respectively, normalized to a constant monitor count rate. The empty beam is a scan which is the same as a SAXS scan in every regard except that the sample is removed.

It may be assumed that all effects except the scattering from the sample and a small additional background will be found in both R_s and R_e. The instrumentally-smeared small-angle scattering plus small additional background in arbitrary units is then separated by scaling the sample data by its transmission factor and subtracting the empty beam, as

$$\tilde{I}(h) = R_s(h) - T_s R_e(h). \tag{3.4}$$

3.8 Absolute Intensity Conversion

Conversion of the scattering data into differential cross-section in units of m^{-1} involves measuring the ratio of the number of photons scattered per second into unit solid angle to the number of photons in the incident beam. The as-measured slit-smeared intensity profile in ph·s^{-1},

$$\tilde{I}(h) = \Phi_o A t T \varepsilon \Omega \frac{d\tilde{\Sigma}}{d\Omega}(h), \tag{3.5}$$

is measured by a detector with efficiency, ε, and subtending a solid angle, Ω, with the sample. Φ_o is the incident flux in ph s^{-1} area^{-1} illuminating an area, A, on the sample and $d\tilde{\Sigma}/d\Omega(h)$ is the slit-smeared differential scattering cross-section per unit volume per unit solid angle. The measured transmission is given by $T = e^{-\mu t}$ where μ is the linear absorption coefficient.

With the double-crystal instrument, the same detector, of area a where $a > A$, that measures $\tilde{I}(h)$ is used to measure $\Phi_o A$ with the sample removed from the instrument, so the detector efficiency cancels and primary conversion of the measured intensity into units of $d\tilde{\Sigma}/d\Omega(h)$ involves only the measurement of t, T, Ω, and $\Phi_o A$. That is, the slit-smeared SAXS in absolute units measured by the double-crystal instrument is

$$\frac{d\tilde{\Sigma}}{d\Omega}(h) = \frac{R_s(h)/T_s - R_e(h)}{R_e(0)\Delta\theta_w\Delta\theta_l t} \tag{3.6}$$

where $\Delta\theta_w$ and $\Delta\theta_l$, which define the detector solid angle Ω, are the angular width and length of the beam intercepted by the detector. In a SAXS camera that utilizes geometric collimation with a concomitantly small illuminated area,[145] the solid angle is defined by the area of the beam on the detector element, Δa, and the distance between the sample and detector, r. However, in the double-crystal instrument, the angle in the scanning direction is more highly-collimated by the rocking curve of the crystal optics. Therefore, $\Delta\theta_w$ is measured from the experiment as the full width at half maximum of the empty beam. With no crystal optics in the slit-length direction, $\Delta\theta_l$ is

defined in the geometric sense. For a large illuminated sample area defined by the width and length of the source slits, where $A = W_S \times L_S$, and a detector diameter of L_D, where $L_S < L_D$,

$$\Delta\theta_l = \frac{L_D + L_S}{2r} + \frac{L_D - L_S}{2r} = \frac{L_D}{2r} \tag{3.7}$$

The detector diameter (diameter of the active area of the photodiode) is 5.5 mm and the sample-to-detector distance was 280 $\pm$5 mm. The additional distance due to the double reflection in the analyzer is negligible with respect to this error. Thus it is evident that although primary calibration usually requires special equipment, a standard sample, and can be difficult and time-consuming to perform, the present instrument requires no additional beam time for calibration since all of the parameters are available in the normal course of performing scattering measurements.

3.9 Slit-Length Desmearing

The measured data was corrected for smearing in the slit-length direction by the method of Lake[81] as explained earlier. The desmearing of the measured data was performed iteratively until a plot of the standardized residuals became featureless as a function of scattering vector or data point index number. In this section, the small-angle scattering will be referred to as $\tilde{I}$. The standardized residual,

$$z = \left(\tilde{I}_o - \tilde{I}_i\right) \div \sigma_o, \tag{3.8}$$

is the statistically weighted difference between the measured intensity data, $\tilde{I}_o$, and the smear of the i^{th} iterative trial solution, $\tilde{I}_i$, divided by the reported error on the measured intensity, σ_o. To illustrate, Fig. 3.3a and 3.3b are a pair of plots excerpted from the screen output of a desmearing session. Fig. 3.3a shows the standardized residuals of the third trial solution, $\tilde{I}_3$. Fig. 3.3b shows the standardized residuals of the fourteenth trial solution, $\tilde{I_{14}}$, which is accepted as the desmeared data.

3.10 Size Distribution Analysis

The desmeared data was analyzed in terms of a size distribution from a dilute concentration of non-interacting, homogeneous scatterers by the maximum entropy technique, as implemented by Daniell and Potton[105] in the FORTRAN code `Maxe.FOR`. An adaptation of this code, `MaxSAS.FOR` was made to enable the analysis of SAS data from the double-crystal diffractometer.

Because of the oscillations in the distributions perceived to be a result of the Skilling and Bryan[127] implementation of the maximum entropy algorithm as described in the theoretical section, the form factor used to model the particles was modified to a less oscillatory form. The standard form factor (squared) for spheres,

$$F^2(h,r) = 9(hr)^{-6}\left[\sin(hr) - (hr)\cos(hr)\right]^2, \tag{3.9}$$

was modified to minimize the effect of the cosine waves as hr becomes much larger than one. In this case, the completely damped form factor averages to the Porod dependence,

$$P(h,r) = \frac{9}{2}(hr)^{-4}. \tag{3.10}$$

The cosine waves are harmonics of the particle dimension and thus provide useful information in the size analysis. However, the problem with the Skilling and Bryan[127] method is a sensitivity to strong gradients in the form factor such as these cosine waves. An abrupt transition between F^2 and P would provide a strong gradient and so an empirical weighting function was conceived that would provide a smooth transition from the form of F^2 to the form of P while retaining some of the cosine waves of F^2. Empirically, it was determined that at least ten percent of F^2 should remain in the modified form factor ($\nu = 0.9$) at all times and that the transition, $\psi = (hr)_{\text{transition}}$, between F^2 and P should occur at $\psi \simeq 8$. For $hr << \psi$, there should be no modification of the standard form factor for spheres. A weighting function incorporating these features is

$$W(h,r) = (1-\nu) + \nu \exp\left[-\left(\frac{hr}{\psi}\right)^2\right]. \tag{3.11}$$

Using this weighting, the modified form factor for spheres,

$$\hat{F}^2(h,r) = WF^2 + \frac{1-W}{1+1/P}, \tag{3.12}$$

damps 90% of the cosine oscillations in the Porod region. The last term is written to prevent P from dominating

(a)

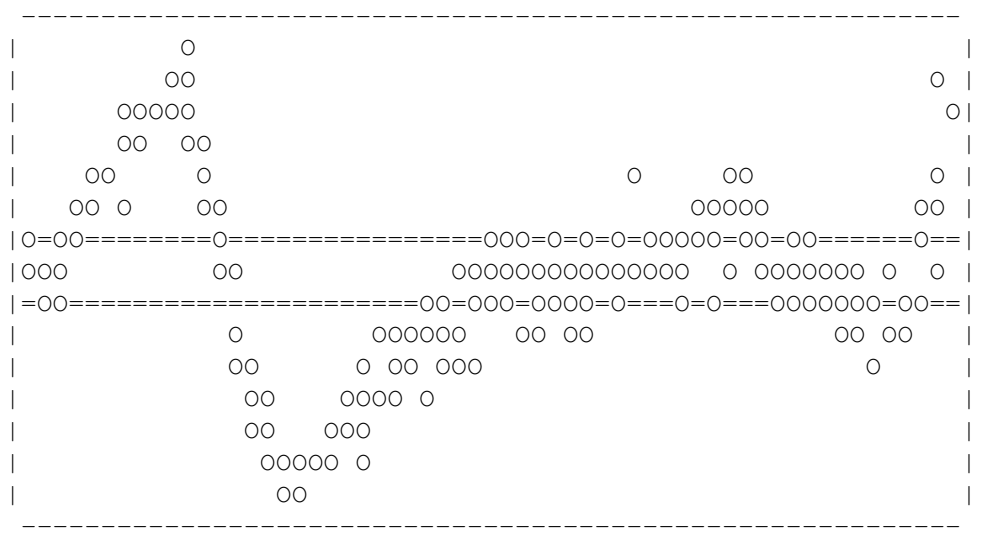

(b)

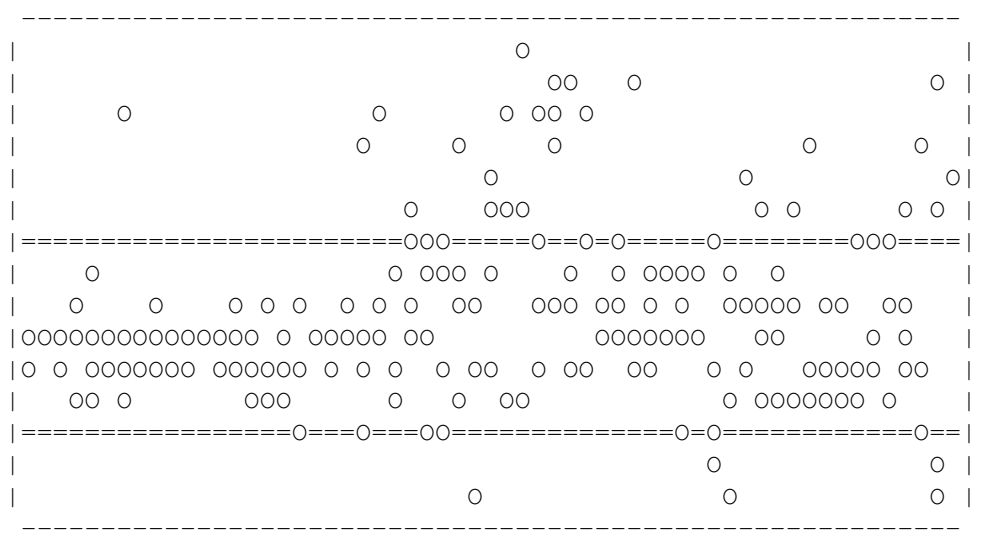

Figure 3.3: Plot of the standardized residuals as a function of data point sequence number after completion of (a) three iterations and (b) fourteen iterations of the Lake desmearing technique. Note the strong feature in (a) indicating a poor fit between the smear of the iterative trial solution and the measured data while in (b), that feature has dissipated. The ===== bars indicate plus one and minus one standard deviation using the error estimated by *shot noise* counting statistics.

the result as hr goes to zero. Application of two limiting cases shows that

$$\lim_{hr\to 0} \hat{F}^2(h,r) = F^2(h,r) \tag{3.13}$$

and

$$\lim_{hr\to \infty} \hat{F}^2(h,r) = 0.1F^2(h,r) = 0.9P(h,r). \tag{3.14}$$

Use of $\hat{F}^2(h,r)$ to analyze scattering data calculated from synthetic distributions shows that it models the scattering exactly as intended, delivering a good approximation of the synthetic distribution with the correct volume fraction and no ill side-effects. This modified form factor was used to model the scattering from the features in both of the steel alloys examined in this dissertation.

Some of the samples, the Modified Fe9Cr1Mo steels for example, were known by other techniques to contain several different types of scatterer, each with its own scattering contrast. For the purposes of size distribution analysis, the scattering from these samples was analyzed for a size distribution weighted by the scattering contrast of all scatterers. As a result, the relative heights of peaks in the scattering strength size distributions cannot accurately reveal the relative amounts of each scatterer without additional information on the scattering contrast. This subject is treated in the ASAXS scattering contrast analysis below.

Chapter 4

Results and Discussion

The first section will describe the manner in which the new DCD SAXS camera and silicon photodiode X-ray detector was tested. Then, the principal results for steel will be given: first the Modified Fe9Cr1Mo alloy, then the AF1410. Several types of small-angle scattering curves will be presented and will be referred to by type as follows: type 1) scattering from features of uniform size; type 2) scattering from features with a broad distribution of sizes and negligible feature-to-feature scattering; type 3) scattering from a regularly-spaced arrangement of features such that interference effects exist.

4.1 Validation of Equipment

For any newly-developed piece of scientific equipment, it is necessary to subject it to tests to verify that the equipment will return the correct answers. The double-crystal diffractometer SAXS camera is sufficiently complex that several different types of test were applied. Scatterers of known size were used to verify the angular scale and to demonstrate the improvement in detection capability provided by the silicon photodiode detector. Finally, as a comparison, samples that were examined by means of the double-crystal diffractometer SAXS camera were also examined by means of other SAXS and SANS cameras in other laboratories using their own secondary methods of calibration to absolute intensity.

4.1.1 Polystyrene Spheres: 255 and 460 nm diameters

The scattering from polystyrene spheres was measured from several samples and was found to exhibit both type 1 and type 3 scattering behavior. For samples that are nearly monodisperse, the intensity profile assumes a characteristic shape of peaks (secondary maxima), typical of type 1 scattering, which are regularly-spaced in h. The average spacing of these peaks, Δh, is related to the mean sphere diameter, $\bar{D}$, by the relation

$$\Delta h \bar{D} = 2\pi. \tag{4.1}$$

However, for $h < \Delta h$, type 3 scattering (interference effects) were clearly observed, indicating that the spheres were densely-packed.

The samples were prepared from liquid suspensions of reported polydispersity $\sigma(\bar{D})/\bar{D} \simeq 1\%$, where $\sigma(\bar{D})$ defines the width of the Gaussian distribution as in $\exp\left[-(D-\bar{D})^2/2\sigma^2(\bar{D})\right]$. Drops were placed in the center of a piece of transparent tape substrate and dried, creating a densely-packed cake of uniform diameter spheres. The cakes could be suspended on edge by fixing the tape to a metal sample support ring. The scattering profile of the tape substrate was observed to be insignificant compared to the scattering from the cake of spheres. Cakes were prepared from spheres of reported diameter 240, 255, 460, 655, and 804 nm.

The scattering from the 255 nm and 460 nm spheres are reported here. The thickness of each cake is not uniform, making conversion of the SAXS intensity into absolute units impossible. In Fig.s 4.1 and 4.2, the collimation-corrected SAXS in arbitrary units is plotted as a function

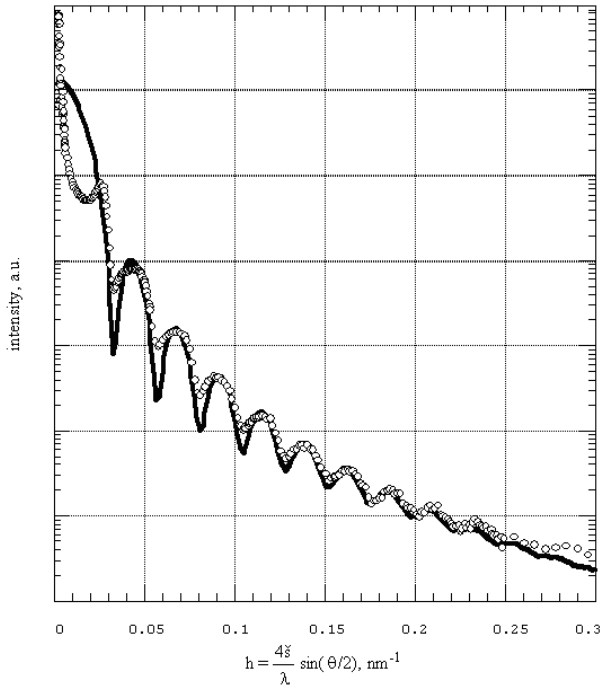

Figure 4.1: Collimation-corrected SAXS intensity in arbitrary units from a sample of uniform diameter polystyrene spheres of reported diameter 255 nm. The measured diameter is 267 nm with a Gaussian σ of 9 nm. Note the interference effects at very low scattering vector. The experimental data is shown in open circles, the SAXS calculated from the Gaussian distribution model is shown as the solid line.

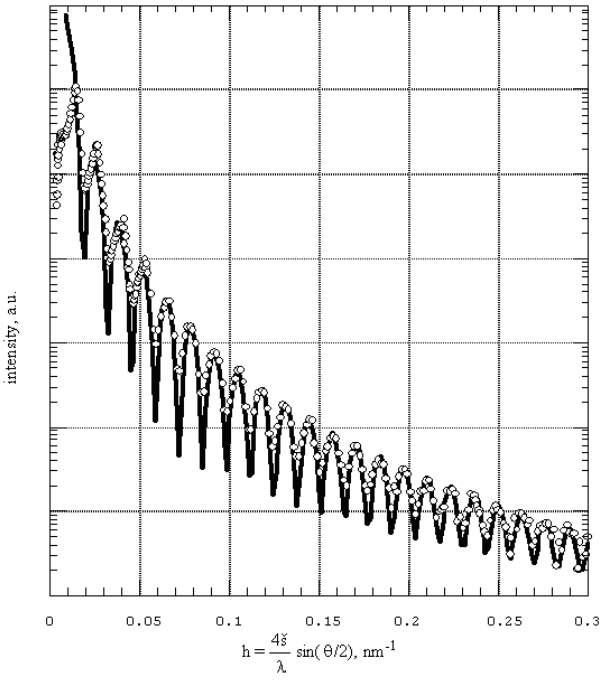

Figure 4.2: Collimation-corrected SAXS intensity in arbitrary units from a sample of uniform diameter polystyrene spheres of reported diameter 460 nm. The measured diameter is 477 nm with a Gaussian σ of 4 nm. Note the interference effects at very low scattering vector. The experimental data is shown in open circles, the SAXS calculated from the Gaussian distribution model is shown as the solid line.

Table 4.1: Parameters of the model Gaussian distribution for polystyrene spheres samples.

spheres sample	255 nm	460 nm
$\bar{D}$	267 ± 9	477 ± 4
$\sigma(\bar{D})$	9 ± 1	4 ± 1
polydispersity	3.4%	0.8%

of h against the SAXS calculated from a Gaussian distribution of spheres as open circles. The fit of the model, drawn as the solid line, with the experimental data is quite good. This provides a measure of confidence in both the experimental equipment that recorded the data and the method by which the raw data were reduced to a SAXS profile. Note the interference effects at very low scattering vectors in each figure. Table 4.1 gives the parameters of the Gaussian distribution for each sample.

It is evident that type 3 (interference) scattering is present for both samples although it is much stronger for the 255 nm spheres. The observed intensity for this sample was lower than that of the 460 nm sample, indicating greater absorption due to a greater thickness. Such an increase in thickness would increase the effects of particle interference, as observed. Also, the polydispersity is greater for the 255 nm spheres; this is directly seen as a reduction in the sharpness of the secondary maxima for $h > 0.15$ nm^{-1}.

While the SAXS is closely approximated by the scattering calculated from a Gaussian-shaped distribution of low polydispersity, as seen from Fig.s 4.1 and 4.2, an attempt was made to analyze the SAXS using the maximum entropy size technique described elsewhere in this thesis. The code was not able to converge upon a distribution close to the reported size, even when the region of SAXS with particle interference effects was removed. This failure may be viewed as a limitation of the code to resolve such a narrow, well-defined distribution and not the maximum entropy technique itself. The conclusion is that the `MaxSAS.FOR` code should be applied to samples with a polydispersity greater than a few percent.

A finite amount of polydispersity was required for each distribution so that its calculated scattering would fit the measured data that had been corrected for collimation. Delta-function size *distributions* provide deep valleys in the intensity curve between the secondary maxima. By adding some width to the distributions, the fit improves remarkably. Bonse and Hart, in their analysis of very similar scattering curves,[10] did not consider distribution polydispersity but demonstrated that the valleys were filled in by multiple scattering from a thick sample consisting of a close-packed array of spheres, such as exists in the caked samples. While such an explanation is valid, it is also possible that the spheres have a slight polydispersity and that this polydispersity may be the primary cause of the loss of sharpness in the valleys between the secondary maxima. Asphericity, as shown in Fig. 1.a on page 169 in Glatter and Kratky,[43] could cause some broadening of the secondary maxima leading to valleys that are more shallow. The spheres used, both in this study and in that of Bonse, were prepared on Earth and are probably aspherical on account of gravitational effects. That this could have some effect on the measured scattering could by tested by comparing the scattering from spheres prepared on Earth with that from spheres prepared in space. Such spheres already exist from one of the NASA space shuttle missions. In conclusion, the shallowness of the valleys between the secondary maxima are most probably due to (in order of decreasing importance) polydispersity, multiple scattering, and asphericity.

4.1.2 Silicon Photodiode Detector vs. Scintillation Counter

A demonstration of the marked improvement in the quality of SAXS data directly attributable to the silicon photodiode detector (PD) is shown in Fig.s 4.3 and 4.4, in which are plotted the detector counts (normalized to a constant monitor ionization chamber) versus h. The curves are a superposition of the SAXS from the sample of *460* nm polystyrene spheres onto the rocking curve of the double-crystal diffractometer optics. Neither curve was corrected for collimation effects in Fig.s 4.3 and 4.4. The data in Fig. 4.3 were taken over the course of eight hours with a scintillation counter (SC), attenuated by aluminum filters for $|h| < 0.05$ nm^{-1}. The optics for this experiment were a flat Si_{111}, two-reflection monochromator and a one-reflection analyzer. Fig. 4.4 shows SAXS data from the same sample, taken in forty minutes, with the PD and flat Ge_{111} optics, a two-reflection monochromator and a two-reflection analyzer. The difference in the optics of the

two experiments is visible only in the width of the central peak of the data, as is shown in detail later by Fig. 4.7 and 4.8.

Nine maxima are visible in the data recorded by means of a SC after which the peaks are lost in the background, whereas data collection was stopped after twenty-three secondary maxima were observed with the PD. Both curves, after collimation-correction, reveal that the mean diameter of spheres is 477 nm. It is difficult to discern from these plots the region of overlap between scan segments. Several different scan segments comprise each curve, each segment with a different fixed step size, $\Delta\theta$, and a different starting position. With each new starting position, it is possible that the angular rotation of the double-crystal diffractometer analyzer suffers a small mechanical backlash shift on the order of 0.0003°which may be corrected later by numerically shifting the entire segment along the angular scale. Corresponding to each scan segment may be, depending on the intensity, a different amount of filter-attenuation (for the SC), or a different sensitivity scale (for the PD). Using the PD, it is possible to align the different scan segments more precisely in angle than with the SC because of the greater precision to which the intensity is measured. In fact, the PD enabled the diagnosis and correction of operations of the beam line mechanics that had gone unnoticed in prior experiments with the SC. Additionally, it was not necessary to correct the output of the PD for dead-time or linearity.

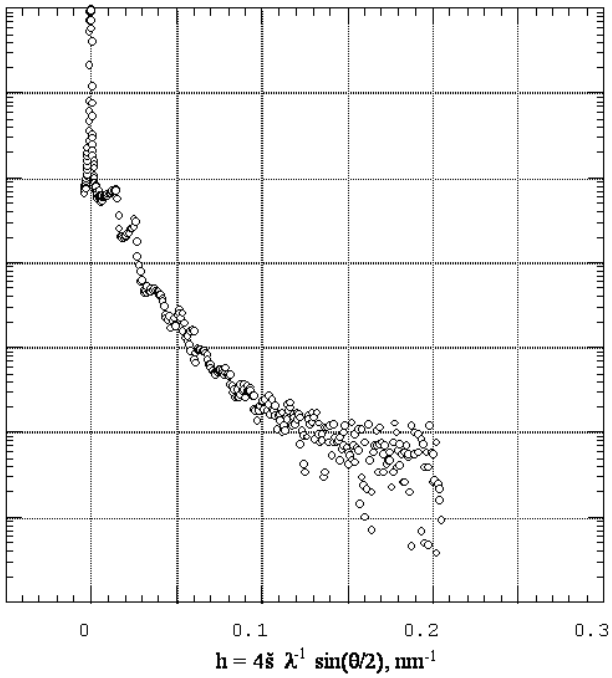

Figure 4.3: Intensity data recorded using a scintillation counter. Superposition of small-angle X-ray scattering intensity in arbitrary units from a sample of uniform diameter polystyrene spheres of reported diameter 460 nm onto the optics of the double-crystal diffractometer. The data has not been corrected for collimation effects. Additionally, the optics were Si_{111}, two-reflection monochromator and one-reflection analyzer. The data were recorded in eight hours. Compare with Fig. 4.4.

4.1.3 Absolute Intensity Correlation

The method by which the data are placed onto an absolute scale of intensity was tested by several different techniques. The most satisfying test would be to measure the SAXS from a sample of known distribution and amount of scatterers. For use as such secondary standards, several different types of sample were proposed. In one such method, (Gerold, et al., 1978) used a liquid suspension of spheres with a well-known volume fraction and size. Another suggestion was to record the SAXS from Guinier-Preston zones in an alloy of aluminum and zinc. Voids in glassy carbon or colloidal silica[56, 113, 114, 145] have been accepted as secondary standards. A different test would be to compare the data placed onto an absolute scale by the primary method described above with the scattering from the same sample reported by another laboratory. The

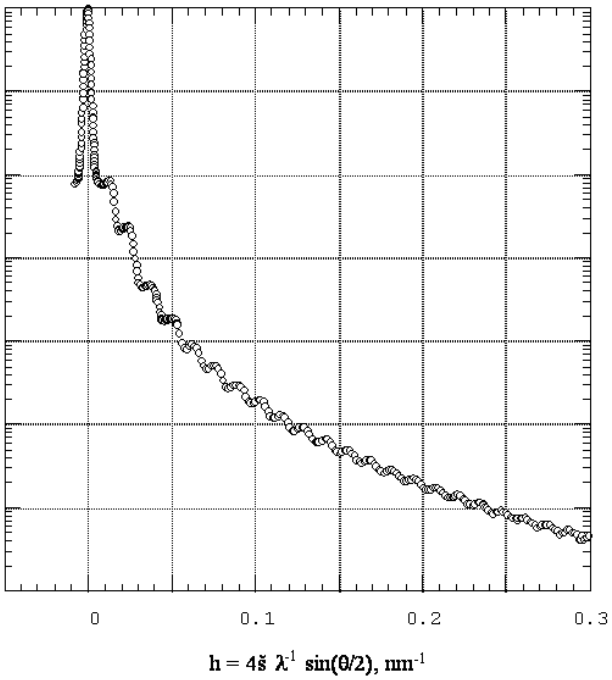

Figure 4.4: Intensity data recorded using a silicon photodiode detector. Superposition of small-angle X-ray scattering intensity in arbitrary units from a sample of uniform diameter polystyrene spheres of reported diameter 460 nm onto the optics of the double-crystal diffractometer. The data has not been corrected for collimation effects. The optics were Ge_{111}, two-reflection monochromator and two-reflection analyzer. The data were recorded in forty minutes. Compare with Fig. 4.3.

comparison test was used to evaluate the primary calibration technique used.

Six samples of Modified Fe9Cr1Mo steel, each aged at a different temperature for 5000 hours, were sent to the National Center for Small-Angle Scattering Research at Oak Ridge National Laboratory for measurement on the 10 meter X-ray pinhole camera.[57] The absolute intensity calibration method used was a secondary calibration with the scattering from polyethylene. While the experimental arrangement is significantly different from the double-crystal diffractometer, the absolute intensities of the Oak Ridge data are in agreement, within the scatter of the data, with the primary method described above for all six samples examined. In Fig. 4.5 are plotted the SAXS from one of the six Modified Fe9Cr1Mo steel samples as measured on both instruments. The scattering contrast of the most abundant scatterer, $Cr_{23}C_6$, is nearly identical for the 17.44 keV photons in the Oak Ridge data and the 6 keV photons of the DCD data. Small-angle scattering from five samples of colloidal silica / potassium silicate, described in Appendix A, were measured on the double-crystal diffractometer camera and on the 8 m SANS pinhole instrument installed at the 20 MW research reactor at the National Institute of Standards and Technology. The SANS camera makes use of a helical channel velocity selector to choose the incident neutron wavelength where the wavelength resolution, defined as $\Delta\lambda/\lambda$, is 0.25. The mean wavelength for these measurements was 0.6 nm. A detailed description of the SANS facility is given by Glinka, et al.[44]

After correcting the SAXS data for slit-length smearing, adjusting the SANS data by the ratio of $|\Delta\rho|^2$ for X-rays and neutrons, and subtracting the experimental backgrounds, excellent agreement is obtained, as shown in Fig. 4.6. This test is a more rigorous evaluation of the entire experimental procedure than is the previous one, as even the incident radiation is different. No other scaling has been applied. Similar agreements between SAXS and SANS may be found in the other four samples.

4.1.4 Slit-Width Correction

The SAXS from the 460 nm polystyrene spheres, presented above, is also useful to demonstrate the effect of the slit-width instrumental smearing. The primary difference between Fig.s 4.3 and 4.4 demonstrated the supe-

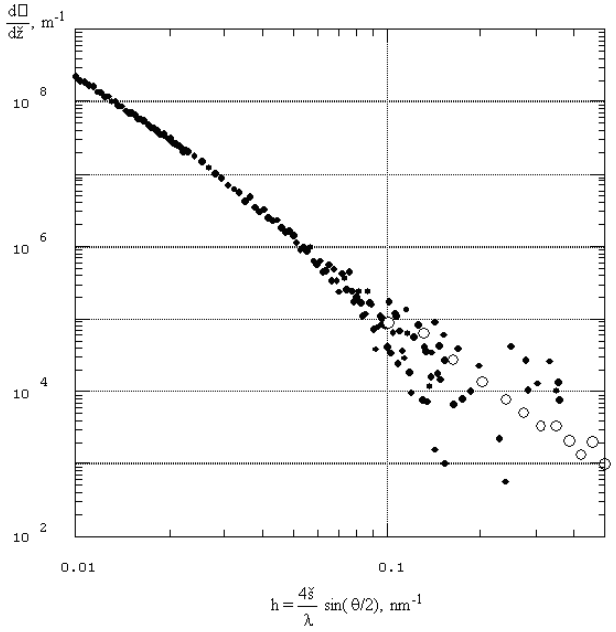

Figure 4.5: Comparison of absolute intensity scales for the SAXS from a sample of the Modified Fe9Cr1Mo steel. While the incident photon energies used are very different, 17.44 keV for the Oak Ridge data versus 5.789 keV for the DCD data, the $|\Delta\rho|^2$ of the most abundant scatterer, $Cr_{23}C_6$, is nearly identical in each case. The open symbols correspond to the Oak Ridge data, the closed symbols to the DCD data.

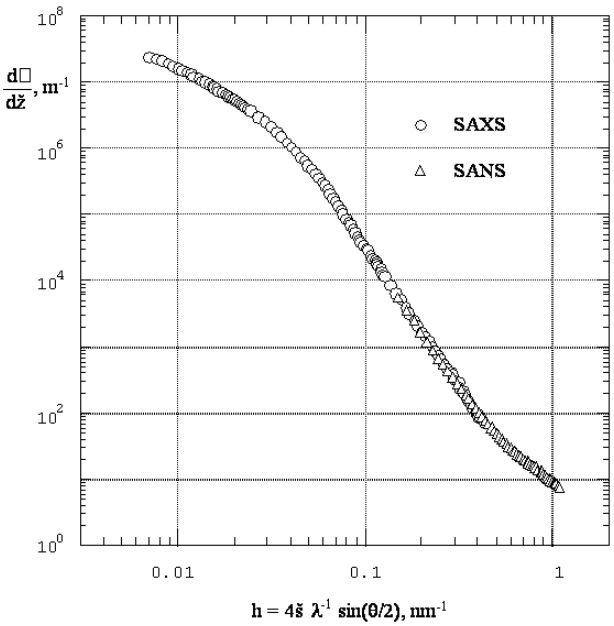

Figure 4.6: $d\Sigma/d\Omega(h)$ for SAXS (circles) and SANS (triangles) from a sample (10% colloidal silica / 90% potassium silicate) of bulk microporous silica. The SANS data have been scaled by the ratio of the X-ray-to-neutron scattering contrast.

rior performance of the silicon photodiode detector over that of a scintillation counter. These two data sets were measured from the same sample but were taken some 33 months apart. In Fig. 4.7, the rocking curve of the optics is emphasized, using the same data plotted together. The width of the rocking curve of the experiment with germanium optics is about three times that of the silicon optics experiment. Consequently, the incident photon flux on the sample is greater in the experiment with germanium optics. In the region of scattering vectors where the first secondary maximum is observed, at $h \sim 0.013$ nm^{-1}, the two coincide. At scattering vectors greater than $h \sim 0.013$ nm^{-1}, the two curves are identical except that the counting statistics are much better in the experiment with Ge optics because a silicon photodiode X-ray detector was used. To demonstrate how the difference in optics affect the measurement of the SAXS, Fig. 4.8 shows the region of overlapping data for both experiments, starting with the first secondary maximum at top-left.

The Si optics / scintillation counter data is noisy about the quiet Ge optics / photodiode data but both curves show the same profile. Uncertainties in the filter attenuation correction and linearity correction for the scintillation counter data may explain why the intensities differ to the left of the first secondary maximum in addition to proximity to the incident beam. The slit-width instrumental smearing is a convolution along the h-axis of the SAXS from the sample with the rocking curve of the analyzer. If the smearing is significant, features would be seen to become less sharp. The softening of the second secondary maximum for the Ge optics data is significant and may be due to the increased slit-width but this is the only place on the curve where such an effect may be observed.

The last difference to be noted between the two experiments concerns the number of crystal reflections in the analyzer. In the Si optics experiment, only one reflection was used while in the Ge optics experiment, two reflections were used. As has been noted before by Bonse,[10] the tails of the rocking curve will fall off proportional to a power that is twice the number of reflections. For an analyzer with only a single reflection, the rocking curve tails fall off as h^{-2} while the SAXS measured with a DCD decreases by h^{-3} and it is possible for the rocking curve tail to dominate the SAXS data from weakly-scattering samples. By using an analyzer with at least two reflections, this problem is avoided. With regard to the data

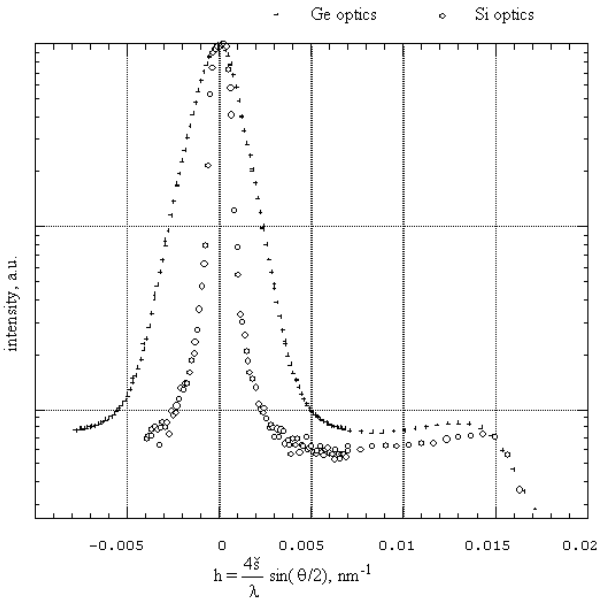

Figure 4.7: Magnification of the SAXS from 460 nm spheres shown in Fig.s 4.3 and 4.4, showing the effect of the DCD optics (germanium or silicon) on the central peak. The slit-width for the Ge optics (recorded with a photodiode detector) is $\sim 3\times$ that of the Si optics (recorded with a scintillation counter).

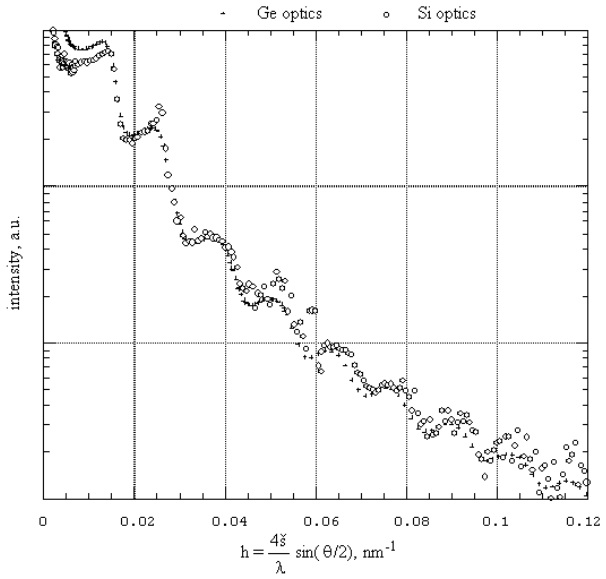

Figure 4.8: Magnification of the SAXS from 460 nm spheres shown in Fig.s 4.3 and 4.4, showing the effect of the DCD optics (germanium or silicon) on the measured SAXS. The slit-width for the Ge optics (recorded with a photodiode detector) is $\sim 3\times$ that of the Si optics (recorded with a scintillation counter).

presented, this particular sample was a strong scatterer so that at no point within the measured h-range did the tails of the rocking curve in either experiment dominate the SAXS data from the sample.

In summary, experiment has shown that a correction for slit-width instrumental smearing is not necessary. Additionally, utilization of Ge optics and an asymmetrically-cut first monochromator crystal has improved the quality of data from the instrument without compromising resolution.

4.2 Modified Fe9Cr1Mo Steel

The measurements of the SAXS from the Modified Fe9Cr1Mo steel will be described. Multiple-photon energy (wavelength) ASAXS experiments were conducted to accentuate the scattering from $Cr_{23}C_6$ precipitates. From these experiments, size distributions of the $Cr_{23}C_6$ were deduced via the maximum entropy method and making use of calculated scattering contrasts. Because precision calculations of the scattering contrast are essential to the ASAXS analyses, the anomalous dispersion corrections of chromium were determined using transmission measurements near the Cr K absorption edge.

4.2.1 Sample Thickness Measurements

In SAXS experiments, measurement of the sample thickness is crucial to accurate scaling of the intensity onto an absolute scale. The optimum thickness of steel SAXS samples near the Cr edge is 15 to 20 μm which is difficult to measure by direct methods. Using a precision micrometer, calibrated against foils of known thickness, the sample thickness may be measured to $\pm 5\mu$m. This 25% precision of measurement, passed directly to the SAXS absolute intensity scale, is not acceptable for ASAXS experiments. Traditional absolute intensity scale calibration methods[113,114,145] are much better, within 5%. Furthermore, while precision micrometers measure a thickness over the area of the platens, that value is the maximum thickness and does not indicate variation or uniformity. It is possible to measure the thickness of the sample by transmission measurements, but imprecision in the knowledge of the mass absorption coefficient is problematic with a measurement using a single photon energy.

Table 4.2: Thickness, μm, of the Modified Fe9Cr1Mo steel SAXS samples. All thicknesses are ± 0.3 μm.

sample	thickness
N&T	24.3 μm
482° C	24.6 μm
538° C	17.5 μm
593° C	21.3 μm
649° C	16.8 μm
704° C	22.3 μm

With experiments conducted on six steel samples, each at three photon energies, it was possible to determine the sample thicknesses in a direct, statistical method from the SAXS experiments by using the sample transmission, T_s. Measurements of T_s were taken from all ASAXS scans. Each of these measurements is related to the energy-dependent mass absorption coefficient, $\mu_m(E)$, and to the sample-dependent thickness, t. Because all samples are of the same composition, they will have equivalent $\mu_m(E)$. Initially, values for μ_m were calculated from the composition for each energy. These were then combined with T_s and the mass density, ρ_m, calculated from the composition, to get t. The three values of t obtained for each sample were then averaged and used to reverse-calculate new values for μ_m. The six values of m obtained for each energy were then averaged and fed back in to get t again. This back-and-forth method was iterated to minimize the least-squares deviations of calculated T_s. With this method, the thickness of each sample, spatially averaged over the 3×3 mm^2 illuminated area, was determined to ± 0.3 μm as reported in Table 4.2. The thickness of the N&T sample used for the measurement of the dispersion corrections was determined as part of this six sample, three energy grid. Prior to the thickness measurements, each sample was inspected by X-ray transmission radiography using the experimental equipment available at the X23A3 beam line. These measurements were performed by viewing the absorption contrast at 6 keV using a television camera in place of the double-crystal diffractometer analyzer. The illuminated area of each sample was adjusted by moving either the sample or the slits until an area of even contrast was observed.

4.2.2 Measurement of Anomalous Dispersion Corrections

In order to predict how the contrast for a precipitate would change with photon energy, the dispersion corrections f' and f'' were calculated for all the elements in the reported composition of Modified Fe9Cr1Mo using the method of Cromer and Liberman,[21] which will be referred to below as CL. For precise work though, it is preferable also to measure the dispersion corrections from the sample to be studied. Because it was not expected that the dispersion corrections would differ significantly between samples of the same material, only one sample was measured. Also, because the ASAXS work was to be done only at energies near the chromium K edge (5989 eV), only the dispersion corrections near the Cr K edge were measured.

The data collection method is the same as that for an Extended X-ray Absorption Fine-Structure (EXAFS) measurement. The ratio of intensity transmitted through a sample to the intensity incident, I/I_o, is measured as a function of photon energy by measuring the intensity in detectors placed before and after a sample as the photon energy is step-scanned. The energy range required for measurement of the dispersion corrections may be larger than that for EXAFS because the limits on the Kramers-Kronig integration are *infinite.* To minimize the number of energies required to span the range, small energy steps were taken near the Cr K edge while the step size was increased further from the edge.

The sample used for this measurement was in the N&T condition (1038° C for 1 hr, air cool / 760° C for 1 hr, air cool). All measurements were normalized for the decay of the stored electron beam in the storage ring, as measured in the exit ionization chamber in the monochromator box. The N&T sample was placed in the beam between the beryllium window and the He transport tube and the intensity of the transmitted monochromatic beam was measured as a function of photon energy using the ionization chamber in the He transport tube. The ratio of intensities in the two detectors, I/I_o, is equal to the sample transmission, T_s, and is shown in Fig. 4.9.

The strong vertical feature at 5.989 keV is the K absorption edge of Cr. Inflections in the transmission curve in the region of the absorption edge were used to calibrate the energy scale of the monochromator by comparison with a secondary standard curve (EXAFS Materials,

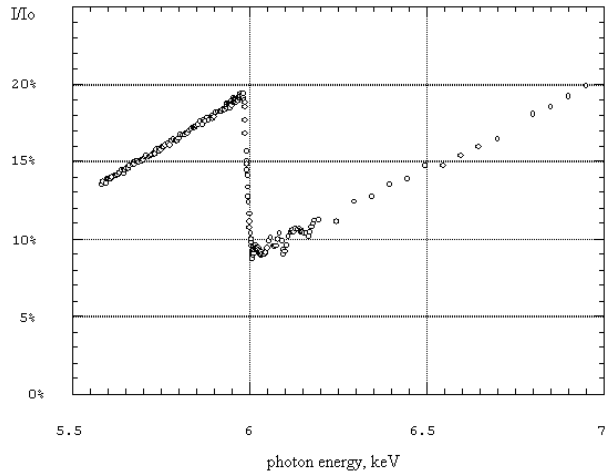

Figure 4.9: Transmission coefficient, I/I_o, of a normalized and tempered Modified Fe9Cr1Mo steel as a function of X-ray energy in the vicinity of the Cr absorption edge (5.989 keV).

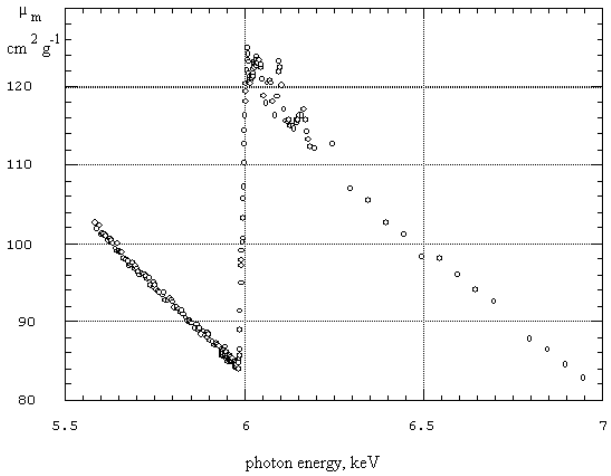

Figure 4.10: Mass absorption coefficient of a normalized and tempered Modified Fe9Cr1Mo steel as a function of X-ray energy in the vicinity of the Cr absorption edge.

1988) for pure chromium which was, in turn, calibrated against published tables of binding energies.[4] Four inflection points were matched over a range of 20 eV to fix the energy calibration to within 1 eV. The energy bandpass of the Ge optics was ~ 3 eV.

At 6.539 keV, a small shift is seen which may be due to the K edge of Mn (0.46% weight). The margin of error in the intensities, due to counting statistics, is comparable with the size of the plotted symbols. An EXAFS analysis of the fine structure above the Cr K edge would not be directly relevant to an ASAXS measurement of the $Cr_{23}C_6$ population because the EXAFS comes from all the Cr in the sample, not just that in the precipitates.

By calculating the mass density from the reported composition and obtaining the thickness as above, the mass absorption coefficient, μ_m, for the sample was calculated, and is shown in Fig. 4.10.

Using the reported composition and the mass absorption coefficients calculated by the CL method for all elements except Cr, the mass absorption coefficient of Cr was calculated and is plotted in Fig. 4.11 against the value calculated by the CL method. Good agreement is found between data and the theoretical calculation of CL. It is obvious that the CL method does not account for the solid-

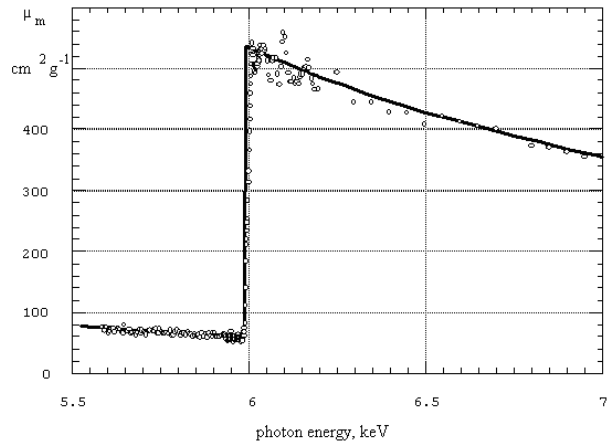

Figure 4.11: Mass absorption coefficient of Cr plotted as a function of X-ray energy in the vicinity of the Cr K absorption edge. The solid curve is calculated by the method of Cromer and Liberman.[21] The points are derived from transmission measurements on Modified Fe9Cr1Mo steel.

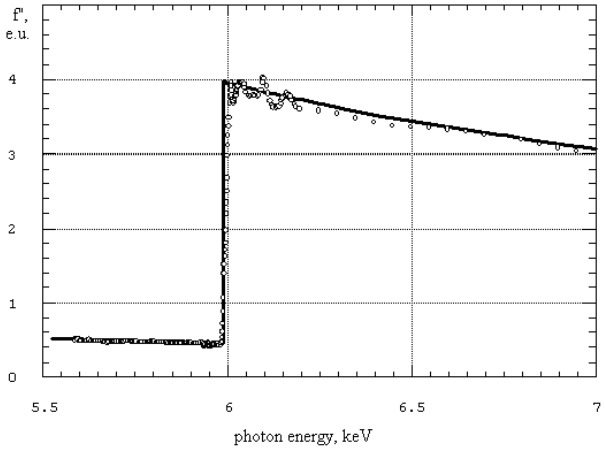

Figure 4.12: Imaginary part of the anomalous dispersion correction, f'', to the Cr scattering factor plotted as a function of X-ray energy in the vicinity of the Cr K absorption edge. The solid curve is calculated by the method of Cromer and Liberman.[21] The points are derived from transmission measurements on Modified Fe9Cr1Mo steel.

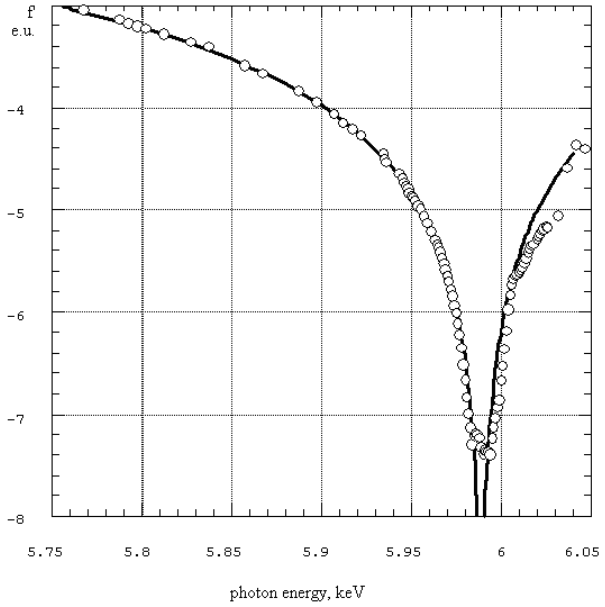

Figure 4.13: Real part of the anomalous dispersion correction, f', to the Cr scattering factor plotted as a function of X-ray energy in the vicinity of the Cr K absorption edge (5.989 keV). The solid curve is calculated by the method of Cromer and Liberman.[21] The points are derived from transmission measurements on Modified Fe9Cr1Mo steel via the Kramers-Kronig integral. The energies used for the ASAXS experiments were 5.789, 5.949, and 5.974 keV.

state physics effects giving rise to the EXAFS. The relationship between m and f'', given earlier in the section covering ASAXS theory, is a proportionality also involving the photon energy. A plot of the measured f'' is given in Fig. 4.12, along with the curve calculated by the CL method.

Each evaluation of f' was made at an energy, E, situated halfway between the energies, ϵ, of available f'' values to avoid the singularity of $E = \epsilon$ in the Kramers-Kronig integral. For the integration, f'' values were extrapolated both below (to 1 keV) and above (to 425 keV) the range of available data using the empirical constants of McMaster.[95] The limits on the range of integration were taken at the suggestion of Hoyt, et al.[62] Such extrapolations fit experimentally-measured cross sections much better than does a simple power law relation and take the form of

$$f'' = \frac{E}{2r_e ch} \exp\left[\sum_{i=0}^{3} a_i (\log E)^i\right] \qquad (4.2)$$

where the a_i are the energy-range dependent tabulated coefficients, r_e is the radius of an electron, c is the velocity of light, and h is Planck's constant. The integrand was then evaluated at each available $f''(e)$ and extrapolated f'' and the resulting curve was then evaluated by the trapezoid rule.

The calculated value of f'_{Cr} in the Modified Fe9Cr1Mo steel versus corrected photon energy is plotted in Fig. 4.13 against the f' calculated by the CL method. A comparison of a magnification of the f'_{Cr} well from Fig. 4.13 with figures 1, 3, and 4 of Hoyt,[62] which concentrates on the very near-edge region of f'_{Ni}, reveals that the f' wells in both cases have a similar structure. Such a magnified plot follows in Fig. 2.3 in comparison to the CL values.

The oscillations on the high energy side of the absorption edge at 5.989 keV are due to electron transitions into discrete states, such transitions which are not addressed by the CL calculation. That these oscillations are not as

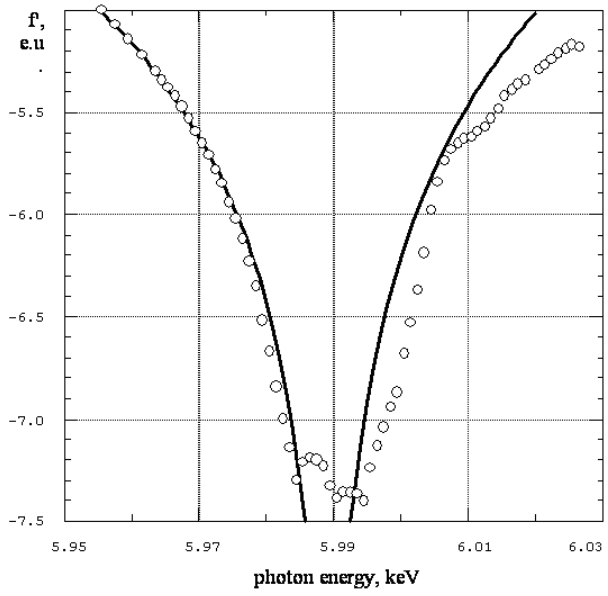

Figure 4.14: Magnification of Fig. 4.13 in the bottom region of the $f'(E)$ well.

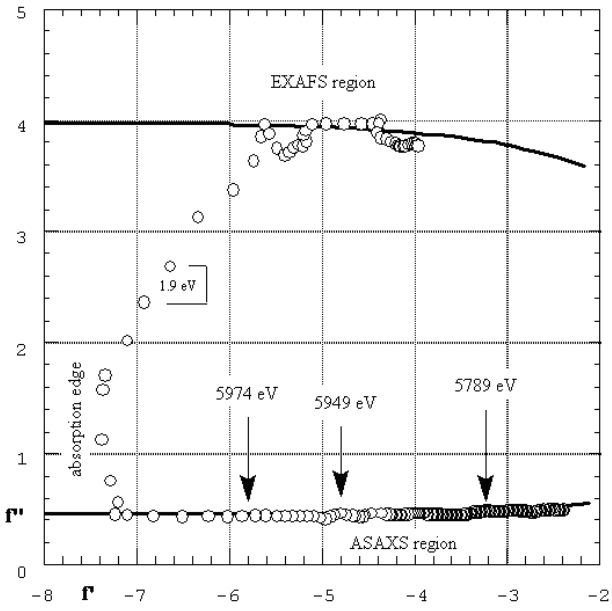

Figure 4.15: Argand diagram showing the relation between the real and imaginary parts of the anomalous dispersion corrections of chromium at the K edge. X-ray photon energy increases in a clockwise direction in even 1.9 eV steps. The energies of the ASAXS measurements are indicated. The solid curve was calculated by the CL method.

well-defined as others which have been presented in the literature[62, 120, 139] is to be expected due to the $\sim$3 eV energy resolution of the germanium optics. The optics were designed to improve upon the angular collimation of the source for the benefit of small-angle scattering at a small increase in energy bandpass. With narrow energy bandpass, the oscillations would be more sharp, however the curves presented represent the actual f', f'', and μ_m values available with the Ge optics used for the ASAXS measurements. For the range of energies plotted, the agreement with the CL curve is within $\sim$0.2 electrons overall which is about the limit of precision for this measurement. Adjustments to the sample thickness could cause a vertical shift of 0.2 to 0.3 electrons[62] as could inclusion of the energy correction term.[21] The general shape of the two curves is the same for the energy region below the absorption edge important to SAXS and it is apparent that the energy scale has been calibrated, to within 1 eV. The experimental values for the f' and f'' of Cr, measured from the N&T sample of Modified Fe9Cr1Mo steel, will be used to calculate the scattering contrast of the carbides in both the AF1410 steel and the Modified Fe9Cr1Mo steel. The amount of Cr present in the AF1410 alloy (2% by weight) is not sufficient to establish transmission data that may be reliably converted into f'. The CL method will be used to calculate f' and f'' for the other elements and for Cr at energies outside the range of the above plots. The Argand diagram in Fig. 4.15 summarizes these results by plotting the imaginary versus the real part of the dispersion correction. Regions for ASAXS and EXAFS experiments are clearly marked, including those energies used in the ASAXS experiments to be described.

4.2.3 Scattering Strength-Weighted Size Distribution Analyses

Samples were prepared from each of the five aging temperatures (482, 538, 593, 649, & 704° C) and from the N&T condition. The N&T sample corresponds to a 5000

hour aging at 25° C. SAXS from each sample was measured at three energies (5.789, 5.949, 5.974 keV) near the Cr K edge, corresponding to 200 eV, 40 eV, and 15 eV, respectively, below the Cr edge. Each individual SAXS curve of collimation-corrected $d\Sigma/d\Omega$ vs. h was analyzed for a scattering strength-weighted distribution of spherical scatterers by the maximum entropy method described earlier. The program used, `MaxSAS.FOR`, was a modification of the Potton code, `Maxe.FOR`, written to accept the angular range of data from the double crystal instrument as well as that from instruments with higher angular ranges.

The Cr-ASAXS series from a typical Modified Fe9Cr1Mo steel sample (aged at 482° C) is plotted in Fig. 2.5. Each curve corresponds to an experiment at a different photon energy near the Cr K absorption edge. The solid curves are the intensities calculated from the maximum entropy distribution. There is a distinct difference between the curves which is systematic with the change in the scattering factor of chromium. For clarity, the error bars have been left off Fig. 4.16. Consult the appendix for the values of the margin of error.

For the Modified Fe9Cr1Mo steel samples, the smallest scattering vector, hmin, at which the SAXS was significantly different from the rocking curve of the optics was usually about 0.01 nm^{-1} while in a few cases it was as low as 0.006 nm^{-1}. The scattering vector at which the SAXS met the background (with S/N $\sim$ 1), h_{max}, was about 0.15 to 0.2 nm^{-1} although the data collection was continued, in most cases, to $h \sim 1$ nm^{-1}, to collect a good measure of the experimental background. To allow `MaxSAS.FOR` to make a good estimate of that experimental background, hmax was taken as 0.4 nm^{-1}. Between 150 and 200 experimental data points fall between hmin and hmax. The range of dimensions visible from the experimental data should be from 40 nm to 300 nm. The peripheral vision of the experiment extends these limits by about a factor of two in each direction although the information content of that extension is less certain. The rocking curve width defines the variation of scattering vectors sampled at each h as $\Delta h = 0.0015$ nm^{-1}.

The complete set of SAXS curves are presented as an appendix to this dissertation. The errors, as estimated by the desmearing program `Lake.FOR`, were increased by 30 to 50% for `MaxSAS.FOR` to converge upon a solution. This corresponds to additional error propagation due

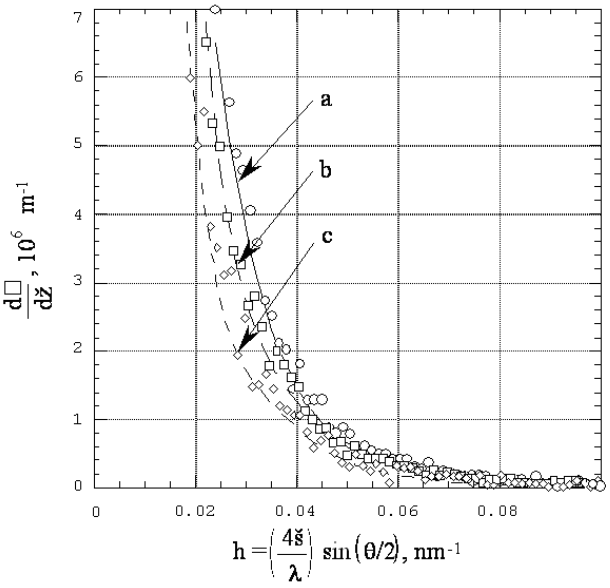

Figure 4.16: SAXS from a sample of Modified Fe9Cr1Mo steel aged 5000 hours at 482° C. For each curve, the points are experimentally measured (and desmeared) and the solid line is the intensity curve back-calculated from the maximum entropy distribution. Curves a, b, and c correspond to photon energies 5.974, 5.949, and 5.789 keV.

to the desmearing process itself. It must be noted that, although Glatter[43] remarks that the Lake technique requires some preliminary smoothing of the data, it is evident from the spheres data presented earlier that this comment is not justified. Experience with the numerical implementation of the algorithm has shown that it is sensitive to the quality of the integration used in the forward smearing processes as well as the quality of the input data. In general, it is found that the present implementation of the Lake technique increases the scatter in the data by three to five times. While this is undesirable, it is a much smaller penalty than an arbitrary smoothing of data.

For the maximum entropy analyses, all eighteen SAXS curves were analyzed over the range $0.01 \leq h \leq 0.4$ nm^{-1}. Each distribution was binned with 100 diametral size bins from 8 nm to 800 nm distributed evenly in a geometric series to span the visible range of dimensions, including peripheral vision. By using a geometric series rather than an arithmetic series, the size distributions neither oversample the SAXS data from large sizes nor undersample that from small sizes. Convergence was achieved in 10 to 20 iterations of `MaxSAS.FOR`. All features within each of the eighteen distributions were confined to within this range. The maximum entropy solution of the size distributions of the three SAXS curves of Fig. 4.16 are plotted in Fig. 4.17. Each distribution was obtained separately. Note that the central peak in each of the curves falls at about the same diameter, indicating good consistency in the procedure.

In a broad sense, a slight decrease in the level of background is observed as photon energy is increased, lending support that the fundamental source of the experimental background is the scattering of the transmitted beam by the air path intervening between the sample and the detector. The transmission coefficient of air decreases as the photon energy is increased, therefore less intensity will be scattered.

The multi-modal distributions presented above are typical for all of the distributions obtained for the Modified Fe9Cr1Mo SAXS analyses. It is believed that not all the oscillations correspond to actual peaks in the size distribution. Some may be due to systematic errors produced by approximating the scattering features by perfect spheres and also due to the S-B search technique as previously discussed in the theoretical section on the maximum entropy method. Taking these arguments as caveats, each

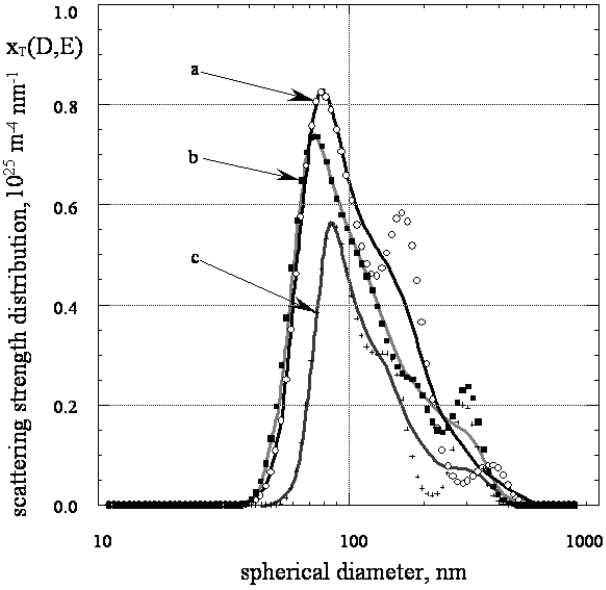

Figure 4.17: Maximum entropy scattering strength distributions for the 482° C sample. Each data set corresponds with the same-labeled SAXS experiment shown in Fig. 4.16. The smooth curves are drawn by hand. Several factors serve to raise the background in these SAXS experiments. The fundamental source of the average 4×10^4 m^{-1} experimental background, shown in Table 4.3, was scattering of the transmitted beam by the 285 mm air path between the sample and the detector. Backgrounds estimated by `MaxSAS.FOR` were about an order of magnitude larger than the dark noise of the photodiode detector and about three times the magnitude of the visible light leakage into the photodiode box. Background due to fluorescence of vanadium or resonant Raman scattering of chromium is not conducted through the DCD optics as that radiation is at the wrong photon energy for the angles used in the SAXS experiments.

Table 4.3: Backgrounds of SAXS experiments on the Modified Fe9Cr1Mo steel near the Cr K absorption edge of 5989 eV as determined via the maximum entropy analysis. All backgrounds are ± 400 m^{-1}.

aging temperature	background at Cr-200, m^{-1}	background at Cr-40, m^{-1}	background at Cr-15, m^{-1}
N&T	49,900	49,400	43,400
482° C	101,100	42,800	39,200
538° C	26,300	21,900	11,100
593° C	51,500	41,000	44,300
649° C	66,800	23,600	30,000
704° C	24,800	20,800	23,300

curve can be interpreted as a guide to the general shape of the distribution and smooth curves have been drawn by hand to indicate the trend. Valleys in the distributions (at about 200 - 300 nm) are most probably of low significance as the maximum entropy method only generates features in the distribution for which there is strong statistical support, i.e. good signal-to-noise ratio. Hence the valleys in the distributions above are most probably not real but exist due to a lack of statistical support in the SAXS data for a greater value of the distribution at that diameter. While it is possible to model the scattering features with a different shape function, such an effort would bias the entire solution to that particular shape function. The difficulty in deconvolving the resultant size distributions into the proper shape function for each scatterer (MX vs. $M_{23}X_6$) would be enormous. It would be preferable to re-write the maximum entropy program to consider a different shape function for each particle and a different contrast for each particle and energy and use this as the constant matrix by which the maximum entropy program would solve for all three distributions (VC, NbC, and $Cr_{23}C_6$) simultaneously. This problem was already addressed in the theoretical section as Model II. In conclusion, while the spherical shape may not be the best model for each individual scatterer, it is the most general (and generally-accepted) shape by which to model all of the scatterers simultaneously in absence of a priori information, so the distributions may be interpreted as *sphere-equivalent* distributions. In the maximum entropy distributions obtained using the spherical shape function, the most important feature is the largest peak in the distribution. Secondary peaks are more suspect as to absolute diametral position and height.[107] Valleys show a lack of information content in the input data.

Additionally, the distributions plotted above show the volume fraction that is weighted by scattering contrast. Particles with high contrast and low volume fraction will appear on par with the reverse situation. In a simple system with only one type of particle, the volume fraction is the area under each curve divided by the particle contrast. However, in a complex system with many types of particles scattering in the visible range of the camera, the analysis is more involved. It is exactly this type of analysis that will be addressed in the next section where the scattering of $Cr_{23}C_6$ precipitates will be isolated.

It is possible to generalize each of the scattering strength distributions by determining the mean diameter and the total scattering strength, X, of each distribution from Eq. (50). X is plotted in Fig. 4.18 for each of the eighteen SAXS experiments as a function of the 5000 hour aging temperature. From room temperature up to 482° C, there is no significant change in the total scattering strength, indicative of a static population of precipitates. For the four temperatures above 482° C, X increased in all cases. The increase in the scattering strength was greatest for 5000 hour aging at 649° C. It is not expected that the composition of any of the precipitates will change significantly over the range of aging temperatures chosen, hence the scattering contrast of each particle will remain constant with aging temperature. The changes in the scattering contrast with aging temperature may thus be viewed as due to changes in the volume fractions of the various precipitate species in the steel.

The mean particle diameter for each distribution, plotted in Fig. 4.19, shows a trend very similar to that of the scattering strength. The significant difference is that the largest particles are found for aging 5000 hours at 704° C. The distribution widths are all at about 50% of the mean

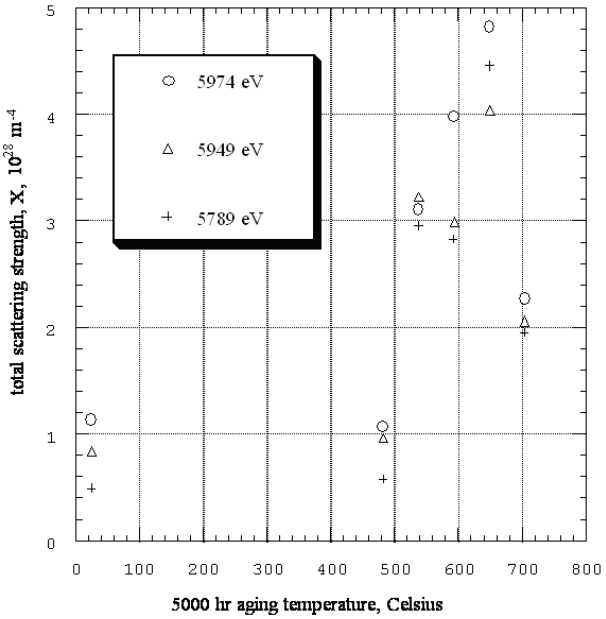

Figure 4.18: Total scattering strength, X, of all scatterers in Modified Fe9Cr1Mo steel as a function of 5000 hour aging temperature.

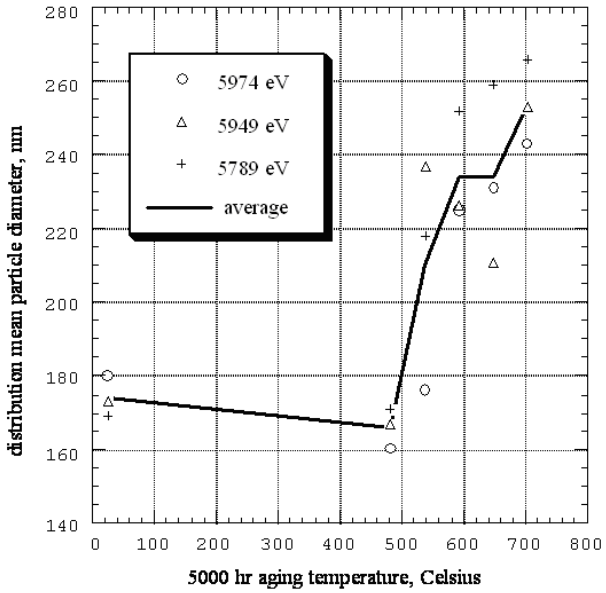

Figure 4.19: Mean diameter of all scatterers in Modified Fe9Cr1Mo steel as a function of 5000 hour aging temperature, derived from the scattering strength distributions. The solid line is the average at each energy. The distribution widths are approximately one-half the mean diameter in all cases.

diameter.

It is appropriate at this point to compare the sizes just reported with microphotographs from the transmission electron microscope. Fig.s 4.20 to 4.21 are characteristic micrographs of TEM samples from each of the six aging conditions. Micrographs were recorded using both the JEOL JEM 100B at Northwestern University and the high voltage electron microscope at Argonne National Laboratory using samples prepared by jet polishing.

By comparison, the SAXS results on the precipitate populations are consistent with the observations of the microstructure using the transmission electron microscope. The micrographs show that there are a variety of sizes and particle shapes in the various samples and that those particles have dimensions consistent with those determined from the small-angle X-ray scattering. Additionally, although many of the particles appear to be situated on martensitic lath boundaries, those boundaries appear to be randomly dispersed in the polycrystalline samples. Because each sample volume examined by SAXS is quite large (ca. 2×10^{-10} m^3) compared to that examined by the TEM (ca. 3×10^{-18} m^3), it may be assumed that the precipitates examined by SAXS are randomly distributed and that particle-to-particle interactions are minimal. The SAXS was analyzed using these assumptions as well as assuming that the scatterers were spherical in shape, which is roughly supported by the TEM micrographs. It is difficult to gain information about the total amount of scatterers or the density of scatterers from the micrographs as the sample thickness is not consistent neither between nor within the photographs. Therefore, these TEM results can neither support nor reject the SAXS result about the total scattering strength. Of note, is the micrograph of the 482° C aged sample which seems to indicate significant precipitation. The dominant features, which are of light contrast, are surface contamination of the sample. Only the dark features are the carbides.

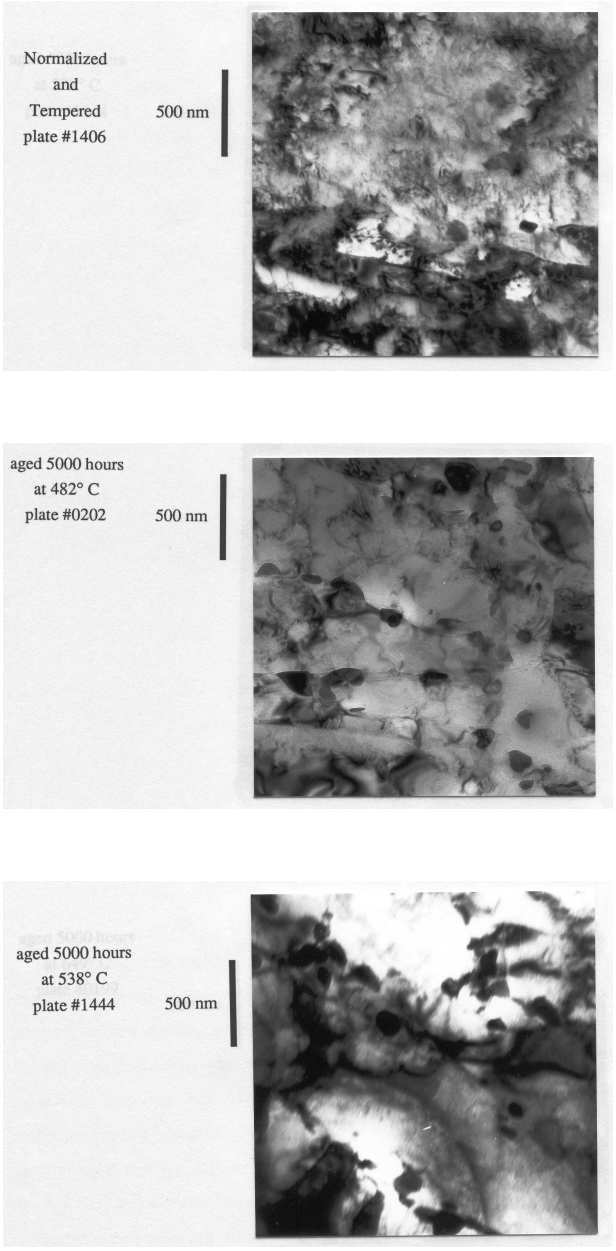

Figure 4.20: Transmission electron micrographs of Modified Fe9Cr1Mo steel. The upper and lower photos were taken using the JEOL JEM 100B at Northwestern University at an accelerating voltage of 100 kV. The middle photo was taken using the high voltage electron microscope at Argonne National Laboratory at an accelerating voltage of 1.2 MV.

4.2.4 Calculation of the Scattering Contrasts

To isolate the scattering due to $Cr_{23}C_6$ from the distributions above, it is necessary to calculate the scattering contrast, $|\Delta\rho|^2$, of $Cr_{23}C_6$ with respect to the matrix composition of the Modified Fe9Cr1Mo steel. Table 4.4 lists

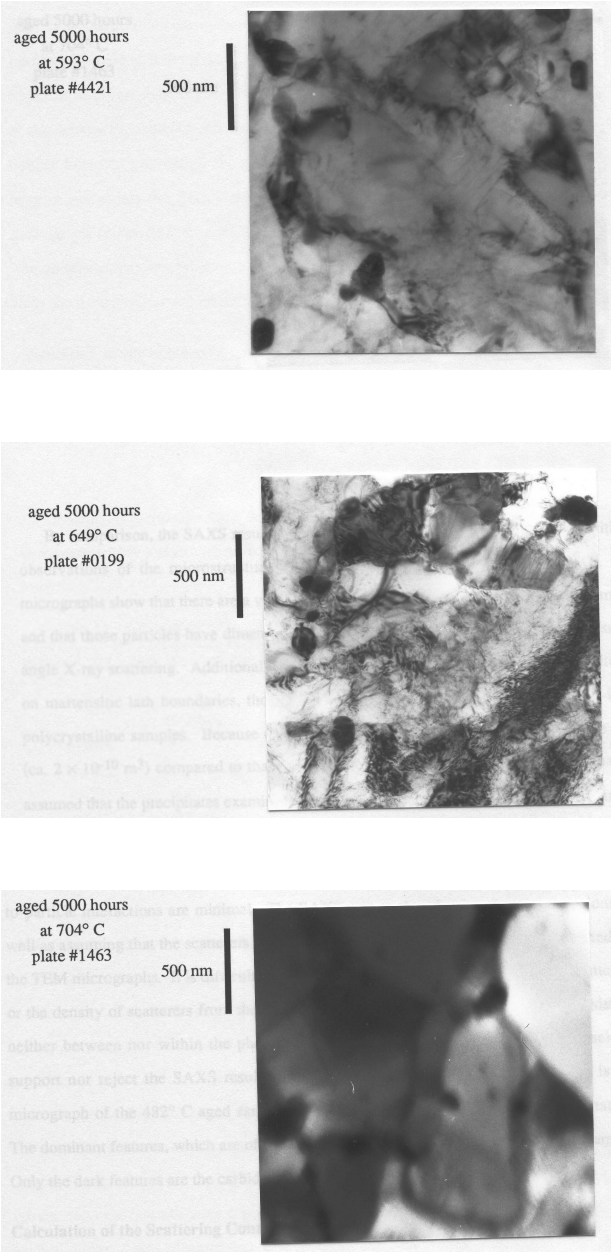

Figure 4.21: Transmission electron micrographs of Modified Fe9Cr1Mo steel. The upper and middle photos were taken using the high voltage electron microscope at Argonne National Laboratory at an accelerating voltage of 1.2 MV. The lower photo was taken using the JEOL JEM 100B at Northwestern University at an accelerating voltage of 100 kV.

the crystallographic information used in the calculation. For refinement, it is necessary to assume a volume fraction for each carbide and deplete the matrix concentration by a mass balance. Anomalous dispersion corrections for all elements in the composition were calculated by the CL method with the exception of chromium which was calculated from measured transmission data via the Kramers-Kronig integral.

The X-ray scattering contrast, $|\Delta\rho|^2$, of each precipitate, reported in Table 4.5, was calculated assuming several different conditions for the precipitates and the matrix composition given in Table 1.1. The energies in Table 4.5 are near the chromium K absorption edge and correspond to those of Fig.s 4.16 and 4.17. First, it was assumed that the precipitates are in stoichiometric composition. Then by assuming a volume fraction for each precipitate and calculating the mass balance of the matrix, it was determined that the variation in the calculated scattering contrasts produced by uncertainty in precipitate volume fractions is about 2 - 10%. These variations are indicated in Table 4.5 as the "$\pm$" values. The volume fractions assumed were 1.5% for $Cr_{23}C_6$, 0.25% for VC, and 0.05% for NbC. Next it was assumed that 35% of the carbon sites would be occupied by nitrogen. This produced a variation in the calculated scattering contrasts of a few percent. There is evidence for partial substitution of carbon in $Cr_{23}C_6$, VC, and NbC by nitrogen, as reported in a comprehensive study of precipitation in austenitic steels using convergent beam electron diffraction in the TEM.[132] Finally, the scattering contrasts of Cr-rich $M_{23}X_6$, V-rich MX, and Nb-rich MX were calculated, where $X = (C_{0.65}, N_{0.35})$, were calculated. The values used for M are reported in Table 4.5, after Sklad and Sikka.[129] For the ASAXS analyses, the stoichiometric precipitate composition of chromium carbide was used.

Values from Table 4.5, corresponding to the SAXS data at the three energies shown in the previous section, are plotted in Fig. 4.22. NbC has a relatively low scattering contrast which is nearly constant for the three energies plotted. This is expected as the Nb K edge is at 18.986 keV, far from the chromium K edge. The 20% drop in VC contrast, seen near the chromium K edge, is due to the rising f' of vanadium as the photon energy moves away from the vanadium K edge at 5.465 keV. These effects are quite small when compared to the factor-

Table 4.4: Crystallographic structure information used in calculating the scattering contrast for the precipitates in Modified Fe9Cr1Mo steel. Pearson and Strukturbericht numbers are given by Barrett.[3] Lattice parameters are from Hansen and Anderko.[55]

	matrix	$Cr_{23}C_6$	VC	NbC
structure	cI2, A2	cF116, D84	cF8, B1	cF8, B1
metal sites	2	92	4	4
carbon sites	6	24	4	4
lattice parameter (a_o)	0.287 nm	1.0621 nm	0.4168 nm	0.4470 nm

Table 4.5: X-ray scattering contrast, $|\Delta\rho|^2$, (with respect to the matrix composition) of carbo-nitrides in Modified Fe9Cr1Mo. $|\Delta\rho|^2$ is calculated in units of 10^{28} m^{-4} ($= 10^{20}$ cm^{-4}). The variation, in parentheses, is calculated from mass balances with different volume fractions of precipitates.

photon energy, keV	c = 5.789	b = 5.949	a = 5.974
$E - E_K$	-200 eV	-40 eV	-15 eV
$Cr_{23}C_6$	80(2)	143(2)	195(4)
VC	253(2)	213(2)	203(2)
NbC	20(1)	21(1)	22(1)
Cr-rich $M_{23}X_6$	13(1)	30(2)	45(2)
V-rich MX	147(3)	130(3)	128(3)
Nb-rich MX	21(1)	17(1)	16(1)

of-two increase in the $Cr_{23}C_6$ contrast.

Based on a mass balance argument, production of $Cr_{23}C_6$ in Modified Fe9Cr1Mo steel is limited to 1.63% (volume) by the matrix carbon concentration, if production of neither VC nor NbC occurs. When both VC and NbC are produced, as in the case of Modified Fe9Cr1Mo steel, the maximum possible amount of $Cr_{23}C_6$ calculated is significantly lower, dependent on the volume fractions of VC and NbC that are produced. By considering that nitrogen could substitute for some of the carbon in $Cr_{23}C_6$, the maximum amount of Cr23(C,N)6 can increase above 1.63% before a mass balance indicates that all of the matrix carbon has been consumed by Cr23(C,N)6 production. The ratio of carbon atoms to nitrogen atoms from the reported alloy composition (Table1.1) is 65:35. The assumption of up to 35% nitrogen substitution allows maximum mass balance volume-fractions of Cr23(C,N)6 comparable with those observed in the TEM from extraction replicas.[94, 128, 129] Nitrogen has only one more electron than does carbon and the consideration of the precipitates as carbo-nitrides rather than just carbides has lit-

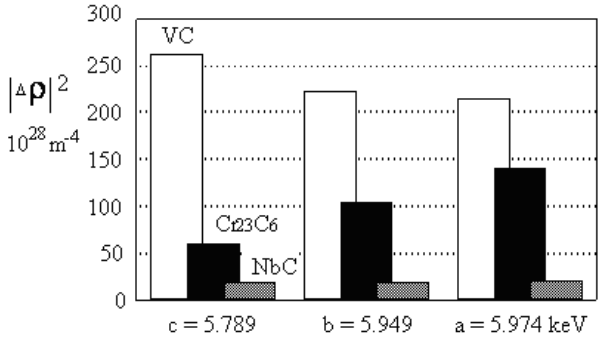

Figure 4.22: X-ray scattering contrast, $|\Delta\rho|^2$, (with respect to the matrix composition) for the carbides $Cr_{23}C_6$, VC, and NbC in the Modified Fe9Cr1Mo steel, calculated for three energies near the chromium K absorption edge. The contrast of the $Cr_{23}C_6$ increases by more than a factor of two over the range of energies while that of the MC carbides changes by less than 20%.

tle effect on the scattering contrast. However, a strong dilution of the scattering contrast by two to four times is seen when the metal site fraction is considered to be altered. This sort of variation has a strong bearing on the volume fractions determined by the ASAXS analysis. The contrast-weighting favors the scattering from the less-diluted compositions but this lends an uncertainty to the volume-fraction analysis that cannot be resolved by small-angle scattering alone.

4.2.5 $Cr_{23}C_6$ Volume Fraction Distribution Isolated by ASAXS

The 20% variation in VC contrast and scant variation in contrast of NbC renders the numerical matrix of contrasts ill-conditioned with respect to VC and NbC. The variation in scattering contrasts with photon energy is not sufficient to separate all three distributions simultaneously using SAXS data at photon energies only near the chromium K edge. This is exactly the situation addressed by Eq. (63), the ASAXS gradient method, where the volume fraction distribution of $Cr_{23}C_6$, f(D,$Cr_{23}C_6$), can be determined from the slope of a plot of $x_T(D,E)$ vs. $|\Delta\rho|^2(E,Cr_{23}C_6)$. The intercept is the scattering strength from all other scatterers. By the least-squares technique, it is possible that the slope of the line could be negative, indicating a negative volume fraction of $Cr_{23}C_6$. Such unphysical values were set to a small insignificant positive value. As was seen by analyzing the standard deviation of the least-squares slope at each diametral bin, the correction applied was always less than the standard deviation, signifying a lack of statistical certainty in the SAXS data for that particular size of $Cr_{23}C_6$. This method is also used within the program `MaxSAS.FOR` by the S-B[127] search technique to ensure positive trial distributions.

Fig. 4.23 shows the volume-fraction size distribution of $Cr_{23}C_6$ in each sample of the Modified Fe9Cr1Mo steel as determined by the ASAXS gradient method. The vertical bars are the standard deviation of each measurement and indicate the estimated margin of error in the analysis. With such low signal-to-noise ratios and so many features in the distributions, each distribution was subsequently smoothed to *guide the eye* over statistically insignificant features in the distributions. The smoothing technique[110,111] considers the reported error for each value. The results of the smoothing are indicated by the solid line.

A summary analysis of the $Cr_{23}C_6$ distributions derived from ASAXS is given in Tables 4.6-4.8. The tabulated values are also presented in Fig.s 4.24 to 4.27. The area under each of the size distribution curves is the total observed volume fraction, $\Delta V/V$, of $Cr_{23}C_6$. The volume fractions obtained from the raw analysis and the smoother version provide an indication of the error in the analytical procedure. Also measured from each distribution is the volume-weighted mean diameter, $\bar{D}_V$, and standard deviation of the mean, $\sigma(\bar{D}_V)$. For comparison with distributions reported by counting methods such as TEM, other parameters are also reported. The definitions of all terms are given in Table 4.9. With such a low S/N, one must be more cautious in the interpretation of the other parameters which are derived from transformations of the maximum entropy volume fraction distributions, not measured directly. The rather large margins of error reported with the size distributions are due to systematic errors in the maximum entropy analysis of the scattering. As such, these errors represent the level of confidence one can expect from each of the maximum entropy size distributions.

There is little substantive change between the chromium carbide distributions for samples aged for 5000 hours at room temperature and 482° C. The volume fraction distribution of the 538°sample shows an overall increase in the volume fraction, but especially at the smaller diameters. This additional volume fraction of small $Cr_{23}C_6$ produces a drop in the calculated mean diameter and a peak in the number density. As the aging temperature is raised between 538°and 649°, the volume fraction and the mean diameter increase, the number density decreases slightly, and the mean particle spacing remains relatively constant. The largest mean diameter is calculated for the sample at 704°but the volume fraction indicated by the ASAXS analysis, significantly lower than that for the 649°sample, is only slightly higher than the starting condition (N&T). Additionally, because the mean diameter is at a maximum and the volume fraction is relatively low, the calculated number density is the lowest of all the samples and the mean spacing, calculated from the number density, is the greatest. The overall variation in the mean diameter is about 50% over the range of aging temperatures.

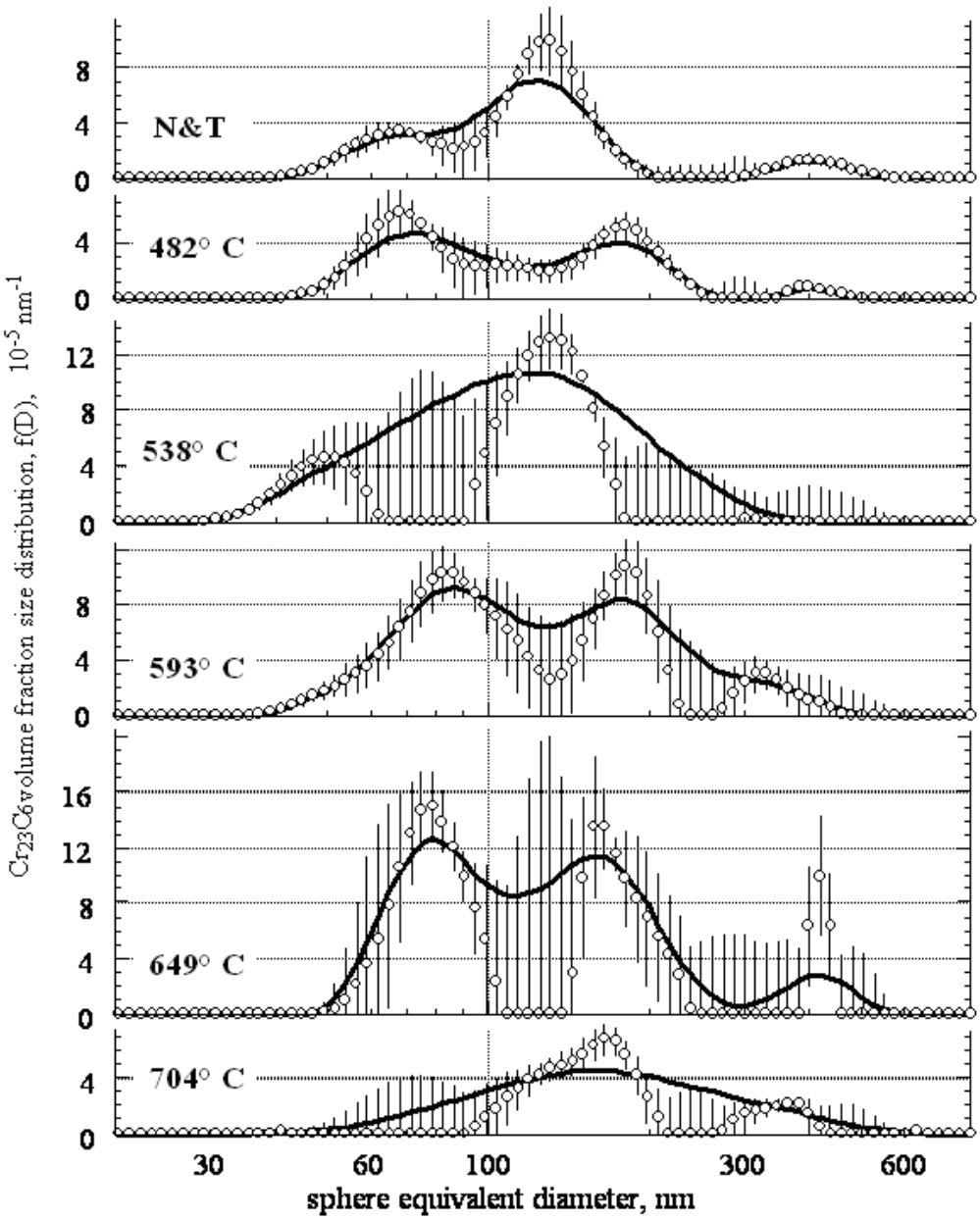

Figure 4.23: Volume-fraction size distributions of $Cr_{23}C_6$ in Modified Fe9Cr1Mo steel, determined by the ASAXS gradient method. The vertical bars represent the margin of error. The solid line is smoothed via the technique of Reinsch.[110]

Table 4.6: Statistical summary from volume fraction size distributions of the $Cr_{23}C_6$ scatterers in Modified Fe9Cr1Mo steel as determined by ASAXS. The "±" values represent the 3σ variation of values from calculated and smoothed distributions. The smoothing technique[110] considers the margin of error in the data. Each term is defined in Table 4.9.

sample	V_f	$\bar{D_v}$,nm	$\sigma(\bar{D_v})$,nm	S_v, μm^{-1}
N&T (25° C)	0.85 ± 0.09	194 ± 1	134 ± 6	0.38 ± 0.03
482°	0.71 ± 0.03	169 ± 1	97 ± 2	0.34 ± 0.02
538°	1.31 ± 1.90	138 ± 54	52 ± 66	0.67 ± 0.85
593°	1.70 ± 0.75	187 ± 20	97 ± 0.05	0.72 ± 0.22
649°	1.93 ± 1.10	208 ± 36	127 ± 16	0.80 ± 0.51
704°	0.96 ± 0.90	230 ± 42	111 ± 33	0.31 ± 0.28

Table 4.7: Statistical summary from number density size distributions of the $Cr_{23}C_6$ scatterers in Modified Fe9Cr1Mo steel as determined by ASAXS. The "±" values represent the 3σ variation of values from calculated and smoothed distributions. The smoothing technique[110] considers the margin of error in the data. Each term is defined in Table 4.9.

sample	N_v, 10^{18} m^{-3}	Λ,nm	$\bar{D_N}$,nm	$\sigma(\bar{D_N})$,nm
N&T (25° C)	13.3 ± 0.3	422 ± 3	87 ± 3	39 ± 3
482°	13.8 ± 1.6	417 ± 16	80 ± 3	37 ± 1
538°	30.6 ± 29.0	323 ± 104	73 ± 15	38 ± 2
593°	24.5 ± 2.8	344 ± 13	86 ± 7	43 ± 8
649°	25.9 ± 12.7	339 ± 56	90 ± 8	41 ± 1
704°	5.8 ± 8.9	574 ± 306	121 ± 55	59 ± 7

Table 4.8: Statistical summary from the total particle surface area of the $Cr_{23}C_6$ scatterers in Modified Fe9Cr1Mo steel as determined by ASAXS. The "±" values represent the 3σ variation of values from calculated and smoothed distributions. The smoothing technique[110] considers the margin of error in the data. Each term is defined in Table 4.9.

	${}^sD_p$,nm	${}^sN_v$, 10^{18} m^{-3}	${}^s\Lambda$,nm
N&T (25° C)	134 ± 5	6.69 ± 0.03	531 ± 1
482°	126 ± 2	6.76 ± 0.53	529 ± 14
538°	116 ± 23	15.37 ± 13.70	406 ± 122
593°	141 ± 19	11.45 ± 0.54	444 ± 7
649°	145 ± 10	12.08 ± 9.24	439 ± 113
704°	185 ± 5	2.92 ± 2.48	706 ± 202

Table 4.9: Definition of each term in the statistical summary of the size distributions.

ΔD_i**: width of the diameter bin** i

$\varphi_i \Delta D_i$**: volume fraction in the diameter bin** i

f_i**: volume fraction size distribution**
determined by the ASAXS Gradient Method

V_f**: volume fraction**

$$V_f = \sum_i \varphi_i, \quad \varphi_i = f_i \Delta D_i$$

D_v**: mean diameter, volume distribution**

$$D_v = (\sum_i \varphi_i D_i)/V_f$$

$\sigma(\bar{D}_v)$**: standard deviation of** $\bar{D}_v$

$$\sigma(\bar{D}_v) = \sqrt{(\sum_i \varphi_i D_i^2)/V_f - (\bar{D}_v)^2}$$

representing the distribution width

S_v**: specific surface area**

$$S_v = 6 \sum_i \varphi / D_i$$

N_v**: number density**

$$N_v = \sum_i n_i, \quad n_i = \varphi_i / (\tfrac{\pi}{6} D_i^3)$$

Λ**: mean particle spacing**

$$\Lambda = N_v^{1/3}$$

D_n**: mean diameter, number distribution**

$$D_n = (\sum_i n_i D_i)/N_v$$

$\sigma(\bar{D}_n)$**: standard deviation of** $\bar{D}_N$

$$\sigma(\bar{D}_n) = \sqrt{(\sum_i n_i D_i^2)/N_v - (\bar{D}_n)^2}$$

representing the distribution width

${}^s D_p$**: *Porod* diameter**

$${}^s D_p = 6 V_f / S_v$$

weighted by the specific surface area

${}^s N_v$**: number density**

$${}^s N_v = S_v / (\pi {}^s D_p^2)$$

weighted by the specific surface area

${}^s \Lambda$**: mean particle spacing**

$${}^s \Lambda = {}^s N_v{}^{-1/3}$$

weighted by the specific surface area

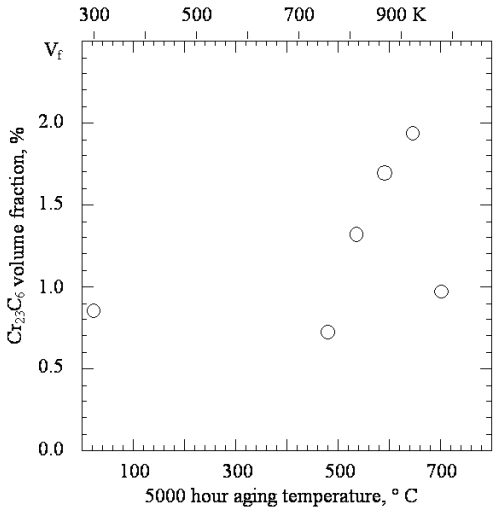

Figure 4.24: Total estimated volume fraction of $Cr_{23}C_6$ in Modified Fe9Cr1Mo steel as a function of sample aging temperature. These ASAXS results are derived using three photon energies near the Cr K absorption edge.

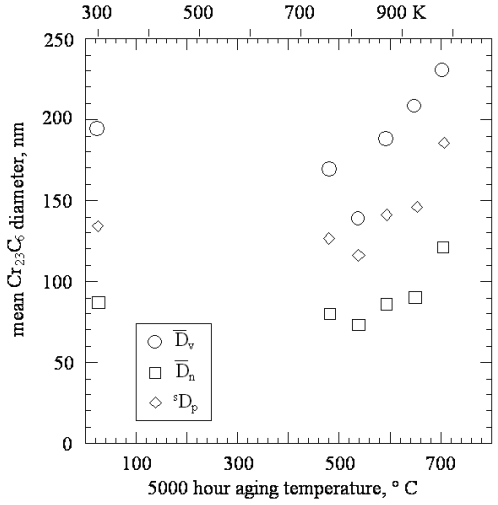

Figure 4.25: Mean diameter of $Cr_{23}C_6$ in Modified Fe9Cr1Mo steel as a function of sample aging temperature. These ASAXS results are derived using three photon energies near the Cr K absorption edge. See Table 4.9 for definitions of the various diameters.

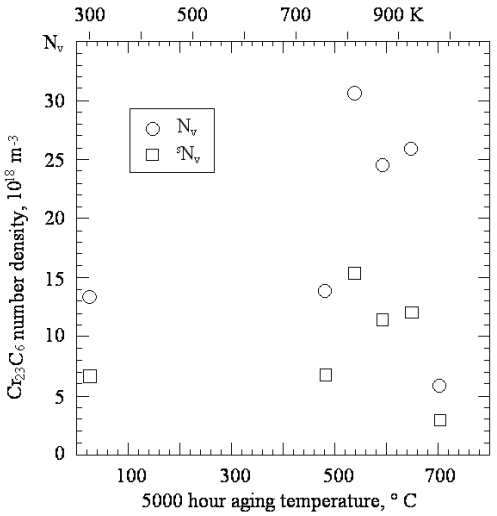

Figure 4.26: Number density of $Cr_{23}C_6$ in Modified Fe9Cr1Mo steel as a function of sample aging temperature. See Table 4.9 for definitions of the various number densities.

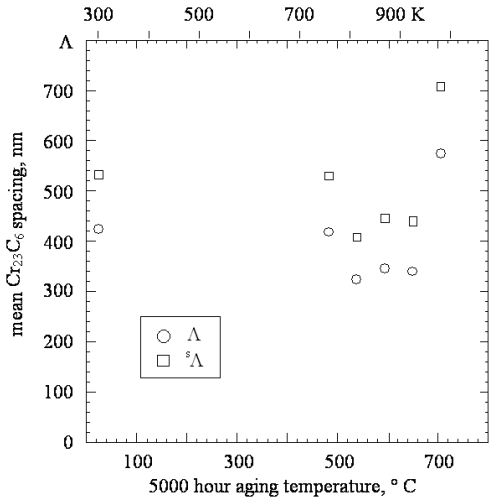

Figure 4.27: Mean particle spacing of $Cr_{23}C_6$ in Modified Fe9Cr1Mo steel as a function of sample aging temperature. See Table 4.9 for definitions of the various mean spacings.

One possible analysis of the ASAXS results is based on the assumption that as the 5000 hour aging temperature is raised, the chromium carbide population moves closer towards equilibrium in both volume fraction and composition. The N&T sample is the farthest from equilibrium, while the sample aged 5000 hours at 649° C is probably at equilibrium, based on the volume fractions determined by ASAXS. Thermodynamical calculations by Dr. G. Ghosh of Northwestern University using the ThermoCalc™ database (unpublished research, 1989) indicate an equilibrium volume fraction ∼1.6% of $M_{23}C_6$ that is relatively constant over the temperature range from 500°through 704° C. ThermoCalc™ indicated that $(Cr_{.85}Fe_{.01}Mo_{.4})_{23}C_6$ is the equilibrium chromium carbide composition at 500° C. This composition is predicted to change monotonically with temperature to $(Cr_{.76}Fe_{.12}Mo_{.12})_{23}C_6$ at 704° C. At the tempering temperature of 760° C, ThermoCalc™ indicates an equilibrium chromium carbide composition of $(Cr_{.70}Fe_{.18}Mo_{.12})_{23}C_6$.

It could be argued that the ThermoCalc™ results are qualitatively supported by the metal site fraction analysis reported by Maziasz.[94] Using particle extractions, $(Cr_{.63}Fe_{.27}Mo_{.05})_{23}C_6$ was the chromium carbide composition found by X-ray energy dispersive spectroscopy for the N&T sample while $(Cr_{.67}Fe_{.21}Mo_{.05})_{23}C_6$ was the composition of chromium carbide in a sample aged 10000 hours at 650° C. Trace amounts of Si, P, V, Mn, Ni, and Nb account for the difference from 100% in the metal site fractions of these two compositions. The composition of chromium carbide in the N&T sample of Maziasz is close to that predicted by ThermoCalc™ for composition equilibrium at the tempering temperature of 760° C, indicating that the sample is far from the equilibrium room temperature composition. As the aging temperature is raised, the composition moves closer towards the equilibrium value predicted by ThermoCalc™ for that aging temperature. That is, the metal site fraction of chromium in $M_{23}C_6$ was found by Maziasz to increase as a function of aging temperature. The effect of chromium carbide composition variation from $(Cr_{.85}Fe_{.01}Mo_{.14})_{23}C_6$ to $(Cr_{.70}Fe_{.18}Mo_{.12})_{23}C_6$ on the ASAXS-determined volume fraction, by means of changing the scattering contrast, is at most 25%. Considering the margin of error in determining the volume fraction, this variation does not change the results qualitatively.

The drop of the calculated chromium carbide volume fraction for the 704° C sample, indicated by the ASAXS analysis, is unexpected. Such a drop would suggest a phase transition between 649°and 704°, in contradiction to ThermoCalc™ which predicts no such sharp features between 500°and 850° C. If the volume fraction of chromium carbide in the 704°sample were fixed at the value for the 649°sample, which was assumed to be close to equilibrium, the ASAXS results would imply a sudden decrease in the scattering contrast. Such a decrease in scattering contrast could be due to either a chromium carbide lattice dilatation or a decrease in the atomic concentration difference of Cr between the carbide and matrix. The amount of dilatation necessary to accommodate the change in scattering contrast would be about 2%, a value which is not physical. The results of Maziasz suggest that no sudden changes in chromium carbide composition occur between 650°and 704°for samples aged 25000 hours.

The empty beam scans for the small-angle scattering data were also checked to verify that they had not introduced an artifact into the analysis. The empty beam scans used by the 704°sample were shared with the AF1410 steel sample austenitized at 1000° C (1 hour) and aged at 510° C (1/4 hour). Because the amount of scattering observed at this aging time of the AF1410 steel was quite low, any problems with the empty beam scan would be magnified in the analysis. No such problems were found in the analysis of SAXS from the AF1410 steel samples, as will be shown later. All parameters necessary to the absolute intensity conversion of the ASAXS data were verified, indicating no artifacts were introduced by the data reduction. Therefore, the ASAXS analysis suggests that the drop in the calculated chromium carbide volume fraction between samples aged 5000 hours at 649°and 704° C is real, although no supporting evidence for such a change has been reported.

The volume fractions determined for the $Cr_{23}C_6$ are consistent with the total residue extracted from an N&T sample (0.94%) and a sample crept at 650° C for an unspecified time (1.74%) reported by Sklad and Sikka.[129] The ASAXS-determined volume fraction of the 649°aged sample is also consistent with that reported by Maziasz and Sikka[94] for a sample aged twice as long, 104 hours. For 25,000 hour aging at 650° C, Maziasz reported that Laves phase, $(Fe,Cr,Si)_2Mo$, production doubled the amount of total extracted residue. Laves phase was not

observed by Maziasz in the sample aged 104 hours at 650° C. By using the metal site fractions reported in Maziasz and Sikka[94] or Sklad and Sikka,[129] the ASAXS-determined volume fraction of $Cr_{23}C_6$ would be between two and four times higher than that reported. This is not consistent with either Maziasz or a mass balance of the reported alloy composition. Other parameters also affected by a different scattering contrast are N_v, Λ, and S_v, but these changes in calculated volume fractions due to different assumed carbide compositions do not affect $\bar{D_v}$, $\bar{D_N}$, or ${}^s D_p$.

If the volume fraction of Cr-rich $M_{23}X_6$ is 1.8%, where the M is that reported by Sklad and X = $C_{0.65}$,$N_{0.35}$, then a 0.20% volume fraction of V-rich MX and 0.07% of Nb-rich MX will consume all the carbon and nitrogen in the matrix, leaving 88% of Cr, 40% of V, and 3% of Nb still in the matrix. This calculation matches quite well with the results reported by Fujita[37] for Fe11CrVNb steels. In that steel, 80% of the Cr and 35% of the V were left in the matrix after complete precipitation but the carbon content of those steels, 0.2%, was more than double that of the Modified Fe9Cr1Mo alloy, hence the greater precipitation of the $Cr_{23}C_6$ and reduction in the matrix chromium content. There is a drop in the mean diameter for the 538° C sample, indicative of an increase in the number of smaller particles within the visible range of the experiment. This drop is seen both in the volume-mean diameter and the number-mean diameter as well as a peak in the number density. In the SANS data of Kim,[71,73] the most precipitation was also observed in the 538° C aged sample. The visible range of that experiment was limited to dimensions less than 100 nm, and is believed by this author to have only resolved the MX clearly. The ASAXS technique used here isolates the scattering from features enriched in chromium, primarily $Cr_{23}C_6$, to dimensions as small as about 50 nm. It is possible that if there is a finite amount of Cr in the lattice of the MX, the Cr contribution of that MX population could be counted with the $Cr_{23}C_6$. The introduction of this smaller population would cause the effect observed.

The specific surface area of the $Cr_{23}C_6$ was also calculated from the ASAXS-determined volume fraction size distributions. Because the maximum entropy code has already fit the size distribution to the scattered intensities, including the reported errors in the intensities, it is possible to determine the specific surface area, directly from the size distribution for spherical scatterers. The value of S_v obtained from the size distribution was compared with that obtained from a conventional Porod analysis of the SAXS intensity (i.e., plot of $I \cdot h^4$ vs. h^4) for one of the samples (482° C aged) at each of the three energies near the chromium K absorption edge with identical results to within the margin of error in the reported intensities. In Fig. 4.28 are plotted the S_v as a function of the 5000 hour aging temperature. The SANS results of Kim[71] are also plotted. Although no critical assessment of the SANS data is provided here, it is observed that there is no question that the Porod law fits the SANS data quite well. In fact, one could argue that the Porod law is the only functional dependence observed in that data. For the two highest aging temperatures, both the ASAXS and the SANS are in good agreement while discrepancies exist for the lower temperatures. Probably this is due to the visible range of dimensions accessible to each experiment as well as the scattering vector resolution. Additionally, the SANS did not specifically isolate the scattering of $Cr_{23}C_6$ (as did the ASAXS) so the S_v reported there may also include contributions from other precipitates such as the MC. The MC are believed to be smaller, which would cause an increase in the measure of S_v. In general, the trend observed in the ASAXS analysis of the $Cr_{23}C_6$ population is comparable with the SANS data of Kim[71] and also the diamond pyramid hardness measurements of Kim on the aged steel samples, given in Fig. 73 of his dissertation. Kim found that the hardness peaks for the sample aged 5000 hours at 538° C.

A complete analysis of the scattering-strength distributions would include a description of the residual scattering strength unaccounted for by the ASAXS analysis. While it is possible to construct plots of those residual distributions, the S/N is poor. In general, the residual scattering strength remaining after the ASAXS isolation of the $Cr_{23}C_6$ distribution, is consistent with any volume fraction of VC between 0 and 0.2%. The scattering contrast and the estimated volume fraction for NbC, based on the previous mass balance arguments, combine to render the NbC scattering strength distributions below the limit of detectability.

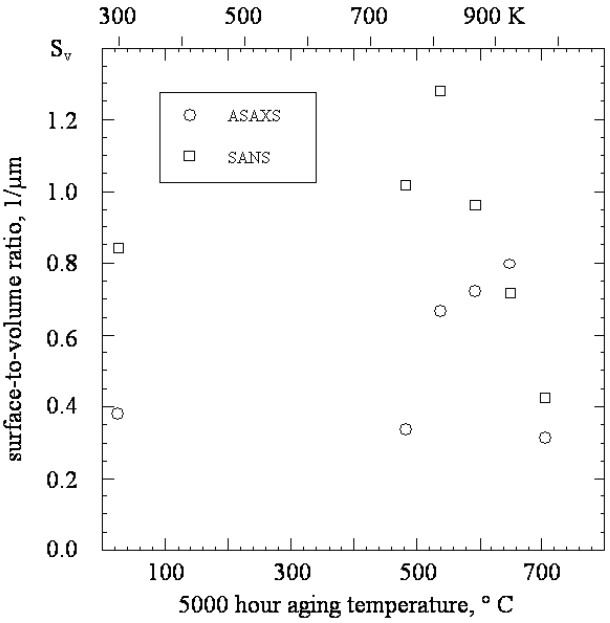

Figure 4.28: Specific surface area of $Cr_{23}C_6$ in Modified Fe9Cr1Mo steel, calculated from size distributions determined by ASAXS. The SANS data are from.[71]

4.2.6 Summary of Modified Fe9Cr1Mo Steel Analyses

Sample thicknesses were determined by multiple photon energy transmission measurements to a precision of 0.3 m on an average SAXS sample thickness of 24 μm. Anomalous dispersion corrections for chromium were determined from a sample of Modified Fe9Cr1Mo steel in the normalized and tempered condition by transmission measurements and the Kramers-Kronig integral. The values calculated agreed with a theoretical calculation of the dispersion corrections to a precision of ± 0.2 electron units.

Small-angle scattering was measured at three photon energies near the chromium K absorption edge from six different samples, aged for 5000 hours at different temperatures. The scattering was modeled by a distribution of spheres giving equivalent scattering using the maximum entropy method. The ASAXS contrast variation technique was used to isolate the volume-fraction size distribution of $Cr_{23}C_6$ from the total measured size distribution of scatterers in this engineering alloy, Modified Fe9Cr1Mo steel. Those distributions are found to remain constant for 5000 hour aging between room temperature and 482° C. For isothermal 5000 hour aging at temperatures between 482°and 649°, the volume fraction of chromium carbide increases, while for the sample aged at 704°, the volume fraction was slightly larger than the N&T sample. The volume fractions determined were found to be in agreement with those reported by Maziasz of the Oak Ridge National Laboratory. To support the volume fractions measured, it was rationalized that some of the carbon lattice sites in the $Cr_{23}C_6$ could be occupied by nitrogen as in $Cr_{23}(C_x,N_{1-x})_6$ although the partitioning between C and N cannot be determined from the SAXS data. The results from the ASAXS analysis are consistent with an explanation that the chromium carbide population moves towards thermal equilibrium as the aging temperature is raised and that the 649°sample aged for 5000 hours is close to equilibrium.

The total observed change in the mean diameter of $Cr_{23}C_6$ is $\sim$50% and increases monotonically with aging temperature while the volume fraction can more than double over the observed range of aging temperatures and is peaked at 649° C. The specific surface area of the $Cr_{23}C_6$ was in general agreement with the SANS data

of.[71] The distributions of MX precipitates were not obvious in these small-angle scattering experiments using the double-crystal diffractometer.

4.3 AF1410 Steel

The measurements of SAXS from the AF1410 steel will be described. ASAXS experiments were conducted at several photon energies (wavelengths) near the chromium K absorption edge to accentuate the scattering from precipitates enriched in chromium. An additional set of ASAXS experiments were conducted near the iron K absorption edge to accentuate the scattering from iron-deficient precipitates.

4.3.1 ASAXS Analyses

The matrix of AF1410 steel is deficient in chromium and enriched in iron so that any ASAXS variation in intensity at photon energies near the chromium and iron K edges will expose scatterers enriched in chromium and/or deficient in iron. To examine the samples for any ASAXS due to Cr-enriched scatterers, three photon energies near the chromium edge of 5989 eV were chosen: 5789, 5949, and 5974 eV. Testing for Fe-deficiency in the scatterers, three photon energies near the iron edge of 7112 eV were chosen: 6912, 7072, and 7097 eV. For the experiments above 5989 eV, it was known that the 2.1% (weight) Cr in the alloy would fluoresce but that radiation is at the wrong photon energy to be conducted by the DCD analyzer optics at the angles used to measure the SAXS. Experimental results from the DCD, using a variety of samples and photon energies as reported in this dissertation, show that the SAXS intensity measured using the DCD is background limited. In general for the collimation-corrected SAXS from AF1410 steel, the background intercepted the SAXS at about $h \sim 0.1$ to 0.15 nm^{-1} which corresponds to a minimum visible dimension of 40 to 60 nm. Thus the visible range of dimensions in this data does not include any of the 2 - 5 nm population of M_2C reported by Allen[1] from SANS data using samples prepared identically to the present experiment. The source of this experimental background is most likely due to parasitic scattering of the transmitted beam by the 285 mm intervening air-path between the sample and the detector required for the double-crystal analyzer.

If Cr fluorescence were to be a problem, the experimental background would be higher in the Fe-edge experiments than the Cr-edge experiments. No such increase was observed, consistent with the conclusion that the DCD optics reject the lower energy photons. The SAXS observed at 7097 eV, 15 eV below the Fe K absorption edge, had the poorest ratio of signal-to-noise (S/N), as may be observed in the plots of SAXS located in the appendix. In fact, the distributions determined by the maximum entropy analyses were discarded for all samples at this energy due to poor information content, characterized by bad fitting of intensities using the maximum entropy method.

In general, S/N in the raw data was ≤ 10 before collimation-correction, as shown in Fig. 4.29. There was no detectable change with photon energy in the desmeared $d\Sigma/d\Omega(h)$ for any of the samples, indicative of no ASAXS. The lack of both Cr- and Fe-ASAXS strongly indicates that the visible scatterers observed are neither enriched in chromium nor are they deficient in iron although the latter is not as well supported by the low S/N data near the Fe K edge.

The SAXS data from a single sample measured at several different photon energies reveal no difference in the profile of $d\Sigma/d\Omega(h)$ as a function of energy within the scatter of the data and the reported errors. Therefore, the distributions derived from a maximum entropy analysis of each SAXS curve from a single sample at different photon energies were averaged together and systematic errors in the data reduction and analysis procedure were estimated from the standard deviation of the average. In general, useful SAXS data for the angular range 0.01 h 0.15 nm^{-1} corresponding to visible dimensions of 40 to 300 nm were available from all the photon energies except 7097 eV. At early aging times, lenticular M_3C (cementite) has been observed in the TEM. At longer aging times, spheroidal M_6C, $M_{23}C_6$, and austenite have been observed in addition to cementite. Calculations of the AF1410 steel thermodynamics at 510° C by Haidemenopoulos[51] using ThermoCalc™ show that the equilibrium volume fractions of M_6C, $M_{23}C_6$, and austenite are 0.021%, 2.5%, and 16.7% respectively. The X-ray scattering contrast of M_6C is about on par with that of austenite. Combined with its low equilibrium volume fraction, the M_6C is undetectable to SAXS because of its low scattering strength.

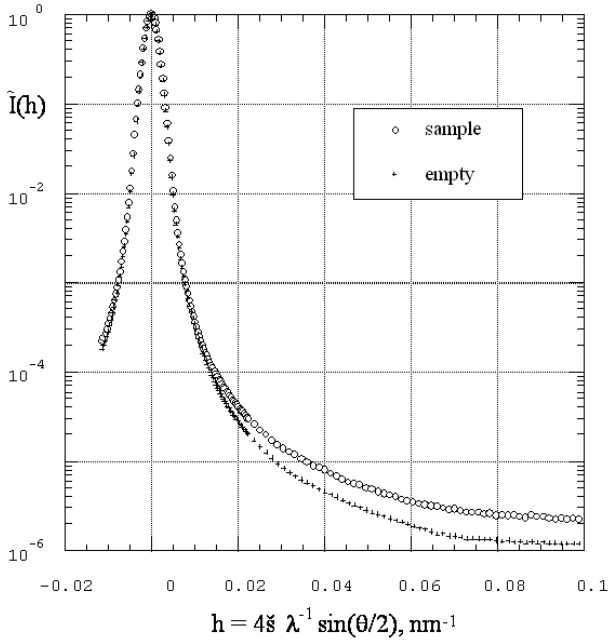

Figure 4.29: Raw data showing the low signal-to-noise ratio typical for the SAXS (difference between the two curves) from the AF1410 steel samples. This particular sample was austenitized at 1000° C for 1 hour (oil quench) and then aged at 510° C for 5 hours (water quench). The photon energy is 5789 eV. Statistical uncertainties for each intensity are smaller than the plotting symbols.

Table 4.10: Compositions of cementite at para-equilibrium and 510° C ortho-equilibrium.

para-equilibrium M_3C
$(Cr_{.0229}\ Fe_{.7350}\ Co_{.1372}\ Ni_{.0988}\ Mo_{.0061})_3C$
(no partitioning of the metal substitutional elements)

ortho-equilibrium M_3C (510° C)
$(Cr_{.7011}\ Fe_{.1878}\ Co_{.0168}\ Ni_{.0845}\ Mo_{.0098})_3C$
(complete partitioning of the metal substitutional elements)

$M_{23}C_6$ is Cr-rich and the lack of detectable ASAXS indicates that no $M_{23}C_6$ precipitates were observed.

The calculated volume fraction of cementite in equilibrium with ferrite in AF1410 at 510° C is 2.27%, calculated by Ghosh (private communication, 1990) using ThermoCalc™. At the earliest stages of cementite formation, assuming that the formation is carbon-diffusion controlled, it is reasonable to assume that the metal site fraction will be that of the matrix. Compositions of these two equilibrium conditions are given Table 4.10. A direct consequence of the para-equilibrium composition (no partitioning of the metal substitutional elements) is that the X-ray scattering contrast is due only to the difference in the carbon concentration from the matrix making the para-equilibrium M_3C invisible to the SAXS experiment. However, any change in the metal site fraction from para-equilibrium will produce a significant increase in the contrast, to the range of 10^{28} – 10^{29} m^{-4}. To consider the possibility of the measured scattering at the earliest aging times coming from cementite, it is assumed that M_3C is not exactly at the para-equilibrium composition. The ortho-equilibrium cementite (complete partitioning of the metal substitutional elements) is highly enriched in chromium which would be exposed by a significant Cr-ASAXS effect. Because no Cr-ASAXS was observed, it is believed that the cementite is not close to the ortho-equilibrium composition. Haidemenopoulos reports that there is a significant variation from particle-to-particle in the compositions of both the M_3C and the austenite in AF1410, measured by STEM microanalysis. Such variations lead to a loss of precision in calculations of the contrasts of the various scatterers.

In the following presentation, the SAXS results will

be separated into two sections. The first section will describe results from the samples austenitized at the temperature predicted by ThermoCalc™ (1000° C) as necessary to dissolve all carbides. The second section describes the scattering from samples austenitized at the standard temperature of 830° C. In either case, the samples were austenitized for one hour and then quenched in oil to room temperature. The samples were then aged at 510° C for the specified time and then quenched in water to room temperature. A full description of these procedures is given elsewhere.[99] The damped-spheres shape function described earlier was used in the maximum entropy analysis of the scattering to determine sphere-equivalent distributions. All SAXS curves were analyzed over the range $0.01 \leq h \leq 0.4$ nm^{-1} by the program `MaxSAS.FOR`, where the higher limit allowed the program to make a good determination of the experimental background.

Continuous curvature was observed in the SAXS data when plotted as $\log(d\Sigma/d\Omega)$ vs. h^2 indicating that the underlying distribution of scatterers is too broad for a Guinier relationship to be established within the experimental range of scattering vectors. Low S/N, ≤ 10, casts significant uncertainty on the results of any Porod analysis, $h^4 d\Sigma/d\Omega$ vs. h^4. Therefore, only the maximum entropy analysis of the data will be presented. The margin of error in the maximum entropy distributions is always greatest at the lower dimensions where the information content is derived from, generally, the lowest intensities in the experiment at the highest scattering vectors.

4.3.2 Austenitized at 1000° C

The scattering from nine samples of AF1410 steel austenitized one hour at 1000° C was measured at photon energies near the Cr K absorption edge. Each sample was aged at 510° C for either: 1/4, 1/2, 1, 2, 5, 8, 10, 50, or 100 hours. Additionally, the SAXS from three of these samples (1/4, 5, and 10 hours aged) were measured near the Fe K edge. All of the SAXS curves are reported in the appendix, including the intensity calculated from the maximum entropy scattering strength distribution. As mentioned before, the data from the experiment closest to the iron K edge were discarded due to poor information content. Because no ASAXS was observed, the size distributions at different photon energies for a single sample were averaged. These averaged maximum entropy scattering strength distributions are shown in Fig. 4.30 for all nine samples, including the estimated margin of error plotted as vertical bars. Indicated on the left of each distribution is the number of SAXS experiments contributing to the average. For two samples, 2 and 8 hours aging, SAXS data were recorded at only one photon energy. Because it was not possible to estimate a margin of error in their distributions, those distributions are not shown. The estimated margin of error was taken as the standard deviation of the average of several distributions from the same sample. The vertical scale of each plot is the same.

The sample thicknesses were determined from multiple photon energy transmission measurements, the same method as used in the analysis of the SAXS from the Modified Fe9Cr1Mo steel. The SAXS results may be categorized into three regions of aging time as follows: 1) between 1/4 and one hour, the size and scattering strength remain constant; 2) between 1 and 5 hours, the size remains roughly constant but the scattering strength increases; 3) from 5 to 100 hours, nucleation and growth of a second population is observed. This distribution dominates the scattering at the longest aging times. Presumably, the population at the shortest aging times is the M_3C, where the breadth of the distributions is due to systematic errors in modeling the particle shape. Starting with 1 - 5 hours aging, the distributions grow taller and slightly more narrow as the second population (presumably precipitated austenite) appears to be undergoing nucleation and growth.

In Fig. 4.31, the total scattering strength observed in the SAXS experiments,

$$\begin{aligned} X &= \int_0^\infty x(D)dD \qquad (4.3) \\ &= \left(|\Delta\rho|^2 V_f\right)_{\mathbf{M_2C}} \\ &\quad + \left(|\Delta\rho|^2 V_f\right)_{\text{austenite}} \\ &\quad + \left(|\Delta\rho|^2 V_f\right)_{\ldots} \end{aligned}$$

as measured from the averaged maximum entropy scattering strength distributions, $x(D)$, is reported as a function of aging time. Between 1/4 and 1/2 hours, the scattering strength drops corresponding to a slight decrease in the volume fraction of cementite. The higher scattering strength at 1 hour could be due to an increase in

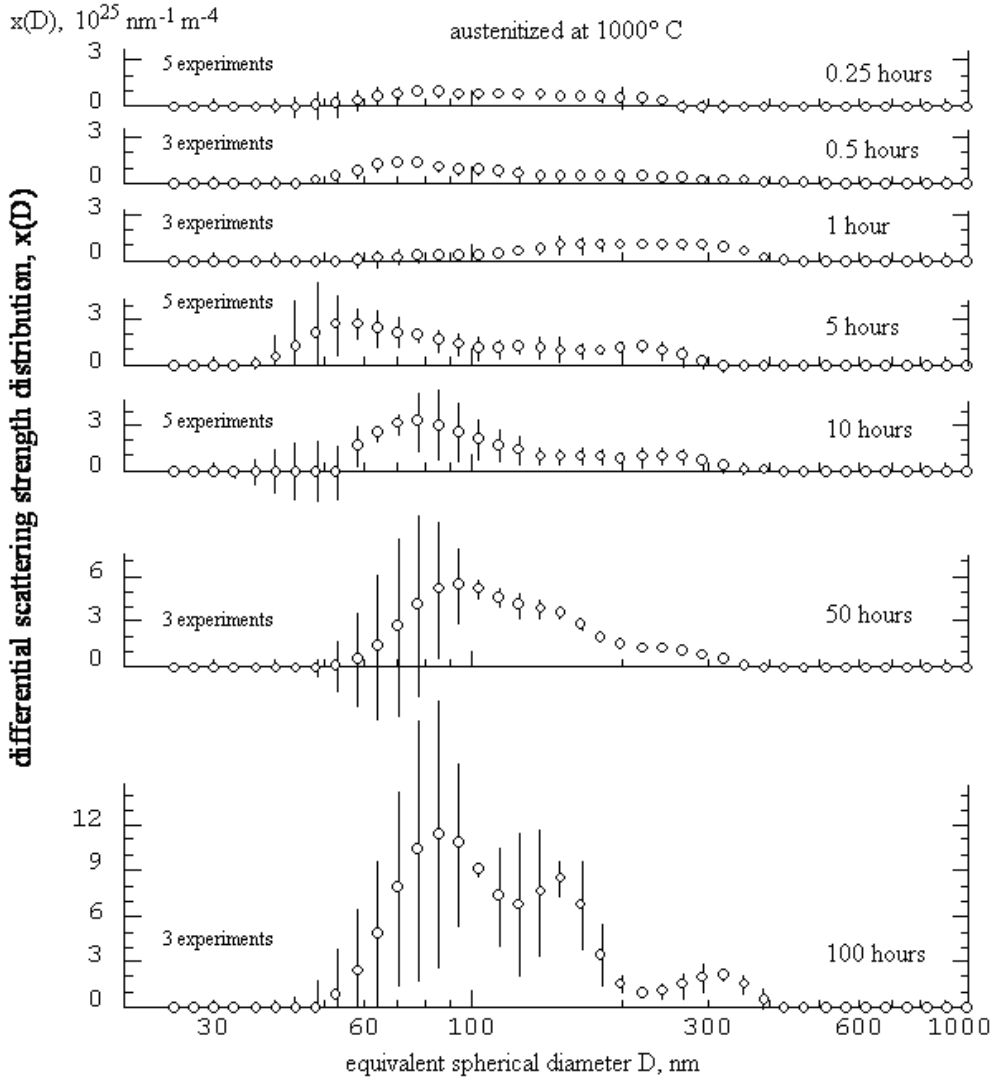

Figure 4.30: Scattering strength weighted distributions of sphere-equivalent scatterers in AF1410 steel samples austenitized at 1000°C as a function of the isothermal (510° C) aging time. The vertical bars indicate the margin of error estimated by averaging several SAXS experiments.

Table 4.11: Summary of maximum entropy distributions for AF1410 austenitized at 1000° C.

aging time, hr	$\bar{D}_x$, nm	$\sigma(\bar{D}_x)$, nm	$\bar{V}_x$, μm^3	$\sigma(\bar{V}_x)$, μm^3
0.25	144	54	0.00222	0.00218
0.5	178	103	0.0064	0.0101
1	237	82	0.00954	0.00842
2	255	171	0.0226	0.0363
5	141	72	0.00269	0.0323
8	190	112	0.0079	0.0125
10	158	82	0.00393	0.00539
50	153	67	0.00309	0.00427
100	160	85	0.00403	0.00686

the scattering contrast of cementite as its composition moves closer towards ortho-equilibrium. Using X-ray diffraction, Montgomery[99] estimated the volume fraction of cementite and showed it to decrease for aging times greater than a few hours. Additionally, the volume fraction of austenite was also measured (private communication, 1990) and shown to increase with aging time. This increase in the austenite volume fraction is consistent with the observed maximum entropy scattering strength distributions.

The total scattering strength observed as a function of aging time can be modeled as the sum of the scattering strengths from two separate distributions,

$$\begin{aligned} X(t) &= x_\theta(t) + x_\gamma(t) \\ &= \left[|\Delta\rho|^2 V_f\right]_\theta + \left[|\Delta\rho|^2 V_f\right]_\gamma \end{aligned} \tag{4.4}$$

where θ indicates cementite and γ indicates austenite and the scattering contrast of each phase is assumed to be independent of aging time. Using the volume fractions of Montgomery, listed in Table 4.12, the total scattering strength as a function of aging time at 510° C observed by SAXS was reproduced by assuming a scattering contrast of $1.2\pm0.3\times10^{29}$ m^{-4} for M_3C and $1.5\pm0.3\times10^{29}$ m^{-4} for austenite. These calculated scattering strengths are plotted as the thick line in Fig. 4.31. The numerical precision of the best-fit scattering contrasts could easily mask time-dependencies in the composition of either precipitate, assuming that the initial composition of cementite is not at para- or ortho-equilibrium. Montgomery also has measured the volume fraction of austenite and estimated that of cementite by X-ray diffraction. These values have

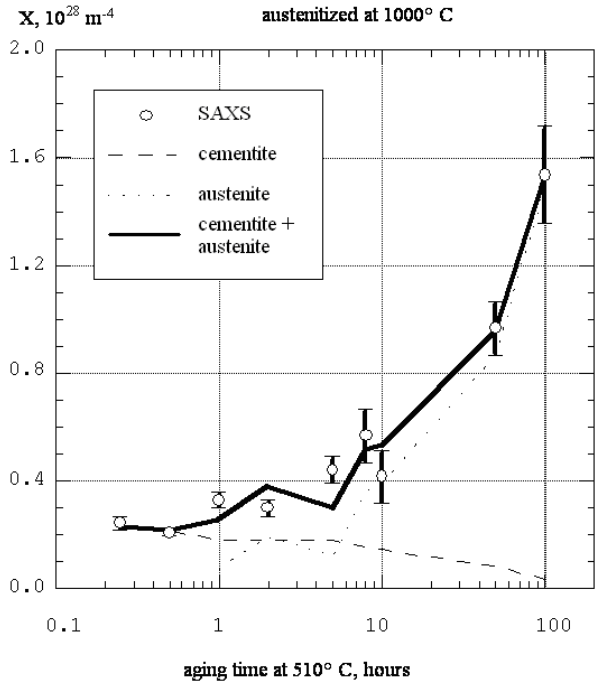

Figure 4.31: Total scattering strength from distributions of scatterers in AF1410 steel austenitized at 1000° C as a function of the isothermal (510° C) aging time. The margins of error in the determinations are indicated. The solid curve is calculated from volume fractions measured by Montgomery.

Table 4.12: Volume fraction of precipitates in AF1410 steel austenitized at 1000° C determined by X-ray diffraction by Montgomery. Samples were aged at 510° C for the time specified.

aging time, hr	Vf, M_3C	Vf, austenite
0.25	$.019 \pm .005$	
0.5	$.018 \pm .002$	
1	$.015 \pm .002$	$.005 \pm .003$
2	$.015 \pm .0025$	$.013 \pm .003$
5	$.015 \pm .0025$	$.008 \pm .003$
8	$.013 \pm .002$	$.024 \pm .003$
10	$.012 \pm .002$	$.026 \pm .003$
50	$.007 \pm .002$	$.058 \pm .003$
100	$.003 \pm .001$	$.100 \pm .003$

been combined with the X-ray scattering strengths determined from the SAXS scattering strength distributions to set limits on the range of probable metal site fractions for the observed scatterers, assumed to be either M_3C or austenite in the analysis below.

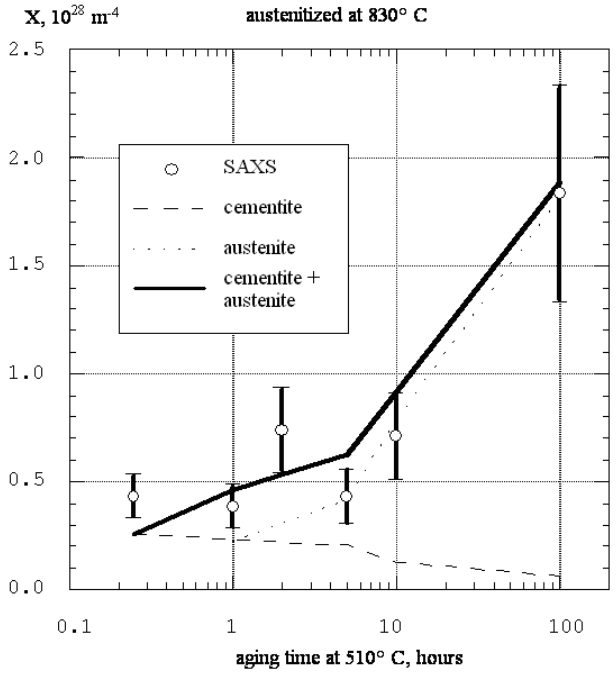

Figure 4.33: Total scattering strength from distributions of scatterers in AF1410 steel austenitized at 830° C as a function of the isothermal (510° C) aging time. The margins of error in the determinations are indicated. The solid curve is calculated from volume fractions measured by Montgomery.

4.3.3 Austenitized at 830° C

The scattering from six samples of AF1410 steel austenitized one hour at 830° C was measured at photon energies near the Cr K absorption edge. Each sample was aged at 510° C for either: 1/4, 1, 2, 5, 10, or 100 hours. All of the SAXS curves are reported in the appendix, including the intensity calculated from the maximum entropy distribution. As with the sample austenitized at 1000° C, because no ASAXS was observed and so the size distributions at different photon energies for a single sample were averaged. The total scattering strengths observed are higher by about 30for the samples austenitized at 830° C than those from the 1000° C temperature.

As with the 1000° C series, the SAXS results may be categorized into three regions of aging time as follows: 1) between 1/4 and one hour, the size decreases slightly and the scattering strength remains constant; 2) between 1 and 5 hours, the size remains roughly constant but the scattering strength increases; 3) from 5 to 100 hours, a second population appears at lowest dimensions and is observed to nucleate and grow. The two distributions are presumed to be cementite and austenite, with assumed scattering contrasts of $1.3 \pm 0.5 \times 10^{29}$ m^{-4} and $1.4 \pm 0.3 \times 10^{29}$ m^{-4}, respectively. The maximum entropy distributions are plotted in Fig. 4.32. Indicated at the left of each distribution is the number of SAXS experiments contributing.

4.3.4 Discussion

The results from the SAXS analyses are very similar for the 830° C series and the 1000° C series. The total scattering strength of the 830° C series samples is about 30% higher than that from the 1000°series an increase which is easily accounted for by the volume fraction measurements of Montgomery. Differences in the assumed scattering contrasts between samples for cementite and austenite are

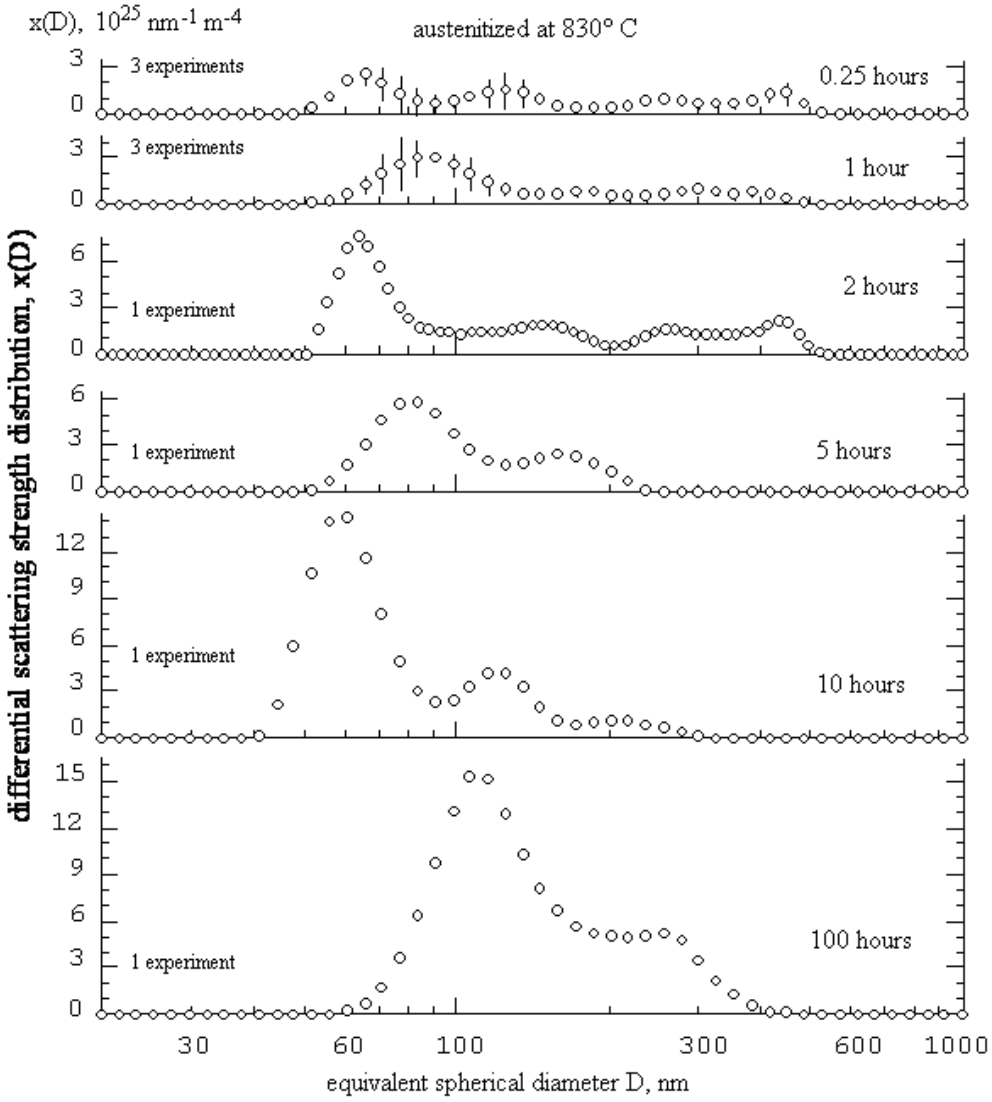

Figure 4.32: Scattering strength weighted distributions of sphere-equivalent scatterers in AF1410 steel samples austenitized at 830°C as a function of the isothermal (510° C) aging time. The vertical bars indicate the margin of error estimated by averaging several SAXS experiments.

Table 4.13: Summary of maximum entropy distributions for AF1410 austenitized at 830° C.

aging time, hr	$\bar{D}_x$, nm	$\sigma(\bar{D}_x)$, nm	$\bar{V}_x$, μm^3	$\sigma(\bar{V}_x)$, μm^3
0.25	274	144	0.0196	0.0203
1	220	124	0.0113	0.0141
2	254	145	0.0171	0.019
5	123	46	0.0014	0.00146
10	106	58	0.0013	0.0023
100	181	78	0.005	0.00625

Table 4.14: Volume fraction of precipitates in AF1410 steel austenitized at 830° C determined by X-ray diffraction by Montgomery. Samples were aged at 510° C for the time specified.

aging time, hr	Vf, M_3C	Vf, austenite
0.25	$.020 \pm .005$	
1	$.018 \pm .002$	$.016 \pm .003$
2	$.017 \pm .003$	$.022 \pm .003$
5	$.016 \pm .002$	$.030 \pm .003$
10	$.010 \pm .003$	$.056 \pm .003$
100	$.005 \pm .001$	$.130 \pm .003$

within the precision of the measurement, precluding an observation of any time-dependent behavior. A prediction of the composition of cementite and of austenite that will produce a scattering contrast equivalent to that observed is beyond the limit of precision in the current measurement. To illustrate, the scattering contrast for cementite will be calculated as a function of the composition of the metal sites in the unit cell. In Table 4.15, the structural information necessary to calculate the X-ray scattering contrast is given. The lattice parameters have been supplied by Montgomery.

As postulated above, if the formation of cementite is controlled by the rate of carbon-diffusion, then the initial composition of cementite should be that of para-equilibrium which is iron-rich and chromium deficient. The ortho-equilibrium composition calculated by ThermoCalc™ is chromium-rich and iron-deficient. By considering that the cementite follows a linear composition trajectory during the course of aging at 510°C between the para-equilibrium and ortho-equilibrium compositions, the X-ray scattering contrast of cementite was calculated and is shown in Fig. 4.34 using the photon energies for the SAXS experiments. The two highest photon energies correspond to Fe-ASAXS while the lower three would expose Cr-ASAXS effects. In addition to data from Table 4.15, the contrast calculations required anomalous dispersion corrections for all elements present. These were calculated by the method of Cromer and Liberman[21] except for that of chromium which was calculated from X-ray transmission measurements from a sample of Modified Fe9Cr1Mo steel. Also indicated on that plot is the contrast assumed for cementite from the present SAXS data in concert with the estimated cementite volume fractions of Montgomery.

Strong Fe-ASAXS effects are observed throughout the range of compositions while Cr-ASAXS effects only become important above ∼10% on the abscissa, corresponding to a chromium site fraction of ∼0.10. In the present experiment, neither strong Cr-ASAXS nor strong Fe-ASAXS effects were observed, suggesting that the composition of cementite is not represented on Fig. 4.34. While the limit imposed by the lack of Cr-ASAXS is not likely to change appreciably, nothing else may be said about the composition of the metal sites.

The present set of experiments describe useful information about the limits of the ASAXS technique. The minimum detectable limit of total scattering strength should be greater than $3 \sim 5 \times 10^{27}$ m^{-4} while the change produced by ASAXS should be no less than 30scattering strength. With S/N $\sim$ 3, the average total scattering strength of $3 \sim 5 \times 10^{27}$ m^{-4} in these experiments is at the threshold of the measurement. Any total scattering strength less than $\sim 10^{27}$ m^{-4} can be termed a weak scatterer.

Table 4.15: Crystallographic structure information used in calculating the scattering contrast for the precipitates in AF1410 steel. Pearson and Strukturbericht structure numbers are from Barrett.[3] Lattice parameters after Montgomery (private communication, 1990).

	matrix	austenite	M_3C
structure	cI2, A2	cF4, A1	oP16, DO_{11}
metal sites in unit cell	2	4	12
carbon sites in unit cell	6	4	4
experimental lattice parameter	$a_o = 287$ pm	$a_o = 360$ pm	$a_o = 509$ pm $b_o = 674$ pm $c_o = 452$ pm

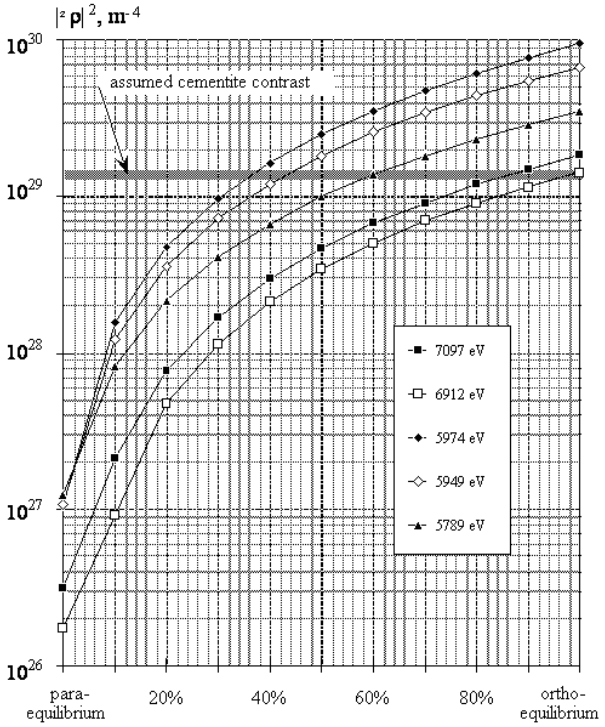

Figure 4.34: X-ray scattering contrast calculated for cementite in AF1410 steel as the metal site fraction progresses linearly from para-equilibrium to ortho-equilibrium. The photon energies used to test for ASAXS are indicated.

4.3.5 Summary of the AF1410 SAXS analysis

The observed small-angle scattering intercepted the background at a scattering vector of ca. 0.15 nm^{-1} and was too high to permit measurement of the SAXS from the M2C population observed by Allen. Within the experimental range of scattering vectors $0.01 \leq h \leq 0.15$ nm^{-1}, no variations in SAXS were observed as the incident photon energy was changed near either the chromium or iron K edges. This lack of Cr-ASAXS and lack of Fe-ASAXS indicates that the visible scatterers of dimensions between 40 and 300 nm in AF1410 steel are neither enriched in chromium nor are they deficient in iron. The observed SAXS is very weak with a signal-to-noise ratio ≤ 10. Only for samples aged the longest time, 100 hours at 510° C, does the total scattering strength rise above 10^{28} m^{-4}. Using volume fractions measured by Montgomery, it is possible to account for all of the total scattering strength by considering a two-component model of cementite and austenite populations. The breadths of the cementite distributions are most probably due to systematic errors in modeling the scattering from the lenticular particle shape by a spherical form factor. The SAXS results for samples austenitized at either 830°or 1000° C are principally the same although the total scattering strength of the 830°series was the higher by about 30%.

Chapter 5

Summary

The double-crystal diffractometer SAXS camera [1] developed for this work seems to be a very good instrument. It is capable of recording the small-angle scattering from a wide variety of materials. Additionally, absolute intensity scaling parameters have been shown to be available directly from the SAXS experiment. Correction of the recorded SAXS curves for the effects of slit-length collimation smearing is possible using the technique of Lake,[81] although the scatter in the data appears to be increased by this step. The versatility of the DCD as well as the desmearing process have been demonstrated on a variety of samples. Additionally, utilization of Ge optics and an asymmetrically-cut first monochromator crystal has improved the quality of data from the instrument without compromising resolution. The improvements were gained by optimizing the design of the optics for the synchrotron radiation source. The silicon photodiode X-ray detector proved to be an integral component of the scattering experiment. Its use obviated the need for separate transmission measurements and calibration runs as the parameters for each of these are available during the regular course of the SAXS experiment. The photodiode detector demonstrated a significant improvement in data collection capability and efficiency over that of a scintillation counter; *i.e.* faster data collection, lower noise, higher incident count rate, and no damage due to high intensities.

SAXS from samples of polystyrene spheres were used to demonstrate the quality of the data reduction procedure. Good agreement was found between the desmeared intensity and a direct calculation of the scattered intensity from a model Gaussian size distribution. The shallowness of the valleys observed between the secondary maxima in the SAXS data are most probably due to (in order of decreasing importance) polydispersity of a few percent, multiple scattering, and asphericity. These data were also used to demonstrate that slit-width smearing in the SAXS data taken with the DCD is negligible.

A primary method for converting the data to units of absolute intensity was given using parameters measured during the normal course of the SAXS experiment. Comparison tests of this methods were performed in two other laboratories. In both cases, the excellent agreement validated the procedures described here.

A recipé for a chemical thinning solution was given that allows reproducible preparation of steel samples of less than 20 μm thickness over areas as large as 100 mm^2 without mechanical deformation. This solution is good for the preparation of steel samples for SAXS as well as pre-thinning steel samples for TEM measurements to minimize magnetic effects. Thicknesses of these samples were determined by multiple photon energy transmission measurements to a precision of 0.3 μm on an average SAXS sample thickness of 24 μm. X-ray transmission radiography was used to check the uniformity of sample thickness and to avoid any pinholes within the illuminated area for the SAXS experiments. Anomalous dispersion corrections for chromium were determined from a sample of Modified Fe9Cr1Mo steel in the normalized and tempered condition by transmission measurements and the Kramers-Kronig integral. The values calculated agreed with a theoretical calculation of the dispersion corrections

[1] Double-crystal diffractometer SAXS cameras of the Bonse-Hart design are now also known as USAXS - Ultra-Small-Angle X-ray Scattering.

to a precision of ± 0.2 electron units.

Small-angle X-ray scattering was measured at three photon energies near the chromium K absorption edge at 5989 eV from six different samples of Modified Fe9Cr1Mo steel, aged for 5000 hours at different temperatures ranging from room temperature up to 704° C. The scattering was modeled by a distribution of spheres giving scattering equivalent to that observed by use of the maximum entropy method. The sphere-equivalent, maximum entropy size distributions were shown to be in agreement with TEM observations.

The ASAXS contrast variation technique was used to isolate the volume-fraction size distribution of $Cr_{23}C_6$ from the total measured size distribution of scatterers in this engineering alloy, Modified Fe9Cr1Mo steel. Those distributions are found to remain constant for 5000 hour aging between room temperature and 482° C. For isothermal 5000 hour aging at temperatures between 482° and 649°, the volume fraction of chromium carbide increases, while for the sample aged at 704°, the volume fraction was slightly larger than the N&T sample. The volume fractions determined were found to be in agreement with those reported by Maziasz of the Oak Ridge National Laboratory. To support the volume fractions measured, it was rationalized that some of the carbon lattice sites in the $Cr_{23}C_6$ could be occupied by nitrogen as in $Cr_{23}(C_x,N_{1-x})_6$ although the partitioning between C and N cannot be determined from the SAXS data. The results from the ASAXS analysis are consistent with an explanation that the chromium carbide population moves towards thermal equilibrium as the aging temperature is raised and that the 649° sample aged for 5000 hours is close to equilibrium.

The total observed change in the mean diameter of $Cr_{23}C_6$ is 50% and increases monotonically with aging temperature while the volume fraction can more than double over the observed range of aging temperatures and is peaked at 649° C. The specific surface area of the $Cr_{23}C_6$ was in general agreement with the SANS data of Kim.[71] The distributions of MX precipitates were not obvious in these small-angle scattering experiments using the double-crystal diffractometer.

In SAXS data recorded from samples of steel alloy AF1410, the observed small-angle scattering intercepted the background at a scattering vector of ca. 0.15 nm^{-1} and was too high to permit measurement of the SAXS from the M_2C population observed by Allen. No variations in SAXS were observed as the incident photon energy was changed near either the chromium or iron K edges, indicating that the visible scatterers of dimensions between 40 and 300 nm are neither Cr-rich nor Fe-deficient. Using volume fractions measured by Montgomery, it was possible to account for all of the total scattering strength by considering a two-component model of cementite and austenite populations. The breadths of the cementite distributions are most probably due to systematic errors in modeling the scattering from the lenticular particle shape by a spherical form factor. The SAXS results for samples austenitized at either 830° or 1000° C for 1 hour are principally the same although the total scattering strength of the 830° series was the higher by about 30%.

Analysis of small-angle scattering data for size distributions via the maximum entropy method[106] appears to yield satisfactory results although improvements to the procedure are possible. The most important of these is to decrease the sensitivity of the procedure to strong gradients in the particle form factor. These gradients are believed to cause spurious oscillations in the derived distributions that suggest a greater information content in the scattering data than is extant. Modification of the particle form factors by a weighted smoothing process confirms this suspicion and improves the perceived quality of the answer obtained without degrading algorithm performance.

The technique of anomalous small-angle X-ray scattering has been successfully applied to the problem of isolating the size distribution of a single type of scatterer in a multi-component alloy. The volume fraction size distribution was isolated using a contrast gradient method. From the volume fraction size distribution, the mean diameter, volume fraction, number density, and particle surface surface-to-volume ratio were been calculated. Results from other analytical methods, such as atom probe field ion microscopy, transmission electron microscopy, X-ray energy dispersive spectroscopy, and small-angle neutron scattering, provided information necessary to the interpretation of the ASAXS data.

5.1 Suggestions for Future Work

The SAXS data recorded using the double-crystal diffractometer camera and silicon photodiode detector is limited by a high experimental background. Presumably, the source of this background is scattering of the transmitted beam by the 285 mm air path intervening between the sample and the detector required for the motions of the DCD analyzer. Reduction of this distance is not possible. As a major modification of the experimental arrangement, it is suggested to build an environmental chamber to contain virtually all of the DCD camera equipment currently place in the experimental hutch. Such a modification is not trivial as all of the motions provided by the two sets of hutch mechanical arms would need to be provided within the confines of the chamber. However, the use of such a chamber with just above one atmosphere of helium gas would reduce the air scattering as well as absorption of the scattered intensity. The advantage to be gained from this modification is the measure of scatterer of dimensions less than ~ 40 nm in the weakly-scattering steel samples. Examples of these scatterers are the MX in Modified Fe9Cr1Mo or M2C in AF1410.

There is still room for several improvements to the photodiode detector system as it has been built. By incorporating phase-detection, synchronized to the pulses of the synchrotron radiation, uncorrelated sources of noise could be eliminated which would then reduce the background and indirectly increase the highest scattering vector in the SAXS experiment. Either a log-ranging amplifier or an auto-ranging feedback circuit would allow the detector to operate unattended.

Because the expected SAXS from the steel samples at scattering $h \geq .15$ nm^{-1} was masked by the experimental background, it would be useful to measure the SAXS on another camera which operates in helium or vacuum so that the background is not a problem. Both ORNL and NIST have pinhole cameras equipped with an area detector at a distance of a few meters from the sample. The X-ray generator for each of these is a rotating anode. For these experiments, it is necessary to use a chromium anode as even an iron anode would fluoresce the 9% Cr in the Modified Fe9Cr1Mo steel.

In order to extract more information from the SAXS data from AF1410 steel, it is necessary to have a reliable measure of the composition of the cementite and austenite as well as the lattice parameters of each for a more precise calculation of the scattering contrasts. Also needed for the interpretation of the SAXS is a particle form factor for the lenticular shape of the cementite as they are not well-characterized as spheres. With this information, it should be possible to extract more precise information about the number density and mean particle size from the existing SAXS data as well as probe for any ASAXS.

Last, but most important, it would be very satisfying to know that the DCD camera developed for this work will continue to be applied to problems in materials science. One obvious application that comes to mind is to perform a primary calibration of a set or sets of secondary standards for use by other small-angle scattering facilities.

Appendix: Other Samples Examined with the Double-Crystal Diffractometer

Two other materials have been examined with the double-crystal diffractometer SAXS camera. The SAXS from each of these materials are distinct and different from each other. The first sample, bulk microporous silica, has been used by others as a secondary calibration standard of absolute intensity. The second material is porous Vycor^{TM}glass, which exhibits strong interference effects indicative of an ordered structure of scattering centers.

A Bulk Microporous Silica

The microstructure of low-density microporous silica precursor (unsintered) bodies was studied as a function of the starting chemistry. The ratio of colloidal silica sol to potassium silicate is known to have a marked effect on the size distribution of pores in this material, which in turn have a major impact on the resultant physical properties of the sintered product.

To study the effect of the starting chemistry, five samples were prepared by the sol gel process with varying ratios of colloidal silica to potassium silicate from 10 to 30% and 5% intervals (i.e., 10:90, 15:85, 20:80, 25:75, and 30:70). Exact details of the sample preparation method are given elsewhere.[84] The gels were dried at 70° to 80° C and then, with no other intermediate steps, sliced into disks. Sample thicknesses were quite uniform across the entire sample and ranged from 660 to 940 μm between samples. Final particle densities of the precursor samples were 14 to 18% of theoretical, with the 10:90 being the most dense and the 30:70 the least dense. The scattering contrast of colloids, with respect to voids, was calculated to be 3.48×10^{30} m^{-4}.

With such a high particle density, the samples may not be adequately dilute to avoid either multiple scattering or interparticle interference. Multiple scattering was manifest in SAXS data recorded using 6 and 7 keV photons, but none was observed at 10 or 11 keV. Because the polydispersity of the scattering system is very large, every major portion of the size distribution is dilute and it is assumed that interparticle interaction potentials are negligible.

SAXS from the 10:90 sample with 10 keV photons, shown in Fig. A1, and repeated with 11 keV show no differences after collimation correction. From this it is concluded that multiple scattering is negligible at these two photon energies. Scattering curves from all five samples are plotted in Fig. A2. These curves have been scaled to absolute intensity and desmeared by the author using methods described in Chapter 3. The superb quality of the data presented demonstrates the integrity of all components of the small-angle X-ray scattering camera and silicon photodiode detector as well as the numerical transformations that reduce the raw data to SAXS curves.

Differences between the SAXS curves are systematic with the sample chemistry where the 10:90 sample shows the most scattering and the 30:70 the least, with data from the other samples falling between. By the absence of regularly-spaced oscillations, the underlying size distributions giving rise to the scattering must be polydisperse. Analysis of the lowest scattering vectors by the Guinier law shows additional results that are systematic with the sample chemistry as shown in Table A1. Further analysis of the SAXS data by the maximum entropy method described above is presented elsewhere.[85] In conclusion, the SANS data have confirmed the absolute intensity scaling method of this dissertation. The SAXS data from bulk mi-

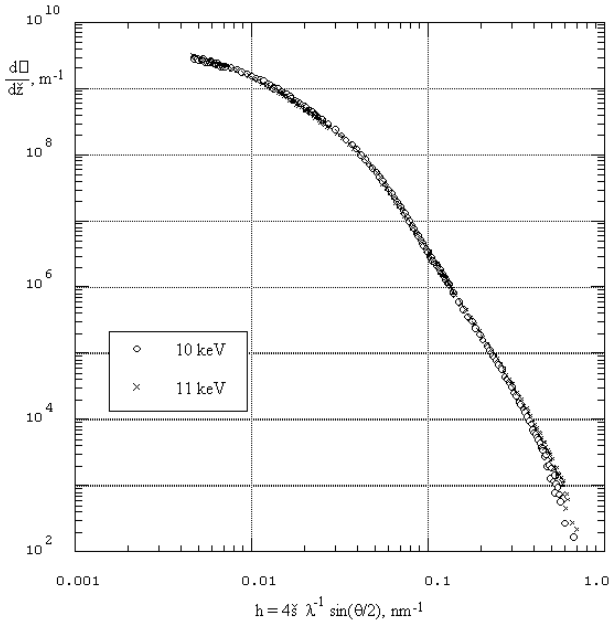

Figure A1: Collimation-corrected SAXS of bulk microporous silica sample with a ratio of colloidal silica to potassium silicate of 10:90 recorded with the double-crystal diffractometer using 10 and 11 keV X-ray photons. Because the two curves are identical, multiple scattering is assumed to be negligible.

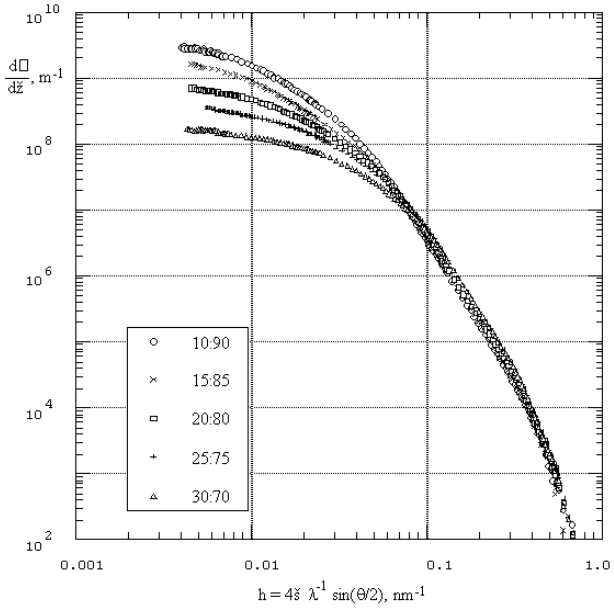

Figure A2: Collimation-corrected SAXS of bulk microporous silica samples with the indicated ratio of colloidal silica to potassium silicate recorded with the double-crystal diffractometer using 10 keV X-ray photons.

Table A1: Sample thickness, SAXS experimental background, and results of Guinier analyses on SAXS from bulk microporous silica samples using 10 keV photons. Scattering vectors $0.007 \leq h \leq 0.015$ nm-1 were included in the analyses.

sample	thickness, μm	background, m^{-1}	Guinier radius, nm
10:90	890	4000	126
15:85	890	3750	122
20:80	660	2950	104
25:75	910	3100	93
30:70	940	3450	75

croporous silica samples, measured on the double-crystal diffractometer, have been observed to be systematic with the starting chemistry of the samples.

B Porous Vycor^{TM} Glass

The small-angle scattering from samples of porous Vycor^{TM} glass is significantly different than that from the steel alloys. The scatterers, pores in this case, fail some of the most basic assumptions used to analyze the scattering in terms of a distribution of scatterers: the pores are not dilute in concentration nor can they be expected to be non-interacting. The pores have been modeled as a bicontinuous distribution with a spinodal structure by Berk.[5] Wiltzius[147] reported small-angle neutron scattering data that displayed an interference peak that was attributed to the bicontinuous distribution. The small-angle scattering from the porous Vycor^{TM} glass is exemplary of type 3 scattering where interference effects are present. The section that follows has been excerpted from Mendoza.[96]

Using the double-crystal diffractometer at the NSLS, SAXS was recorded from four samples of porous Vycor^{TM} glass (PVG) of thickness ca. 50 μm provided by M. Rafailovich of SUNY Stony Brook. The samples were: unconsolidated Vycor^{TM} glass (PVG/nC), unconsolidated Vycor^{TM} glass impregnated with iron oxide (PVG+FeO/nC), consolidated Vycor^{TM} glass impregnated with iron oxide (PVG+FeO/C), and consolidated Vycor^{TM} glass impregnated with tin oxide (PVG+SnO/C). In this context, *consolidation* means heating to 1200° C. The photon energy, 7.031 keV, was chosen to be below the K absorption edge of Fe at 7.112 keV. All four collimation-corrected SAXS curves in Fig. B3 display an interference peak at $h \simeq 0.18$ nm^{-1}, where h is defined as before. Results from three of the samples (PVG/nC, PVG+FeO/nC, and PVG+SnO/C) show similar SAXS with intensity differences which could be mostly attributed to differences in scattering contrast and sample thickness. The peak in the data from the fourth sample, PVG+FeO/C, is much less pronounced. Incidentally, after the ca. one hour exposure to the monochromatic X-ray beam, the VG+Sn/C sample was visibly discolored. The other three samples were not visibly altered after equivalent exposures.

In theory, heating a PVG sample to 1200° C would con-

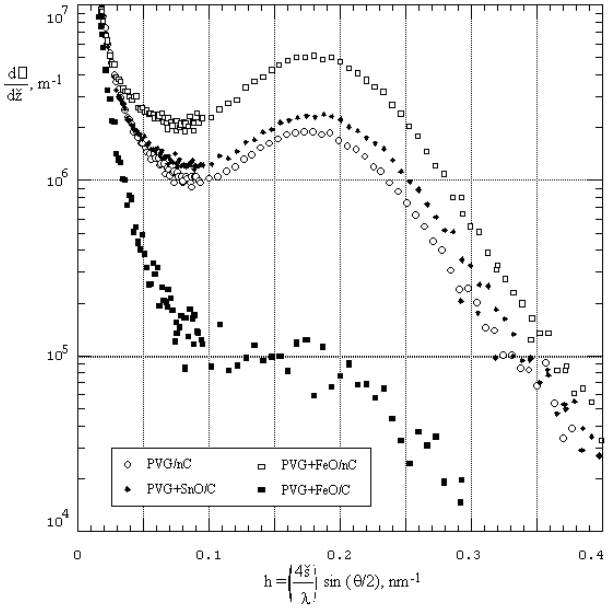

Figure B3: Collimation-corrected SAXS from samples of porous Vycor^{TM} glass measured with the double-crystal diffractometer used at the National Synchrotron Light Source, beam line X23A3. The interference peak at $h \simeq 0.18$ nm^{-1} is due to a bicontinuous network of pores with a spinodal structure. Of the two samples heated at 1200° C (closed symbols), only the one with FeO shows a reduction in the height of the interference peak.

solidate the sample and consequently cause the scattering peak to disappear as the spinodal ordering is lost. This is observed in the PVG+FeO/C sample; the scattering peak is almost entirely eliminated in the SAXS from this sample. The suppression of the peak suggests that the spinodal structural ordering is diminished and the iron oxide becomes a distributed component within the glass matrix.

The presence of the interference peak, and the absence of higher-order peaks, suggests that the sample microstructure can be modeled by a bicontinuous spinodal structure as shown by Berk.[5] The present data are very similar to the small-angle neutron scattering results of Wiltzius mentioned above in which the peak was observed at $h = 0.23$ nm^{-1}.

In both cases, the peaks in the scattering data indicate the presence of a bicontinuous network with a spinodal structure. This structure arises when the original borosilicate melt is cooled below its phase-transition temperature. The boron-oxide / alkali-oxide phase separates and, on acid leaching, yields a microporous network where pore size is determined by the time in which the melt is allowed to decompose. The scattering from this structure in the immediate region of the interference peak is given by Cahn[18] and Wiltzius.[147]

$$I(\bar{h}, \bar{t}) = \frac{I(0,0)}{1+\bar{h}^2} \exp\left[-2\bar{h}^2\bar{t}(\bar{h}^2-1)\right] \qquad \text{(B1)}$$

where $I(0,0)$ is a normalization intensity, $\bar{t}$ is the dimensionless time evolved since the quench, and $\bar{h}$ is the dimensionless scattering vector, defined as

$$\bar{h} = \frac{hl}{2\pi} \qquad \text{(B2)}$$

where h is as defined before and l is the wavelength of composition fluctuations. SAXS data from each sample for the range of scattering vectors $0.1 \leq h \leq 0.25$ nm^{-1} were fit by a least-squares technique. The results are given in Table B2.

SAXS from the PVG+SnO/C sample that was heated at the consolidation temperature of 1200° C is quite different from that of PVG+FeO/C sample. The broad peak at $h = 0.18$ nm^{-1} persists despite the heat treatment. The measured correlation length of $l = 23$ nm is the same as that for unconsolidated PVG, with or without impregnation of iron oxide. Thus the glass impregnated with tin oxide apparently retains its original ordered spinodal structure. This result is further confirmed by Rutherford backscattering.[96]

Table B2: Parameters obtained from least squares fitting of desmeared SAXS data from porous Vycor™ glass to the intensity model of Wiltzius[147] in the scattering vector range $0.1 \leq h \leq 0.25$ nm^{-1}. l is the wavelength of composition fluctuations, $\bar{t}$ is the dimensionless time evolved since the quench, $I(0,0)$ is a normalization intensity, and r is the regression coefficient (goodness-of-fit). The SAXS data were recorded with the double-crystal instrument described earlier.

sample	l, nm	$\bar{t}$	$I(0,0)$, m^{-1}	r
PVG/nC	23.2	3.3	5.25×10^5	0.987
PVG+FeO/nC	22.9	3.7	1.15×10^6	0.986
PVG+FeO/C	26.4	0.7	1.00×10^5	0.90
PVG+SnO/C	22.7	3.3	6.45×10^5	0.989

Appendix: Description of the Silicon Photodiode Detector

In this section will be given the physical details of the modular silicon photodiode X-ray detector system including details of the implementation and exact electrical schematics for the modules as they have been built. At this time, two complete systems have been constructed which are almost identical, differing only in the dark noise of the photodiode itself. As such, one system is held as a backup for the other, should a quick replacement be necessary.

C Implementation of the Silicon Photodiode Detector

The silicon photodiode detector was designed as a modular system that would provide a raw counting rate at TTL voltage levels to standardized electronics. A block diagram for this system is shown in Fig. C1. The modules were organized by specific functions. The detector module converts X-ray flux into a positive DC voltage proportional to that flux which may be measured directly (on a chart recorder or voltmeter) and/or sent to a voltage-frequency converter. The VFC module accepts a positive DC voltage and converts it into a counting rate proportional to the voltage. The output of the VFC is connected to a counter-timer for computer data acquisition. The amplifier sensitivity is user-adjusted by the remote control. The power supply is a commercial unit, typical of those required by personal computers. While the X-ray response is different, such a modular detector system may replace, in function, a detector chain of scintillation counter (or proportional counter), pulse shaper, single-channel analyzer, and corresponding high-voltage supply without modification of other experimental hardware.

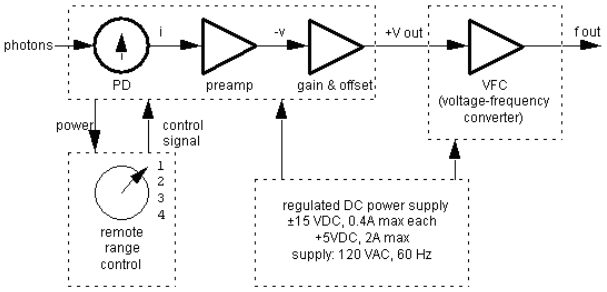

Figure C1: Block diagram for the modular silicon photodiode detector system. Each dashed line corresponds to a separate module. The detector module converts X-rays to a positive voltage which can be measured directly and/or sent to the VFC which generates TTL voltage pulses for standardized electronics. The remote range control allows the user to change the amplification of the preamplifier and draws its power from the power supply via the detector module. The power supply is a commercial unit.

A low-noise UV photodiode (EG&G model UV 215 BQ) was selected as the photodiode. One of the possible substitutions for this component is the Hamamatsu model S1337 - 66BQ. The glass window was removed from the metal case to permit absorption of X rays by the photodiode. The circuit implemented, shown in Fig. C2, was the multiple-scale CV converter electrometer. Four resistors (scales) were used, chosen at two decade intervals. With each scale spanning 3.5 decades, the electrometer spans the required nine decade range while providing a reasonable overlap between each scale for calibration. An ultra-low bias current FET op amp (Burr Brown model OPA 128 LM) was used as the electrometer amplifier. One of the possible substitutions for this component is the Analog Devices model AD-515. The output of the electrometer was inverted using a unity-gain inverting amplifier with a low-pass filter (RC-pair) so that the output of the detector would be between +0.0005 V to +12 V. An offset voltage of ca. 5 mV was added to the output of the inverter to drive the signal positive, a requirement of the voltage-to-frequency (VF) converter appearing later in the circuit. The transfer function for the PD,

$$V_{out} = -\alpha R_{effective} I + V_{offset}, \qquad \text{(C1)}$$

where α is a constant of order unity.

To minimize input capacitance to the amplifier, all connections from the output of the photodiode to the scale resistors and to the electrometer were Teflon™-coated wire, no more than 1 centimeter in length, attached to Teflon™ support posts. The circuit board was coated with a metallized surface layer connected to ground potential to absorb any surface charges.

Special consideration was given to the most sensitive (high feedback resistance) scale of the electrometer due to the 0.6 pA offset current of the electrometer. The voltage generated by this current would result in a large overall negative voltage from the inverter. A relay-selected offset circuit was added to the inverter which overrides the standard offset circuit to drive the output voltage positive. The 99 GΩ glass-encapsulated feedback resistor was wrapped with a few turns of bare wire connected to ground to dissipate any surface charges. Because of the open-circuit capacitance of the relays, no smoothing capacitors were included on either of the two most sensitive scales. This changed the time constant noticeably only for the most sensitive scale.

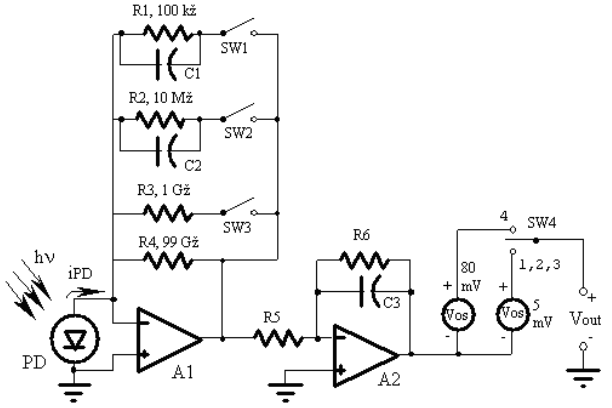

Figure C2: Schematic of the CV electrometer circuit used to measure the photocurrent. Four scales, two decades apart, are employed to span the nine+ decades. A1 converts the photocurrent to a negative voltage according to the scale selected by the switch. A2 inverts that voltage and applies a small offset to drive low voltages positive. A2 also functions as a low-pass noise frequency filter. The voltage output from A2 may be recorded directly or transmitted to a voltage-frequency recorder.

The photodiode is extremely sensitive to visible light so it was necessary to cover its face with two sheets of aluminized Mylar™ and enclose it and the electrometer circuit in a lightproof box. By making the box out of metal, maintained at ground potential, it can serve as an effective Faraday cup to shield the sensitive electrometer circuit from stray electron charges in the environment.

The photodiode and electrometer circuitry were assembled on a 40×75 mm^2 circuit board and mounted in a standard aluminum *blue box* with card slots. The photodiode was placed directly behind a 10 mm diameter hole drilled in one of the cover plates. The hole was covered with two layers of aluminized Mylar™ to reduce visible light leakage into the box, as mentioned above. Controlling circuitry for the TTL relays was assembled on a second circuit board and placed in the same box as the photodiode. Electrical and mechanical connections between the two boards were made by inserting the pins from two eight-pin wire-wrap IC sockets located at opposite ends of the upper (PD) board into similar IC sockets on the lower (TTL) board.

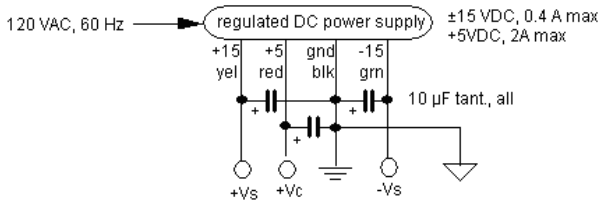

Figure D3: Modifications to the commercial regulated DC power supply which provides power for all components in the modular detector system.

The photodiode detector module generates an output voltage which can be sent to a strip chart recorder and/or to a VFC. The VFC was built in a separate box to minimize heat buildup within the PD housing. In operation, a scale (amplifier sensitivity) is selected by closing a low-leakage TTL reed relay, remotely actuated by a four-position switch. This switch is located on the end of a 20 meter cable for operation from outside of the experimental hutch. It is possible to switch scales without interrupting the experiment such as would have been necessary with an SC or GPC to install or remove an attenuating foil.

Although cooling the photodiode with a thermoelectric refrigerator can reduce its thermal noise, the benefits are exceeded by the penalties in this application. The circuitry necessary to cool the diode is too large to fit in the photodiode enclosure and the refrigerator would require its own power supply. Finally, because the photodiode is operated in air, cooling the photodiode involves the risk of condensing water onto the surface of the photodiode.

D Circuit Diagrams for the Modular Detector

The remainder of this appendix gives the exact circuit diagrams for the modular detector system as it has been built.

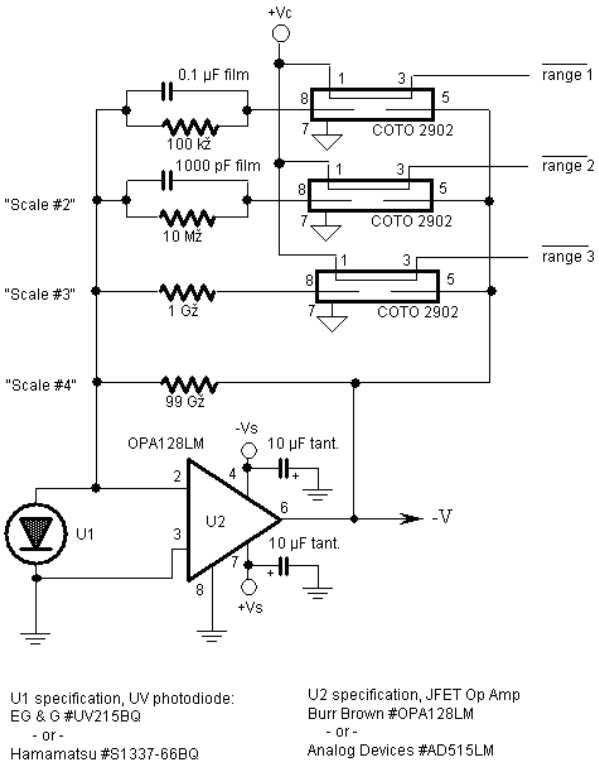

Figure D4: Electronic circuit diagram for the upper (photodiode) board in the PD detector module as built. Four separate amplifier gain scales are used. The low-leakage TTL relays are selected individually by driving the voltage to a logic “0”.

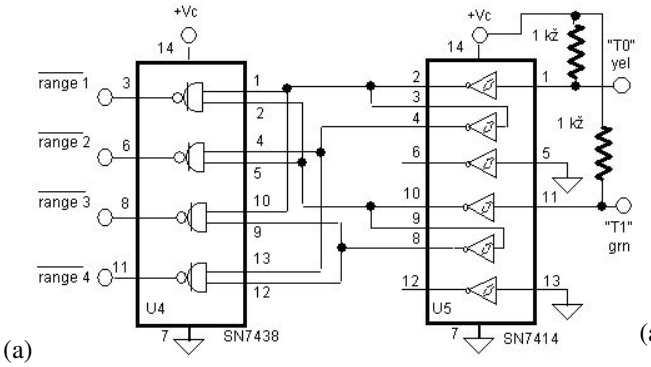

(a)

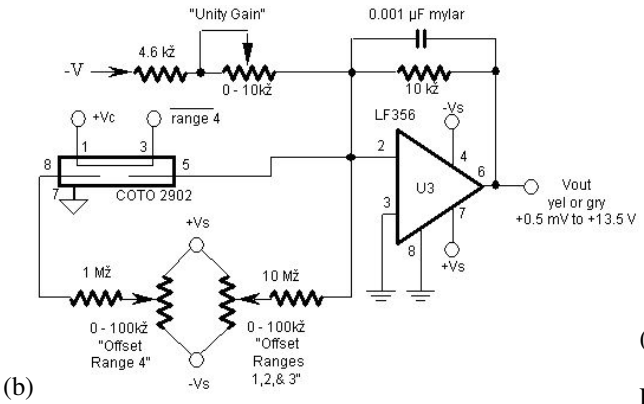

(b)

Figure D5: Electronic circuit diagram for the lower (TTL control) board in the PD detector module as built. In (a), the TTL chips are used as a line buffer and a 1-of-4 decoder. In (b), the unity gain inverter is shown including the details of the special circuitry to offset range #4.

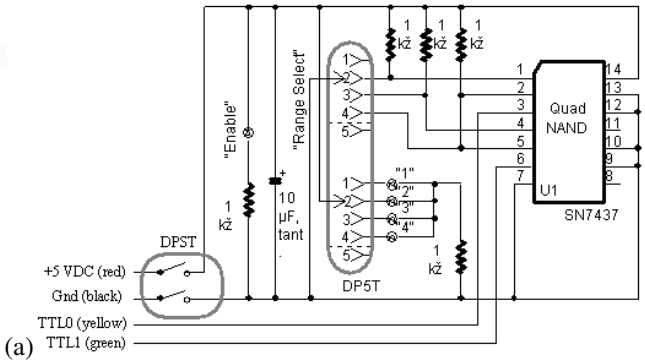

(a)

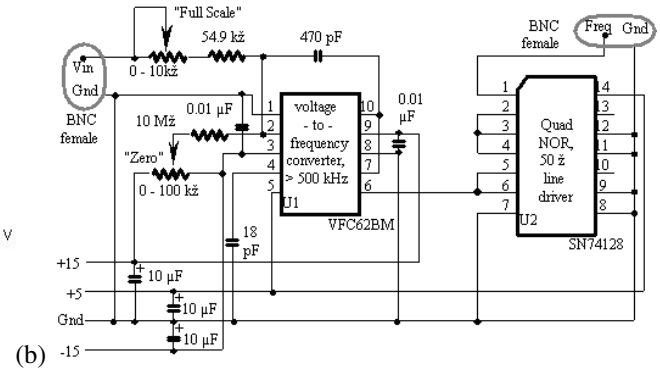

(b)

Figure D6: Electronic circuit diagrams, as-built, for (a) the remote control module, and (b) the voltage-frequency converter. The remote control is used to select the amplifier sensitivity. The output is a two-bit binary TTL signal which value is the range number-1. The VFC is used as an analog-to-digital converter to get the detector signal into the beam line computer.

Appendix: FORTRAN Computer Programs

E `Lake.FOR`: Iterative Collimation-Correction

The following computer program corrects small-angle scattering for slit-length desmearing. Comments are provided to describe the various processes.

```
        PROGRAM Lake
C       Lake.FOR  14 November 1989
C       ref: J.A. Lake; ACTA CRYST 23 (1967) 191-194.
C       by: Pete R. Jemian, Northwestern University

C       Also see: O. Glatter; ACTA CRYST 7 (1974) 147-153
C         W.E. Blass & G.W.Halsey (1981).  "Deconvolution of
C           Absorption Spectra."  New York City: Academic Press
C         P.A. Jansson.  (1984) "Deconvolution with Applications
C           in Spectroscopy."  New York City: Academic Press.
C         G.W.Halsey & W.E. Blass.  "Deconvolution Examples"
C           in "Deconvolution with Applications in Spectroscopy."
C           Ed. P.A. Jansson.  (see above)

C       Compatible with FORTRAN on:
C               DEC VAX
C               Macintosh, Microsoft v2.2
C               Macintosh, Language Syst. v1.2.1 with MPW v. 3.0

C         This program applies the iterative desmearing technique of Lake
C           to small-angle scattering data.  The way that the program works
C           is that the user selects a file of data (x,y,dy) to be desmeared.
C           If a file was not chosen, the program will end.  Otherwise the
C           user is then asked to specify the slit-length (in the units of the
C           x-axis); the X at which to begin fitting the last data points to a
C           power-law of X, the output file name, and the number of iterations
C           to be run.  Then the data file is opened, the data is read, and the
C           data file is closed.  The program begins iterating and shows an
C           indicator of progress on the screen in text format.
C         It is a mistake to run this program on data that has been desmeared
C           at least once (by this program) as you will see.  The problem is
C           that the program expects that the input data has been smeared, NOT
C           partially desmeared.  Lake's technique should be made to iterate
C           with the original, smeared data and subsequent trial solutions
C           of desmeared data.
C         The integration technique used by this program to smear the data
C           is the trapezoid-rule where the step-size is chosen by the
C           spacing of the data points themselves.  A linear
```

```
C           interpolation of the data is performed.  To avoid truncation
C           effects, a power-law extrapolation of the intensity
C           is made for all values beyond the range of available
C           data.  This region is also integrated by the trapezoid
C           rule.  The integration covers the region from l = 0
C           up to l = lo. (see routine SMEAR).
C           This technique allows the slit-length weighting function
C           to be changed without regard to the limits of integration
C           coded into this program.
        IMPLICIT REAL*8 (A-H, O-Z)
        IMPLICIT INTEGER*4 (I-N)
        PARAMETER ( LakeUnit = 1, LakeFast = 2, LakeChi2 = 3)
        PARAMETER ( MaxPts = 500 )      ! also in SMEAR & FindIc
        CHARACTER*1 MTstr
        PARAMETER (MTstr = ' ', iZero=0, fZero = 0.0, InfItr = 10000)
        CHARACTER*80 reply

        COMMON /PrepCm/ sLengt, sFinal, fSlope, fConst, mForm
        COMMON /DatCom/ NumPts, iLo, iHi, h, C, dC
        COMMON /stats/ count, sumX, sumX2, sumY, sumY2, sumXY

        REAL*8  h(MaxPts)
        REAL*8  E(MaxPts),dE(MaxPts)
        REAL*8  S(MaxPts)
        REAL*8  C(MaxPts),dC(MaxPts)
        REAL*8  resid(MaxPts)
C       h       : scattering vector, horizontal axis
C       E, dE   : experimental intensity and estimated error
C       S       : re-smeared intensity
C       C, dC   : corrected intensity and estimated error
C       resid   : normalized residuals, = (E-S)/dE

        CHARACTER*80 InFile, OutFil

C  Next line for Lang. Sys. v1.2.1 / MPW on Macintosh only
C  Comment this out for other compilers
C  This is the only compiler-dependent line in this source code!!!!!!
C       CALL OutWindowScroll (1000)  ! for 1-line advance screen

C Initial default answers to the user parameters
        sLengt = 1.0    ! the slit length as defined by Lake
        sFinal = 1.0    ! to start evaluating the constants for extrapolation
        mForm = 4       ! model final data with a Porod law
        LakeForm = 2    ! shows the fastest convergence most times

    1   WRITE (*,*)
        WRITE (*,*) ' 14 November 1989, Lake.FOR, Pete R. Jemian'
        WRITE (*,*) ' SAS data desmearing using the iterative',
     >                 ' technique of JA Lake.'
        WRITE (*,*) ' J.A. Lake; ACTA CRYST 23 (1967) 191-194.'

        CALL GetInf (InFile, OutFil, sLengt, sFinal,
     >                 NumItr, InfItr, mForm, LakeForm)
        IF (InFile .EQ. MTstr) STOP
        IF (NumItr .EQ. iZero) NumItr = InfItr

        WRITE (*,1000) 'Input', InFile
```

```
 1000   FORMAT (1X, A6, ' file: ', A60)
        CALL GetDat (InFile, h, E, dE, NumPts, MaxPts)
        IF (NumPts .EQ. iZero) GO TO 1
        IF (sFinal .GT. h(NumPts-1)) GO TO 1

        WRITE (*,*) NumPts, ' points were read.'
        WRITE (*,1000) 'Output', OutFil
        WRITE (*,*) ' Slit length = ', sLengt
        WRITE (*,*) ' Final form approx. will begin at ', sFinal
        IF (mForm .EQ. 1) WRITE (*,1001) 'flat background, I(h) = B.'
        IF (mForm .EQ. 2) WRITE (*,1001) 'linear, I(h) = b + h * m.'
        IF (mForm .EQ. 3) WRITE (*,1001) 'power law, I = b * h**m.'
        IF (mForm .EQ. 4) WRITE (*,1001) 'Porod, I*h**4 = Cp+B*h**4.'
 1001   FORMAT (' Final form is ', A40)

        IF (NumItr .GE. InfItr) WRITE (*,*) ' Infinite iterations.'
        IF (NumItr .LT. InfItr) WRITE (*,*) ' iterations =', iterations

        IF (LakeForm .EQ. LakeUnit) WRITE (*,*) ' unit weight'
        IF (LakeForm .EQ. LakeFast) WRITE (*,*) ' fast weight'
        IF (LakeForm .EQ. LakeChi2) WRITE (*,*) ' ChiSqr weight'

C       To start Lake's method, assume that the 0-th approximation
C         of the corrected intensity is the measured intensity.
        DO 3  i = 1, NumPts
          C(i) = E(i)
          dC(i) = dE(i)
    3   CONTINUE

        WRITE (*,*)
        WRITE (*,*) ' Smearing to get first approximation...'
        CALL Smear (S)

        ChiSqr = fZero          ! find the ChiSqr
        DO 8  j = 1, NumPts
    8     ChiSqr = ChiSqr + ((S(j) - E(j))/dE(j))**2
        ChiSq0 = ChiSqr         ! remember the first one

        DO 4, i = 1, NumItr
          WRITE (*,*)
          IF (NumItr .LT. InfItr) THEN
            WRITE (*,*) ' #', i, ' of ', NumItr, ' iteration(s).'
          ELSE
            WRITE (*,*) ' Iteration #', i
          END IF

          WRITE (*,*) ' Applying the iterative correction ...'

          IF (LakeForm .EQ. LakeUnit) weighting = 1.0
          IF (LakeForm .EQ. LakeChi2) weighting = 2*SQRT(ChiSq0/ChiSqr)

          DO 7, j = 1, NumPts
            IF (LakeForm .EQ. LakeFast) weighting = C(j) / S(j)
            C(j) = C(j) + weighting * (E(j) - S(j))
    7     CONTINUE

          WRITE (*,*) ' Examining scatter to calculate the errors...'
```

```
      CALL FixErr (NumPts, h, E, dE, C, dC)

      WRITE (*,*) ' Smearing again... '
      CALL Smear (S)

      ChiSqr = fZero
      DO 5, j = 1, NumPts
        resid(j) = (S(j) - E(j))/dE(j)
        ChiSqr = ChiSqr + resid(j)**2
 5    CONTINUE
      WRITE (*,*) ' Residuals plot for iteration #', i
      CALL ResPlt (NumPts-1, resid)
      WRITE (*,*) ' ChiSquare = ',ChiSqr,' for ',NumPts,' points.'

      IF (NumItr .EQ. InfItr) THEN
        WRITE (*,*) ' Save this data? (Y=yes, N=no) <N>'
        reply = MTstr
        READ (*,'(A1)') reply
        IF (reply .EQ. 'y'  .OR.  reply .EQ. 'Y') THEN
          reply = MTstr
          WRITE (*,*) ' Output file name? ==>', OutFil
          READ (*,'(A80)') reply
          IF (reply .EQ. MTstr) reply = OutFil
          CALL SavDat (reply, h, C,dC, NumPts)
93        WRITE (*,*) ' Continue iterating? (Y,<N>)'
          reply = MTstr
          READ (*,'(A1)') reply
          IF (reply .EQ. ' ') reply = 'N'
          IF (reply .EQ. 'n') reply = 'N'
          IF (reply .EQ. 'y') reply = 'Y'
          IF (reply .EQ. 'N') GO TO 10
          IF (reply .NE. 'Y') GO TO 93
        END IF
      END IF
 4    CONTINUE

      IF (NumItr .LT. InfItr) THEN
        WRITE (*,*)
        WRITE (*,1000) 'Saving', OutFil
        CALL SavDat (OutFil, h, C,dC, NumPts)
      END IF

10    WRITE (*,*) ' Plot of log(desmeared intensity) vs. h ...'
      DO 11 i = 1, NumPts
11      C(i) = LOG (ABS(C(i)))
      CALL Plot (NumPts, h, C)

      WRITE (*,*)
      WRITE (*,*) ' Same, but now log-log...'
      DO 12 i = 1, NumPts
12      h(i) = LOG (ABS(h(i)))
      CALL Plot (NumPts, h, C)

      WRITE (*,1000) 'Last', OutFil
      GO TO 1
      END
```

```
      SUBROUTINE GetInf (InFile, OutFil, sLengt, sFinal,
     >          NumItr, MaxItr, mForm, LakeForm)
C     Get information about the desmearing parameters.
C     This is designed to be independent of wavelength
C       or radiation-type (i.e. neutrons, X rays, etc.)
      IMPLICIT REAL*8 (A-H, O-Z)
      IMPLICIT INTEGER*4 (I-N)
      CHARACTER*80 InFile, OutFil
      CHARACTER*1 NoName, answer
      PARAMETER (NoName=' ', fZero=0.0, iZero=0)
      LOGICAL Guess
    6 WRITE (*,*) ' What is the data file name? <Quit>'
        InFile = NoName
        READ (*,'(A80)') InFile
        IF (InFile .EQ. NoName) RETURN

    4 WRITE (*,*) ' What is the output data file?'
        OutFil = NoName
        READ (*,'(A80)') OutFil
        IF (OutFil .EQ. NoName) GO TO 4
        IF (OutFil .EQ. InFile) GO TO 6

    2 WRITE (*,*) ' What is the slit length (x-axis units)?', sLengt
        temp = fZero
        READ (*,'(F15.0)') temp
        IF (temp .LT. fZero) GO TO 2
        IF (temp .GT. fZero) sLengt = temp

      WRITE (*,*) ' Extrapolation forms to avoid truncation-error.'
        WRITE (*,*) '   1 = flat background, I(h) = B'
        WRITE (*,*) '   2 = linear, I(h) = b + h * m'
        WRITE (*,*) '   3 = power law, I(h) = b * h**m'
        WRITE (*,*) '   4 = Porod law, I(h) = Cp + Bkg * h**4'
   21   WRITE (*,*) ' Which form? ', mForm
        mTemp = iZero
        READ (*,'(I5)') mTemp
        IF (mTemp .LT. 0  .OR.  mTemp .GT. 4) GO TO 21
        IF (mTemp .GT. iZero) mForm = mTemp

    3 WRITE (*,*) ' What X to begin evaluating extrapolation',
     >         ' (x-axis units)? ', sFinal
        temp = fZero
        READ (*,'(F15.0)') temp
        IF (temp .LT. fZero) GO TO 3
        IF (temp .GT. fZero) sFinal = temp

    5 WRITE (*,*) ' How many iteration(s)? <unlimited>'
        NumItr = iZero
        READ (*,'(I5)') NumItr
        IF (NumItr .LT. iZero .OR. NumItr .GT. MaxItr) GO TO 5

      WRITE (*,*) ' Weighting methods for iterative corrections:'
      WRITE (*,*) ' Correction = weight * (MeasuredI - SmearedI)'
      WRITE (*,*) '   #1) weight = 1.0'
      WRITE (*,*) '   #2) weight = CorrectedI / SmearedI'
      WRITE (*,*) '   #3) weight = 2*SQRT(ChiSqr(0) / ChiSqr(i))'
```

```
    9   WRITE (*,*) ' Which method? ', LakeForm
          mTemp = iZero
          READ (*,'(I5)') mTemp
          IF (mTemp .LT. 0 .OR. mTemp .GT. 3) GO TO 9
          IF (mTemp .GT. iZero) LakeForm = mTemp
        RETURN
        END

        SUBROUTINE FixErr (n, x, y, dy, z, dz)
C       Estimate the error on Z based on data point scatter and
C       previous error values and smooth that estimate.
        IMPLICIT REAL*8 (A-H, O-Z)
        IMPLICIT INTEGER*4 (I-N)
        REAL*8 x(1), y(1), dy(1), z(1), dz(1)

C       Error based on scaled errors of smeared (input) data.
        DO 1  i = 1, n
          dz(i) = z(i) * dy(i) / y(i)
    1   CONTINUE

C       Error based on scatter of desmeared data points.
C         Determine this by fitting a line to the points
C         i-1, i, i+1 and take the difference.  Add this to dz.
        CALL SumClr
        CALL SumAdd (x(1), z(1))
        CALL SumAdd (x(2), z(2))
        CALL SumAdd (x(3), z(3))
        CALL SumLR (slope, const)
        dz(1) = dz(1) + ABS (const + slope*x(1) - z(1))
        dz(2) = dz(2) + ABS (const + slope*x(2) - z(2))
        DO 2  i = 3, n-1
          CALL SumClr
C         CALL SumSub (x(i-2), z(i-2))
          CALL SumAdd (x(i-1), z(i-1))
          CALL SumAdd (x(i), z(i))
          CALL SumAdd (x(i+1), z(i+1))
          CALL SumLR (slope, const)
          zNew = const + slope * x(i)
          dz(i) = dz(i) + ABS (zNew - z(i))
    2   CONTINUE
        dz(n) = dz(n) + ABS (const + slope*x(n) - z(n))

C       Smooth the error by a 3-point moving average filter.
C         Do this 5 times.  Don't smooth the end points.
C         Weight the data points by distance^2 (as a penalty)
C         using the function weight(u,v)=(1 - |1 - u/v|)**2
C         By its definition, weight(x0,x0) == 1.0.  I speed
C         computation using this definition.  Why I can't use
C         this definition of weight as a statement function
C         with some compilers is beyond me!
C       Smoothing is necessary to increase the error estimate
C         for some grossly under-estimated errors.
        DO 4  j = 1, 5
          DO 3  i = 2, n-1
            w1 = (1 - ABS (1 - (x(i-1)/x(i))))**2
            w2 = (1 - ABS (1 - (x(i+1)/x(i))))**2
            dz(i) = (w1 * dz(i-1) + dz(i) + w2 * dz(i+1))
```

```
     >                 / (w1 + 1.D0 + w2)
    3     CONTINUE
    4   CONTINUE
        RETURN
        END

        SUBROUTINE Prep (x, y, dy, NumPts)
C       Calculate the constants for an extrapolation fit
C       from all the data that satisfy x(i) >= sFinal.
        IMPLICIT REAL*8 (A-H, O-Z)
        IMPLICIT INTEGER*4 (I-N)
        REAL*8 x(1), y(1), dy(1)
        COMMON /PrepCm/ sLengt, sFinal, fSlope, fConst, mForm
        CALL SumClr
        DO 1, i = 1, NumPts-1
          IF (x(i) .GE. sFinal) THEN
            IF (mForm .EQ. 1) THEN
              CALL SwtAdd (x(i), y(i), dy(i))           ! weighted
            ELSE IF (mForm .EQ. 2) THEN
              CALL SwtAdd (x(i), y(i), dy(i))           ! weighted
            ELSE IF (mForm .EQ. 3) THEN
              CALL SumAdd (LOG(x(i)), LOG(y(i)))        ! un-weighted
            ELSE IF (mForm .EQ. 4) THEN
              h4 = x(i)**4
              CALL SwtAdd (h4, y(i)*h4, dy(i)*h4)       ! weighted
            END IF
          END IF
    1   CONTINUE
        IF (mForm .EQ. 1) THEN
          CALL MeanXY (fSlope, fConst)
          fSlope = 0.
        ELSE IF (mForm .GE. 2  .AND.  mForm .LE. 4) THEN
          CALL SumLR (fSlope, fConst)
        END IF
        RETURN
        END


        SUBROUTINE Smear (z)
C       Smear the data of C(h) into z using the slit-length
C         weighting function "Plengt" and a power-law extrapolation
C         of the data to avoid truncation errors.  Assume that
C         Plengt goes to zero for l > lo (the slit length).
C       Also assume that the slit length  function is symmetrical
C         about l = zero.
C       This routine is written so that if "Plengt" is changed
C         (for example) to a Gaussian, that no further modification
C         is necessary to the integration procedure.  That is,
C         this routine will integrate the data out to "lo".
        IMPLICIT REAL*8 (A-H,O-Z)
        IMPLICIT INTEGER*4 (I-N)
        REAL*8 z(1)
        COMMON /PrepCm/ sLengt, sFinal, fSlope, fConst, mForm
        COMMON /DatCom/ NumPts, iLo, iHi, h, C, dC
        PARAMETER ( MaxPts = 500 )      ! also in main routine
        REAL*8 h(500), C(500), dC(500)
        REAL*8 x(MaxPts), w(MaxPts)
```

```
      CALL Prep (h, C, dC, NumPts)    ! get coefficients
      IF (mForm .EQ. 1) WRITE (*,41) fConst
      IF (mForm .EQ. 2) WRITE (*,42) fConst, fSlope
      IF (mForm .EQ. 3) WRITE (*,43) EXP (fConst), fSlope
      IF (mForm .EQ. 4) WRITE (*,44) fConst, fSlope
 41   FORMAT (' constant background fit: I = ', 1PE15.7)
 42   FORMAT (' linear fit: I = ', 1PE15.7, ' + h*', E15.7)
 43   FORMAT (' Power law fit: I = ', 1PE15.7, ' * h**', 0PF10.5)
 44   FORMAT (' Porod law fit: I = ', 1PE15.7, ' + h**4 * ', E15.7)

      hLo = h(1)
      ratio = sLengt / (h(NumPts) - hLo)
      DO 1  i = 1, NumPts
        x(i) = ratio * (h(i) - hLo)   ! values for "l"
        w(i) = Plengt (x(i))          ! probability at "l"
  1   CONTINUE

      w(1) = w(1) * (x(2) - x(1))
      DO 2  i = 2, NumPts-1
        w(i) = w(i) * (x(i+1) - x(i-1))       ! step sizes
  2   CONTINUE
      w(NumPts) = w(NumPts) * (x(NumPts) - x(NumPts-1))

      DO 3  i = 1, NumPts             ! evaluate each integral
        hNow = h(i)                   ! ... using trapezoid rule
        sum = w(1) * FindIc (hNow, x(1))
        DO 4  k = 2, NumPts-1
          sum = sum + w(k) * FindIc (hNow, x(k))
  4     CONTINUE
        z(i) = sum + w(NumPts) * FindIc (hNow, x(NumPts))
  3   CONTINUE

      RETURN
      END


      REAL*8 FUNCTION Plengt (x)
C     Here is the definition of the slit-length weighting function.
C       It is defined for a rectangular slit of length 2*sLengt
C       and probability 1/(2*sLengt).  It is zero elsewhere.
C     It is not necessary to change the limit of the integration
C       if the functional form here is changed.  You may, however,
C       need to ask the user for more parameters.  Pass these
C       around to the various routines through the use of the
C       /PrepCm/ COMMON block.
      IMPLICIT REAL*8 (A-H,O-Z)
      IMPLICIT INTEGER*4 (I-N)
      COMMON /PrepCm/ sLengt, sFinal, fSlope, fConst, mForm
      IF (ABS(x) .GT. sLengt) THEN
        z = 0.0
      ELSE
        z = 0.5 / sLengt
      END IF
      Plengt = z
      RETURN
      END
```

```
        REAL*8 FUNCTION FindIc(x, y)
C       Determine the "corrected" intensity at u = SQRT (x*x + y*y)
C       Note that only positive values of "u" will be searched!
        IMPLICIT REAL*8 (A-H, O-Z)
        IMPLICIT INTEGER*4 (I-N)
        COMMON /PrepCm/ sLengt, sFinal, fSlope, fConst, mForm
        COMMON /DatCom/ NumPts, iLo, iHi, h, C, dC
        PARAMETER ( MaxPts = 500 )      ! also in main routine
        REAL*8 h(500), C(500), dC(500)
        GetIt(x,x1,y1,x2,y2) = y1 + (y2-y1) * (x-x1) / (x2-x1)

        u = SQRT (x*x + y*y)    ! circularly symmetric
        CALL BSearch (u, h, NumPts, iLo, iHi, iTest)    ! find index
        IF (iTest .LT. 1) THEN
          WRITE (*,*) ' Bad value of U or array H in routine FindIc'
          STOP
        END IF
        IF (iTest .LE. NumPts) THEN
          IF (u .EQ. h(iLo)) THEN
            value = C(iLo)              ! exactly!
          ELSE                          ! linear interpolation
            value = GetIt(u, h(iLo),C(iLo), h(iHi),C(iHi))
          END IF
        ELSE                            ! functional extrapolation
          IF (mForm .EQ. 1) THEN
            value = fConst
          ELSE IF (mForm .EQ. 2) THEN
            value = fConst + fSlope * u
          ELSE IF (mForm .EQ. 3) THEN
            value = EXP (fConst + fSlope * LOG (u))
          ELSE IF (mForm .EQ. 4) THEN
            value = fSlope + fConst / u**4      ! modified form!
          END IF
        END IF
        FindIC = value
        RETURN
        END


C       Pete R. Jemian, 15 May 1989
C       The routines that follow are part of my general
C         mathematical "toolbox".  Some of them are taken
C         (with reference) from book(s) but most, I have
C         developed on my own.  They are modular in construction
C         so that they may be improved, as needed.


        SUBROUTINE BSearch (z, x, NumPts, iLo, iHi, iTest)
C       Search the array "x" for (iLo) <= z < x(iHi)
C       On exit, iLo and iHi will exactly bracket the datum
C         and iTest will be the same as iLo.
C       If z is below [above] the range, iTest = -1 [NumPts+1].
        IMPLICIT REAL*8 (A-H, O-Z)
        IMPLICIT INTEGER*4 (I-N)
        REAL*8 x(1)
```

```
      iTest = -1      ! assume that z < x(1) and test
      IF (z .LT. x(1)) RETURN
      iTest = NumPts + 1      ! assume z > x(n) and test
      IF (z .GT. x(NumPts)) RETURN
      IF (iLo .LT. 1 .OR. iHi .GT. NumPts .OR. iLo .GE. iHi) THEN
        iLo = 1
        iHi = NumPts
      END IF
1     IF (z .LT. x(iLo)) THEN         ! expand down?
        iLo = iLo / 2
        GO TO 1
      END IF
2     IF (z .GT. x(iHi)) THEN         ! expand up?
        iHi = (iHi + 1 + NumPts) / 2
        GO TO 2
      END IF
3     iTest = (iLo + iHi) / 2
      IF (z .GE. x(iTest)) THEN       ! which half?
        iLo = iTest
      ELSE
        iHi = iTest
      END IF
      IF (iHi - iLo .GT. 1) GO TO 3
      RETURN
      END


      SUBROUTINE GetDat (InFile, x, y, dy, n, MaxPts)
      CHARACTER*80 InFile
      REAL*8 x(1), y(1), dy(1)
      INTEGER*4 n, MaxPts
      PARAMETER (ioPath = 1)
      OPEN (UNIT = ioPath, FILE = InFile, STATUS = 'old')
      DO 1  n = 1, MaxPts
        READ (ioPath, *, END = 2, ERR = 3) x(n), y(n), dy(n)
1     CONTINUE
2     n = n - 1       ! ignore any lines without an explicit EOL mark
      CLOSE (UNIT = ioPath, STATUS = 'keep')
      RETURN
3     n = 0           ! ignore any/all data yet received
      CLOSE (UNIT = ioPath, STATUS = 'keep')
      RETURN
      END


      SUBROUTINE SavDat (OutFil, x, y, dy, n)
      CHARACTER*80 OutFil
      REAL*8 x(1), y(1), dy(1)
      INTEGER*4 n
      CHARACTER*1 Tab
      PARAMETER (ioPath = 1)
      Tab = CHAR(9)
      OPEN (UNIT = ioPath, FILE = OutFil, STATUS = 'new')
        DO 2, i = 1, n
        WRITE (ioPath, 1) x(i), Tab, y(i), Tab, dy(i)
1       FORMAT (1X, 1PE15.7, 2(A1, E15.7))
2     CONTINUE
```

```
      CLOSE (UNIT = ioPath, STATUS = 'keep')
      RETURN
      END


      INTEGER*4 FUNCTION Imax (a,b)
      INTEGER*4 a, b, c
      c = a
      IF (b .GT. a) c = b
      Imax = c
      RETURN
      END

      INTEGER*4 FUNCTION Imin (a,b)
      INTEGER*4 a, b, c
      c = a
      IF (b .LT. a) c = b
      Imin = c
      RETURN
      END


      SUBROUTINE Iswap (a,b)
      INTEGER*4 a, b, c
      c = a
      a = b
      b = c
      RETURN
      END


      SUBROUTINE Plot (n,x,y)
C     Make a scatter plot on the default display device (UNIT=*).
C     MaxRow and MaxCol correspond to the display dimensions.
      IMPLICIT REAL*8 (A-H, O-Z)
      IMPLICIT INTEGER*4 (I-N)
      REAL*8 x(1), y(1)
      PARAMETER (MaxCol = 75, MaxRow = 19)
      PARAMETER (MxC2 = MaxCol+2, MxR2 = MaxRow+2)
      CHARACTER*1 screen(MxR2, MxC2), Blank, Symbol
      CHARACTER*1 hBordr, vBordr
      PARAMETER (Blank = ' ', Symbol = 'O')
      PARAMETER (hBordr = '-', vBordr = '|')

C     prepare the "screen" for drawing
      DO 1  j = 1, MxC2
        DO 1  i = 1, MxR2
          screen(i,j) = Blank
    1 CONTINUE
      DO 2  i = 2, MaxCol+1
        screen(MxR2,i) = hBordr
    2   screen(1,i) = hBordr
      DO 3  i = 2, MaxRow+1
        screen(i,MxC2) = vBordr
    3   screen(i,1)  = vBordr

C     get the data limits
```

```
        xMin = x(1)
        xMax = x(1)
        yMin = y(1)
        yMax = y(1)
        DO 4 i = 2, n
          IF (x(i).GT.xMax) xMax=x(i)
          IF (x(i).LT.xMin) xMin=x(i)
          IF (y(i).GT.yMax) yMax=y(i)
          IF (y(i).LT.yMin) yMin=y(i)
    4   CONTINUE
        ColDel = (MaxCol - 1) / (xMax - xMin)
        RowDel = (MaxRow - 1) / (yMax - yMin)

C       data scaling functions are offset by +1 for plot frame
        DO 5  i = 1, n
          mCol = 1 + INT((x(i) - xMin)*ColDel + 1)
          mRow = 1 + INT((y(i) - yMin)*RowDel + 1)
    5     screen(mRow, mCol) = Symbol

C       convey the "screen" to the default output
        WRITE (*,*) 1./ColDel, ' units per column'
        WRITE (*,*) 1./RowDel, ' units per row'
        DO 6  i = MaxRow + 2, 1, -1
    6     WRITE (*,*) (screen(i,j), j = 1, MaxCol + 2)
        RETURN
        END


        SUBROUTINE ResPlt (n, x)
C       Draw a plot of the standardized residuals on the screen.
C       Mark the rows of + and - one standard deviation.
        IMPLICIT REAL*8 (A-H, O-Z)
        IMPLICIT INTEGER*4 (I-N)
        REAL*8 x(1)
        PARAMETER (MaxCol = 75, MaxRow = 15)
        PARAMETER (MxC2 = MaxCol+2, MxR2 = MaxRow+2)
        CHARACTER*1 screen(MxR2, MxC2), Blank, Symbol
        CHARACTER*1 hBordr, vBordr, resSym
        PARAMETER (Blank = ' ', Symbol = 'O', resSym = '=')
        PARAMETER (hBordr = '-', vBordr = '|')

C       Find out how many points to pack per column and how many columns
        nPack = 1 + INT(FLOAT (n) / MaxCol - 1./n)
        nCol = INT((n - 1./n)/nPack + 1)

C       prepare the "screen" for drawing
        DO 1  j = 1, nCol + 2
          DO 1  i = 1, MxR2
            screen(i,j) = Blank
    1   CONTINUE
        DO 2  i = 2, nCol + 1
          screen(MxR2,i) = hBordr
    2     screen(1,i) = hBordr
        DO 3  i = 2, MaxRow + 1
          screen(i,nCol+2) = vBordr
    3     screen(i,1) = vBordr
```

```
C       get the data limits
        xMax = 1.
        xMin = -1.
        DO 4 i = 1, n
          IF (x(i).GT.xMax) xMax=x(i)
          IF (x(i).LT.xMin) xMin=x(i)
    4   CONTINUE
        RowDel = (MaxRow - 1) / (xMax - xMin)

C       show the standard deviation bars
        mPlus = 1 + INT((1.D0 - xMin)*RowDel + 1)
        mMinus = 1 + INT((-1.D0 - xMin)*RowDel + 1)
        DO 5  i = 2, nCol + 1
          screen(mMinus,i) = resSym
    5     screen(mPlus,i) = resSym

C       draw the data (overdrawing the residuals bars if necessary)
C       data scaling functions (offset by +1 for the plot frame)
        DO 6  i = 1, n
          mCol = 1 + INT((i - 1./n)/nPack + 1)
          mRow = 1 + INT((x(i) - xMin)*RowDel + 1)
    6     screen(mRow, mCol) = Symbol

C       convey the "screen" to the default output
        WRITE (*,*) nPack, ' point(s) per column'
        WRITE (*,*) 1./RowDel, ' standard deviations per row'
        DO 7  i = MxR2, 1, -1
    7     WRITE (*,*) (screen(i,j), j = 1, nCol + 2)

        RETURN
        END


C       Implement a set of statistics registers in the
C         style of a pocket calculator.
C         The routines that are available are:
C               SumClr  : clear the stats registers
C               SumAdd  : add an X,Y pair
C               SwtAdd  : add an X,Y pair with weight Z
C               SumSub  : remove an X,Y pair
C               SwtSub  : remove an X,Y pair with weight Z
C               MeanXY  : arithmetic mean of X & Y
C               SDevXY  : standard deviation of X & Y
C               SErrXY  : standard error of X & Y
C               SumLR   : linear regression
C               VarLR   : variance in linear regression constants
C               CorLR   : correlation coefficient of X & Y data
C               CorCoe  : cor. coeff. of errors in slope and intercept


        SUBROUTINE SumClr
        IMPLICIT REAL*8 (A-H, O-Z)
        IMPLICIT INTEGER*4 (I-N)
        COMMON /stats/ count, sumX, sumX2, sumY, sumY2, sumXY
        PARAMETER (fZero = 0.0)
        count = fZero
        sumX = fZero
```

```
sumX2 = fZero
sumY = fZero
sumY2 = fZero
sumXY = fZero
RETURN
END

SUBROUTINE SumAdd (x, y)
IMPLICIT REAL*8 (A-H, O-Z)
IMPLICIT INTEGER*4 (I-N)
DATA one /1.0/
CALL SwtAdd (x, y, one)         ! unit weighting
RETURN
END

SUBROUTINE SwtAdd (x, y, z)
IMPLICIT REAL*8 (A-H, O-Z)
IMPLICIT INTEGER*4 (I-N)
COMMON /stats/ count, sumX, sumX2, sumY, sumY2, sumXY
weight = 1/z**2
xWt = x * weight
yWt = y * weight
count = count + weight
sumX = sumX + xWt
sumX2 = sumX2 + xWt*xWt
sumY = sumY + yWt
sumY2 = sumY2 + yWt*yWt
sumXY = sumXY + xWt*yWt
RETURN
END

SUBROUTINE SumSub (x, y)
IMPLICIT REAL*8 (A-H, O-Z)
IMPLICIT INTEGER*4 (I-N)
DATA one /1.0/
CALL SwtSub (x, y, one)         ! unit weighting
RETURN
END

SUBROUTINE SwtSub (x, y, z)
IMPLICIT REAL*8 (A-H, O-Z)
IMPLICIT INTEGER*4 (I-N)
COMMON /stats/ count, sumX, sumX2, sumY, sumY2, sumXY
weight = 1/z**2
xWt = x * weight
yWt = y * weight
count = count - weight
sumX = sumX - xWt
sumX2 = sumX2 - xWt*xWt
sumY = sumY - yWt
sumY2 = sumY2 - yWt*yWt
sumXY = sumXY - xWt*yWt
RETURN
END

SUBROUTINE MeanXY (xMean, yMean)  ! arithmetic mean of X & Y
IMPLICIT REAL*8 (A-H, O-Z)
```

```
      IMPLICIT INTEGER*4 (I-N)
      COMMON /stats/ count, sumX, sumX2, sumY, sumY2, sumXY
      xMean = sumX / count
      yMean = sumY / count
      RETURN
      END

      SUBROUTINE SDevXY (xDev, yDev)  ! standard deviation on X & Y
      IMPLICIT REAL*8 (A-H, O-Z)
      IMPLICIT INTEGER*4 (I-N)
      COMMON /stats/ count, sumX, sumX2, sumY, sumY2, sumXY
      xDev = 0.
      IF (sumX2 .GT. ((sumX**2)/count) )
     >   xDev = SQRT(( sumX2 - ( (sumX**2)/count) )/count)
      yDev = 0.
      IF (sumY2 .GT. ((sumY**2)/count) )
     >   yDev = SQRT(( sumY2 - ((sumY**2)/count) )/count)
      RETURN
      END

      SUBROUTINE SErrXY (xErr, yErr)  ! standard error on X & Y
      IMPLICIT REAL*8 (A-H, O-Z)
      IMPLICIT INTEGER*4 (I-N)
      COMMON /stats/ count, sumX, sumX2, sumY, sumY2, sumXY
      xErr = 0.
      IF (sumX2 .GT. ((sumX**2)/count) )
     >   xErr = SQRT(( sumX2 - ( (sumX**2)/count) )/( count-1 ))
      yErr = 0.
      IF (sumY2 .GT. ((sumY**2)/count) )
     >   yErr = SQRT(( sumY2 - ((sumY**2)/count) )/( count-1 ))
      RETURN
      END

      SUBROUTINE SumLR (slope, const)  ! linear regression
      IMPLICIT REAL*8 (A-H, O-Z)
      IMPLICIT INTEGER*4 (I-N)
      COMMON /stats/ count, sumX, sumX2, sumY, sumY2, sumXY
      determ = (count*sumX2 - sumX**2)
      slope = (count*sumXY - sumX*sumY) / determ
      const = (sumX2*sumY - sumX*sumXY) / determ
      RETURN
      END

      SUBROUTINE VarLR (slope, const) ! est. errors of slope & intercept
      IMPLICIT REAL*8 (A-H, O-Z)
      IMPLICIT INTEGER*4 (I-N)
      COMMON /stats/ count, sumX, sumX2, sumY, sumY2, sumXY
      determ = (count*sumX2 - sumX**2)
      slope = SQRT (count / determ)
      const = SQRT (sumX2 / determ)
      RETURN
      END

      REAL*8 FUNCTION CorLR   ! the regression coefficient
      IMPLICIT REAL*8 (A-H, O-Z)
      IMPLICIT INTEGER*4 (I-N)
      COMMON /stats/ count, sumX, sumX2, sumY, sumY2, sumXY
```

```
VarX = count * sumX2 - sumX**2
VarY = count * sumY2 - sumY**2
CorLR = (count * sumXY - sumX*sumY) / SQRT (VarX * VarY)
RETURN
END

REAL*8 FUNCTION CorCoe   ! relation of errors in slope & intercept
IMPLICIT REAL*8 (A-H, O-Z)
IMPLICIT INTEGER*4 (I-N)
COMMON /stats/ count, sumX, sumX2, sumY, sumY2, sumXY
CorCoe = -sumX / SQRT (count * sumX2)
RETURN
END
```

F MaxSAS.FOR: Size Distribution Analysis

The following computer program interprets small-angle scattering in terms of scattering from a distribution of scatterers of a specified shape by means of the maximum entropy method. This code is an adaptation of Maxe.FOR from the UKAEA-Harwell Laboratory. Comments have been added to describe some of the various processes.

```
        PROGRAM MaxSAS
        IMPLICIT REAL*8 (A-H,O-Z)
        IMPLICIT INTEGER*4 (I-N)
        CHARACTER*25 ProgVers, EditDate
        PARAMETER (ProgVers = '3.0 (PRJ)')
        PARAMETER (EditDate = '27 November 1989')
C       Analysis of small-angle scattering data using the technique of
C       entropy maximization.

C       Credits:
C       G.J. Daniell, Dept. of Physics, Southampton University, UK
C       J.A. Potton, UKAEA Harwell Laboratory, UK
C       I.D. Culverwell, UKAEA Harwell Laboratory, UK
C       G.P. Clarke, UKAEA Harwell Laboratory, UK
C       A.J. Allen, UKAEA Harwell Laboratory, UK
C       P.R. Jemian, Northwestern University, USA

C       References:
C       1. J Skilling and RK Bryan; MON NOT R ASTR SOC
C               211 (1984) 111 - 124.
C       2. JA Potton, GJ Daniell, and BD Rainford; Proc. Workshop
C               Neutron Scattering Data Analysis, Rutherford
C               Appleton Laboratory, UK, 1986; ed. MW Johnson,
C               IOP Conference Series 81 (1986) 81 - 86, Institute
C               of Physics, Bristol, UK.
C       3. ID Culverwell and GP Clarke; Ibid. 87 - 96.
C       4. JA Potton, GK Daniell, & BD Rainford,
C               J APPL CRYST 21 (1988) 663 - 668.
C       5. JA Potton, GJ Daniell, & BD Rainford,
C               J APPL CRYST 21 (1988) 891 - 897.

C       This progam was written in BASIC by GJ Daniell and later
C         translated into FORTRAN and adapted for SANS analysis.  It
C         has been further modified by AJ Allen to allow use with a
C         choice of particle form factors for different shapes.  It
C         was then modified by PR Jemian to allow portability between
C         the Digital Equipment Corporation VAX and Apple Macintosh
C         computers.
C       The input data file format is three columns of "Q I dI" which
C         are separated by spaces or tabs.  There is no header line
C         in the input data file.

        PARAMETER (cm2m = 0.01) ! convert cm to m units, but why?
        PARAMETER (MaxPts = 300, MaxBin = 102)
        PARAMETER (isLin = 1, isLog = 2, ioUnit = 1)

C  point-by-point mapping between reciprocal and real space
        COMMON /space1/ grid
        DIMENSION grid(MaxBin,MaxPts)

C  terms used in entropy maximization
```

```
      COMMON /space5/ chisq, chtarg, chizer, fSum, blank
      COMMON /space2/ beta, c1, c2, s1, s2
      DIMENSION beta(3), c1(3), c2(3,3), s1(3), s2(3,3)

C  terms used only by subroutine MaxEnt, allocated here to make memory tidy
      COMMON /space3/ ox, z, cgrad, sgrad, xi, eta
      DIMENSION ox(MaxPts), z(MaxPts)
      DIMENSION cgrad(MaxBin), sgrad(MaxBin)
      DIMENSION xi(MaxBin,3), eta(MaxPts,3)

C  space for the plotting frame, allocated here to make memory tidy
C    note the limits: MaxCol <= 100, MaxRow <= 150 (really large screens!)
      PARAMETER (MaxCol = 75, MaxRow = 15)
      PARAMETER (MxC2 = MaxCol+2, MxR2 = MaxRow+2)
      COMMON /space4/ screen, nCol, nRow, nCol2, nRow2
      CHARACTER*1 screen(100, 150)

C  space for main segment arrays
      DIMENSION q(MaxPts), datum(MaxPts), sigma(MaxPts)
      DIMENSION r(MaxBin), f(MaxBin), base(MaxBin), dNdr(MaxBin)
      DIMENSION fit(MaxPts), BinWid(MaxPts)
      CHARACTER*40 InFile, OutFil
      LOGICAL Yes
      CHARACTER*1 YN, aTab

      DATA one, zero /1.0, 0.0/       ! compiler-independence!
      DATA hrDamp /8.0/       ! model 7: sets transition range
      DATA htDamp /0.9/       ! model 7: amount of damping
C  The value "hrDamp" sets the range where the transistion occurs.
C  The value "htDamp" sets the maximum proportion of damping.

C ... Define (initially) the default responses
      DATA iOption    /4/     ! usual form factor for spheres
      DATA Aspect     /1.0/   ! particle aspect ratio
      DATA LinLog     /isLin/ ! linear binning scale
      DATA n          /40/    ! number of bins
      DATA Dmin, Dmax /8.00, 400.0/   ! particle diameters
      DATA IterMax    /20/    ! maximum number of iterations to try
      DATA RhoSq      /1.0/   ! scattering contrast, x10**28 1/m**4
      DATA fac, err   /1.0, 1.0/      ! scalars for intensity and errors
      DATA qMin, qMax /1.e-8, 100./   ! range to accept
      DATA Bkg        /0.0/   ! intensity to subtract
      DATA sLengt     /100.0/ ! rectangular slit-length, 1/A

C  Next line for MPW/Language Systems version 1.2.1, Macintosh only
C  Comment this out for other compilers
C  This is the only compiler-dependent line in this source code!!!!!!
C       CALL OutWindowScroll (1000)  ! for 1-line advance screen

      pi = 4. * ATAN(1.)
      aTab = CHAR (9)

C  screen dimension variables for plots, in COMMON /space4/
      nCol = MaxCol
      nRow = MaxRow
      nCol2 = MxC2
      nRow2 = MxR2
```

```
    1   WRITE (*,*)
        WRITE (*,*) 'Size distributions from SAS data using the',
     >              ' maximum entropy criterion'
        WRITE (*,*) '       version: ', ProgVers
        WRITE (*,*) '   Last edited: ', EditDate

        CALL GetInf (InFile, OutFil, iOption, Aspect, LinLog,
     >          n, Dmin, Dmax, IterMax, RhoSq, fac, err, qMin,
     >          qMax, Bkg, sLengt)
        IF (InFile .EQ. ' ') STOP

C   Read in the SAS data from the file "InFile"
        WRITE (*,*)  ' Reading from file: ', InFile
        OPEN (UNIT = ioUnit, FILE = InFile, STATUS = 'old')
        DO 94  j = 1, MaxPts
          READ (ioUnit, *, END = 95) q(j), datum(j), sigma(j)
   94   CONTINUE
   95   npt=j-1         ! ignore any lines without an explicit EOL mark
        CLOSE (UNIT = ioUnit, STATUS = 'keep')
        WRITE (*,*) npt, ' points were read from the file'

C   Subtract background, convert to 1/m units and
C       shift for the selected data range
        i = 0
        DO 2  j = 1, npt
          IF (q(j) .GE. Qmin .AND. q(j) .LE. Qmax) THEN
            i = i + 1
            q(i) = q(j)
            datum(i) = fac * (datum(j)-Bkg) / cm2m
            sigma(i) = fac * err * sigma(j) / cm2m
          END IF
    2   CONTINUE
        npt = i
        WRITE (*,*) npt, ' points were selected from the data'

C  PRJ: 24 May 1989
C       BinWid: actual radial width of the indexed bin number
C       Step:   radial increment factor (for geometric series)
C       rWid:   radial width (for algebraic series)
        IF (LinLog .EQ. isLog) THEN     ! geometric series
          Step = (Dmax/Dmin)**(1. / FLOAT(n-1)) - 1.
          rWid = 0.
        ELSE                            ! algebraic series
          Step = 0.
          rWid = 0.5*(Dmax - Dmin) / FLOAT(n-1)
        END IF
        r(1) = 0.5 * Dmin
        BinWid(1) = r(1) * Step + rWid
        DO 48  i = 2, n
          r(i) = r(i-1) + BinWid(i-1)
          BinWid(i) = r(i) * Step + rWid
   48   CONTINUE

        WRITE (*,*) ' Preparation of the GRID function...'
C  Calculate the form-factor pre-terms
  111   IF (iOption .EQ. 1) THEN        ! Rods, using model of AJ Allen
```

```
          alphan1 = 2. * pi * Aspect
          alphan2 = 4. * pi
          preform = alphan1
          sLengt = 0.                   ! "pinhole" collimation
        ELSE IF (iOption .EQ. 2) THEN   ! Disks, using model of AJ Allen
          alphan1 = 2. * pi / (Aspect**2)
          alphan2 = 2. * pi
          preform = alphan1
          sLengt = zero
        ELSE IF (iOption .EQ. 3) THEN   ! Globules, using model of AJ Allen
          alphan1 = 4. * pi * Aspect / 3.
          IF (Aspect .LT. 0.99) THEN    ! hamburger-shaped
            sqqt = SQRT (one - Aspect**2)
            argument = (2. - Aspect**2 + 2. * sqqt) / (Aspect**2)
            surchi = (one + Aspect**2 * LOG(argument) / (2.*sqqt) )
     >          / (2. * Aspect)
          ELSE IF (Aspect .GT. 1.01) THEN       ! peanut shaped
            sqqt = SQRT(Aspect**2 - one)
            argument = sqqt / Aspect
            surchi = (one + Aspect**2 * ASIN(argument) / sqqt)
     >          / (2. * Aspect)
          ELSE                          ! spheroidal
            surchi = one
          END IF
          alphan2 = 6. * pi * surchi
          preform = alphan1
          sLengt = zero
        ELSE IF (iOption .EQ. 4) THEN   ! Spheres, delta-function
          alphan1 = 4. * pi / 3.
          alphan2 = 6. * pi
          preform = 9. * alphan1
          sLengt = zero
        ELSE IF (iOption .EQ. 5) THEN   ! Spheres, box-distribution
          alphan1 = 4. * pi / 3.        ! This model by PRJ
          alphan2 = 6. * pi
          preform = 48. * pi
          sLengt = zero
        ELSE IF (iOption .EQ. 6) THEN   ! smeared, spheroidal globs
          preform = 4. * Pi / 3.        ! This model by PRJ
          alphan1 = preform
          alphan2 = 6. * Pi
          Cgs = SQRT (3. * Pi)          ! for low-Q region
          Cps = 9. * Pi / 4.            ! for med. high-Q region
          Cp = 9. / 2.                  ! for high-Q region
        ELSE IF (iOption .EQ. 7) THEN   ! spheroidal globs, no smearing
          preform = 4. * Pi / 3.        ! This model by PRJ
          alphan1 = preform
          alphan2 = 6. * Pi
          sLengt = zero
        END IF

C  alphaN1 is RhoSq * the particle volume
C  alphaN2 is RhoSq * the particle surface area / the particle volume
C       ... and later divided by q**4
        alphan1 = cm2m * alphan1 * rhosq * r(1)**3
        alphan2 = cm2m * alphan2 * rhosq / r(n)
        preform = cm2m * preform * rhosq
```

```
        DO 226  i = 1, n
          rCubed = r(i)**3
          DO 226  j = 1, npt
            Qr = q(j) * r(i)
            IF (iOption .EQ. 1) THEN
              QH = q(j) * Aspect * r(i)          ! rod 1/2 - length
              topp = one + 2.*Pi* QH**3 * Qr / (9 * (4 + Qr**2))
     >                   + (QH**3 * Qr**4) / 8.
              bott = one + QH**2 * (one + QH**2 * Qr)/9
     >                   + (QH**4 * Qr**7) / 16
            ELSE IF (iOption .EQ. 2) THEN
              h = r(i)                   ! disk 1/2 - thickness
              Rd = h / Aspect            ! disk radius
              Qh = q(j) * h
              QRd = q(j) * Rd
              topp = one + QRd**3 / (3. + Qh**2)
     >                   + (Qh**2 * QRd / 3.)**2
              bott = one + QRd**2 * (one + Qh * QRd**2) / 16
     >                   + (Qh**3 * QRd**2 / 3.)**2
            ELSE IF (iOption .EQ. 3) THEN
              topp = one
              bott = one + Qr**2 * (2. + Aspect**2) / 15.
     >                   + 2. * Aspect * Qr**4 / (9. * surchi)
            ELSE IF (iOption .EQ. 4) THEN
              topp = (SIN(Qr) - Qr * COS(Qr))**2
              bott = Qr**6
            ELSE IF (iOption .EQ. 5) THEN
              Qj = q(j)
              rP = r(i) + BinWid(i)
              rM = r(i)
              bP = 0.5*rP + (Qj**2)*(rP**3)/6.
     >          + (0.25*(Qj * rP**2) - 0.625/Qj) * SIN (2.*Qj*rP)
     >          + 0.75 * rP * COS (2.*Qj*rP)
              bM = 0.5*rM + (Qj**2)*(rM**3)/6.
     >          + (0.25*(Qj * rM**2) - 0.625/Qj) * SIN (2.*Qj*rM)
     >          + 0.75 * rM * COS (2.*Qj*rM)
              topp = bP - bM
              bott = Qj**6 * (rP**4 - rM**4) * rCubed
            ELSE IF (iOption .EQ. 6) THEN
              rL = r(i) * sLengt
              topp = Cgs
              bott = rL*(one + (Qr**2)/5. + Cgs/Cps * Qr**3)
     >                 + Cgs/Cp * Qr**4
            ELSE IF (iOption .EQ. 7) THEN
C  The value "hrDamp" sets the range where the transistion occurs.
C  The value "htDamp" sets the maximum proportion of damping.
C  The weight is a "step" function with a broad edge.
              weight = htDamp * EXP (-((Qr/hrDamp)**2)) + (one - htDamp)
              topp = 3. * (SIN(Qr) - Qr * COS(Qr)) / Qr**3
              bott = 4.5 / Qr**4         ! bott=<topp**2> for large Qr
              topp = weight * topp**2 + (one-weight) / (one + one/bott)
              bott = one
            END IF
            grid(i,j) = preform * rCubed * topp / bott
C               factors of 4Pi/3 are already included in "preform"
  226   CONTINUE
```

```
C       Attempt to account for scattering from very large and very small
C       particles by use of the limiting forms of grid(i,j).
        DO 227  j = 1, npt
          grid(n+1,j) = alphan1 ! next line accounts for a slit-length
          grid(n+2,j) = alphan2 / (q(j)**3 * SQRT(q(j)**2 + sLengt**2))
  227   CONTINUE

C  Try to solve the problem
  228   basis = 1.0e-12 / RhoSq         ! Originally was 1.0e-6
        CALL MaxEnt (n+2,npt, f,datum,sigma, basis,base, max,itermax)

C       "Max" counts the number of iterations inside MAXENT.
C       If Max < IterMax, then the problem has been solved.
        IF (max .GE. itermax) THEN
          WRITE (*,*) ' No convergence! # iter. = ', max
          WRITE (*,*) ' File was: ', InFile
          GO TO 1
        END IF

C   Otherwise, SUCCESS!... so calculate the volume distribution
C       from the model SAS data
        CALL opus (n+2, npt, f, fit)

C   ... and remove the bin width effect.
C   Also, calculate the total volume fraction, the mode, mean, and
C       standard deviations of the volume and number distributions.
        SumV   = zero
        SumVR  = zero
        SumVR2 = zero
        SumN   = zero
        SumNR  = zero
        SumNR2 = zero
        modeV = 1
        modeN  = 1
        DO 1919  i = 1, n
          size = r(i)
          frac = f(i)
          pVol = 4*Pi/3 * (size * 1.e-8)**3     ! particle volume, cm**3
          IF (iOption .EQ. 1)  pVol = pVol * Aspect     ! rods
          IF (iOption .EQ. 2)  pVol = pVol / Aspect     ! disks
          IF (iOption .EQ. 3)  pVol = pVol * Aspect     ! globs
          amount = frac / pVol                  ! number / cm**3
          f(i) = frac / BinWid(i)
          dNdr(i) = amount / BinWid(i)
          IF (i .GT. 3) THEN                    ! ignore 1st few bins
            SumN   = SumN   + amount
            SumNR  = SumNR  + amount * size
            SumNR2 = SumNR2 + amount * size**2
          END IF
          IF (dNdr(i) .GT. dNdr(modeN)) modeN = i       ! get the mode
          SumV   = SumV   + frac
          SumVR  = SumVR  + frac * size
          SumVR2 = SumVR2 + frac * size**2
          IF (f(i) .GT. f(modeV)) modeV = i             ! get the mode
 1919   CONTINUE
        DnMean = 2.0 * SumNR / SumN
```

```
        DnSDev = 2.0 * SQRT((SumNR2 / SumN) - (SumNR / SumN)**2)
        DvMean = 2.0 * SumVR / SumV
        DvSDev = 2.0 * SQRT((SumVR2 / SumV) - (SumVR / SumV)**2)

        Entropy = zero
        DO 1920  i = 1, n
          frac = BinWid(i) * f(i) / SumV        ! Skilling & Bryan, eq. 1
          Entropy = Entropy - frac * LOG (frac)
 1920   CONTINUE

C  Show the final distribution, corrected for bin width.

        WRITE (*,*)
        WRITE (*,*) ' Input file: ', InFile
        WRITE (*,*) ' Volume weighted size dist.: V(r)N(r) versus r'
        CALL Plot (n, r, f)

C   Estimate a residual background that remains in the data.
        Sum1 = zero
        Sum2 = zero
        DO 918 j = 1, npt
          weight = one / (sigma(j)**2)
          Sum1 = Sum1 + weight * (fit(j) -  datum(j))
          Sum2 = Sum2 + weight
  918   CONTINUE
        shift = Sum1 / Sum2

C  Scale the data back to 1/cm units and calculate Chi-squared
        ChiSq  = zero
        Chi2Bk  = zero
        DO 919 j = 1, npt
          z(j)  = (datum(j) - fit(j)) / sigma(j)
          ChiSq   = ChiSq + z(j)**2
          Chi2Bk  = Chi2Bk + (z(j) + shift/ sigma(j))**2
          datum(j) = cm2m * datum(j)
          sigma(j) = cm2m * sigma(j)
          fit(j) = cm2m * fit(j)
  919   CONTINUE
        shift = cm2m * shift / fac

        WRITE (*,*) ' standardized residuals vs. point number'
        CALL ResPlt (npt, z)

C  Let the file output begin!

        OPEN (UNIT = ioUnit, FILE=OutFil, STATUS='new')
        WRITE (ioUnit,*) ' Results of maximum entropy analysis of SAS'
        WRITE (ioUnit,*) '    version ',ProgVers, ', edited:', EditDate
        WRITE (ioUnit,*)
        WRITE (ioUnit,*) ' input file: ',  aTab, InFile
        WRITE (ioUnit,*) ' output file: ', aTab, OutFil
        WRITE (ioUnit,*) ' ------------------------------------------'
        WRITE (ioUnit,*)
        WRITE (ioUnit,*) ' N(D) dD is number of particles/cm**3'
        WRITE (ioUnit,*) '    of size between D and D + dD'
        WRITE (ioUnit,*)
        WRITE (ioUnit, 35591) 'D, A', aTab, 'V(D)*N(D), 1/A',
```

```
     >                 aTab, 'N(D), 1/A/cm^3'
       WRITE (ioUnit, 35591) '----', aTab, '--------------',
     >                 aTab, '--------------'
35591  FORMAT (1X, A12, A1, 1X, A15, A1, 1X, A15)

       DO 1001 i = 1, n
 1001    WRITE (ioUnit,3559) 2.*r(i), aTab, 0.5*f(i), aTab, 0.5*dNdr(i)
 3559  FORMAT (1X, F12.2, A1, 1X, 1PE15.5, A1, 1X, E15.5)


       WRITE (ioUnit,'(///)')
       WRITE (ioUnit, 1011) 'Q 1/A', aTab, 'I 1/cm', aTab,
     >                 '^I 1/cm', aTab, 'dI 1/cm', aTab, 'z'
       WRITE (ioUnit, 1011) '-----', aTab, '------', aTab,
     >                 '-------', aTab, '-------', aTab, '----'
 1011  FORMAT (A12, 3(A1, A12), 1X, A1, A12, 1X, A1, A12)

       DO 101  j = 1, npt
  101    WRITE (ioUnit,560) q(j), aTab, datum(j), aTab, fit(j),
     >          aTab, sigma(j), aTab, z(j)
  560    FORMAT (1PE12.4, 3(A1, E12.4), 1X, A1, 0PF12.6, 1X, A1, F12.6)

       WRITE (ioUnit,3301) InFile
       WRITE (*,3301) InFile
 3301  FORMAT (//' Input data: ', A40)

       WRITE (ioUnit,3302) RhoSq
       WRITE (*,3302) RhoSq
 3302  FORMAT (' Contrast = ', F15.7,' x 10^28 m^-4.')

       IF (iOption .EQ. 1) THEN
         WRITE (ioUnit,*) ' rods: dia=D, length=D*', Aspect
         WRITE (*,*) ' rods: dia=D, length=D*', Aspect
       ELSE IF (iOption .EQ. 2) THEN
         WRITE (ioUnit,*) ' disks: thickness=D, dia=D/', Aspect
         WRITE (*,*) ' disks: thickness=D, dia=D/', Aspect
       ELSE IF (iOption .EQ. 3) THEN
         WRITE (ioUnit,*) ' globs: D x D x D*', Aspect
         WRITE (*,*) ' globs: D x D x D*', Aspect
       ELSE IF (iOption .EQ. 4) THEN
         WRITE (ioUnit,*) ' delta-function Spheres: diameter=D'
         WRITE (*,*) ' delta-function Spheres: diameter=D'
       ELSE IF (iOption .EQ. 5) THEN
         WRITE (ioUnit,*) ' box-function Spheres: diameter=D'
         WRITE (*,*) ' box-function Spheres: diameter=D'
       ELSE IF (iOption .EQ. 6) THEN
         WRITE (ioUnit,*) ' slit-smeared spheroidal globs: diameter=D'
         WRITE (*,*) ' slit-smeared spheroidal globs: diameter=D'
         WRITE (ioUnit,*) ' slit-length (1/A) = ', sLengt
         WRITE (*,*) ' slit-length (1/A) = ', sLengt
       ELSE IF (iOption .EQ. 7) THEN
         WRITE (ioUnit,*) ' spheroidal globs: diameter=D'
         WRITE (*,*) ' spheroidal globs: diameter=D'
       END IF

       WRITE (ioUnit,53303) fac
       WRITE (*,53303) fac
```

```
53303   FORMAT (' Data conversion factor to 1/cm = ', 1PE12.5)

        WRITE (ioUnit,63303) err
        WRITE (*,63303) err
63303   FORMAT (' Error scaling factor = ', 1PE12.5)

        IF (LinLog .EQ. isLog) THEN
          WRITE (ioUnit,13304) 'geometric'
          WRITE (*,13304) 'geometric'
        ELSE
          WRITE (ioUnit,13304) 'algebraic'
          WRITE (*,13304) 'algebraic'
        END IF
13304   FORMAT (' Histogram bins are distributed in an increasing ',
     >          A9, ' series.')

        WRITE (ioUnit,3304) 'Minimum', Dmin
        WRITE (*,3304) 'Minimum', Dmin
        WRITE (ioUnit,3304) 'Maximum', Dmax
        WRITE (*,3304) 'Maximum', Dmax
 3304   FORMAT (1X, A7, ' particle dimension D = ',F12.2,' A.')

        WRITE (ioUnit,3306) n
        WRITE (*,3306) n
 3306   FORMAT (' Number of histogram bins = ',I4,'.')

        WRITE (ioUnit,3307) itermax
        WRITE (*,3307) itermax
 3307   FORMAT (' Maximum number of iterations allowed = ',I4,'.')

        WRITE (ioUnit,3314) max
        WRITE (*,3314) max
 3314   FORMAT (' Program left MaxEnt routine after ',
     *    I4,' iterations.')

        WRITE (ioUnit,3308) npt
        WRITE (*,3308) npt
 3308   FORMAT (' Target chi-squared (# data points) = ',I5,'.')

        WRITE (ioUnit,3309) ChiSq
        WRITE (*,3309) ChiSq
 3309   FORMAT (' Best value of chi-squared achieved = ',F12.6,'.')

        WRITE (ioUnit, 33091) 'the final', Entropy
        WRITE (*, 33091) 'the final', Entropy
        WRITE (ioUnit, 33091) 'a flat', LOG (FLOAT (n))
        WRITE (*, 33091) 'a flat', LOG (FLOAT (n))
33091   FORMAT (' Entropy of ', A9, ' distribution = ', F12.7,'.')

        WRITE (ioUnit,33101) SumN
        WRITE (*,33101) SumN
33101   FORMAT (' Total particles  = ', 1PE15.5,' per cubic cm.')

        WRITE (ioUnit,3310) SumV
        WRITE (*,3310) SumV
 3310   FORMAT (' Total volume fraction of all scatterers = ',
     *    F15.9,'.')
```

```
        WRITE (ioUnit,3311) 'smaller', Dmin, f(n+1)
        WRITE (ioUnit,3311) 'larger',  Dmax, f(n+2)
        WRITE (*,3311) 'smaller', Dmin, f(n+1)
        WRITE (*,3311) 'larger',  Dmax, f(n+2)
 3311   FORMAT (' Volume fraction ',A7,' than ', F12.2,
     *    ' A = ', 1PE13.5,'.')

        WRITE (ioUnit,3312) 'Volume', 'mode D value', 2.0 * r(modeV)
        WRITE (*,3312) 'Volume', 'mode D value', 2.0 * r(modeV)
        WRITE (ioUnit,3312) 'Volume', 'mean D value', DvMean
        WRITE (*,3312) 'Volume', 'mean D value', DvMean
        WRITE (ioUnit,3312) 'Volume', 'std. deviation', DvSDev
        WRITE (*,3312) 'Volume', 'std. deviation', DvSDev
        WRITE (ioUnit,3312) 'Number', 'mode D value', 2.0 * r(modeN)
        WRITE (*,3312) 'Number', 'mode D value', 2.0 * r(modeN)
        WRITE (ioUnit,3312) 'Number', 'mean D value', DnMean
        WRITE (*,3312) 'Number', 'mean D value', DnMean
        WRITE (ioUnit,3312) 'Number', 'std. deviation', DnSDev
        WRITE (*,3312) 'Number', 'std. deviation', DnSDev
 3312   FORMAT (1X, A6, '-weighted ', A14, ' = ', F12.5, ' A.')

        WRITE (ioUnit,3313) 'Min', q(1)
        WRITE (*,3313) 'Min', q(1)
        WRITE (ioUnit,3313) 'Max', q(npt)
        WRITE (*,3313) 'Max', q(npt)
 3313   FORMAT (1X, A3,'imum Q-vector = ', 1PE15.7, ' 1/A.')

        WRITE (ioUnit,3315) 'User-specified', Bkg
        WRITE (*,3315) 'User-specified', Bkg
        WRITE (ioUnit,3315) 'Suggested', Bkg - shift
        WRITE (*,3315) 'Suggested', Bkg - shift
 3315   FORMAT (1X, A14, ' background = ', F18.9,' input data units')

        WRITE (ioUnit,*) ' New background should give ChiSq = ', Chi2Bk
        WRITE (*,*) ' New background should give ChiSq = ', Chi2Bk

        CLOSE (UNIT=ioUnit, STATUS='keep')

C  Adjust the background default setting
C  Shift the intensity data just in case the user wants a Stability Check
C  Remember: background shifts down, intensity shifts up
C  Don't forget to put the data back into 1/m units!
        Bkg = Bkg - shift
        DO 4010  j = 1, npt
          datum(j) = (datum(j) + shift) / cm2m
          sigma(j) = sigma(j) / cm2m
 4010   CONTINUE

        IF (ABS ((Chi2Bk-ChiSq)/FLOAT (npt)) .LE. 0.05) THEN
          WRITE (*,*) ' The change in ChiSquared should be < 5%.'
 4000     WRITE (*,*) ' Run the Stability Check? (Y/<N>)'
          READ (*,'(A1)') YN
          IF (YN .EQ. 'y'  .OR.  YN .EQ. 'Y') GO TO 228
          IF (YN.NE.' ' .AND. YN.NE.'n' .AND. YN.NE.'N') GO TO 4000
        END IF
```

```
      WRITE (*,3200) OutFil
3200  FORMAT (/,' The program is finished.', /,
     1   ' The output file is: ', A40)
      GO TO 1

3199  STOP
      END


      SUBROUTINE GetInf (InFile, OutFil, iOption, Aspect, LinLog,
     >         nBin, Dmin, Dmax, IterMax, RhoSq, fac, err, qMin,
     >         qMax, Bkg, sLengt)
      IMPLICIT REAL*8 (A-H,O-Z)
      IMPLICIT INTEGER*4 (I-N)
      CHARACTER*40 InFile, OutFil
      PARAMETER (Ro2Max = 1.e6, ItrLim = 200, AbsMax = 1.e3)
      PARAMETER (DiaMin = 1., DiaMax = 1.e6, ErrMax = 1.e6)
      PARAMETER (MaxPts = 300, MaxBin = 102)
      PARAMETER (isLin = 1, isLog = 2)

   1  WRITE (*,*) ' Input file? <Quit>'
        READ (*, 2) InFile
   2    FORMAT (A40)
        IF (InFile.EQ.' ') RETURN

   3  WRITE (*,*) ' Output file?'
        READ (*, 2) OutFil
        IF (OutFil .EQ. ' ') GO TO 3
        IF (OutFil .EQ. InFile) GO TO 1

      suggest = qMin
  16  WRITE (*,*) ' Minimum q-vector? [1/A] <', suggest, '>'
      READ (*, '(F10.0)') qMin
      IF (qMin .LT. 0) GO TO 16
      IF (qMin .EQ. 0) qMin = suggest

      suggest = qMax
  17  WRITE (*,*) ' Maximum q-vector? [1/A] <', suggest, '>'
      READ (*, '(F10.0)') qMax
      IF (qMax .EQ. 0) qMax = suggest
      IF (qMax .LE. 0) GO TO 17
      IF (qMax .LE. qMin) GO TO 1

      suggest = RhoSq
  13  WRITE (*,*) ' Scattering contrast? [10^28 m^-4] <',suggest,'>'
      READ (*, '(F10.0)') RhoSq
      IF (RhoSq .EQ. 0) RhoSq = suggest
      IF (RhoSq .LT. 0 .OR. RhoSq .GT. Ro2Max) GO TO 13

      suggest = fac
  14  WRITE (*,*) ' Factor to convert data to 1/cm? <', suggest, '>'
      READ (*, '(F10.0)') fac
      IF (fac .EQ. 0) fac = suggest
      IF (fac .LE. 0 .OR. fac .GT. AbsMax) GO TO 14

      suggest = err
  15  WRITE (*,*) ' Error scaling factor? <', suggest, '>'
```

```
      READ (*, '(F10.0)') err
      IF (err .EQ. 0) err = suggest
      IF (err .LE. 0 .OR. err .GT. ErrMax) GO TO 15

      suggest = Bkg
 18   WRITE (*,*) ' Background? <', suggest, '>'
      READ (*, '(F10.0)') Bkg
      IF (Bkg .EQ. 0) Bkg = suggest

      Last = iOption
  4     WRITE (*,*) '  Select a form model for the scatterer:'
        WRITE (*,*) '  (See the User Guide for complete explanations)'
        WRITE (*,*) ' 1: rods        2: disks       3: globules'
        WRITE (*,*) ' 4: spheres (usual form)       ',
     >              '5: spheres (integrated)'
        WRITE (*,*) ' 6: spheroids (slit-smeared)   ',
     >              '7: spheroids (not smeared)'
        WRITE (*,*) '  Which option number?  <', Last, '>'
        READ (*, '(I4)') iOption
        IF (iOption .EQ. 0) iOption = Last
        IF (iOption .LT. 1  .OR.  iOption .GT. 7) GO TO 4

      suggest = Aspect
  6   IF (iOption .GE. 1  .AND.  iOption .LE. 3) THEN
        WRITE (*,*) ' AR = Aspect Ratio, useful ranges are indicated'
        IF (iOption .EQ. 1) THEN
          WRITE (*,*) ' diameter D, length D * AR, AR > 5'
        ELSE IF (iOption .EQ. 2) THEN
          WRITE (*,*) ' thickness D, diameter D / AR, AR < 0.2'
        ELSE IF (iOption .EQ. 3) THEN
          WRITE (*,*) ' D x D x D * AR, 0.3 < AR < 3'
        END IF
        WRITE (*,*) ' Aspect ratio?  <', suggest, '>'
        READ (*,'(F10.0)') Aspect
        IF (Aspect .EQ. 0) Aspect = suggest
        IF (Aspect .LT. 0) GO TO 6
      END IF

      suggest = sLengt
 61   IF (iOption .EQ. 6) THEN
        WRITE (*,*) ' Slit-smeared globs.  ',
     >        'Slit-length [1/A]? <', suggest, '>'
        READ (*,'(F10.0)') sLengt
        IF (sLengt .EQ. 0) sLengt = suggest
        IF (sLengt .LT. 0) GO TO 61
      END IF

      Last = LinLog
  7   WRITE (*,*) ' Bin step scale? (1=Linear, 2=Log) <', Last, '>'
      READ (*, '(I4)') LinLog
      IF (LinLog .EQ. 0) LinLog = Last
      IF (LinLog .NE. isLin  .AND. LinLog .NE. isLog) GO TO 7

      Last = nBin
  8   WRITE (*,*) ' Number of histogram bins? <', Last, '>'
      READ (*, '(I4)') nBin
      IF (nBin .EQ. 0) nBin = Last
```

```
      IF (nBin .LT. 2 .OR. nBin .GT. (MaxBin-2)) GO TO 8

      suggest = Dmax
    9 WRITE (*,*) ' Maximum value of D? [A] <', suggest, '>'
      READ (*, '(F10.0)') Dmax
      IF (Dmax .EQ. 0) Dmax = suggest
      IF (Dmax .LT. nBin*DiaMin .OR. Dmax .GE. DiaMax) GO TO 9

      Suggest = Dmax / FLOAT (nBin)
   11 WRITE (*,*) ' Minimum value of D? [A] <', suggest, '>'
      READ (*, '(F10.0)') Dmin
      IF (Dmin .EQ. 0) Dmin = suggest
      IF (Dmin .GE. DMax .OR. Dmin .LT. DiaMin) GO TO 1

      IF (IterMax .GT. ItrLim) IterMax = ItrLim
      Last = IterMax
   12 WRITE (*,*) ' Maximum number of iterations? <', Last, '>'
      READ (*, '(I4)') IterMax
      IF (IterMax .EQ. 0) IterMax = Last
      IF (IterMax .LT. 0 .OR. IterMax .GT. ItrLim) GO TO 12

      RETURN
      END


      SUBROUTINE opus(n,npt,x,ox)     ! solution-space -> data-space
      IMPLICIT REAL*8 (A-H,O-Z)
      IMPLICIT INTEGER*4 (I-N)
      PARAMETER (MaxPts=300, MaxBin=102)
      COMMON /space1/ grid
      DIMENSION x(MaxBin), grid(MaxBin,MaxPts), ox(MaxPts)
      DO 3  j = 1, npt
        sum = 0.
        DO 4  i = 1, n
         sum = sum + x(i) * grid(i,j)
    4   CONTINUE
        ox(j) = sum
    3 CONTINUE
      RETURN
      END


      SUBROUTINE tropus(n,npt,ox,x)   ! data-space -> solution-space
      IMPLICIT REAL*8 (A-H,O-Z)
      IMPLICIT INTEGER*4 (I-N)
      PARAMETER (MaxPts=300, MaxBin=102)
      COMMON /space1/ grid
      DIMENSION x(MaxBin), grid(MaxBin,MaxPts), ox(MaxPts)
      DO 5  i = 1, n
        sum = 0.
        DO 6  j = 1, npt
          sum = sum + ox(j) * grid(i,j)
    6   CONTINUE
        x(i) = sum
    5 CONTINUE
      RETURN
      END
```

```
      SUBROUTINE MaxEnt(n,npt, f,datum,sigma, flat,base,iter,itermax)
      IMPLICIT REAL*8 (A-H,O-Z)
      IMPLICIT INTEGER*4 (I-N)
      PARAMETER (MaxPts=300, MaxBin=102)
      DIMENSION f(MaxBin), datum(MaxPts), sigma(MaxPts)
      DIMENSION base(MaxBin)

      COMMON /space1/ grid
      DIMENSION grid(MaxBin,MaxPts)

      COMMON /space5/ chisq, chtarg, chizer, fSum, blank
      COMMON /space2/ beta, c1, c2, s1, s2
      DIMENSION beta(3), c1(3), c2(3,3), s1(3), s2(3,3)

      COMMON /space3/ ox, z, cgrad, sgrad, xi, eta
      DIMENSION ox(MaxPts), z(MaxPts)
      DIMENSION cgrad(MaxBin), sgrad(MaxBin)
      DIMENSION xi(MaxBin,3), eta(MaxPts,3)

      DIMENSION Entropy(201), Convrg(201)
      PARAMETER (TstLim = 0.05)       ! for convergence
      DATA one, zero /1.0, 0.0/       ! compiler-independence!

      blank = flat
      exp1 = EXP(one)

      IF (blank .EQ. zero) THEN
        DO 1004 i = 1, n
1004      blank = blank + base(i)
        blank = blank / FLOAT(n)
        WRITE (*,*) ' Average of BASE = ', blank
      ELSE
        WRITE (*,*) ' Setting BASE constant at ', blank
        DO 1003 i = 1, n
1003      base(i) = blank
      ENDIF

      WRITE (*,*) ' MaxEnt routine beginning ...'

      chizer = FLOAT(npt)
      chtarg = chizer
      m = 3
      DO 8 i = 1, n
   8    f(i) = base(i)        ! initial distribution is featureless

      iter = 0
   6  iter = iter + 1         ! The iteration loop begins here!
      CALL opus (n, npt, f, ox)       ! calc. the model intensity from "f"
      chisq = zero
      DO 10 j = 1, npt
        a = (ox(j) - datum(j)) / sigma(j)
        chisq = chisq + a**2
  10    ox(j) = 2. * a / sigma(j)
      CALL tropus(n,npt,ox,cgrad)     ! cGradient = Grid * ox
      test = zero     ! mismatch between entropy and ChiSquared gradients
```

```
      snorm = zero    ! entropy term
      cnorm = zero    ! ChiSqr term
      tnorm = zero    ! norm for the gradient term TEST
      fSum = zero     ! find the sum of the f-vector
      DO 12  i = 1, n
        fSum = fSum + f(i)
        sgrad(i) = -LOG(f(i)/base(i)) / (blank*exp1)
        snorm = snorm + f(i) * sgrad(i)**2
        cnorm = cnorm + f(i) * cgrad(i)**2
        tnorm = tnorm + f(i) * sgrad(i) * cgrad(i)
12    CONTINUE
      snorm = SQRT(snorm)
      cnorm = SQRT(cnorm)
      a = one
      b = one / cnorm
      IF (iter .GT. 1) THEN
        test = SQRT(0.5*(one-tnorm/(snorm*cnorm)))
        a = 0.5 / (snorm * test)
        b = 0.5 * b / test
      ENDIF
      DO 13 i = 1, n
        xi(i,1) = f(i) * cgrad(i) / cnorm
        xi(i,2) = f(i) * (a * sgrad(i) - b * cgrad(i))
13    CONTINUE
      CALL opus (n,npt,xi(1,1),eta(1,1))
      CALL opus (n,npt,xi(1,2),eta(1,2))
      DO 14 j = 1, npt
        ox(j) = eta(j,2) / (sigma(j)**2)
14    CONTINUE
      CALL tropus (n,npt,ox,xi(1,3))
      a = zero
      DO 15 i = 1, n
        b = f(i) * xi(i,3)
        a = a + b * xi(i,3)
        xi(i,3) = b
15    CONTINUE
      a = one / SQRT(a)
      DO 16 i = 1, n
        xi(i,3) = a * xi(i,3)
16    CONTINUE
      CALL opus (n,npt,xi(1,3),eta(1,3))
      DO 17 k = 1, m
        s1(k) = zero
        c1(k) = zero
        DO 18 i = 1, n
          s1(k) = s1(k) + xi(i,k) * sgrad(i)
          c1(k) = c1(k) + xi(i,k) * cgrad(i)
18      CONTINUE
        c1(k) = c1(k) / chisq
17    CONTINUE
      DO 19 k = 1, m
        DO 19 l = 1, k
          s2(k,l) = zero
          c2(k,l) = zero
          DO 20 i = 1, n
            s2(k,l) = s2(k,l) - xi(i,k) * xi(i,l) / f(i)
20        CONTINUE
```

```
            DO 21 j = 1, npt
              c2(k,l) = c2(k,l) + eta(j,k) * eta(j,l) / (sigma(j)**2)
   21       CONTINUE
            s2(k,l) = s2(k,l) / blank
            c2(k,l) = 2. * c2(k,l) / chisq
   19   CONTINUE
        c2(1,2) = c2(2,1)
        c2(1,3) = c2(3,1)
        c2(2,3) = c2(3,2)
        s2(1,2) = s2(2,1)
        s2(1,3) = s2(3,1)
        s2(2,3) = s2(3,2)
        beta(1) = -0.5 * c1(1) / c2(1,1)
        beta(2) = zero
        beta(3) = zero
        IF (iter .GT. 1) CALL Move(3)

C  Modify the current distribution (f-vector)
        fSum = zero             ! find the sum of the f-vector
        fChange = zero          ! and how much did it change?
        DO 23 i = 1, n
          df = beta(1)*xi(i,1)+beta(2)*xi(i,2)+beta(3)*xi(i,3)
          IF (df .LT. -f(i)) df = 0.001 * base(i) - f(i)        ! a patch
          f(i) = f(i) + df              ! adjust the f-vector
          fSum = fSum + f(i)
          fChange = fChange + df
   23   CONTINUE

        s = zero
        DO 24  i = 1, n
          temp = f(i) / fSum            ! fraction of f(i) in this bin
          s = s - temp * LOG (temp)     ! from Skilling and Bryan, eq. 1
   24   CONTINUE

        CALL opus (n, nPt, f, z)        ! model the data-space from f(*)
        ChiSq = zero                    ! get the new ChiSquared
        DO 25  j = 1, nPt
          z(j) = (datum(j) - z(j)) / sigma(j)   ! the residuals
          ChiSq = ChiSq + z(j)**2       ! report this ChiSq, not the one above
   25   CONTINUE

        Entropy(iter) = s
        Convrg(iter) = LOG (ChiSq)
        IF (iter .GT. 2) THEN   ! show our progress
          temp = (Convrg(iter) + Convrg(iter-1) + Convrg (iter-2))/3.
          IF (ABS (one - Convrg(iter)/temp) .GT. 0.02) THEN
            WRITE (*,*)
            WRITE (*,*) ' LOG (ChiSq) vs. iteration number'
            CALL BasPlt (iter, Convrg, LOG (ChiZer))
          END IF
          WRITE (*,*)
          WRITE (*,*) ' Entropy vs. iteration number'
          temp = LOG (FLOAT (n))        ! the maximum entropy possible
          CALL BasPlt (iter, Entropy, temp)
        END IF

  300   WRITE (*,*)
```

```
        WRITE (*,*) ' Residuals'
        CALL ResPlt (npt, z)

        WRITE (*,*)
        WRITE (*,*) ' Distribution'
        CALL BasPlt (n, f, blank)

        WRITE (*,*) ' #', iter, ' of ', itermax, ',  n  = ', npt
        WRITE (*,200) test, s
        WRITE (*,201) 'target',SQRT(chtarg/npt), 'now',SQRT(chisq/npt)
        WRITE (*,202) 'sum', fSum, ' % change', 100.*fChange/fSum
  200   FORMAT (' test = ', F9.5, ',  Entropy = ', F12.7)
  201   FORMAT (' SQRT((Chi^2)/n):', A8,' = ', F12.8,A10,' = ', F12.8)
  202   FORMAT ('        f-vector:', A8,' = ', F12.8,A10,' = ', F12.8)

C  See if we have finished our task.
        IF (ABS(chisq/chizer-one) .LT. 0.01) THEN  ! hardest test first
          IF (test .LT. TstLim) THEN            ! same solution gradient?
C               We've solved it but now must check for a bizarre condition.
C               Calling routine says we failed if "iter = iterMax".
C               Let's increment (maybe) iterMax so this doesn't happen.
            IF (iter .EQ. iterMax) iterMax = iterMax + 1
            RETURN
          END IF
        END IF
        IF (iter .LT. iterMax) GO TO 6

C  Ask for more time to finish the job.
        WRITE (*,*)
        WRITE (*,*) ' Maximum iterations have been reached.'
 2001   WRITE (*,*) ' How many more iterations? <none>'
        READ (*,'(I4)') more
        IF (more .LT. 0) GO TO 2001
        IF (more .EQ. 0) RETURN
        iterMax = iterMax + more
        GO TO 6
        END


        SUBROUTINE Move(m)
        IMPLICIT REAL*8 (A-H,O-Z)
        IMPLICIT INTEGER*4 (I-N)
        PARAMETER ( MxLoop = 500 )      ! for no solution
        PARAMETER ( Passes = 1.e-3 )    ! convergence test
        COMMON /space5/ chisq, chtarg, chizer, fSum, blank
        COMMON /space2/ beta, c1, c2, s1, s2
        DIMENSION beta(3), c1(3), c2(3,3), s1(3), s2(3,3)
        DATA one, zero /1.0, 0.0/       ! compiler-independence!
        a1 = zero                       ! lower bracket  "a"
        a2 = one                        ! upper bracket of "a"
        cmin = ChiNow (a1, m)
        IF (cmin*chisq .GT. chizer) ctarg = 0.5*(one + cmin)
        IF (cmin*chisq .LE. chizer) ctarg = chizer/chisq
        f1 = cmin - ctarg
        f2 = ChiNow (a2,m) - ctarg
        DO 1  loop = 1, MxLoop
          anew = 0.5 * (a1+a2)          ! choose a new "a"
```

```
          fx = ChiNow (anew,m) - ctarg
          IF (f1*fx .GT. zero) a1 = anew
          IF (f1*fx .GT. zero) f1 = fx
          IF (f2*fx .GT. zero) a2 = anew
          IF (f2*fx .GT. zero) f2 = fx
          IF (abs(fx) .LT. Passes) GO TO 2
    1   CONTINUE

C  If the preceding loop finishes, then we do not seem to be converging.
C       Stop gracefully because not every computer uses control-C (etc.)
C       as an exit procedure.
        WRITE (*,*) ' Loop counter = ', MxLoop
        PAUSE ' No convergence in alpha chop (MOVE).  Press return ...'
        STOP ' Program cannot continue.'

    2   w = Dist (m)
        IF (w .LE. 0.1*fSum/blank) GO TO 1042
        DO 1044 k=1,m
          beta(k) = beta(k) * SQRT(0.1 * fSum/(blank * w))
 1044   CONTINUE
 1042   chtarg = ctarg * chisq
        RETURN
        END


        REAL*8 FUNCTION Dist (m)
        IMPLICIT REAL*8 (A-H,O-Z)
        IMPLICIT INTEGER*4 (I-N)
        COMMON /space5/ chisq, chtarg, chizer, fSum, blank
        COMMON /space2/ beta, c1, c2, s1, s2
        DIMENSION beta(3), c1(3), c2(3,3), s1(3), s2(3,3)
        DATA one, zero /1.0, 0.0/       ! compiler-independence!
        w = zero
        DO 26  k = 1, m
          z = zero
          DO 27  l = 1, m
            z = z - s2(k,l) * beta(l)
   27     CONTINUE
          w = w + beta(k) * z
   26   CONTINUE
        Dist = w
        RETURN
        END


        REAL*8 FUNCTION ChiNow(ax,m)
        IMPLICIT REAL*8 (A-H,O-Z)
        IMPLICIT INTEGER*4 (I-N)
        COMMON /space5/ chisq, chtarg, chizer, fSum, blank
        COMMON /space2/ beta, c1, c2, s1, s2
        DIMENSION beta(3), c1(3), c2(3,3), s1(3), s2(3,3)
        DIMENSION a(3,3), b(3)
        DATA one, zero /1.0, 0.0/       ! compiler-independence!
        bx = one - ax
        DO 28  k = 1, m
          DO 29  l = 1, m
            a(k,l) = bx * c2(k,l)  -  ax * s2(k,l)
```

```
   29     CONTINUE
          b(k) = -(bx * c1(k)  -  ax * s1(k))
   28   CONTINUE
        CALL ChoSol(a,b,m,beta)
        w = zero
        DO 31  k = 1, m
          z = zero
          DO 32  l = 1, m
            z = z + c2(k,l) * beta(l)
   32     CONTINUE
          w = w + beta(k) * (c1(k) + 0.5 * z)
   31   CONTINUE
        ChiNow = one +  w
        RETURN
        END


        SUBROUTINE ChoSol(a, b, n, beta)
        IMPLICIT REAL*8 (A-H,O-Z)
        IMPLICIT INTEGER*4 (I-N)
        DIMENSION fl(3,3), a(3,3), bl(3), b(3), beta(3)
        DATA one, zero /1.0, 0.0/       ! compiler-independence!
        IF (a(1,1) .LE. zero) THEN
          WRITE (*,*) ' Fatal error in CHOSOL: a(1,1) = ', a(1,1)
          PAUSE ' Press <RETURN> to end program ...'
          STOP ' Program cannot continue.'
        END IF
        fl(1,1) = SQRT(a(1,1))
        DO 35  i = 2, n
          fl(i,1) = a(i,1) / fl(1,1)
          DO 35  j = 2, i
            z = zero
            DO 36  k = 1, j-1
              z = z + fl(i,k) * fl(j,k)
   36       CONTINUE
            z = a(i,j) - z
            IF (j .EQ. i) fl(i,j) = SQRT(z)
            IF (j .NE. i) fl(i,j) = z / fl(j,j)
35      CONTINUE
        bl(1) = b(1) / fl(1,1)
        DO 37  i=2, n
          z = zero
          DO 38  k = 1, i-1
            z = z + fl(i,k) * bl(k)
   38     CONTINUE
          bl(i) = (b(i) - z) / fl(i,i)
   37   CONTINUE
        beta(n) = bl(n) / fl(n,n)
        DO 39  i1 = 1, n-1
          i = n - i1
          z = zero
          DO 40  k = i+1, n
            z = z + fl(k,i) * beta(k)
   40     CONTINUE
          beta(i) = (bl(i) - z) / fl(i,i)
   39   CONTINUE
        RETURN
```

```
        END


        SUBROUTINE ResPlt (n, x)
C       Draw a plot of the standardized residuals on the screen.
C       Mark the rows of + and - one standard deviation.
        IMPLICIT REAL*8 (A-H,O-Z)
        IMPLICIT INTEGER*4 (I-N)
        DIMENSION x(1)
        CHARACTER*1 Blank, Symbol, hBordr, vBordr, resSym
        PARAMETER (Blank = ' ', Symbol = 'O', resSym = '=')
        PARAMETER (hBordr = '-', vBordr = '|')
        COMMON /space4/ screen, MaxCol, MaxRow, MxC2, MxR2
        CHARACTER*1 screen(100, 150)
        IF (n .LT. 2) RETURN    ! not enough data

C  Find out how many points to pack per column and how many columns
        nPack = 1 + INT(FLOAT (n) / MaxCol - 1./n)
        nCol = INT((n - 1./n)/nPack + 1)

C  prepare the "screen" for drawing
        DO 1  j = 1, nCol + 2
          DO 1  i = 1, MxR2
            screen(i,j) = Blank
    1   CONTINUE
        DO 2  i = 2, nCol + 1
          screen(MxR2,i) = hBordr
    2     screen(1,i) = hBordr
        DO 3  i = 2, MaxRow + 1
          screen(i,nCol+2) = vBordr
    3     screen(i,1) = vBordr

C  get the data limits
        xMax = 1.
        xMin = -1.
        DO 4 i = 1, n
          IF (x(i) .GT. xMax) xMax = x(i)
          IF (x(i) .LT. xMin) xMin = x(i)
    4   CONTINUE
        RowDel = (MaxRow - 1) / (xMax - xMin)

C  show the standard deviation bars
        mPlus = 1 + INT((1 - xMin)*RowDel + 1)
        mMinus = 1 + INT((-1 - xMin)*RowDel + 1)
        DO 5  i = 2, nCol + 1
          screen(mMinus,i) = resSym
    5     screen(mPlus,i) = resSym

C  draw the data (overdrawing the residuals bars if necessary)
        DO 6  i = 1, n
          mCol = 1 + INT((i - 1./n)/nPack + 1)          ! addressing function
          mRow = 1 + INT((x(i) - xMin)*RowDel + 1)      ! +1 for the plot frame
          screen(mRow, mCol) = Symbol
    6   CONTINUE

C  convey the "screen" to the default output
        WRITE (*,*) nPack, ' point(s) per column'
```

```
        WRITE (*,*) 1./RowDel, ' standard deviations per row'
        DO 7  i = MxR2, 1, -1
    7     WRITE (*,*) (screen(i,j), j = 1, nCol + 2)

        RETURN
        END


        SUBROUTINE BasPlt (n, x, basis)
C       Draw a plot of some data and indicate a basis line on the
C       the plot.  That is, that line below which the data is
C       not meaningful.  The basis here is taken to be a constant.
        IMPLICIT REAL*8 (A-H,O-Z)
        IMPLICIT INTEGER*4 (I-N)
        DIMENSION x(1)
        CHARACTER*1 Blank, Symbol, hBordr, vBordr, BasSym
        PARAMETER (Blank = ' ', Symbol = 'O', BasSym = '=')
        PARAMETER (hBordr = '-', vBordr = '|')

        COMMON /space4/ screen, MaxCol, MaxRow, MxC2, MxR2
        CHARACTER*1 screen(100, 150)

        IF (n .LT. 2) RETURN    ! not enough data

C  Find out how many points to pack per column and how many columns
        nPack = 1 + INT(FLOAT (n) / MaxCol - 1./n)
        nCol = INT((n - 1./n)/nPack + 1)

C  prepare the "screen" for drawing
        DO 1  j = 1, nCol + 2
          DO 1  i = 1, MxR2
            screen(i,j) = Blank
    1   CONTINUE
        DO 2  i = 2, nCol + 1
          screen(MxR2,i) = hBordr
    2     screen(1,i) = hBordr
        DO 3  i = 2, MaxRow + 1
          screen(i,nCol+2) = vBordr
    3     screen(i,1) = vBordr

C  get the data limits
        xMax = basis
        xMin = basis
        DO 4 i = 1, n
          IF (x(i) .GT. xMax) xMax = x(i)
          IF (x(i) .LT. xMin) xMin = x(i)
    4   CONTINUE
        RowDel = (MaxRow - 1) / (xMax - xMin)

C  show the basis line
        mPlus = 1 + INT((basis - xMin)*RowDel + 1)
        DO 5  i = 2, nCol + 1
    5     screen(mPlus,i) = basSym

C  draw the data (overdrawing the basis bars if necessary)
        DO 6  i = 1, n
          mCol = 1 + INT((i - 1./n)/nPack + 1)          ! addressing function
```

```
          mRow = 1 + INT((x(i) - xMin)*RowDel + 1)      ! +1 for the plot frame
          screen(mRow, mCol) = Symbol
    6   CONTINUE

C  convey the "screen" to the default output
        WRITE (*,*) nPack, ' point(s) per column'
        WRITE (*,*) 1./RowDel, ' units per row'
        DO 7  i = MxR2, 1, -1
    7     WRITE (*,*) (screen(i,j), j = 1, nCol + 2)

        RETURN
        END


        SUBROUTINE Plot (n,x,y)
C       Make a scatter plot on the default display device (UNIT=*).
C       MaxRow and MaxCol correspond to the display dimensions.
        IMPLICIT REAL*8 (A-H,O-Z)
        IMPLICIT INTEGER*4 (I-N)
        DIMENSION x(1), y(1)
        CHARACTER*1 Blank, Symbol, hBordr, vBordr
        PARAMETER (Blank = ' ', Symbol = 'O')
        PARAMETER (hBordr = '-', vBordr = '|')

        COMMON /space4/ screen, MaxCol, MaxRow, MxC2, MxR2
        CHARACTER*1 screen(100, 150)

        IF (n .LT. 2) RETURN    ! not enough data

C  prepare the "screen" for drawing
        DO 1  j = 1, MxC2
          DO 1  i = 1, MxR2
            screen(i,j) = Blank
    1   CONTINUE
        DO 2  i = 2, MaxCol+1
          screen(MxR2,i) = hBordr
    2     screen(1,i) = hBordr
        DO 3  i = 2, MaxRow+1
          screen(i,MxC2) = vBordr
    3     screen(i,1)  = vBordr

C  get the data limits
        xMin = x(1)
        xMax = x(1)
        yMin = y(1)
        yMax = y(1)
        DO 4 i = 2, n
          IF (x(i).GT.xMax) xMax=x(i)
          IF (x(i).LT.xMin) xMin=x(i)
          IF (y(i).GT.yMax) yMax=y(i)
          IF (y(i).LT.yMin) yMin=y(i)
    4   CONTINUE
        ColDel = (MaxCol - 1) / (xMax - xMin)
        RowDel = (MaxRow - 1) / (yMax - yMin)

C  data scaling functions are offset by +1 for plot frame
        DO 5  i = 1, n
```

```
          mCol = 1 + INT((x(i) - xMin)*ColDel + 1)
          mRow = 1 + INT((y(i) - yMin)*RowDel + 1)
    5     screen(mRow, mCol) = Symbol

C  convey the "screen" to the default output
        WRITE (*,*) 1./ColDel, ' units per column'
        WRITE (*,*) 1./RowDel, ' units per row'
        DO 6  i = MaxRow + 2, 1, -1
    6     WRITE (*,*) (screen(i,j), j = 1, MaxCol + 2)
        RETURN
        END
```

Bibliography

[1] A. J. ALLEN, D. GAVILLET, AND J. R. WEERTMAN, *SANS and TEM Studies of Isothermal M_2C Carbide Precipitation in Ultrahigh Strength AF1410 Steels*, Acta Metall Mater, 41 (1993), pp. 1869–1884.

[2] G. E. BACKUS AND F. GILBERT, *The Resolving Power of Gross Earth Data*, Geophys J R Astron Soc, 16 (1968), pp. 169–205.

[3] C. S. BARRETT, *Crystal structure of metals*, in Metallography and Microstructures, K. Mills, J. R. Davis, J. D. Destefani, D. A. Dieterich, G. M. Crankovic, and H. J. Frissell, eds., vol. 9, American Society for Metals, Metals Park, Ohio, ninth ed., 1985, pp. 706–720.

[4] J. BEARDEN AND A. BURR, *Reevaluation of x-ray atomic energy levels*, Rev Mod Phys, 39 (1967), pp. 125–142.

[5] N. F. BERK, *Scattering properties of a model bicontinuous structure with a well-defined length scale*, Phys Rev Lett, 58 (1987), p. 2718.

[6] W. E. BLASS AND G. W. HALSEY, *Deconvolution of Absorption Spectra*, Academic Press, Inc., New York City, 1981.

[7] G. BODINE AND R. MCDONALD, *Laboratory and Pilot Commercial Process / Product Development of Modified 9Cr-1Mo Ferritic Alloy*, in Ferritic Steels for High Temperature Applications, A. K. Khare, ed., Metals Park, Ohio, 1983, American Society for Metals, pp. 9–20.

[8] G. C. BODINE, B. CHAKRAVARTI, S. HARKNESS, C. OWENS, B. ROBERTS, D. VANDERGRIFF, AND C. WARD, *The Development of a 9 Cr Steel with Improved Strength and Toughness*, in Ferritic Steels for Fast Reactor Steam Generators, S. Pugh and E. Little, eds., London, 1978, British Nuclear Energy Society, pp. 160–164.

[9] U. BONSE AND M. HART, *Tailless x-ray single-crystal reflection curves obtained by multiple reflection*, Appl Phys Lett, 7 (1965), pp. 238–240.

[10] ——, *Small angle x-ray scattering by spherical particles of polystyrene and polyvinyltoluene*, Z fur Physik, 189 (1966), pp. 151–162.

[11] U. BONSE AND G. MATERLIK, *Interferometric dispersion measurements with synchrotron radiation*, in Anomalous Scattering, S. Ramaseshan and S. Abrahams, eds., Munksgaard, Copenhagen, 1985, pp. 107–109.

[12] U. BONSE, G. MATERLIK, AND W. SCHRODER, *Perfect crystal monochromators for synchrotron radiation*, J Appl Cryst, 9 (1976), pp. 223–230.

[13] M. BOOKER, V. K. SIKKA, AND B. BOOKER, *Comparison of the Mechanical Strength Properties of Several High-Chromium Ferritic Steels*, in Ferritic Steels for High Temperature Applications, A. K. Khare, ed., Metals Park, Ohio, 1983, American Society for Metals, pp. 257–273.

[14] C. BOULDIN, R. FORMAN, AND M. BELL, *Silicon photodiode detector for flourescence exafs*, Rev Sci Instrum, 58 (1987), pp. 1891–1894.

[15] P. BROWN, *Languages: Three interviews*, Comm ACM, 27 (1984), pp. 352–355.

[16] H. BRUMBERGER, ed., *Small-Angle X-ray Scattering*, Gordon and Breach, Syracuse University, 1965.

[17] J. CADWALLADER-COHEN, W. ZYSICZK, AND R. DONNELLY, *The chaostron: An important advance in learning machines*, Comm ACM, 27 (1984), pp. 356–357.

[18] J. W. CAHN, *On spinodal decomposition*, Acta Metall, 9 (1961), pp. 795–801.

[19] L. CHANG, G. D. W. SMITH, AND G. B. OLSON, *Ageing and Tempering of Ferrous Martensites*, ???to appear in J de Physique, ??? (1985), p. ???

[20] H. CHEN AND M. KURIYAMA, *A high-resolution x-ray facility*, J Appl Cryst, 14 (1981), p. 280.

[21] D. T. CROMER AND D. LIBERMAN, *Relativistic calculation of anomalous scattering factors for x-rays*, J Chem Phys, 53 (1970), pp. 1891–1898.

[22] B. D. CULLITY, *Elements of X-ray Diffraction*, Addison-Wesley Series in Metallurgy and Materials, Addison-Wesley Publishing Company, Inc., Reading, Massachusetts, second ed., 1978.

[23] I. D. CULVERWELL AND G. CLARKE, *Validation of the Maximum Entropy Method for Interpreting Small-Angle Neutron Scattering Data*, Inst Phys Conf Ser, #81, Chap. 3 (1986), pp. 87–96.

[24] M. DEUTSCH, *The Asymmetrically Cut Bonse-Hart X-ray Diffractometer. I. Design Principles and Performance*, J Appl Cryst, 13 (1980), pp. 252–255.

[25] ——, *The Asymmetrically Cut Bonse-Hart X-ray Diffractometer. II. Comparison with the Kratky Camera*, J Appl Cryst, 13 (1980), pp. 256–258.

[26] M. DEUTSCH AND M. LUBAN, *Exact Solution of the Slit-Height Correction Problem in Small-Angle X-ray Scattering. I. The General Method and its Accuracy in Application to Simulated Data*, J Appl Cryst, 11 (1978), pp. 87–97.

[27] ——, *Exact Solution of the Slit-Height Correction Problem in Small-Angle X-ray Scattering. II. A Method for Arbitrary Slit Transmission Functions*, J Appl Cryst, 11 (1978), pp. 98–101.

[28] ——, *The Primitive Functions for Slit-Height Desmearing in SAXS*, J Appl Cryst, 20 (1987), pp. 179–181.

[29] Y. S. DING, S. R. HUBBARD, K. O. HODGSON, R. A. REGISTER, AND S. L. COOPER, *Anomalous Small-Angle X-ray Scattering from a Sulfonated Polystyrene Ionomer*, Macromolecules, 21 (1988), pp. 1698–1703.

[30] P. EISENBERGER, P. PLATZMAN, AND H. WINICK, *Resonant x-ray raman scattering studies using synchrotron radiation*, Phys Rev B, 13 (1976), pp. 2377–2380.

[31] J. EPPERSON AND P. THIYAGARAJAN, *Anomalous and Resonance Small-Angle Scattering*, J Appl Cryst, 21 (1988), pp. 652–662.

[32] ——, *International Conference on Applications and Techniques of Small-Angle Scattering*, vol. 21, Munksgaard, Copenhagen, 1988.

[33] I. FANKUCHEN AND M. H. JELLINEK, *Low-angle x-ray scattering*, Phys Rev, 67 (1945), p. 201.

[34] T. FUJITA, *Advanced High-Chromium Ferritic Steels for High Temperatures*, Metal Progress, August (1986), pp. 33–40.

[35] T. FUJITA, K. ASAKURA, AND T. SATO, *Development and Properties of New 10Cr-2Mo-V-Nb Heat Resisting Steel*, Trans ISIJ, 19 (1979), pp. 605–613.

[36] T. FUJITA, T. SATO, AND N. TAKAHASHI, *Effects of Mo and W on Long Term Creep Rupture Strength of 12%Cr Heat-Resisting Steel Containing V, Nb, and B*, Trans ISIJ, 18 (1978), pp. 115–124.

[37] T. FUJITA AND N. TAKAHASHI, *Effects of V and Nb on the Long Period Creep Rupture Strength of 12%Cr Heat-Resisting Steel Containing Mo and B*, Trans ISIJ, 18 (1978), pp. 269–278.

[38] ——, *The Effects of Small Amounts of Vanadium and Niobium on the Microstructure and the Creep Rupture Strength of 12% Chromium Heat Resisting Steels*, Trans ISIJ, 18 (1978), pp. 739–746.

[39] T. FUJITA, K. YAMASHITA, AND H. MIYAKE, *The Effect of Nickel and Cobalt on Elevated Temperature Properties and Microstructures of 10Cr-2Mo Heat Resisting Steels*, Trans ISIJ, 20 (1980), pp. 384–391.

[40] D. GAVILLET, *TEM examinations of AF1410 steel*. 1988.

[41] P. GEORGOPOULOS AND J. B. COHEN, *Study of Supported Platinum Catalysts by Anomalous Scattering*, J Catal, 92 (1985), pp. 211–215.

[42] O. GLATTER AND B. HAINISCH, *Improvements in Real-Space Deconvolution of SAS Data*, J Appl Cryst, 17 (1984), pp. 435–441.

[43] O. GLATTER AND O. KRATKY, *Small-Angle X-ray Scattering*, Academic Press, London, 1982.

[44] C. GLINKA, J. ROWE, AND J. LAROCK, *The small-angle neutron scattering spectrometer at the national bureau of standards*, J Appl Cryst, 19 (1986), pp. 427–439.

[45] M. GORE, *Grain-Refining Dispersions and Mechanical Properties in Ultrahigh-Strength Steels*, ph. d., Massachusetts Institute of Technology, 1989.

[46] P. GOUDEAU, A. FONTAINE, A. NAUDON, AND C. WILLIAMS, *Anomalous Small-Angle X-ray Scattering in Metallurgy: a Feasibility Experiment with an Al-Zn Alloy*, J Appl Cryst, 19 (1986), pp. 19–24.

[47] P. GOUDEAU, A. NAUDON, B. RODMACQ, P. MARGIN, AND A. CHAMBEROD, *??*, J de Physique Coll, 48 (1985), pp. C8–479.

[48] P. GOUDEAU, A. NAUDON, AND J. M. WELTER, *Small Angle X-ray Scattering Study of the Decomposition Process of the Powder Metallurgy Alloy Cu-15wt%Ni-8wt%Sn*, Scripta Metall, 22 (1988), pp. 1019–1022.

[49] M. GRUJICIC, *Design of M_2C Carbides for Secondary Hardening*, in 34th Sagamore Army Materials Research Conference, M. Azrin, ed., vol. In preparation, Lake George, NY, 1989.

[50] A. GUINIER AND G. FOURNET, *Small-Angle Scattering of X-rays*, John Wiley & Sons, New York, 1955.

[51] G. N. HAIDEMENOPOULOS, *Dispersed-Phase Transformation Toughening in Ultrahigh-Strength Steels*, ph. d., Massachusetts Institute of Technology, 1988.

[52] G. W. HALSEY AND W. E. BLASS, *Deconvolution Examples*, in Deconvolution with Applications in Spectroscopy, New York City, Academic Press, Inc., 1984, pp. 187–225.

[53] J. P. HAMMOND, *Effects of Alloying and Mechanical-Thermal Treatments on Hardness Tempering Curves of Modified 9 and 12 Cr - 1 Mo Steels*, tech. rep., Oak Ridge National Laboratory, Oak Ridge, TN 37830, 1981.

[54] R. HAMSTRA AND P. WENDLAND, *Noise and frequency response of silicon photodiode operational amplifier combination*, Appl Opt, 11 (1972), pp. 1539–1547.

[55] M. HANSEN AND K. ANDERKO, *Constitution of Binary Alloys*, Metallurgy and Metallurgical Engineering Series, McGraw-Hill Book Company, Inc., New York City, second ed., 1958.

[56] R. HENDRICKS, *A Unified Theory of Absolute Intensity Measurements in Small-Angle X-ray Scattering*, J Appl Cryst, 5 (1972), pp. 315–324.

[57] ——, *The 10-meter SAXS Camera at ORNL*, J Appl Cryst, 11 (1978), pp. 15–30.

[58] M. HILL, B. TANNER, M. HALLIWELL, AND M. LYONS, *Simulation of X-ray Double-Crystal Rocking Curves of Multiple and Inhomogeneous Heteroepitaxial Layers*, J Appl Cryst, 18 (1985), pp. 446–451.

[59] J. HOYT, O. LYON, J. SIMON, B. CLARK, B. DAVIS, AND D. DE FONTAINE, *The Determination of Partial Structure Functions in an Al-Zn-Ag Alloy*, Sol State Comm, 57 (1986), pp. 155–158.

[60] J. HOYT, M. SLUITER, B. CLARK, M. KRAITCHMAN, AND D. DE FONTAINE, *Anomalous X-ray Scattering Study of Early-Stage Precipitation in Al-Zn-Ag*, Acta Metall, 35 (1987), pp. 2315–2322.

[61] J. J. HOYT, *Applications of Anomalous Small-Angle X-ray Scattering*, in Chemical Applications of Synchrotron Radiation: Workshop Report, M. Beno and S. Rice, eds., Argonne National Laboratory, 1989, Advanced Photon Source, pp. 115–126.

[62] J. J. HOYT, D. DE FONTAINE, AND W. K. WARBURTON, *Determination of the Anomalous Scattering Factors for Cu, Ni and Ti using the Dispersion Relation*, J Appl Cryst, 17 (1984), pp. 344–351.

[63] T. JACH AND P. L. COWAN, *Pin diodes as detectors in the energy region 500 ev - 10 kev*, Nucl Instrum and Meth Phys Res, 208 (1983), pp. 423–425.

[64] R. W. JAMES, *The Optical Principles of the Diffraction of X-rays*, in The Optical Principles of the Diffraction of X-rays, L. Bragg, ed., vol. II of The Crystalline State, Cornell University Press, Ithaca, NY, 1965, p. 664.

[65] P. A. JANSSON, *Deconvolution with Applications in Spectroscopy*, Academic Press, Inc., New York City, 1984.

[66] P. R. JEMIAN AND G. G. LONG, *Silicon photodiode detector for small-angle x-ray scattering*, J Appl Cryst, 23 (1990), pp. 430–432.

[67] W. B. JONES, *Effects of Mechanical Cycling on the Substructure of Modified 9Cr-1Mo Ferritic Steel*, in Ferritic Steels for High Temperature Applications, A. K. Khare, ed., Metals Park, Ohio, 1983, American Society for Metals, pp. 221–235.

[68] P. KAESBERG, *The Use of the Double Crystal Spectrometer in the Analysis of Small-Angle Scattering*, ph. d., University of Wisconsin, 1949.

[69] P. KAESBERG, H. RITLAND, AND W. BEEMAN, *Small-angle reflections from collagen*, Phys Rev, 74 (1948), pp. 1255–1256.

[70] ——, *The use of the double crystal spectrometer in the analysis of small-angle scattering*, Phys Rev, 74 (1948), pp. 71–73.

[71] S. T. KIM, *Microstructural Evaluation of Ferritic Stainless Steels Deformed at High Temperatures*, ph. d., Northwestern University, 1985.

[72] S. T. KIM AND J. R. WEERTMAN, *Investigation of Microstructural Changes in a Ferritic Steel Caused by High Temperature Fatigue*, Metall. Trans. A, 19A (1988), pp. 999–1007.

[73] S. T. KIM, J. R. WEERTMAN, S. SPOONER, C. GLINKA, V. K. SIKKA, AND W. B. JONES, *Microstructural Evaluation of a Ferritic Stainless Steel by Small-Angle Neutron Scattering*, in Nondestructive Evaluation: Application to Materials Processing, O. Buck and S. M. Wolf, eds., Metals Park, Ohio, 1983, American Society for Metals, p. 8 total.

[74] R. KING AND L. EGNELL, *Historical Development of Steels Containing 8-10% Cr & 0-2% Mo and Future Directions for LMFBR Applications*, in Ferritic Steels for Fast Reactor Steam Generators, S. Pugh and E. Little, eds., London, 1978, British Nuclear Energy Society, pp. 74–81.

[75] J. KIRKLAND, T. JACH, R. NEISER, AND C. BOULDIN, *PIN Diode Detectors for Synchrotron X-rays*, Nucl Instrum and Meth Phys Res, A266 (1988), pp. 602–607.

[76] J. KIRKLAND, R. NEISER, W. ELAM, J. RIFE, AND W. HUNTER, *Synchrotron Radiation Beam Lines as X-ray Calibration Sources*, SPIE - X-ray Calibration: Techniques, Sources, Detectors, 689 (1986), pp. 188–197.

[77] C. KITTEL, *Introduction to Solid-State Physics*, John Wiley and Sons, Inc., New York City, third ed., 1966.

[78] M. H. J. KOCH AND J. BORDAS, *X-ray diffraction and scattering on disordered systems using synchrotron radiation*, Nucl Instrum and Meth Phys Res, 208 (1983), pp. 461–469.

[79] G. KOSTORZ, *Small Angle Scattering and its Application to Material Science*, vol. 15, in Neutron Scattering, vol. 15, New York City, Academic Press, 1979, pp. 227–289.

[80] R. D. L. KRONIG AND H. KRAMERS, *Zur theorie der absorptionen und dispersion in den röntgenspektren*, Z Phys, 48 (1928), pp. 174–179.

[81] J. A. LAKE, *An Iterative Method of Slit-Correcting Small-Angle X-ray Data*, Acta Cryst, 23 (1967), pp. 191–194.

[82] H. M. LEE, *Stability and Coarsening Resistance of M_2C Carbides in the Secondary Hardening Reaction*, ph. d., Massachusetts Institute of Technology, 1989.

[83] C. LITTLE AND P. MACHMEIER, *Development of a Weldable High Strength Steel*, Final Report Covering period March 1973 - February 1975 AFML-TR-75-148, General Dynamics, Fort Worth, TX and Air Force Materials Laboratory (LLM), Wright-Patterson Air Force Base, Dayton, Ohio, 1975.

[84] G. G. LONG, S. KRUEGER, D. R. BLACK, J. CLINE, P. R. JEMIAN, AND R. A. GERHARDT, *Small-angle neutron scattering and small-angle x-ray scattering from bulk microporous silica*, in Neutron Scattering for Materials Science, S. Shapiro, S. Moss, and J. Jorgensen, eds., vol. 166, Pittsburg, PA, 1990, Materials Research Society, pp. 421–426.

[85] G. G. LONG, S. KRUEGER, P. R. JEMIAN, D. R. BLACK, H. E. BURDETTE, J. CLINE, AND R. A. GERHARDT, *Small-angle scattering determination of the microstructure of porous silica precursor bodies*, J Appl Cryst, 23 (1990), pp. 535–544.

[86] M. LUBAN AND M. DEUTSCH, *Exact Solution of the Slit-Height Correction Problem in Small-Angle X-ray Scattering. III. Derivation of Slit Correction Functions*, J Appl Cryst, 13 (1980), pp. 233–243.

[87] G. LUTZ, W. BUTLER, H. BERGMANN, P. HOLL, B. HOSTICKA, P. MANFREDI, AND G. ZIMMER, *Low noise monolithic cmos front end electronics*, Nucl Instrum and Meth Phys Res, A263 (1988), pp. 163–173.

[88] O. LYON, J. HOYT, R. PRO, B. DAVIS, B. CLARK, D. DE FONTAINE, AND J. SIMON, *Anomalous Small-Angle X-ray Scattering on Al-Zn and Al-Zn-Ag Alloys*, J Appl Cryst, 18 (1985), pp. 480–486.

[89] O. LYON AND J. SIMON, *Composition Changes During Unmixing of Ternary AlZnAg Alloys Studied by Anomalous Small-Angle Scattering*, Acta Metall, 34 (1986), pp. 1197–1202.

[90] ——, *Quantitative Measurement of Anomalous Small-Angle X-ray Scattering (ASAXS) in Some Al-Zn-Ag Alloys*, in Atomic Transport and Defects in Metals by Neutron Scattering, C. Janot, W. Petry, D. Richter, and T. Springer, eds., Berlin, 1986, Springer-Verlag, pp. 99–103.

[91] ——, *Anomalous Small-Angle X-ray Scattering Determination of the Partial Structure Factors and Kinetic Study of Unmixed Cu-Ni-Fe Alloys*, Phys Rev B, 35 (1987), pp. 5164–5174.

[92] S. MANNINEN, P. SUORTTI, M. COOPER, J. CHOMILIER, AND G. LOUPIAS, *X-ray resonant raman cross-section and yield in nickel*, Physical Review B, 34 (1986), pp. 8351–8356.

[93] S. MATSUOKA, S. T. KIM, AND J. R. WEERTMAN, *Mechanical & Microstructural Behavior of a Ferritic Stainless Steel under High Temperature Cycling*, in Proceedings of Topical Conference on Ferritic Alloys for use in Nuclear Energy Technologies, J. W. Davis and D. J. Michel, eds., vol. 6, Snowbird, Utah, 1983, TMS-AIME, pp. 507–516.

[94] P. J. MAZIASZ AND V. K. SIKKA, *The Effects of 25,000 h Aging at 480 to 700° C on Precipitation and Microstructural Stability in Several Heats of Tempered 9Cr-1MoVNb Steel*, Semiannual Progress Report for Period Ending September 30, 1985 DOE/ER-0045/15, Oak Ridge National Laboratory, 1986.

[95] W. MCMASTER, N. K. DEL GRANDE, J. MALLETT, AND J. HUBBELL, *Compilation of x-ray cross sections*, 1969.

[96] E. A. MENDOZA, E. WOLKOW, H. D. GAFNEY, D. SUNIL, M. RAFAILOVICH, J. SOKOLOV, G. G. LONG, AND P. R. JEMIAN, *The effect of photodeposited iron oxide and tin oxide on the consolidation of porous vycor glass*, Appl Phys Lett, 57 (1990), pp. 209–211.

[97] N. D. MERMIN, *Whats wrong with these equations?*, Physics Today, (1989), pp. 9–11.

[98] H. B. MICHAELSON, *How to Write and Publish Engineering Papers and Reports*, The Professional Writing Series, iSi Press, Philadelphia, 1982.

[99] J. S. MONTGOMERY, *M_2C Carbide Precipitation in Martensitic Cobalt-Nickel Steels*, ph. d., Northwestern University, 1990.

[100] P. J. NEDGINN AND T. L. BWORN, *Clog: An ada package for automatic footnote generation in unix*, Comm ACM, 27 (1984), p. 351.

[101] T. H. OD́ELL, *Electronic Circuit Design: Art and Practice*, Cambridge University Press, Cambridge, 1988.

[102] J. ORR, F. BECKITT, AND G. FAWKES, *The Physical Metallurgy of Chromium-Molybdenum Steels for Fast Reactor Boilers*, in Ferritic Steels for Fast Reactor Steam Generators, S. Pugh and E. Little, eds., London, 1978, British Nuclear Energy Society, pp. 91–109.

[103] I.-M. PARK, T. FUJITA, AND K. ASAKURA, *Microstructure and Creep Rupture Properties of a Low Si-12Cr-Mo-V-Nb Steel*, Trans ISIJ, 20 (1980), pp. 99–107.

[104] G. POROD, *General Theory*, in Small Angle X-Ray Scattering, New York City, Academic Press, 1982, pp. 17–52.

[105] J. POTTON, G. DANIELL, AND B. RAINFORD, *Application of Maximum Entropy to Small-Angle Neutron Scattering Data and Liquid and Amorphous Material Diffraction Data Analysis*, Inst Phys Conf Ser, #81, Chap. 3 (1986), pp. 81–86.

[106] ——, *A New Method for the Determination of Particle Size Distributions from Small-Angle Neutron Scattering Measurements*, J Appl Cryst, 21 (1988), pp. 891–897.

[107] ——, *Particle Size Distributions from SANS Data Using the Maximum Entropy Method*, J Appl Cryst, 21 (1988), pp. 663–668.

[108] B. POULSON, *The Effect of Sensitisation on the Stress Corrosion Resistance of 9%Cr 1%Mo Steel*, in Ferritic Steels for Fast Reactor Steam Generators, S. Pugh and E. Little, eds., London, 1978, British Nuclear Energy Society, pp. 413–418.

[109] L. RAYLEIGH, *The Incidence of Light upon a Transparent Sphere of Dimensions Comparable with the Wave-Length*, Roy Soc (London) Proc, A-84 (1911), pp. 25–46.

[110] C. H. REINSCH, *Smoothing by spline functions*, Numerische Mathematik, 10 (1967), pp. 177–183.

[111] ——, *Smoothing by spline functions. ii*, Numerische Mathematik, 16 (1971), pp. 451–454.

[112] L. ROESS AND C. SHULL, *X-ray Scattering at Small Angles by Finely Divided Solids. II. Exact Theory for Random Distributions of Spheroidal Particles*, J Appl Phys, 18 (1947), pp. 308–313.

[113] T. P. RUSSELL, *An Absolute Intensity Standard for SAXS Measured with Position-Sensitive Detectors*, J Appl Cryst, 16 (1983), pp. 473–478.

[114] T. P. RUSSELL, J. LIN, S. SPOONER, AND G. D. WIGNALL, *Intercalibration of Small-Angle X-ray and Neutron Scattering Data*, J Appl Cryst, 21 (1988), pp. 629–638.

[115] A. SALVA-GHILARDUCCI, J. P. SIMON, P. GUYOT, AND I. ANSARA, *Precipitation in Ternary Al-Zn-Ag Alloys Studied by Isotopic Contrast in Neutron Small Angle Scattering*, Acta Metall, 31 (1983), pp. 1705–1713.

[116] S. SANDERSON, *Interrelationships Between Mechanical Properties and Microstructure in a 9Cr1Mo Steel*, in Ferritic Steels for Fast Reactor Steam Generators, S. Pugh and E. Little, eds.,

London, 1978, British Nuclear Energy Society, pp. 120–127.

[117] J. SCHELTEN AND W. SCHMATZ, *Multiple-Scattering Treatment for Small-Angle Scattering Problems*, J Appl Cryst, 13 (1980), pp. 385–390.

[118] C. SHULL AND L. ROESS, *X-ray Scattering at Small Angles by Finely Divided Solids. I. General Approximate Theory and Applications*, J Appl Phys, 18 (1947), pp. 295–307.

[119] V. K. SIKKA, C. WARD, AND K. THOMAS, *Modified 9 Cr - 1 Mo Steel – An Improved Alloy for Steam Generator Application*, in Ferritic Steels for High Temperature Applications, A. K. Khare, ed., Metals Park, Ohio, 1983, American Society for Metals, pp. 65–84.

[120] J. SIMON, J. HOYT, O. LYON, R. PRO, B. DAVIS, D. DE FONTAINE, AND W. WARBURTON, *Determination of Anomalous Scattering Factors for Zinc and Silver in Al-Zn-Ag Alloys*, J Appl Cryst, 18 (1985), pp. 181–183.

[121] J. SIMON AND O. LYON, *A Determination of Partial Structure Factors in an Unmixed CuNiFe Alloy by Anomalous Small-Angle X-ray Scattering*, Phil Mag Lett, 55 (1987), pp. 75–80.

[122] ——, *Phase Separation in a Fe-Cr-Co Alloy Studied by Anomalous Small-Angle X-ray Scattering*, Acta Metall, 37 (1989), pp. 1727–1733.

[123] ——, *The Nature of the Scattering Tail in Cu-Ni-Fe and Invar Alloys Investigated by Anomalous Small-Angle X-ray Scattering*, J Appl Cryst, 24 (1991), pp. 1027–1034.

[124] J. SIMON, O. LYON, AND D. DE FONTAINE, *A Comparison of the Merits of Isotopic Substitution in Neutron Small-Angle Scattering and Anomalous X-ray Scattering for the Evaluation of Partial Structure Functions in a Ternary Alloy*, J Appl Cryst, 18 (1985), pp. 230–236.

[125] J. SIMON, O. LYON, F. FAUDOT, J. RZEPSKI, O. DIMITROV, L. BOULANGER, AND G. MARTIN, *A Study of Phase Stability in INVAR Fe-Ni Alloys by Anomalous X-ray Scattering*, in Physical Metallurgy of Controlled Expansion Invar-Type Alloys, K. Russell and D. Smith, eds., The Minerals, Metals & Materials Society, 1990, pp. 51–63.

[126] J. P. SIMON, O. LYON, A. BRUSON, AND F. RIEUTFORD, *Anomalous Small-Angle X-ray Diffraction of an Nd-Fe Multilayer*, J Appl Cryst, 24 (1991), pp. 156–153.

[127] J. SKILLING AND R. BRYAN, *Maximum Entropy Image Reconstruction: General Algorithm*, Mon Not R Astr Soc, 211 (1984), pp. 111–124.

[128] P. S. SKLAD, R. CARPENTER, AND V. K. SIKKA, *Creep Microstructure of Ferritic Fe-9Cr-1Mo Steel*, Metals and Ceramics Division, Materials Science Program, Annual Progress Report for Period Ending June 30, 1980 ORNL-5672, Oak Ridge National Laboratory, 1980.

[129] P. S. SKLAD AND V. K. SIKKA, *Microstructural Observations of Strain Softening in Modified 9 Cr-1 Mo Ferritic Steel*, Metals and Ceramics Division, Materials Science Program, Annual Progress Report for Period Ending June 30, 1981 ORNL/TM-7970, Oak Ridge National Laboratory, 1981.

[130] J. SPARKS, CULLIE J., *Inelastic resonance emission of x-rays: Anomalous scattering*, Phys Rev Lett, 33 (1974), pp. 262–265.

[131] ——, *Excess diffuse x-ray scattering and anomalous dispersion*, in Anomalous Scattering, S. Ramaseshan and S. Abrahams, eds., Munksgaard, Copenhagen, 1975, pp. 175–196.

[132] J. STEEDS AND J. MANSFIELD, *Convergent Beam Electron Diffraction of Alloy Phases*, A. Hilger, Boston, 1984.

[133] H. STUHRMANN, , A Phys Chem, 72 (1970), p. 177.

[134] ——, *Anomalous Small-Angle Scattering*, Q Rev Biophys, 14 (1981), pp. 433–460.

[135] ——, *Resonance Scattering Macromolecular Structure Research*, Adv Polym Sci, 67 (1985), pp. 123–163.

[136] H. STUHRMANN AND A. GABRIEL, *A SAS Camera for Resonant Scattering Experiments at DORIS*, J Appl Cryst, 16 (1983), pp. 563–571.

[137] H. STUHRMANN AND H. NOTBOHM, *Configuration of the Four Iron Atoms in Dissolved Human Hemoglobin as Studied by Anomalous Dispersion*, Proc Natl Acad Sci USA, 78 (1981), pp. 6216–6220.

[138] H. B. STUHRMANN, *Anomalous Dispersion of Small-Angle Scattering of Horse-Spleen Ferritin at the Iron K Absorption Edge*, Acta Cryst, A36 (1980), pp. 996–1001.

[139] D. H. TEMPLETON, L. K. TEMPLETON, J. C. PHILLIPS, AND K. O. HODGSON, *Anomalous scattering of x-rays by cesium and cobalt measured with synchrotron radiation*, Acta Cryst, A36 (1980), pp. 436–442.

[140] C. TOWNLEY, *Design Codes for Fast Reactor Steam Generators*, in Ferritic Steels for Fast Reactor Steam Generators, S. Pugh and E. Little, eds., London, 1978, British Nuclear Energy Society, pp. 64–68.

[141] J. TULKKI, *Evolution of the inelastic x-ray scattering by l & m electrons into k flourescence in argon*, Phys Rev A, 27 (1983), pp. 3375–3378.

[142] J. TULKKI AND T. ÅBERG, *Statistical theory of electronic raman resonance scattering by oriented atoms*, J Phys B: Atom. Molec. Phys., 13 (1980), pp. 3341–3360.

[143] ——, *Behaviour of raman resonance scattering across the k x-ray absorption edge*, J Phys B: At. Mol. Phys., 15 (1982), pp. L435–L440.

[144] J. VITEK AND R. L. KLUEH, *Precipitation Reactions During the Heat Treatment of Ferritic Steels*, Metall Trans, 14A (1983), pp. 1047–1055.

[145] G. D. WIGNALL AND F. BATES, *Absolute calibration of small-angle neutron scattering data*, J Appl Cryst, 20 (1987), pp. 28–40.

[146] C. WILLBY AND J. WALTERS, *Material Choices for the Commercial Fast Reactor Steam Generators*, in Ferritic Steels for Fast Reactor Steam Generators, S. Pugh and E. Little, eds., London, 1978, British Nuclear Energy Society, pp. 40–49.

[147] P. WILTZIUS, F. BATES, S. DIERKER, AND G. D. WIGNALL, *Structure of porous vycor glass*, Phys Rev A, 36.6 (1987), pp. 2991–2994.

[148] D. WOOD, *Effects of a Sodium Environment on the Mechanical Properties of Ferritic Steels*, in Ferritic Steels for Fast Reactor Steam Generators, S. Pugh and E. Little, eds., London, 1978, British Nuclear Energy Society, pp. 293–299.

[149] W. H. ZACHARIASEN, *Theory of X-ray Diffraction in Crystals*, John Wiley & Sons, Inc., New York City, 1945.

Index

χ^2, 12
h-resolution, 22

absolute intensity, 7, 37, 44
amplifier
    charge integrating, 28
    current-to-voltage electrometer, 28
anomalous dispersion, 14, 16, 49, 52
    data collection method, 49
ASAXS, 1, 14, 48
    detectability, 18
    gradient method, 21
atomic scattering factor, 14

binding energy, electron, 14
Bonse-Hart, 22

desmearing, 10, 38
    convergence, 10
    extrapolation, 11
    feedback equation, 10
    initial guess, 10
    smoothing, 10
    termination effect, 11
detector
    amplifier, 28
    photodiode, 27
dispersion relation, 15

energy
    calibration, 49

`fPrime.FOR`, 15

Guinier equation, 8

Hooke's law, v, vii

interference, 41, 43

Kramers-Kronig integral, 15, 49, 51, 58, 67

`Lake.FOR`, v, 10, 53, 89
linear inverse problem, 11

`Maxe.FOR`, 13, 38, 53, 105
maximum entropy, 11, 38, 43
    convergence, 12, 54
    functional, 12
`MaxSAS.FOR`, v, 13, 38, 43, 53, 54, 60, 70, 105
Model II, 55
Modified Fe9Cr1Mo steel, 31
monochromator, 33

optical theorem, 15
ortho-equilibrium, 69, 72, 75

para-equilibrium, 69, 72, 75
photodiode
    detector, 27, 35
    efficiency, 27
    electrometer, 27, 28
    photocurrent, 27
Porod equation, 8

resonant Raman scattering, 21
rocking curve, 25

samples
    AF1410 steel, 68
    bulk microporous silica, 81
    Modified Fe9Cr1Mo steel, 31, 45
    polystyrene spheres, 41
    porous Vycor™ glass, 83
scattering contrast, 16, 52
scattering invariant, 17
scattering length density, 15
scattering strength, 17

scattering, type 3, 83
scattering, types, 41
size distribution analysis, 38
synchrotron beam line, 32

ThermoCalc™, 65, 68, 70, 75
thickness, 7, 48
thinning solution, 31

USAXS
    data reduction, 36
    instrument, 32, 34
    raw data, 37
    scans, 35

volume fraction, 17